# NONLINEAR MICROPOLAR BEAM AND PLATE THEORIES WITH APPLICATIONS TO LATTICE CORE SANDWICH STRUCTURES AND DUAL MESH CONTROL DOMAIN METHOD FOR STRUCTURAL ELEMENTS

A Dissertation

by

PRANEETH NAMPALLY

Submitted to the Graduate and Professional School of
Texas A&M University
in partial fulfillment of the requirements for the degree of

DOCTOR OF PHILOSOPHY

| | |
|---|---|
| Chair of Committee, | J.N.Reddy |
| Committee Members, | Anastasia Muliana |
| | Alan Palazzolo |
| | Raytcho Lazarov |
| Head of Department, | Andreas A Polycarpou |

August 2021

Major Subject: Mechanical Engineering

ABSTRACT

In the first part of the dissertation we develop nonlinear beam and plate theories based on micropolar elasticity and formulate the corresponding finite element models. The developed nonlinear beam and plate finite element models are then used to analyze the bending of lattice core sandwich beams and plates that are modeled as equivalent-single layer beams or plates based on micropolar elasticity. The rapid growth of manufacturing technologies has enabled the design and development of materials whose microstructure can be architected to achieve desired functionality. Lattice core sandwich structures are among such architected materials whose microstructure is the order of few centimeters. Modeling these structures with complete geometric details can be computationally expensive. Hence, efforts are made to model such structures as equivalent-single layer beams or plates with non-classical continuum theories like micropolar elasticity. One such methodology to construct equivalent-single layer beams [1] of web-core lattice beams is described and extended to other core structures.

The second part of this dissertation deals with formulation of a novel numerical method, named *Dual Mesh Control Domain Method* (DMCDM), for functionally graded structural elements; namely beams and plates. For the past few decades finite element method has been the dominant numerical method for analysis of solids and structures while finite volume method has been dominant in the field of fluid dynamics. Both the methods have their strengths and weaknesses. For example, representing a system as a collection of connected finite elements often results in a discontinuous representation of the gradients of the solution, unless so-called C-continuity is used. However, finite element method retains the concept of duality between the secondary and primary variables of the problem and thereby simplify the process of applying boundary conditions. On the other hand, although finite volume method involves fictitious nodes at the boundary control volumes and thereby complicating the application of boundary conditions, it satisfies the integrals of governing equations (with out any weight functions) on control volumes and calculates secondary variables on the interfaces of the control volume where they are uniquely defined.

Considering these observations, Professor J. N. Reddy has recently proposed a novel numerical method named Dual Mesh Control Domain Method (DMCDM). It incorporates the best features of both finite element method and finite volume method by using two different meshes. A primal mesh for interpolating the primary variables and dual mesh for satisfy the governing equations in integral form without weight functions. The details of this method and its application to structural elements is discussed in detail.

DEDICATION

To my parents

# ACKNOWLEDGMENTS

I would like to thank my teacher and advisor, Dr . J. N. Reddy, for his support and guidance during the course of my Ph.D. studies at Texas A&M University. I am fortunate for having a chance to learn finite element method and mechanics in general from a passionate teacher, Dr. J. N. Reddy. My sincere thanks to Dr. Anastasia Muliana, Dr. Alan Palazzolo and Dr. Raytcho Lazarov for serving on my Ph.D. committee. I thoroughly enjoyed the courses by Dr. Alan Palazzolo and Dr. Raytcho Lazarov.

I would like to thank all the members of Advanced Computational Mechanics Laboratory for their support and help during the course of my Ph.D. Special thanks to Dr. Anssi Karttunen, Dr. Shubhankar Roy Chowdhury and Dr. Archana Arbind for taking time to help me at various stages of my research. I am grateful to my friends Anita, Bajrang, Utkarsh, Vaishnav and Vishav for making life in College Station easier. Finally, I am thankful to my parents and my brother for their constant love and support. This endeavor would have not been possible without their encouragement.

CONTRIBUTORS AND FUNDING SOURCES

## Contributors

This work was carried out under the supervision of a dissertation committee consisting of Professors J. N. Reddy as the advisor, and Alan Palazzolo and Anastasia Muliana of the Department of Mechanical Engineering and Raytcho Lazarov of the Department of Mathematics as the members.

The ABAQUS results used in chapters 4 and 5 for validation of finite element results were provided by Dr. Anssi Karttunen.

## Funding Sources

The research reported herein was supported, in parts, by the Oscar S. Wyatt Jr. Endowed Chair, the O'Donnell Foundation Chair IV, Technical Data Analysis (TDA), and the NSF Grant (FAIN) 1952873.

TABLE OF CONTENTS

Page

LIST OF FIGURES

FIGURE Page

LIST OF TABLES

TABLE Page

# 1. INTRODUCTION AND LITERATURE REVIEW *

## 1.1 Micropolar elasticity

The idea of a continuum whose material particles have independent rotational degrees of freedom along with translational degrees of freedom was first proposed by Cosserat brothers more than one hundred years ago [11], which was later named as a Cosserat (or micropolar) continuum. The theory was left dormant for about fifty years, until it was revived by Eringen and his coworkers [12, 13, 14]. Since then micropolar elasticity has found applications in modeling complex microstructures like soils, polycrystalline and composite materials [15, 16, 17, 18], nano structures [19], porous media and foams [20, 21, 22], and even animal bones [23].

With increased use of micro and nano structures, where the material length scales play an important role, there has been an impetus in developing beam and plate theories that can bring microstructural length scales into the problem. This resulted in a plethora of beam and plate theories based on various non-classical continuum theories. Various beam models are proposed based on modified couple stress theories [24, 25, 26, 27, 28], strain gradient theories [29, 30, 31], Eringen non-local elasticity [32, 33, 34]. Similarly, such beam theories are also developed using micropolar elasticity. For example, [35] proposed a size-dependent micropolar beam which was enhanced by von Kármán nonlinearity. However, the use of micropolar beam and plate theories is not limited to micro and nano structures. Various homogenization techniques have been proposed to model lattice structures [36, 37, 38, 9, 5, 39], metamaterials [40], and nano materials as equivalent micropolar material structures. Such homogenization techniques usually seek to express the constitutive constants of the equivalent micropolar material in terms of the microstructural properties of the considered material (or structure) [4, 9]. Thus, the need for micropolar beam and plate theories is

*Parts of this chapter are reprinted with permission from "Geometrically nonlinear Euler–Bernoulli and Timoshenko micropolar beam theories" by P. Nampally and J. N. Reddy, 2020. Acta Mechanica, vol. 231, no. 10, pp. 4217–4242, Copyright (2020) Springer-Verlag GmbH Austria, part of Springer Nature and from "Nonlinear finite element analysis of lattice core sandwich beams" by P. Nampally, A. T. Karttunen, and J. N. Reddy, 2019, European Journal of Mechanics - A/Solids, vol. 74, pp. 431–439, Copyright (2018) Elsevier Masson SAS and from "A dual mesh finite domain method for the analysis of functionally graded beams" by J. N. Reddy and P. Nampally, 2020. Composite Structures, vol. 251, p. 112648, Copyright (2020) Elsevier Ltd.

warranted by the range of applications of micropolar elasticity, especially for continuum models of microstructures.

While many micropolar beam and plate theories have been proposed (see, e.g., [41, 42]), often they only consider linear strains (or linearized Cosserat deformation gradient) resulting in linear micropolar beam or plate theories. However, certain applications of micropolar elasticity may require the use of nonlinear or moderate nonlinear strains. For example, micro and nano beams usually undergo moderately large rotations which inherently bring nonlinearity into the problem. There have been certain attempts to bring such a nonlinearity into the micropolar beam and plate theories. For example, in [35] the use of the von Kármán nonlinearity to model the moderate rotations of micropolar beams was proposed. In [5] a similar theory was used in modeling the behavior of lattice core beams. A geometrically exact micropolar Timoshenko beam, where the complete nonlinear Cosserat deformation gradient was taken into account was developed in [40]. The approximation of small microrotations to obtain a nonlinear micropolar plate theory was considered in [43]. Considering this, one aspect of this dissertation is to explore the possible nonlinear theories for micropolar beams and plates. These topics are covered in chapters 2 and 3 respectively.

With the revived interest in micropolar elasticity [44, 12], considerable work has been put into developing appropriate finite element models for micropolar continua in general; see, for example, [45, 46, 47, 48]. A few recent papers on the finite element models of micropolar plates include [49, 50, 51]. Various finite element models have been proposed for the bending analysis of micropolar beams as well. In [42] a 3-D non-compatible finite elements were used to analyze the bending of beams, and three different elements for plane micropolar elasticity were proposed and used to analyze thin in-plane beams in [52]. A 1-D micropolar beam finite element model using Lagrange interpolation functions was developed in [53]. A finite element model for a micropolar Timoshenko beam with the microrotation assumed to be equal to the cross-sectional rotation was derived in [54]. More recently, a 27-node 3-D finite element for the analysis of beams was proposed [50]. Most of the literature on the finite element analysis of micropolar beams and plates usually consider only linear strains. Given the difficulty in finding closed-form solutions to nonlinear

equations, generally the finite element method is used in obtaining approximate solutions to the problem. Thus, appropriate finite element models for the nonlinear theories of micropolar beams and plates considered in chapters 2 and 3 are also developed.

### 1.1.1 Kinematics of micropolar continuum

Unlike the classical continuum, in micropolar continuum the material particles are assumed to have orientation [55, 56, 44, 57]. Thus the material particles in micropolar continuum undergo translation and rotation (called microrotation, which account for the change in the orientation of material particle) during deformation. Therefore, the study of micropolar continuum requires a displacement vector $\mathbf{u}$ and an orthogonal microrotation tensor $\mathbf{Q}$. To account for these microrotations in the kinematics of the continuum, two kinematic tensors are defined. These two tensors are called *Cosserat Deformation Gradient* ($\mathbf{E}$) and *Wryness Tensor* ($\mathbf{\Gamma}$) [44]. The definitions of these tensors are as follows [58, 59]:

$$\mathbf{E} = \mathbf{Q}^T(\mathbf{I} + \boldsymbol{\nabla}\mathbf{u}) - \mathbf{I} \tag{1.1.1}$$

$$\mathbf{\Gamma} = -\frac{1}{2}\epsilon : (\mathbf{Q}^T\boldsymbol{\nabla}\mathbf{Q}) \tag{1.1.2}$$

where $\mathbf{u}$ is the displacement vector with three independent components $(u_1, u_2, u_3)$ along the Cartesian coordinates and $\mathbf{Q}$ is second-order microrotation tensor, $\mathbf{I}$ is the second-order identity tensor, and $\epsilon$ is the third-order skew Ricci tensor (permutation tensor). Here $\boldsymbol{\nabla}$ represents the gradient operator with respect to the reference configuration.

Since the microrotation tensor $\mathbf{Q}$ is a proper orthogonal tensor such that $\mathbf{Q}^{-1} = \mathbf{Q}^T$ and det$\mathbf{Q} = 1$, only three of the nine components of the microrotation tensor are independent. Thus, it is helpful to parameterize the microrotation tensor such that it can be represented in terms of a microrotation vector with three independent components [58, 59]:

$$\mathbf{Q} = \cos\theta\mathbf{I} + \frac{1-\cos\theta}{\theta^2}\boldsymbol{\psi}\otimes\boldsymbol{\psi} + \frac{\sin\theta}{\theta}\boldsymbol{\psi}\times\mathbf{I} \tag{1.1.3}$$

$$\mathbf{Q}^T = \cos\theta\mathbf{I} + \frac{1-\cos\theta}{\theta^2}\boldsymbol{\psi}\otimes\boldsymbol{\psi} - \frac{\sin\theta}{\theta}\boldsymbol{\psi}\times\mathbf{I} \tag{1.1.4}$$

where $\boldsymbol{\psi} = \theta\hat{\mathbf{e}}$ is the microrotation vector whose direction is along the unit vector $\hat{\mathbf{e}}$ and has a magnitude $\theta \in (-2\pi, 2\pi)$. The rotation vector can also be written as

$$\boldsymbol{\psi} = \psi_1\hat{\mathbf{e}}_1 + \psi_2\hat{\mathbf{e}}_2 + \psi_3\hat{\mathbf{e}}_3 \tag{1.1.5}$$

where $\psi_1$, $\psi_2$ and $\psi_3$ are the components of the microrotation vector along the Cartesian coordinate $\hat{\mathbf{e}}_1$, $\hat{\mathbf{e}}_2$ and $\hat{\mathbf{e}}_3$ respectively such that

$$\theta = \sqrt{\psi_1^2 + \psi_2^2 + \psi_3^2} \tag{1.1.6}$$

Writing Eq. (1.1.1) and Eq. (1.1.2) in indicial notation we have

$$E_{ij} = (\cos\theta - 1)\,\delta_{ij} + \cos\theta u_{i,j} + \frac{1-\cos\theta}{\theta^2}\left(\psi_i\psi_j + \psi_i\psi_k u_{k,j}\right) - \frac{\sin\theta}{\theta}\left(\epsilon_{mji}\psi_m + \epsilon_{nki}\psi_n u_{k,j}\right) \tag{1.1.7}$$

$$\Gamma_{ij} = \frac{\sin\theta}{\theta}\psi_{i,j} + \frac{\theta - \sin\theta}{\theta^3}\psi_i\psi_k\psi_{k,j} - \frac{1-\cos\theta}{\theta^2}\epsilon_{lki}\psi_l\psi_{k,j} \tag{1.1.8}$$

Since the the material particles in a solid continuum will have restricted microrotations compared to a fluent continuum, it is safe to assume that the magnitude of microrotations of each material particle of a solid continuum are very small, i.e., $|\theta| \to 0$ [44, 59, 60]. Following this approximation we have

$$\begin{aligned}
\lim_{\theta\to 0}\cos\theta = 1, \qquad & \lim_{\theta\to 0}\frac{1-\cos\theta}{\theta^2} = \frac{1}{2} \\
\lim_{\theta\to 0}\frac{\sin\theta}{\theta} = 1, \qquad & \lim_{\theta\to 0}\frac{\theta-\sin\theta}{\theta^3} = \frac{1}{6} \\
\psi_i\psi_j \approx 0, \qquad & \psi_i\psi_k\psi_{k,j} \approx 0 \\
\psi_i\psi_k u_{k,j} \approx 0, \qquad & \psi_l\psi_{k,j} \approx 0
\end{aligned}$$

which will result in

$$E_{ij} \approx e_{ij} = u_{i,j} + \epsilon_{ijm}\psi_m + \epsilon_{ikn}\psi_n u_{k,j} \tag{1.1.9}$$

$$\Gamma_{ij} \approx \eta_{ij} = \psi_{i,j} \tag{1.1.10}$$

If we further assume that the displacement gradients are small [44, 59] then we can linearize the Cosserat deformation tensor to get

$$E_{ij} \approx \varepsilon_{ij} = u_{i,j} + \epsilon_{ijm}\psi_m \tag{1.1.11}$$

We can break the Cosserat deformation gradient tensors in Eq. (1.1.9) and Eq. (1.1.11) into symmetric and anti-symmetric parts, to define the following

$$\begin{aligned} e_{ij}^{(s)} &= \frac{e_{ij} + e_{ji}}{2} = \frac{u_{i,j} + u_{j,i}}{2} + \frac{\epsilon_{ikn}\psi_n u_{k,j} + \epsilon_{jkn}\psi_n u_{k,i}}{2} \\ e_{ij}^{(a)} &= \frac{e_{ij} - e_{ji}}{2} = \frac{u_{i,j} - u_{j,i}}{2} + \epsilon_{ijm}\psi_m + \frac{\epsilon_{ikn}\psi_n u_{k,j} - \epsilon_{jkn}\psi_n u_{k,i}}{2} \end{aligned} \tag{1.1.12}$$

$$\begin{aligned} \varepsilon_{ij}^{(s)} &= \frac{\varepsilon_{ij} + \varepsilon_{ji}}{2} = \frac{u_{i,j} + u_{j,i}}{2} \\ \varepsilon_{ij}^{(a)} &= \frac{\varepsilon_{ij} - \varepsilon_{ji}}{2} = \frac{u_{i,j} - u_{j,i}}{2} + \epsilon_{ijm}\psi_m \end{aligned} \tag{1.1.13}$$

For the linear isotropic micropolar solid we have the following constitutive relations:

$$\sigma_{ij} = \lambda\varepsilon_{kk}\delta_{ij} + (\mu + \kappa)\varepsilon_{ij} + \mu\varepsilon_{ji} \tag{1.1.14}$$

$$r_{ij} = \alpha\eta_{kk}\delta_{ij} + \beta\eta_{ji} + \gamma\eta_{ij} \tag{1.1.15}$$

where $\lambda$, $\mu$, $\kappa$, $\alpha$, $\beta$, $\gamma$ are the micropolar constitutive constants [44]. Defining the symmetric and anti-symmetric stresses as

$$\sigma_{ij}^{(s)} = \frac{\sigma_{ij} + \sigma_{ji}}{2} \qquad \sigma_{ij}^{(a)} = \frac{\sigma_{ij} - \sigma_{ji}}{2}$$

we can write constitutive relation (1.1.14) in terms of the symmetric and anti-symmetric strains and stresses as:

$$\sigma_{ij}^{(s)} = \lambda \varepsilon_{kk}^{(s)} \delta_{ij} + (2\mu + \kappa)\varepsilon_{ij}^{(s)} \tag{1.1.16}$$

$$\sigma_{ij}^{(a)} = \kappa \varepsilon_{ij}^{(a)} \tag{1.1.17}$$

## 1.2 Lattice core sandwich structures

The rapid growth of manufacturing technologies has enabled the design and development of materials whose microstructure can be architected to achieve desired functionalities, including high stiffness-to-weight ratios [61]. The scale of the architected microstructure can range from a few nanometers [62] to several meters. Lattice core sandwich structures are a class of architected materials whose microstructure is typically in the order of centimeters [63, 64]. A variety of manufacturing techniques are available for the production of sandwich panels [65, 66]. A typical sandwich panel consists of a thick, low-stiffness core between two relatively thin but stiff face sheets. The face sheets take bending and in-plane loads while the core carries transverse shear loads [63, 67]. The face sheets and core can be made of the same or different materials and some possible core structures include, for example, foam, solid, honeycomb, and truss cores [68] (see Fig. 1.1). A sandwich panel generally has a high bending stiffness compared to a single solid plate of the same dimensions made of either the face sheet or core material and the panel weighs considerably less than the solid plate making it a weight-efficient structure [67]. Sandwich panels are designed so that the face sheets take the bending loads while the core carries most of the shear loading [69].

Sandwich panels have received a lot of attention because of their superior performance compared to their monolithic counterparts made solely of either the face sheet material or the core material. For example, sandwich panels have found applications in aerospace industry [70, 71] and marine industry [72, 73]. They are also being used in air and underwater blast resistance structures [74]. Laser-welded web-core steel sandwich panels have found applications in shipbuilding

as staircase landings and non-structural walls [75, 76] and also show good potential for applications in bridges and buildings [77, 78, 79, 80].

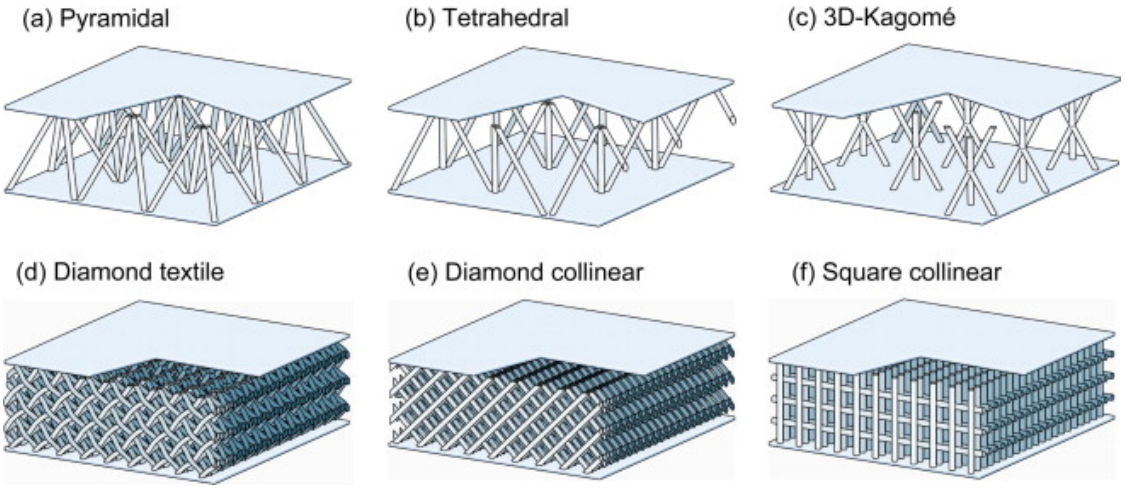


Figure 1.1: Lattice core sandwich panels with with various core topologies (Reprinted with permission from [2]).

The number of applications for sandwich panels is increasing rapidly. The required accuracy in the structural analysis of the panels depends on the type of the application considered. For example, in air-crafts a very detailed response of the sandwich structure may be required, whereas an overall global response may suffice in residential buildings when the natural vibration frequencies are of interest, for example. In any case, there is a need for appropriate modeling tools for different applications. Reviews on the modeling of sandwich structures have been given by several authors [81, 82, 83, 84, 64]. Modeling methods for sandwich panels can be broadly classified as: (a) Complete 3-D analysis (computational or analytical), with complete details of the face sheets and the core structure considered; (b) layer-wise modeling with the faces and core considered as separate continuum layers [85]; (c) statically equivalent single layer (ESL) models. Although computational 3-D and layer-wise analyses give very detailed stress distributions for the panels, they come with the inherent disadvantage of including a large number of variables and, thus, the computational analysis of them can be very burdensome. Therefore, equivalent single layer theories such

as the ESL first-order shear deformation (FSDT) beam and plate models are attractive especially when the global response of the structure is of main interest without accounting for every small detail. Extensive literature exists on the modeling of sandwich beam, plates and shells by ESL theories, see, for example [86, 87, 88, 82, 43].

Of the non-classical continuum mechanics theories to model lattice core sandwich panels, there equivalent single layer models of lattice structures based on the strain gradient theory [89, 90], couple stress theory [91], and micropolar theory [1, 92, 40], which is particularly well-suited for predicting the structural response of bending-dominated lattice panels accurately. This may be attributed to the additional, independent rotational degrees of freedom the micropolar theory provides. Detailed bending-dominated lattice unit cells may be constructed using beam and shell finite elements and the micropolar theory allows us to pass information related to both the translational and the *rotational* degrees of freedom of the beam and shell elements from a detailed FE model into, for example, a 2-D ESL plate model through a homogenization process. Recently, micropolar theory was used to model 2-D web-core sandwich structure, which can be considered as a beam frame, as 1-D equivalent single layer micropolar beam in [1, 4] and 3-D web-core sandwich panels were modeled as 2-D orthotropic equivalent-single layer first-order shear deformation (ESL-FSDT) micropolar plates in [9]. Inspired by these works, in chapter 3 we extend these modeling techniques to other lattice core beams (hexagonal, Y-frame, corrugate) and incorporate geometric nonlinearity into the theory to account for moderate rotations of these beams (see chapter 2). In chapter 4 we consider the nonlinear bending and free vibrations of web-core and pyramid core lattice core sandwich plates, which are modeled as equivalent-single layer micropolar plates following the similar techniques given in [9]. We also incorporate geometric nonlinearity into the problem to model moderate rotations of these plates.

### 1.3 Dual mesh control domain method

With increase in the computational power, numerical methods have developed tremendously during the past few decades with finite element method (FEM) dominating the structural mechanics arena and finite volume method (FVM) dominating the fluid dynamics arena. Typically, all

approximate methods convert a differential equation described by the operator equation $Au = f$ governing a variable $u$ to a set of algebraic equations of the matrix form $\mathbf{Ku} = \mathbf{F}$, among the nodal values of the variable $u$ and its dual variable $F$ at a selected number of points (called nodes) in the domain and on its boundary. The actual process that results in the final matrix equation $\mathbf{Ku} = \mathbf{F}$ differs from one method to another. The FEM is based on the following three-fold idea [93]:

(1) the total domain $\Omega$ can be represented as a collection of a finite number of non-overlapping but interconnected (at the boundaries of the) subdomains, called *finite elements*, $\Omega^e$; the elements are of a particular geometry that allows the construction of approximation (or interpolation) functions;

(2) over each element $\Omega^e$, the dependent unknown $u$ is interpolated through a set of points (nodes) of the element as $u \approx \sum u_j \psi_j$, $u_j$ being the value of $u$ at the $j$th node and $\psi_j$ are suitable approximation functions, and the governing equation is converted to a set of algebraic equations $\mathbf{K}^e\mathbf{u}^e = \mathbf{F}^e$ (called *finite element model*) using a method of approximation (e.g., weak-form Galerkin or Ritz, subdomain, least-squares, and so on); the element equations contain nodal variables from only the element under consideration; and

(3) the element equations from all elements are put together (element assembly) using balance and continuity conditions at element interfaces to obtain a global set of algebraic equations, $\mathbf{Ku} = \mathbf{F}$, which are then solved after applying the boundary conditions at the nodes.

There are two drawbacks of the FEM. First, representing a system as a collection of connected finite elements often results in a discontinuous representation of the gradients of the solution, unless so-called C-continuity is used (which in turn dictates the element type, both in geometry and degrees of freedom per node). Second, the satisfaction of the governing equations in the weak-form or weighted-integral sense tends to smooth the solution and thereby predicts diffuse solutions when applied to problems with steep gradients.

In the FVM [94] one represents a given domain, much like in FEM, as a collection of non-overlapping domains, called *control volumes*. Then an integral (not a weighted-integral) statement

of the governing equation, after invoking the Green–Gauss theorem to covert the domain integral to the boundary integral, is used over a typical control volume to derive the algebraic equations. In the FVM, at the centroid of each control volume lies a mesh point, and the derivatives of the dependent variables at the control volume interfaces are calculated in terms of the values of the dependent variables at the mesh points using Taylor's series approximations (i.e., "finite difference-like" approximations). Thus, there is no explicit interpolation (although there is a polynomial approximation implied by the truncated Taylor's series) of the dependent variables is employed in the FVM. The algebraic equations derived using a typical control volume involve mesh point values from the neighboring control volumes (a notable difference from FEM), naturally connecting the control volumes. The resulting algebraic equations resemble more like finite difference stencils, which are valid for a typical mesh point in the entire domain and include contributions from the neighboring mesh points to obtain the required algebraic equations of the entire mesh. Thus, in the FVM there is no formal assembly of control volumes is involved. The imposition of gradient type boundary conditions involves, sometimes, fictitious nodes from outside the domain, and there is no unique methodology followed for the imposition of boundary conditions or the evaluation of integral expressions in the FVM. The major advantage of the FVM however, is the satisfaction of the global form of the governing equations exactly and thus resulting in a better accuracy for the secondary variables like fluxes and forces.

Recently, Reddy [95] introduced a numerical approach termed the *dual mesh finite domain method* (DMFDM) for the solution of second-order differential equations in one and two dimensions with a single unknown. The dual mesh finite domain was later renamed as *dual mesh control domain method* (DMCDM) in [96]. In the DMCDM, the domain is discretized using two meshes; a primal mesh which connect the nodes at which the primary variables are to be evaluated and a dual mesh upon which the governing equations are satisfied in an integral sense. We call the elements of the primal mesh the *primal mesh elements* and elements of the dual mesh the *control domains*. The primary variables of the problem are approximated using Lagrange interpolation functions upon each of the primal mesh elements similar to the finite element method. However, unlike the finite

element method where the governing equations are satisfied on each finite element in a weighted integral sense, the governing equations in dual mesh control domain method are satisfied on the control domains of each node as an integral statement without any weighting function; a similarity shared with the finite volume method. Further, since the control domain already connects the primal mesh elements which share the node about which the control domain is centered, the connectivity of the primary variables at the nodes is automatically satisfied. Thus, in dual mesh control domain method we obtain the global equations directly unlike in finite element method where we write the finite element equations first and the global equations are then obtained from element equation assembly. Further, in dual mesh control domain method the secondary variables dual to the primary variables are not expressed in terms of the primary variables on the boundaries of the computational domain. This facilitates the retention of the duality concept used in finite element method (see [95, 96]). Thus, the DMCDM can be viewed as a hybrid method that makes use of two best features of the FEM [93], namely, (a) the interpolation of the variables and (b) imposition of physical boundary conditions, and two salient features of the FVM [94]: (a) satisfaction of the global balance equations over the finite domain and (b) computation of the secondary variables at the boundaries of the control domains where they are uniquely defined.

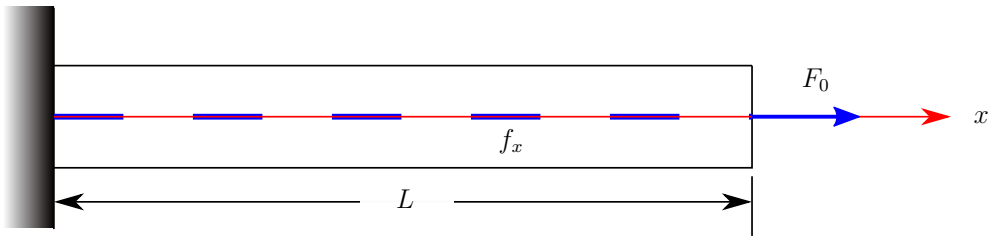


Figure 1.2: Elastic bar fixed at one end with axial distributed load $f_x$ and concentrated load $F_0$ at free end

To illustrate the working of dual mesh control domain method for 1-D problems, we will consider a 1-D elastic bar of length $L$, with one end fixed and a concentrated force acting on the other

end. The area of cross-section of the bar is $A$ and Young's modulus is $E$. The governing equation of the 1-D elastic bar, in the presence of a distributed axial force $f_x$, is given by

$$-\frac{d}{dx}\left[EA\frac{du}{dx}\right] - f_x = 0, \qquad 0 < x < L \tag{1.3.1}$$

$$u(0) = 0, \qquad EA\frac{du}{dx} = F_0 \tag{1.3.2}$$

The exact solution of the bar for the above boundary conditions and constant distributed force $f_x = f$ is given by

$$u(x) = \frac{fx^2}{2EA} + \frac{(F_0 - fL)x}{EA} \tag{1.3.3}$$

Let us discretize the domain with two primal mesh elements, $\Omega_p^{(i)}$ $(i = 1, 2)$, (each of length $h = L/2$) and three dual mesh elements, $\Omega_{CD}^{(I)}$ $(I = 1, 2, 3)$ (see Fig.1.3). The primary variable $u$ is interpolated on each of the primal mesh elements using 1-D linear Lagrange interpolation functions [93]. That is, $u$ can be written as

$$u(x) \approx \begin{cases} U_1\psi_1^{(1)}(x) + U_2\psi_2^{(1)}(x), & \forall \quad x \in (0, L/2) \\ U_2\psi_1^{(2)}(x) + U_3\psi_2^{(2)}(x), & \forall \quad x \in (L/2, L) \end{cases} \tag{1.3.4}$$

where

$$\begin{aligned} \psi_1^{(1)}(x) &= \frac{h - x}{h}, \quad \psi_2^{(1)}(x) = \frac{x}{h} \\ \psi_1^{(2)}(x) &= \frac{2h - x}{h}, \quad \psi_2^{(2)}(x) = \frac{x - h}{h} \end{aligned} \tag{1.3.5}$$

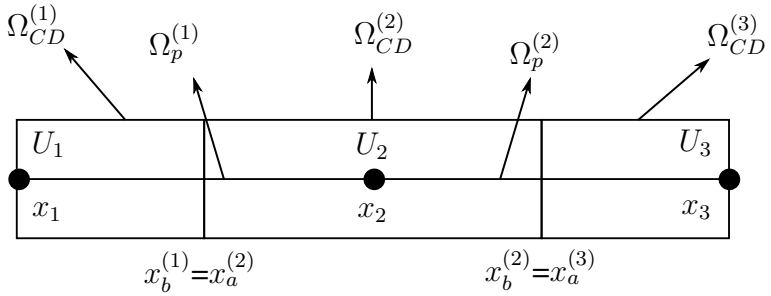


Figure 1.3: Discretization of elastic bar with primal and dual mesh elements.

Now writing the integral statement of the governing equation within the interior control domain we have

$$\int_{x_a^{(2)}}^{x_b^{(2)}} \left\{ -\frac{d}{dx}\left[EA\frac{du}{dx}\right] - f_x \right\} dx = 0 \tag{1.3.6}$$

Carrying out the integral in the above equations such that the resulting boundary terms are secondary variables which are dual to the primary variable $u$, we get

$$-N_1^{(2)} - N_2^{(2)} - \int_{x_a^{(2)}}^{x_b^{(2)}} f_x dx = 0 \tag{1.3.7}$$

Here $N_1^{(2)}$ is the axial force at left end of the control domain and $N_2^{(2)}$ is the axial force at the right end of the control domain. These are given by

$$N_1^{(2)} = -\left[EA\frac{du}{dx}\right]_{x=x_a^{(2)}}, \quad N_2^{(2)} = \left[EA\frac{du}{dx}\right]_{x=x_b^{(2)}} \tag{1.3.8}$$

The negative sign in the definition of $N_1^{(2)}$ indicates that the force is compressive in nature. The force convention is taken such that the force acting along the positive x-axis is taken as tensile. The axial forces in Eq. (1.3.8) (i.e., secondary variables) acting on the interior control domain are expressed in terms of the nodal values of the primary variables using the interpolation of the primary variable on the primal mesh elements given by Eq. (1.3.4). Noting that the interior control

domain spans two primal mesh elements we can write Eq. (1.3.7) as follows:

$$EA\left[U_1\frac{d\psi_1^{(1)}}{dx}+U_2\left(\frac{d\psi_2^{(1)}}{dx}-\frac{d\psi_1^{(2)}}{dx}\right)-U_3\frac{d\psi_2^{(2)}}{dx}\right]-\int_{x_a^{(2)}}^{x_b^{(2)}}f_x dx=0 \tag{1.3.9}$$

$$EA\left[-\frac{U_1}{h_1}+U_2\left(\frac{1}{h_1}+\frac{1}{h_I}\right)-\frac{U_3}{h_2}\right]-fh=0 \tag{1.3.10}$$

Let us now consider the control domain corresponding to node 1. The integral statement of the governing equation on this control domain would be:

$$\int_0^{x_b^{(1)}}\left\{-\frac{d}{dx}\left[EA\frac{du}{dx}\right]-f_x\right\}dx=0 \tag{1.3.11}$$

Carrying out the integration we get

$$-N_1^{(1)}-N_2^{(1)}-\int_0^{x_b^{(1)}}f_x dx=0 \tag{1.3.12}$$

Since the $N_1^{(1)}$ represents the axial force at the left boundary of the bar, we only express $N_2^{(1)}$ in terms of the nodal values of the primary variable using interpolation functions. $N_1^{(1)}$ is retained as is because, on the boundary we either know the primary variable $u$ or secondary variable $N_1^{(1)}$ (reaction force in this case) because of the duality. Thus, when $U_1$ is known we can calculate $N_1^{(1)}$ and when $N_1^{(1)}$ is known we can calculate $U_1$. Hence, Eq. (1.3.12) will take the following form:

$$-N_1^{(1)}-\frac{EA}{h}\left[U_1\frac{d\psi_1^{(1)}}{dx}+U_2\frac{d\psi_2^{(1)}}{dx}\right]-\int_0^{x_b^{(1)}}=0 \tag{1.3.13}$$

$$\frac{EA}{h}\left(U_1-U_2\right)-\frac{fh}{2}-N_1^{(1)}=0 \tag{1.3.14}$$

Similarly, the discretized equation corresponding to third control domain can be written and the

final discretized equations will be of the form:

$$\begin{aligned} \frac{EA}{h}(U_1 - U_2) &= \frac{fh}{2} + N_1^{(1)} \\ \frac{EA}{h}(-U_1 + 2U_2 - U_3) &= fh \\ \frac{EA}{h}(-U_2 + U_3) &= \frac{fh}{2} + N_2^{(3)} \end{aligned} \tag{1.3.15}$$

$$\frac{EA}{h}\begin{bmatrix} 1 & -1 & 0 \\ -1 & 2 & -1 \\ 0 & -1 & 1 \end{bmatrix}\begin{Bmatrix} U_1 \\ U_2 \\ U_3 \end{Bmatrix} = \begin{Bmatrix} \frac{fh}{2} \\ fh \\ \frac{fh}{2} \end{Bmatrix} + \begin{Bmatrix} N_1^{(1)} \\ 0 \\ N_2^{(3)} \end{Bmatrix} \tag{1.3.16}$$

After imposing the boundary condition $U_1 = 0$ and $N_2^{(3)} = F_0$ for $f = 0$ in the above equation, we get displacements of nodes 2 and 3 which are given in Table 1.1.

| $x$ | **Exact** | **DMCDM** |
|---|---|---|
| 0 | 0.0 | 0.0 |
| $h$ | $\frac{F_0 h}{EA}$ | $\frac{F_0 h}{EA}$ |
| $2h$ | $\frac{F_0 2h}{EA}$ | $\frac{F_0 2h}{EA}$ |

Table 1.1: Comparison of elastic bar deflection from DMCDM with exact solution

Following this brief general introduction to dual mesh control domain method, we will consider its application to functionally graded beams [10] in chapter 6. Bending analysis of functionally graded axisymmetric circular plates [7] and functionally graded rectangular plates [8] using dual mesh control domain method is considered in chapter 7.

# 2. NONLINEAR MICROPOLAR BEAM THEORIES*

## 2.1 Introduction

In this chapter we utilize the generally used beam theories of classical Cauchy continuum to construct the beam theories for micropolar continuum. Let the beam considered be such that the $x$-axis of the considered coordinate system passes through the centroid of the cross-section of the beam (called axis of the beam). The length of the beam is $L$, height of the beam is $H$ and width of the beam is $B$. The $z$-axis points downwards and the $y$-axis points out of the paper (see Fig. 2.2). For such a beam we represent the displacement and microrotation vectors as follows:

$$\begin{aligned} \mathbf{u} &= u_1\hat{\mathbf{e}}_1 + u_2\hat{\mathbf{e}}_2 + u_3\hat{\mathbf{e}}_3 \\ \boldsymbol{\psi} &= \psi_1\hat{\mathbf{e}}_1 + \psi_2\hat{\mathbf{e}}_2 + \psi_3\hat{\mathbf{e}}_3 \end{aligned} \tag{2.1.1}$$

## 2.2 The Euler-Bernoulli micropolar beam theory (EMBT)

The displacement field of the Euler-Bernoulli micropolar beam theory† is based on the same assumptions of Euler-Bernoulli beam theory of classical continuum (i.e., the assumptions that the planes perpendicular to the axis of the beam remain plane and perpendicular after deformation and are in-extensible [97] are still valid). Thus we have the following displacement field

$$\begin{aligned} u_1(x,y,z) &= u_0^E(x) - z\frac{dw_0^E}{dx} \\ u_2(x,y,z) &= 0 \\ u_3(x,y,z) &= w_0^E(x) \end{aligned} \tag{2.2.1}$$

*Reprinted with permission from "Geometrically nonlinear Euler–Bernoulli and Timoshenko micropolar beam theories" by P. Nampally and J. N. Reddy, 2020. Acta Mechanica, vol. 231, no. 10, pp. 4217–4242, Copyright (2020) Springer-Verlag GmbH Austria, part of Springer Nature.

†We use superscript $E$ to denote terms corresponding to Euler-Bernoulli micropolar beam theory.

We assume that only the $y$-component of the microroation is non-zero and that it only depends on the $x$-coordinate.

$$\begin{aligned}\psi_1(x,y,z) &= 0\\ \psi_2(x,y,z) &= \psi_y^E(x)\\ \psi_3(x,y,z) &= 0\end{aligned} \tag{2.2.2}$$

This approximation implies that the planes normal to the axis of the beam are made of particles which can only rotate about $y$-axis. Thus $-\frac{dw_0^E}{dx}$ represent the rotation of these planes about $y$-axis, while $\psi_y^E$ represents the rotations of the particles within these planes about $y$-axis (see Fig. 2.1) and clearly these two are independent degrees of freedom.

### 2.3 The Timoshenko micropolar beam theory (TMBT)

The displacement field of the Timoshenko micropolar beam theory[†] is based on the same assumptions of the Timoshenko beam theory of classical continuum (i.e., the assumptions that the planes perpendicular to the axis of the beam remain plane after deformation and are in-extensible [93, 98] are still valid). Thus the displacement field is given by

$$\begin{aligned}u_1(x,y,z) &= u_0^T(x) + z\phi_x^T(x)\\ u_2(x,y,z) &= 0\\ u_3(x,y,z) &= w_0^T(x)\end{aligned} \tag{2.3.1}$$

We assume the microroation field similar to EMBT.

$$\begin{aligned}\psi_1(x,y,z) &= 0\\ \psi_2(x,y,z) &= \psi_y^T(x)\\ \psi_3(x,y,z) &= 0\end{aligned} \tag{2.3.2}$$

Figure (2.1) shows a schematic representation of the displacement and microrotation fields of a micropolar beam. The green circles represent the particles of the micropolar continuum within

[†]We use superscript $T$ to denote terms corresponding to the Timoshenko micropolar beam theory.

the plane normal to the axis of the beam before deformation while the yellow circles represent the particle within the plane normal to the axis of beam after deformation. The red arrows form a pair of perpendicular axis, called directors [44], which represent the orientation of micropolar material particle in undeformed configuration while the blue arrows, which are also a set of perpendicular axis, represent the orientation of the micropolar material particle in deformed configuration. The angle, $\psi_y$, between blue and red arrows represent the microrotation about the $y$-axis of the reference frame. Similarly, the angle between planes normal to the axis of the beam before and after deformation is represented by $\phi_x$. Clearly these two angles are different.

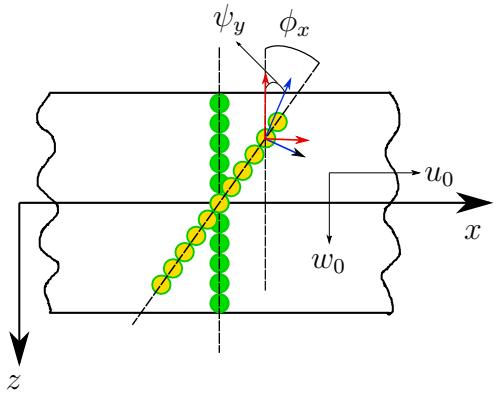


Figure 2.1: The displacements and microrotation of a micropolar beam. For Euler-Bernoulli beam theory $\phi_x = -\frac{dw_0}{dx}$ [3].

## 2.4 The von Kármán nonlinearity and corresponding governing equations

In the classical continuum mechanics, if the displacement gradients are considered to be small then we omit the nonlinear terms of the Green strain tensor, by arguing that the potential energy contribution due to these nonlinear terms is negligible in comparison to the linear terms, and obtain the linearized strain tensor [99]. Further, no distinction between current and reference configurations is made. In the case of a beam, such linearized strains will result in linear beam theories. However, if the rotations of the planes normal to the axis of the beam are moderate while the displacement gradients are still small, we retain the nonlinear terms of the Green strain tensor which

correspond to the rotations of these planes. The resulting beam equations after the retention of such nonlinear terms in the strains are called the von Kármán nonlinear beam theories of classical continuum [100, 101]. In classical continuum the effect of the von Kármán nonlinearity on the beam theories is the addition of nonlinear term $\frac{1}{2}\left(\frac{dw_0}{dx}\right)^2$ to the $\varepsilon_{xx}$ term of the linearized strain [100]. If we extend the same argument to micropolar beams, that is, the displacement gradients are small but the rotations of the planes normal to the axis of beam are moderate, the linearized Cosserat deformation tensor of Eqs. (1.1.11) are inadequate in predicting the correct response of the beam.

From Eqs. (1.1.13) we observe that the symmetric part of the linearized Cosserat deformation tensor is similar to the strain measure of the linearized classical elasticity, while the anti-symmetric part show that the effect of microrotations is to create additional rotations which append to the components of the macrorotation tensor (or rotation tensor) of the linearized classical elasticity. Following this observation, if we assume that the effect of moderate rotations of normal planes is only on the symmetric part of the linearized Cosserat deformation tensor we can extend the von Kármán approximation of classical continuum beam to micropolar beam [35, 5]. That is,

$$\varepsilon_{xx}^{(s)} \approx \frac{\partial u_1}{\partial x} + \frac{1}{2}\left(\frac{dw_0}{dx}\right)^2 \tag{2.4.1}$$

Since the approximation of small displacement gradients is still valid, we can use the constitutive relations of Eq. (1.1.14) and (1.1.15). If $\sigma_{ij}^{(s)}$, $\sigma_{ij}^{(a)}$ and $r_{ij}$ are the symmetric and anti-symmetric stresses and couple stresses conjugate to modified $\varepsilon_{ij}^{(s)}$, $\varepsilon_{ij}^{(a)}$ and $\eta_{ij}$ respectively, we can write the principle of virtual work for a beam with transverse distributed load $q_0$ and axial distributed load $f_x$ as follows [102]:

$$\int_V \left(\sigma_{ij}^{(s)}\delta\varepsilon_{ij}^{(s)} + \sigma_{ij}^{(a)}\delta\varepsilon_{ij}^{(a)} + r_{ij}\delta\eta_{ij}\right) dV - \int_0^L \left(q_0\delta w_0 + f_x\delta u_0\right) dx = 0 \tag{2.4.2}$$

In the following we define the non-zero components of symmetric, anti-symmetric parts of linearized Cosserat deformation tensor after the von Kármán modification and Wryness tensor for

the beam theories considered in section 2.3 and then use principle of virtual work (2.4.2) to derive the governing equations and corresponding boundary conditions.

### 2.4.1 The von Kármán Euler-Bernoulli micropolar beam theory (VEMBT)

$$\begin{aligned}\varepsilon_{xx}^{E(s)} &= \frac{du_0^E}{dx} + \frac{1}{2}\left(\frac{dw_0^E}{dx}\right)^2 - z\frac{d^2w_0^E}{dx^2} \\ \varepsilon_{xz}^{E(a)} &= -\left(\frac{dw_0^E}{dx} + \psi_y^E\right)\end{aligned} \tag{2.4.3}$$

$$\eta_{yx}^E = \frac{d\psi_y^E}{dx} \tag{2.4.4}$$

Now defining the stress, moment and couple stress resultants acting on beam as

$$\left\{N_{xx}^{E(s)}\right\} = \int_A \left\{\sigma_{xx}^{E(s)}\right\} dA, \qquad \left\{M_{xx}^{E(s)}\right\} = \int_A \left\{\sigma_{xx}^{E(s)}\right\} z dA \tag{2.4.5}$$

$$\left\{Q_x^{E(a)}\right\} = \int_A \left\{\sigma_{xz}^{E(a)}\right\} dA, \qquad \left\{P_{yx}^E\right\} = \int_A \left\{r_{yx}^E\right\} dA \tag{2.4.6}$$

we can express the principle of virtual work (2.4.2) in terms of the resultants (2.4.5) and (2.4.6) as follows

$$\begin{aligned}\int_0^L \Bigg\{ & N_{xx}^{E(s)}\left(\frac{d\delta u_0^E}{dx} + \frac{d\delta w_0^E}{dx}\frac{dw_0^E}{dx}\right) - M_{xx}^{E(s)}\frac{d^2\delta w_0^E}{dx^2} - 2Q_x^{E(a)}\left(\frac{d\delta w_0^E}{dx} + \delta\psi_y^E\right) \\ & + P_{yx}^E\frac{d\delta\psi_y^E}{dx} - q_0\delta w_0^E - f_x\delta u_0^E\Bigg\}dx = 0\end{aligned} \tag{2.4.7}$$

The governing equations of VEMBT are obtained by taking the Euler-Lagrange equations of the above variational statement (2.4.7) as

$$\delta u_0^E: \quad \frac{dN_{xx}^{E(s)}}{dx} + f_x = 0 \tag{2.4.8}$$

$$\delta w_0^E: \quad \frac{d^2M_{xx}^{E(s)}}{dx^2} + \frac{d}{dx}\left(\frac{dw_0^E}{dx}N_{xx}^{E(s)}\right) - 2\frac{dQ_x^{E(a)}}{dx} + q_0 = 0 \tag{2.4.9}$$

$$\delta\psi_y^E: \quad \frac{dP_{yx}^E}{dx} + 2Q_x^{E(a)} = 0 \tag{2.4.10}$$

with the corresponding natural boundary conditions

$$N_{xx}^{E(s)} = 0, \qquad \frac{dM_{xx}^{E}}{dx} - 2Q_{x}^{E(a)} + N_{xx}^{E(s)}\frac{dw_0^E}{dx} = 0, \qquad M_{xx}^{E(s)} = 0, \qquad P_{yx}^{E} = 0 \tag{2.4.11}$$

### 2.4.2 The von Kármán Timoshenko micropolar beam theory (VTMBT)

$$\begin{aligned}
\varepsilon_{xx}^{T(s)} &= \frac{du_0^T}{dx} + \frac{1}{2}\left(\frac{dw_0^T}{dx}\right)^2 + z\frac{d\phi_x^T}{dx} \\
\varepsilon_{xz}^{T(s)} &= \frac{1}{2}\left(\frac{dw_0^T}{dx} + \phi_x^T\right) \\
\varepsilon_{xz}^{T(a)} &= \frac{1}{2}\left(\phi_x^T - \frac{dw_0^T}{dx} - 2\psi_y^T\right)
\end{aligned} \tag{2.4.12}$$

$$\eta_{yx}^{T} = \frac{d\psi_y^T}{dx} \tag{2.4.13}$$

Now defining the stress, moment, and couple stress resultants on the beam as

$$\left\{N_{xx}^{T(s)}\right\} = \int_A \left\{\sigma_{xx}^{T(s)}\right\} dA, \qquad \left\{M_{xx}^{T(s)}\right\} = \int_A \left\{\sigma_{xx}^{T(s)}\right\} z dA \tag{2.4.14}$$

$$\begin{Bmatrix} Q_x^{T(s)} \\ Q_x^{T(a)} \end{Bmatrix} = \int_A \begin{Bmatrix} \sigma_{xz}^{T(s)} \\ \sigma_{xz}^{T(a)} \end{Bmatrix} dA, \qquad \left\{P_{yx}^{T}\right\} = \int_A \left\{r_{yx}^{T}\right\} dA \tag{2.4.15}$$

we can express the principle of virtual work (2.4.2) in terms of the resultants (2.4.14) and (2.4.15) as follows

$$\begin{aligned}
\int_0^L \Bigg\{ & N_{xx}^{T(s)}\left(\frac{d\delta u_0^T}{dx} + \frac{d\delta w_0^T}{dx}\frac{dw_0^T}{dx}\right) + M_{xx}^{T(s)}\frac{d\delta\phi_x^T}{dx} + Q_x^{T(s)}\left(\delta\phi_x^T + \frac{d\delta w_0^T}{dx}\right) \\
& + Q_x^{T(a)}\left(\delta\phi_x^T - \frac{d\delta w_0^T}{dx} - 2\delta\psi_y^T\right) + P_{yx}^{T}\frac{d\delta\psi_y^T}{dx} - q_0\delta w_0^T - f_x\delta u_0^T \Bigg\} dx = 0
\end{aligned} \tag{2.4.16}$$

The governing equations of VTMBT are obtained by taking the Euler-Lagrange equations of the

above variational statement (2.4.16) as

$$\delta u_0^T : \quad \frac{dN_{xx}^{T(s)}}{dx} + f_x = 0 \tag{2.4.17}$$

$$\delta w_0^T : \quad \frac{d}{dx}\left(\frac{dw_0^T}{dx} N_{xx}^{T(s)}\right) + \frac{d(Q_x^{T(s)} - Q_x^{T(a)})}{dx} + q_0 = 0 \tag{2.4.18}$$

$$\delta \phi_x^T : \quad \frac{dM_{xx}^{T(s)}}{dx} - Q_x^{T(s)} - Q_x^{T(a)} = 0 \tag{2.4.19}$$

$$\delta \psi_y^T : \quad \frac{dP_{yx}^T}{dx} + 2Q_x^{T(a)} = 0 \tag{2.4.20}$$

with the corresponding natural boundary conditions

$$N_{xx}^{T(s)} = 0, \qquad Q_x^{T(s)} - Q_x^{T(a)} + N_{xx}^{T(s)} \frac{dw_0^T}{dx} = 0, \qquad M_{xx}^{T(s)} = 0, \qquad P_{yx}^T = 0 \tag{2.4.21}$$

## 2.5 Micropolar nonlinearity and corresponding governing equations

In the previous section we derived the nonlinear governing differential equations of micropolar beams based on the assumption that the moderate rotations of the planes normal to the axis of beam can be modeled by von Kármán nonlinear strains terms borrowed from classical elasticity. In this section we shall follow a different route to derive the nonlinear governing differential equations accounting for the moderate rotations of the planes normal to the axis of beam. Here we make appropriate approximations on the symmetric and anti-symmetric nonlinear Cosserat deformation components of Eqs. (1.1.12) which reflect the condition of moderate rotations of planes normal to the axis of beam while the displacement gradients are still assumed to be small.

Since the the only assumption made in deriving Eqs. (1.1.12) is that the microrotations are small, we need to make a distinction between current and reference configurations as the displacements could be large. Thus the gradients in Eqs. (1.1.12) are with respect to reference configuration. For the case of moderate rotations of planes normal to the axis of beam approximation, we assume the displacement gradients are also small. This eliminates the need for a distinction between current and reference configurations. Further, since we assumed that the displacement

gradients, except those that represent the rotations of planes normal to axis of beam, are small we can make the following approximation on the magnitudes of various terms of Eqs. (1.1.12)

$$\begin{aligned} &u_{\alpha,\beta} = o(\rho), \qquad \psi_i = o(\sqrt{\rho}) \\ &u_{3,\alpha} = o(\sqrt{\rho}), \qquad \phi_x = o(\sqrt{\rho}) \\ &\text{where} \quad \rho << 1, \quad \alpha,\beta = 1,2 \quad \text{and} \quad i = 1,2,3 \end{aligned} \tag{2.5.1}$$

Neglecting terms of order greater than $O(\rho)$ in calculating the terms of nonlinear Cosserat deformation components we arrive at the nonlinear Cosserat deformation tensor which represents the moderate rotations and small displacement gradients. Since the approximation of small displacement gradients is still valid, we can use the constitutive relations of Eqs. (1.1.14) and (1.1.15) with corresponding stresses and modified Cosserat deformation tensors. If $\Sigma_{ij}^{(s)}$, $\Sigma_{ij}^{(a)}$ and $m_{ij}$ are the symmetric, anti-symmetric stresses and couple stresses conjugate to $e_{ij}^{(s)}$, $e_{ij}^{(a)}$ and $\eta_{ij}$ after moderate rotation approximation, we can write the principle of virtual work for a beam with transverse distributed load $q_0$ and axial distributed load $f_x$ as follows [102]:

$$\int_V \left( \Sigma_{ij}^{(s)} \delta e_{ij}^{(s)} + \Sigma_{ij}^{(a)} \delta e_{ij}^{(a)} + m_{ij} \delta \eta_{ij} \right) dV - \int_0^L \left( q_0 \delta w_0 + f_x \delta u_0 \right) dx = 0 \tag{2.5.2}$$

In the following we shall define the non-zero components of symmetric and anti-symmetric parts of nonlinear Cosserat deformation tensor after moderate rotations approximation and Wryness tensor for the beam theories considered in section 2.2 and 2.3 and then use the principle of virtual work (2.5.2) to derive the governing equations and corresponding boundary conditions.

### 2.5.1 Nonlinear Euler-Bernoulli micropolar beam theory (NEMBT)

$$\begin{aligned} e_{xx}^{E(s)} &= \left( \frac{du_0^E}{dx} - \psi_y^E \frac{dw_0^E}{dx} \right) - z \frac{d^2 w_0^E}{dx^2} \\ e_{xz}^{E(a)} &= -\left( \frac{dw_0^E}{dx} + \psi_y^E \right) \end{aligned} \tag{2.5.3}$$

$$\eta_{yx}^E = \frac{d\psi_y^E}{dx} \tag{2.5.4}$$

Now defining the stress, moment and couple stress resultants acting on beam as

$$\left\{\mathfrak{N}_{xx}^{E(s)}\right\} = \int_A \left\{\Sigma_{xx}^{E(s)}\right\} dA, \qquad \left\{\mathfrak{M}_{xx}^{E(s)}\right\} = \int_A \left\{\Sigma_{xx}^{E(s)}\right\} z dA \tag{2.5.5}$$

$$\left\{\mathfrak{Q}_{x}^{E(a)}\right\} = \int_A \left\{\Sigma_{xz}^{E(a)}\right\} dA, \qquad \left\{\mathfrak{P}_{yx}^{E}\right\} = \int_A \left\{m_{yx}^{E}\right\} dA \tag{2.5.6}$$

we can express the principle of virtual work (2.5.2) in terms of the resultants (2.5.5) and (2.5.6) as follows

$$\int_0^L \Bigg\{ \mathfrak{N}_{xx}^{E(s)} \left( \frac{d\delta u_0^E}{dx} - \delta\psi_y^E \frac{dw_0^E}{dx} - \psi_y^E \frac{d\delta w_0^E}{dx} \right) - \mathfrak{M}_{xx}^{E(s)} \frac{d^2\delta w_0^E}{dx^2} - 2\mathfrak{Q}_x^{E(a)} \left( \frac{d\delta w_0^E}{dx} + \delta\psi_y^E \right) + \mathfrak{P}_{yx}^E \frac{d\delta\psi_y^E}{dx} - q_0 \delta w_0^E - f_x \delta u_0^E \Bigg\} dx = 0 \tag{2.5.7}$$

The governing equations of NEMBT are obtained by taking Euler-Lagrange equations of the variational statement (2.5.7) as

$$\delta u_0^E : \quad \frac{d\mathfrak{N}_{xx}^{E(s)}}{dx} + f_x = 0 \tag{2.5.8}$$

$$\delta w_0^E : \quad \frac{d^2\mathfrak{M}_{xx}^{E(s)}}{dx^2} - \frac{d}{dx}\left(\psi_y^E \mathfrak{N}_{xx}^{E(s)}\right) - 2\frac{d\mathfrak{Q}_x^{E(a)}}{dx} + q_0 = 0 \tag{2.5.9}$$

$$\delta\psi_y^E : \quad \frac{d\mathfrak{P}_{yx}^E}{dx} + \mathfrak{N}_{xx}^{E(s)} \frac{dw_0^E}{dx} + 2\mathfrak{Q}_x^{E(a)} = 0 \tag{2.5.10}$$

with the corresponding natural boundary conditions

$$\mathfrak{N}_{xx}^{E(s)} = 0, \qquad -\frac{d\mathfrak{M}_{xx}^{E(s)}}{dx} + \mathfrak{N}_{xx}^{E(s)}\psi_y^E + 2\mathfrak{Q}_x^{E(a)} = 0, \qquad \mathfrak{M}_{xx}^{E(s)} = 0, \qquad \mathfrak{P}_{yx}^E = 0 \tag{2.5.11}$$

### 2.5.2 Nonlinear Timoshenko micropolar beam theory (NTMBT)

$$
\begin{aligned}
e_{xx}^{T(s)} &= \left(\frac{du_0^T}{dx} - \psi_y^T \frac{dw_0^T}{dx}\right) + z\left(\frac{d\phi_x^T}{dx}\right) \\
2e_{xz}^{T(s)} &= \left(\frac{dw_0^T}{dx} + \phi_x^T\right) \\
2e_{xz}^{T(a)} &= \left(\phi_x^T - \frac{dw_0^T}{dx} - 2\psi_y^T\right)
\end{aligned} \tag{2.5.12}
$$

$$
\eta_{yx}^T = \frac{d\psi_y^T}{dx} \tag{2.5.13}
$$

Now defining stress, moment and couple stress resultants acting on the beam as

$$
\left\{\mathfrak{N}_{xx}^{T(s)}\right\} = \int_A \left\{\Sigma_{xx}^{T(s)}\right\} dA, \qquad \begin{Bmatrix} \mathfrak{Q}_x^{T(s)} \\ \mathfrak{Q}_x^{T(a)} \end{Bmatrix} = \int_A \begin{Bmatrix} \Sigma_{xz}^{T(s)} \\ \Sigma_{xz}^{T(a)} \end{Bmatrix} dA \tag{2.5.14}
$$

$$
\left\{\mathfrak{M}_{xx}^{T(s)}\right\} = \int_A \left\{\Sigma_{xx}^{T(s)}\right\} z dA, \qquad \left\{\mathfrak{P}_{yx}^{T}\right\} = \int_A \left\{m_{yx}^{T}\right\} dA \tag{2.5.15}
$$

we can express the principle of virtual work (2.5.2) in terms of the resultants (2.5.14) and (2.5.15) as follows

$$
\begin{aligned}
\int_0^L \Bigg\{ & \mathfrak{N}_{xx}^{T(s)} \left(\frac{d\delta u_0^T}{dx} - \delta\psi_y^T \frac{dw_0^T}{dx} - \psi_y^T \frac{d\delta w_0^T}{dx}\right) + \mathfrak{M}_{xx}^{T(s)} \frac{d\delta\phi_x^T}{dx} + \mathfrak{Q}_x^{T(s)} \left(\delta\phi_x^T + \frac{d\delta w_0^T}{dx}\right) \\
& + \mathfrak{Q}_x^{T(a)} \left(\delta\phi_x^T - \frac{d\delta w_0^T}{dx} - 2\delta\psi_y^T\right) + \mathfrak{P}_{yx}^T \frac{d\delta\psi_y^T}{dx} - q_0 \delta w_0^T - f_x \delta u_0^T \Bigg\} dx = 0
\end{aligned} \tag{2.5.16}
$$

The governing equations of NTMBT are obtained by taking the Euler-Lagrange equations of the

above variational statement (2.5.16) as

$$\delta u_0^T : \quad \frac{d\mathfrak{N}_{xx}^{T(s)}}{dx} + f_x = 0 \tag{2.5.17}$$

$$\delta w_0^T : \quad \frac{d}{dx}\left(\psi_y^T \mathfrak{N}_{xx}^{T(s)}\right) - \frac{d}{dx}\left(\mathfrak{Q}_x^{T(s)} - \mathfrak{Q}_x^{T(a)}\right) - q_0 = 0 \tag{2.5.18}$$

$$\delta \phi_x^T : \quad \frac{d\mathfrak{M}_{xx}^{T(s)}}{dx} - \mathfrak{Q}_x^{T(s)} - \mathfrak{Q}_x^{T(a)} = 0 \tag{2.5.19}$$

$$\delta \psi_y^T : \quad \frac{d\mathfrak{P}_{yx}^{T}}{dx} + 2\mathfrak{Q}_x^{T(a)} + \mathfrak{N}_{xx}^{T(s)} \frac{dw_0^T}{dx} = 0 \tag{2.5.20}$$

with the corresponding natural boundary conditions

$$\mathfrak{N}_{xx}^{T(s)} = 0, \qquad \mathfrak{Q}_x^{T(s)} - \mathfrak{Q}_x^{T(s)} - \mathfrak{N}_{xx}^{T(s)} \psi_y^T = 0, \qquad \mathfrak{M}_{xx}^{T(s)} = 0, \qquad \mathfrak{P}_{yx}^{T} = 0 \tag{2.5.21}$$

## 2.6 Finite element models

In this section, we develop the weak-form Galerkin finite element model of the governing equations derived in sections 2.4 and 2.5. We consider the Timoshenko micropolar beam theories and the Euler-Bernoulli micropolar beam theories separately.

### 2.6.1 Timoshenko micropolar beam theories

For the Timoshenko micropolar beam theories considered in this chapter the primary variables are $(u_0^T, w_0^T, \phi_x^T, \psi_y^T)$. These variables are approximated using Lagrange interpolation functions $L_j^{(1)}, L_j^{(2)}, L_j^{(3)}, L_j^{(4)}$ respectively. Here $j = \{1, 2 \ldots n\}$. These interpolation functions are of order $n-1$, where $n$ is the number of nodes in a typical element. Since we are using weak-form Galerkin finite element formulation, the weight functions $w_1, w_2, w_3$ and $w_4$ used in developing the weak form equations are taken to be the same Lagrange interpolation functions used in approximating the primary variables [93]. Thus, we have,

$$
\begin{aligned}
u_0^T &\approx \sum_{j=1}^{n} U_j^T L_j^{(1)}(x), \qquad & w_1(x) &= L_i^{(1)}(x) \\
w_0^T &\approx \sum_{j=1}^{n} W_j^T L_j^{(2)}(x), \qquad & w_2(x) &= L_i^{(2)}(x) \\
\phi_x^T &\approx \sum_{j=1}^{n} \Phi x_j^T L_j^{(3)}(x), \qquad & w_3(x) &= L_i^{(3)}(x) \\
\psi_y^T &\approx \sum_{j=1}^{n} \Psi y_j^T L_j^{(4)}(x), \qquad & w_4(x) &= L_i^{(4)}(x)
\end{aligned}
\tag{2.6.1}
$$

where $i = \{1, 2, 3 \dots n\}$. Now we write the weak form equations of the Timoshenko micropolar beam theories using the constitutive relations given in Appendix A.1.

- *von Kármán nonlinearity*

$$
\begin{aligned}
0 &= \int_{x_a}^{x_b} \left\{ A_{11} \frac{dw_1}{dx} \left( \frac{du_0^T}{dx} + \frac{1}{2} \left( \frac{dw_0^T}{dx} \right)^2 \right) - w_1 f_x \right\} dx - Q_1 w_1(x_a) - Q_2 w_1(x_b) \\
0 &= \int_{x_a}^{x_b} \left\{ A_{11} \frac{dw_2}{dx} \frac{dw_0^T}{dx} \left( \frac{du_0^T}{dx} + \frac{1}{2} \left( \frac{dw_0^T}{dx} \right)^2 \right) + \frac{A_{44}}{2} \frac{dw_2}{dx} \left( \frac{dw_0^T}{dx} + \phi_x^T \right) \right. \\
&\qquad \left. - \frac{A_{77}}{2} \frac{dw_2}{dx} \left( \phi_x - \frac{dw_0^T}{dx} - 2\psi_y^T \right) w_2 q_0 \right\} dx - Q_3 w_2(x_a) - Q_4 w_2(x_b) \\
0 &= \int_{x_a}^{x_b} \left\{ D_{11} \frac{dw_3}{dx} \frac{d\phi_x^T}{dx} + \frac{A_{44}}{2} w_3 \left( \frac{dw_0^T}{dx} + \phi_x^T \right) + \frac{A_{77}}{2} w_3 \left( \phi_x^T - \frac{dw_0^T}{dx} - 2\psi_y^T \right) \right\} dx \\
&\qquad - Q_5 w_3(x_a) - Q_6 w_3(x_b) \\
0 &= \int_{x_a}^{x_b} \left\{ E_{44} \frac{dw_4}{dx} \frac{d\psi_y^T}{dx} - A_{77} w_4 \left( \phi_x^T - \frac{dw_0^T}{dx} - 2\psi_y^T \right) \right\} dx - Q_7 w_4(x_a) - Q_8 w_4(x_b)
\end{aligned}
\tag{2.6.2}
$$

- *Micropolar nonlinearity*

$$
\begin{aligned}
0 = &\int_{x_a}^{x_b} \left\{ A_{11} \frac{dw_1}{dx} \left( \frac{du_0^T}{dx} - \psi_y^T \frac{dw_0^T}{dx} \right) - w_1 f_x \right\} dx - Q_1 w_1(x_a) - Q_2 w_1(x_b) \\
0 = &\int_{x_a}^{x_b} \left\{ -A_{11} \frac{dw_2}{dx} \psi_y^T \left( \frac{du_0^T}{dx} - \psi_y^T \frac{dw_0^T}{dx} \right) + \frac{A_{44}}{2} \frac{dw_2}{dx} \left( \frac{dw_0^T}{dx} + \phi_x^T \right) \right. \\
&\left. - \frac{A_{77}}{2} \frac{dw_2}{dx} \left( \phi_x - \frac{dw_0^T}{dx} - 2\psi_y^T \right) w_2 q_0 \right\} dx - Q_3 w_2(x_a) - Q_4 w_2(x_b) \\
0 = &\int_{x_a}^{x_b} \left\{ D_{11} \frac{dw_3}{dx} \frac{d\phi_x^T}{dx} + \frac{A_{44}}{2} w_3 \left( \frac{dw_0^T}{dx} + \phi_x^T \right) + \frac{A_{77}}{2} w_3 \left( \phi_x^T - \frac{dw_0^T}{dx} - 2\psi_y^T \right) \right\} dx \\
&- Q_5 w_3(x_a) - Q_6 w_3(x_b) \\
0 = &\int_{x_a}^{x_b} \left\{ E_{44} \frac{dw_4}{dx} \frac{d\psi_y^T}{dx} - A_{11} w_4 \frac{dw_0^T}{dx} \left( \frac{du_0^T}{dx} - \psi_y^T \frac{dw_0^T}{dx} \right) \right. \\
&\left. - A_{77} w_4 \left( \phi_x^T - \frac{dw_0^T}{dx} - 2\psi_y^T \right) \right\} dx - Q_7 w_4(x_a) - Q_8 w_4(x_b)
\end{aligned}
\tag{2.6.3}
$$

After using the approximations given in Eq. (2.6.1) in Eqs. (2.6.2) and (2.6.3) separately for each nonlinear theory, we have the following form for the finite element equations:

$$
\mathbf{K}^{(\mathbf{e})^T} \mathfrak{U}^{(\mathbf{e})^T} = \mathbf{F}^{(\mathbf{e})^T} \tag{2.6.4}
$$

where,

$$
\mathbf{K}^{(\mathbf{e})^T} = \begin{bmatrix} \mathbf{K^{11}} & \mathbf{K^{12}} & \mathbf{K^{13}} & \mathbf{K^{14}} \\ \mathbf{K^{21}} & \mathbf{K^{22}} & \mathbf{K^{23}} & \mathbf{K^{24}} \\ \mathbf{K^{31}} & \mathbf{K^{32}} & \mathbf{K^{33}} & \mathbf{K^{34}} \\ \mathbf{K^{41}} & \mathbf{K^{42}} & \mathbf{K^{43}} & \mathbf{K^{44}} \end{bmatrix}^{(e)} \qquad \mathfrak{U}^{(\mathbf{e})^T} = \begin{Bmatrix} \mathbf{U}^{(T)} \\ \mathbf{W}^{(T)} \\ \boldsymbol{\Phi x}^{(T)} \\ \boldsymbol{\Psi y}^{(T)} \end{Bmatrix}^{(e)} \qquad \mathbf{F}^{(\mathbf{e})^T} = \begin{Bmatrix} \mathbf{F^1} \\ \mathbf{F^2} \\ \mathbf{F^3} \\ \mathbf{F^4} \end{Bmatrix}^{(e)} \tag{2.6.5}
$$

The non-zero components of the above matrix are given in Appendix B.1, for both VTMBT and

NTMBT.

### 2.6.2 Euler-Bernoulli micropolar beam theories

For the Euler-Bernoulli micropolar beam theory considered in this chapter the primary variables are $(u_0^E, w_0^E, \psi_y^E)$. The variables $u_0^E$ and $\psi_y^E$ are approximated using Lagrange interpolation functions $L_j^{(1)}$ and $L_j^{(3)}$ respectively. Here $j = \{1, 2 \dots n\}$. These interpolation functions are of order $n-1$, where $n$ is the number of nodes in a typical element. $w_0^E$ is approximated using Hermite interpolation functions $H_J^{(2)}$ of order $2n-1$. Here $J = \{1, 2 \dots 2n\}$. Since we are using weak form Galerkin finite element formulation, we have

$$\begin{aligned} u_0^E &\approx \sum_{j=1}^{n} U_j^E L_j^{(1)}(x), & w_1(x) &= L_i^{(1)}(x) \\ w_0^E &\approx \sum_{j=1}^{2n} \Delta_J^E H_J^{(2)}(x), & w_2(x) &= H_I^{(2)}(x) \\ \psi_y^E &\approx \sum_{J=1}^{n} \Psi y_j^E L_j^{(3)}(x), & w_3(x) &= L_i^{(3)}(x) \end{aligned} \tag{2.6.6}$$

where $i = \{1, 2 \dots n\}$, $I = \{1, 2 \dots 2n\}$. The $\Delta_J^E$ in the approximation of $w_0^E$ are represented such that the odd numbered $\Delta_J^E$, i.e., $\{\Delta_1^E, \Delta_3^E, \dots \Delta_{2n-1}^E\}$, are the vertical deflections, $w_0^E$, at the nodes of the element while even numbered $\Delta_J^E$, i.e., $\{\Delta_2^E, \Delta_4^E, \dots \Delta_{2n}^E\}$, are the rotations of planes normal to the axis of the beam, $-\frac{dw_0^E}{dx}$ , at these nodes. Now we write the weak form equations of the nonlinear micropolar Euler-Bernoulli beam theories using the constitutive relations given in Appendix A.1.

- *von Kármán nonlinearity*

$$
\begin{aligned}
0 &= \int_{x_a}^{x_b} \left\{ A_{11} \frac{dw_1}{dx} \left( \frac{du_0^E}{dx} + \frac{1}{2} \left( \frac{dw_0^E}{dx} \right)^2 \right) - w_1 f_x \right\} dx - Q_1 w_1(x_a) - Q_2 w_1(x_b) \\
0 &= \int_{x_a}^{x_b} \left\{ D_{11} \frac{d^2 w_2}{dx^2} \frac{d^2 w_0^E}{dx^2} + A_{11} \frac{dw_2}{dx} \frac{dw_0^E}{dx} \left( \frac{du_0^E}{dx} + \frac{1}{2} \left( \frac{dw_0^E}{dx} \right)^2 \right) \right. \\
&\qquad \left. + 2A_{77} \frac{dw_2}{dx} \left( \psi_y^E + \frac{dw_0^E}{dx} \right) - w_2 q_0 \right\} dx - Q_3 w_2(x_a) - Q_4 w_2(x_b) \\
0 &= \int_{x_a}^{x_b} \left\{ E_{44} \frac{dw_3}{dx} \frac{d\psi_y^E}{dx} + 2A_{77} w_3 \left( \psi_y^E + \frac{dw_0^E}{dx} \right) \right\} dx - Q_5 w_3(x_a) - Q_6 w_3(x_b)
\end{aligned}
\tag{2.6.7}
$$

- *Micropolar nonlinearity*

$$
\begin{aligned}
0 &= \int_{x_a}^{x_b} \left\{ A_{11} \frac{dw_1}{dx} \left( \frac{du_0^E}{dx} - \psi_y^E \frac{dw_0^E}{dx} \right) - w_1 f_x \right\} dx - Q_1 w_1(x_a) - Q_2 w_1(x_b) \\
0 &= \int_{x_a}^{x_b} \left\{ D_{11} \frac{d^2 w_2}{dx^2} \frac{d^2 w_0^E}{dx^2} - A_{11} \frac{dw_2}{dx} \psi_y^E \left( \frac{du_0^E}{dx} - \psi_y^E \frac{dw_0^E}{dx} \right) \right. \\
&\qquad \left. + 2A_{77} \frac{dw_2}{dx} \left( \psi_y^E + \frac{dw_0^E}{dx} \right) - w_2 q_0 \right\} dx - Q_3 w_2(x_a) - Q_4 w_2(x_b) \\
0 &= \int_{x_a}^{x_b} \left\{ E_{44} \frac{dw_3}{dx} \frac{d\psi_y^E}{dx} - A_{11} w_3 \frac{dw_0^E}{dx} \left( \frac{du_0^E}{dx} - \psi_y^E \frac{dw_0^E}{dx} \right) \right. \\
&\qquad \left. + 2A_{77} w_3 \left( \psi_y^E + \frac{dw_0^E}{dx} \right) \right\} dx - Q_5 w_3(x_a) - Q_6 w_3(x_b)
\end{aligned}
\tag{2.6.8}
$$

After using the approximations given in Eq. (2.6.6) in Eqs. (2.6.7) and (2.6.8) separately for each nonlinear theory, we obtain the form for the finite element equations:

$$
\mathbf{K}^{(\mathbf{e})^E} \mathfrak{U}^{(\mathbf{e})^E} = \mathbf{F}^{(\mathbf{e})^E} \tag{2.6.9}
$$

where,

$$\mathbf{K^{(e)}}^{E} = \begin{bmatrix} \mathbf{K^{11}} & \mathbf{K^{12}} & \mathbf{K^{13}} \\ \mathbf{K^{21}} & \mathbf{K^{22}} & \mathbf{K^{23}} \\ \mathbf{K^{31}} & \mathbf{K^{32}} & \mathbf{K^{33}} \end{bmatrix}^{(e)} \qquad \mathfrak{U}^{(\mathbf{e})E} = \begin{Bmatrix} \mathbf{U}^{(E)} \\ \boldsymbol{\Delta}^{(E)} \\ \boldsymbol{\Psi y}^{(E)} \end{Bmatrix}^{(e)} \qquad \mathbf{F^{(e)}}^{E} = \begin{Bmatrix} \mathbf{F^1} \\ \mathbf{F^2} \\ \mathbf{F^3} \end{Bmatrix}^{(e)} \tag{2.6.10}$$

The non-zero components of the above matrix are given in Appendix B.1, for both VEMBT and NEMBT.

### 2.6.3 Higher order finite elements

It is well known that lower order displacement finite elements for beams are prone to locking [93, 100, 103] when quadrature rules that result in exact integration of element coefficient matrix are employed. Such locking phenomena are usually eliminated using selective full and reduced integration techniques. In place of such numerical remedies, we employ higher order polynomials in approximating the primary variables within an element. For such higher-order polynomials of order $n-1$ on a typical element, there are $n$ nodes. However, when these nodes are equally spaced the polynomial interpolations exhibit oscillations near the end points of the standard interval. This phenomenon is called *Runge effect*.

To overcome the Runge effect we employ an unequal spacing of the nodes within each element. For a master element $\hat{\Omega}^e$ with coordinate $\xi = [-1, +1]$, the nodal coordinates are chosen to be the roots of the following equation:

$$(\xi - 1)(\xi + 1)L_p^{'}(\xi) = 0 \tag{2.6.11}$$

where $L_p(\xi)$ is the Legendre polynomial of order $p$ such that $n = p + 1$ [104]. Thus, the roots $\xi_i$ of Eq. (75), where $i = 1, 2, \ldots, n$, are the nodal coordinates in the master element and are called Gauss-Lobatto-Legendre (GLL) points or spectral points. These points are unequally spaced for

$p > 2$ and are effective in curtailing the Runge effect[†]. The Lagrange interpolation functions, $L_j$, with spectral nodal points are constructed using the formula

$$L_j = \prod_{i=1, i \neq j}^{n} \frac{\xi - \xi_i}{\xi_j - \xi_i}$$

where $\xi_j$ is the $j^{th}$ spectral point in the master element.

The Hermite interpolation functions, $H_J$, where $J = 1, 2, \ldots, 2n$, are obtained using the formulae

$$H_{2j-1} = [1 + 2L_j^{'}(\xi_j)(\xi_j - \xi)]L_j^2(\xi)$$
$$H_{2j} = (\xi - \xi_j)L_j^2(\xi)$$

where $\xi_j$ is the $j^{th}$ spectral point in the master element and $L_j$ is $j^{th}$ Lagrange interpolation function.

### 2.6.4 Solution of nonlinear equations

The nonlinear finite element equations of (2.6.4) and (2.6.9) are solved using Newton's iterative procedure [100], by constructing the tangent stiffness matrix of a typical element at the beginning of $r^{th}$ iteration as

$$\mathbf{T}^{(\mathbf{e})(r)} = \left[\frac{\partial \mathbf{R}^{(\mathbf{e})}}{\partial \mathfrak{U}^{(\mathbf{e})}}\right]^{(r-1)} \tag{2.6.12}$$

such that

$$\mathbf{T}^{(\mathbf{e})(r)} \Delta \mathfrak{U}^{\mathbf{e}} = -\mathbf{R}^{(\mathbf{e})(r-1)} \tag{2.6.13}$$

[†]GLL points are proven to be effective in eliminating the Runge effect in Lagrange interpolation functions, however that is not guaranteed for Hermite interpolation functions. In the present work we used a maximum of 8 nodes per element, located at spectral points and no Runge effect was observed for Hermite interpolation functions used in Euler-Bernoulli micropolar beam theories.

where

$$\mathbf{R}^{(\mathbf{e})} = \mathbf{K}^{(\mathbf{e})}(\mathfrak{U}^{(\mathbf{e})})\mathfrak{U}^{(\mathbf{e})} - \mathbf{F}^{(\mathbf{e})} \quad \text{and} \quad \Delta\mathfrak{U}^{(\mathbf{e})} = \mathfrak{U}^{(\mathbf{e})^{(r)}} - \mathfrak{U}^{(\mathbf{e})^{(r-1)}}$$

The explicit expressions of the components of the element tangent stiffness matrix for all the nonlinear theories considered in this chapter are given in Appendix B.1.

When the normalized difference between solution vectors from two consecutive iterations (measured with Euclidean norm) is less than a preselected tolerance, convergence is declared and further iterations are terminated [100].

## 2.7 Numerical results

Consider the constitutive relations of isotropic micropolar solid written in terms of symmetric (with superscript $(s)$) and anti-symmetric (with superscript $(a)$) stresses and strains,

$$\begin{aligned}
\sigma_{ij}^{(s)} &= \lambda\varepsilon_{kk}^{(s)}\delta_{ij} + (2\mu + \kappa)\varepsilon_{ij}^{(s)} \\
\sigma_{ij}^{(a)} &= \kappa\varepsilon_{ij}^{(a)} \\
r_{ij} &= \alpha\eta_{kk}\delta_{ij} + \beta\eta_{ji} + \gamma\eta_{ij}
\end{aligned}$$

Further the equations of equilibrium in the absence of body forces and body couples are given by

$$\begin{aligned}
\sigma_{ij,i} &= 0 \\
r_{ij,i} + \epsilon_{jmn}\sigma_{mn} &= 0
\end{aligned} \tag{2.7.1}$$

From the above equations we see that when $\kappa = 0$, the anti-symmetric stresses become zero and thereby decoupling the equations (2.7.1) so that the translations can be determined independently of microrotations. It should be noted that in this particular case, Eq. $(2.7.1_1)$ is same as the boundary value problem of classical elasticity [105]. We can completely reduce Eqs. (2.7.1) to those corresponding to classical elasticity by setting $\theta = 0$. Thus, the constitutive parameter $\kappa$ plays an important role in determining the degree of micropolarity exhibited by the material. To quantify

the effect of $\kappa$, a non-dimensional number called *Coupling Number* $(N)$ is defined in the literature [23, 106]:

$$N^2 = \frac{\kappa}{2(\mu + \kappa)}$$

The level of shear stress asymmetry is quantified by the coupling number, there by reflecting the degree of micropolarity exhibited by the material. The coupling number is bounded below by the classical elasticity and above by the so-called constrained Cosserat elasticity (or couple stress theory), where in the microrotation is equal to the conventional rotation (macrorotation) [106].

Another parameter that is frequently associated with micropolarity is the *characteristic length scale* of the material. One such length scale, called *characteristic bending length scale*, $l_b$, [23, 106] is defined as:

$$l_b^2 = \frac{\gamma}{2(2\mu + \kappa)} = \frac{\gamma(1 - 2N^2)}{4\mu(1 - N^2)}$$

The ratio of length scale of the structure to the characteristic length scale of the material has an influence on the micropolarity exhibited by the structure. For the analysis of the beams in this chapter we use the height $H$ of beam as the structural length scale. Thus, $H/l_b$ has an effect on the micropolarity exhibited by the beam. It should be noted that the coupling number affects the degree of micropolarity irrespective of the structural length scale, while it is the ratio of the structural length scale to the characteristic length scale that has influence on the micropolarity of the structure.

With this background we first establish the relation between Euler-Bernoulli and Timoshenko micropolar beam theories in the context of micropolar elasticity. Once this relation is established we will use Timoshenko micropolar beam theories in all subsequent analysis. For the purpose of numerical analysis we consider the following material properties:

$$\lambda = 15513.20 \text{ MPa}, \qquad \mu = 6894.76 \text{ MPa}, \qquad \gamma = 2668.93 \text{ N} \tag{2.7.2}$$

The value of $\kappa$ is calculated using the definition of coupling number such that

$$\kappa = \frac{2\mu N^2}{1 - 2N^2}$$

Unless stated otherwise, the width of the all beams used in the present analysis is taken to be $B = 2H$.

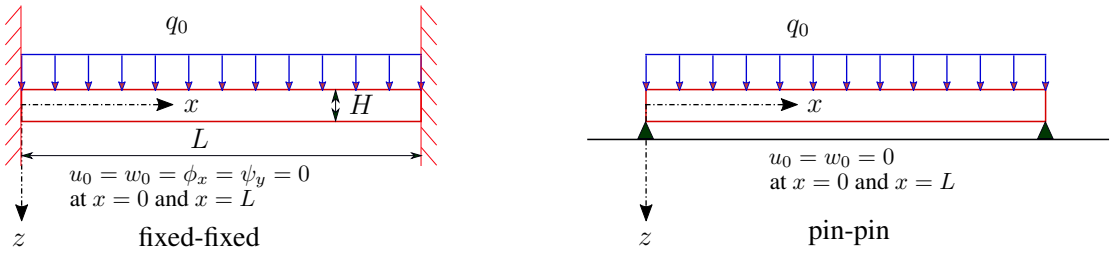


Figure 2.2: Schematic representation of the beam used in the present analysis along with the boundary conditions. For Euler-Bernoulli micropolar beam theory $\phi_x = \frac{-dw_0}{dx}$ [3].

### 2.7.1 Mesh convergence

To study the mesh convergence, we consider a beam with $L/H = 100$ and $N = 0.01$ while $H = l_b$. The rest of the material properties are as given in Eq. (2.7.2). The beam is subjected to fixed-fixed boundary conditions and a uniformly distributed load of $q_0 = 1.75$ N/m is applied on the top face (see Fig. 2.2). For such a beam, Fig. 2.3a shows the mesh convergence when VEMBT is used, while Fig. 2.3b shows the mesh convergence when NTMBT is used. If $p$ represents the number of nodes in a typical element and $h$ represents the number of elements in the mesh then $p = 4$ and $h = 4$ given mesh convergence in both the cases. However, we use $h = 4$ and $p = 8$ in all the subsequent analysis. Although only VEMBT and NTMBT for coupling number $N = 0.01$ has been considered in illustrating the mesh convergence, $h = 4$ and $p = 4$ are observed to give mesh convergent results for all nonlinear beam theories irrespective of the coupling number.

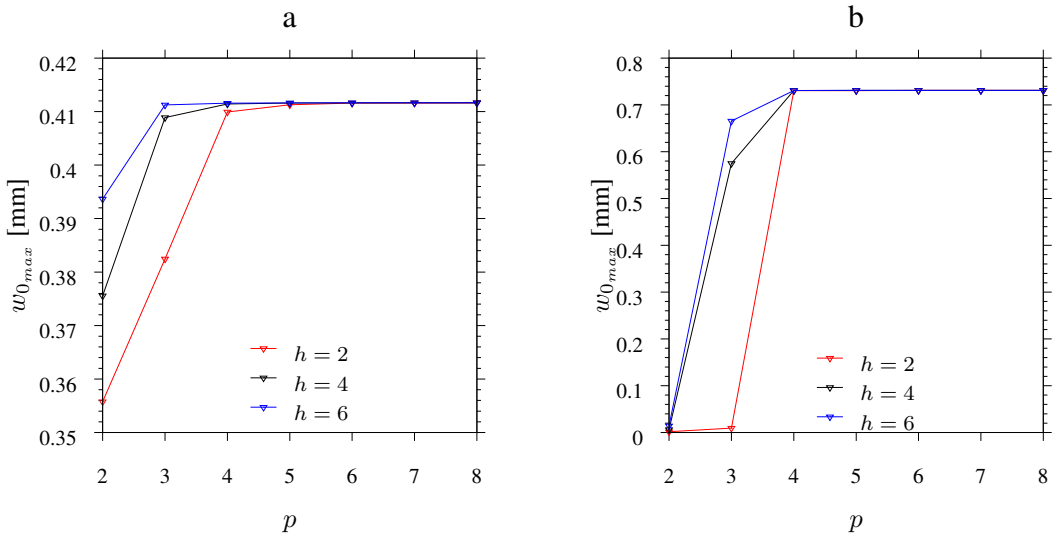


Figure 2.3: Number of nodes in an element *vs* maximum vertical deflection for various number of elements in the finite element mesh of a fixed-fixed beam under uniformly distributed load of $q_0 = 1.75$ N/m. (a) VEMBT (b) NTMBT [3].

### 2.7.2 Euler-Bernoulli vs Timoshenko micropolar beams

It is well known that within the context of classical elasticity Euler-Bernoulli and Timoshenko beam theories diverge as $L/H$ ratio decreases, with Euler-Bernoulli theory being stiffer than Timoshenko theory. We expect a similar behavior even for Euler-Bernoulli and Timoshenko micropolar beam theories. To verify this conjecture, we consider a beam with material properties given in Eq. (2.7.2) while the coupling number is taken to be $N = 0.2$. The height of the beam $H$ is taken to be $H = l_b$ and width $B = 2l_b$ such that the area moment of inertia of beam cross-section is given by $I = \frac{BH^3}{12}$. The beam is subjected to fixed-fixed boundary conditions and a uniformly distributed load of $q_0 = 1.75$ N/m is applied on the top face (see Fig. 2.2). Fig. 2.4 shows that Euler-Bernoulli micropolar beam theories are stiffer than Timoshenko micropolar beam theories for lower values of $L/H$, while both the theories give same results for higher values of $L/H$. With this observation, we use Timoshenko micropolar beam theories for the rest of the analysis carried out in this chapter.

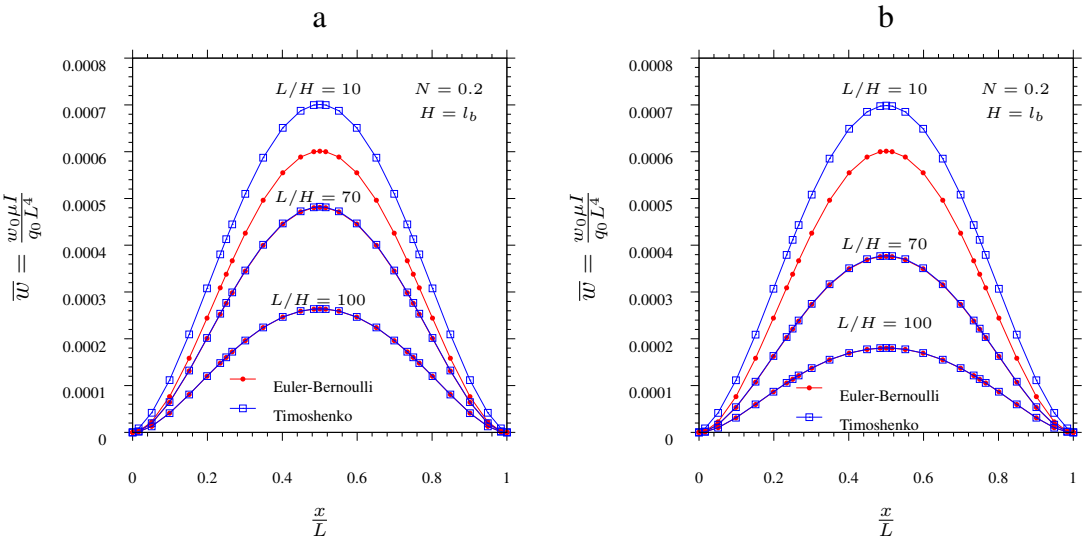


Figure 2.4: (a) Comparison of von Kármán Euler-Bernoulli micropolar beam theory and von Kármán Timoshenko micropolar beam theory for various $L/H$ ratios. (b) Comparison of nonlinear Euler-Bernoulli micropolar beam theory and nonlinear Timoshenko micropolar beam theory for various $L/H$ ratios [3].

### 2.7.3 Effect of coupling number

In this section we illustrate the effect of coupling number on the beam behavior when it is modeled using VTMBT and NTMBT. We consider two different coupling numbers, $N = 0.01$ and $N = 0.5$, for the purpose of illustration. Table 2.1 gives a comparison between VTMBT and NTMBT for $N = 0.01$ and $N = 0.5$. The beam considered has material properties given in Eq. (2.7.2). The height of the beam is taken to be $H = 0.3099$ mm and $L/H = 50$. The top face of the beam is subjected to uniformly distributed load of $q_0 = 17.5$ N/m with pin-pin boundary conditions (see Fig. 2.2).

As stated earlier, there is minimal coupling between microrotations and translations at lower values of coupling number and as the coupling number increases this coupling grows stronger. Thus at higher values of coupling numbers the microrotations $\psi_y$ should approach the macrorotations, $\omega$, giving constrained Cosserat elasticity. The macrorotations for the Timoshenko beam

theories considered in the present chapter is given by

$$\omega^T = \frac{1}{2}\left(\phi_x^T - \frac{dw_0^T}{dx}\right) \tag{2.7.3}$$

From Table 2.1 we see that for $N = 0.01$, the values of microrotations $\psi_y^T$ are equal to the macrorotations $\omega^T$ when the beam is modeled with VTMBT, while $\psi_y^T << \omega^T$ when the beam is modeled with NTMBT. For $N = 0.5$, $\psi_y^T \approx \omega^T$ for both VTMBT and NTMBT. Thus, we see that VTMBT is not sensitive to the change in coupling number in terms of the difference between microrotations and macrorotations and always predict macrorotations equal to microrotations irrespective of coupling number, while NTMBT clearly is sensitive to the changes in coupling numbers in terms of the difference between microrotations and macrorotations. Further, with increasing coupling number VTMBT shows stiffening behavior in terms of axial and transverse deflections and microrotations. However, with increasing coupling number NTMBT show stiffening behavior in terms of transverse deflections, while exhibiting softening behavior in terms of axial deflections and microrotations.

Table 2.1: Comparison of VTMBT and NTMBT for $N = 0.01$ and $N = 0.5$. The beam is subjected to pin-pin boundary conditions with uniformly distributed load $q_0 = 17.5$ N/m on top face. $H = 0.3099$ mm and $L/H = 50$. The values of $u_0^T$ and $w_0^T$ are given in millimeters (mm) [3].

| $\frac{x}{L}$ | $N = 0.01; l_b = 0.3099$ mm | | | | | | | | $N = 0.5; l_b = 0.2540$ mm | | | | | | | |
|---|---|---|---|---|---|---|---|---|---|---|---|---|---|---|---|---|
| | VTMBT | | | | NTMBT | | | | VTMBT | | | | NTMBT | | | |
| | $u_0^T$ | $w_0^T$ | $\psi_y^T$ | $\omega^T$ | $u_0^T$ | $w_0^T$ | $\psi_y^T$ | $\omega^T$ | $u_0^T$ | $w_0^T$ | $\psi_y^T$ | $\omega^T$ | $u_0^T$ | $w_0^T$ | $\psi_y^T$ | $\omega^T$ |
| 0.00000 | 0.00000 | 0.00000 | -0.03355 | -0.03355 | 0.00000 | 0.00000 | -0.00380 | -0.04703 | 0.00000 | 0.00000 | -0.02984 | -0.02984 | 0.00000 | 0.00000 | -0.02138 | -0.02139 |
| 0.01603 | -0.00007 | 0.00834 | -0.03349 | -0.03349 | -0.00002 | 0.01169 | -0.00380 | -0.04695 | -0.00006 | 0.00741 | -0.02979 | -0.02979 | -0.00006 | 0.00532 | -0.02134 | -0.02135 |
| 0.05104 | -0.00023 | 0.02640 | -0.03299 | -0.03299 | -0.00007 | 0.03703 | -0.00375 | -0.04629 | -0.00018 | 0.02348 | -0.02935 | -0.02935 | -0.00019 | 0.01683 | -0.02100 | -0.02101 |
| 0.09884 | -0.00042 | 0.05037 | -0.03155 | -0.03155 | -0.00013 | 0.07069 | -0.00359 | -0.04437 | -0.00033 | 0.04481 | -0.02809 | -0.02809 | -0.00034 | 0.03209 | -0.02005 | -0.02006 |
| 0.15116 | -0.00058 | 0.07503 | -0.02912 | -0.02912 | -0.00018 | 0.10543 | -0.00333 | -0.04107 | -0.00045 | 0.06678 | -0.02595 | -0.02595 | -0.00047 | 0.04775 | -0.01846 | -0.01847 |
| 0.19896 | -0.00066 | 0.09559 | -0.02625 | -0.02625 | -0.00021 | 0.13446 | -0.00301 | -0.03714 | -0.00052 | 0.08510 | -0.02341 | -0.02341 | -0.00054 | 0.06077 | -0.01660 | -0.01661 |
| 0.23397 | -0.00069 | 0.10918 | -0.02382 | -0.02382 | -0.00022 | 0.15372 | -0.00274 | -0.03376 | -0.00054 | 0.09723 | -0.02126 | -0.02126 | -0.00056 | 0.06936 | -0.01503 | -0.01504 |
| 0.25000 | -0.00069 | 0.11496 | -0.02262 | -0.02262 | -0.00022 | 0.16191 | -0.00260 | -0.03210 | -0.00054 | 0.10238 | -0.02020 | -0.02020 | -0.00056 | 0.07301 | -0.01427 | -0.01428 |
| 0.26603 | -0.00068 | 0.12042 | -0.02138 | -0.02138 | -0.00022 | 0.16967 | -0.00246 | -0.03036 | -0.00054 | 0.10727 | -0.01910 | -0.01910 | -0.00055 | 0.07646 | -0.01348 | -0.01349 |
| 0.30104 | -0.00064 | 0.13126 | -0.01853 | -0.01853 | -0.00021 | 0.18508 | -0.00214 | -0.02636 | -0.00051 | 0.11695 | -0.01656 | -0.01656 | -0.00052 | 0.08329 | -0.01166 | -0.01167 |
| 0.34884 | -0.00055 | 0.14346 | -0.01436 | -0.01436 | -0.00018 | 0.20246 | -0.00166 | -0.02047 | -0.00043 | 0.12785 | -0.01284 | -0.01284 | -0.00044 | 0.09097 | -0.00902 | -0.00903 |
| 0.40116 | -0.00039 | 0.15317 | -0.00954 | -0.00954 | -0.00012 | 0.21631 | -0.00110 | -0.01361 | -0.00031 | 0.13653 | -0.00853 | -0.00853 | -0.00031 | 0.09707 | -0.00598 | -0.00599 |
| 0.44896 | -0.00021 | 0.15855 | -0.00496 | -0.00496 | -0.00007 | 0.22399 | -0.00058 | -0.00709 | -0.00017 | 0.14135 | -0.00444 | -0.00444 | -0.00017 | 0.10044 | -0.00311 | -0.00311 |
| 0.48397 | -0.00007 | 0.16032 | -0.00156 | -0.00156 | -0.00002 | 0.22652 | -0.00018 | -0.00223 | -0.00005 | 0.14293 | -0.00140 | -0.00140 | -0.00005 | 0.10155 | -0.00098 | -0.00098 |
| 0.50000 | 0.00000 | 0.16052 | -0.00000 | -0.00000 | 0.00000 | 0.22680 | -0.00000 | -0.00000 | -0.00000 | 0.14311 | 0.00000 | -0.00000 | -0.00000 | 0.10168 | 0.00000 | -0.00000 |
| 0.51603 | 0.00007 | 0.16032 | 0.00156 | 0.00156 | 0.00002 | 0.22652 | 0.00018 | 0.00223 | 0.00005 | 0.14293 | 0.00140 | 0.00140 | 0.00005 | 0.10155 | 0.00098 | 0.00098 |
| 0.55104 | 0.00021 | 0.15855 | 0.00496 | 0.00496 | 0.00007 | 0.22399 | 0.00058 | 0.00709 | 0.00017 | 0.14135 | 0.00444 | 0.00444 | 0.00017 | 0.10044 | 0.00311 | 0.00311 |
| 0.59884 | 0.00039 | 0.15317 | 0.00954 | 0.00954 | 0.00012 | 0.21631 | 0.00110 | 0.01361 | 0.00031 | 0.13653 | 0.00853 | 0.00853 | 0.00031 | 0.09707 | 0.00598 | 0.00599 |
| 0.65116 | 0.00055 | 0.14346 | 0.01436 | 0.01436 | 0.00018 | 0.20246 | 0.00166 | 0.02047 | 0.00043 | 0.12785 | 0.01284 | 0.01284 | 0.00044 | 0.09097 | 0.00902 | 0.00903 |
| 0.69896 | 0.00064 | 0.13126 | 0.01853 | 0.01853 | 0.00021 | 0.18508 | 0.00214 | 0.02636 | 0.00051 | 0.11695 | 0.01656 | 0.01656 | 0.00052 | 0.08329 | 0.01166 | 0.01167 |
| 0.73397 | 0.00068 | 0.12042 | 0.02138 | 0.02138 | 0.00022 | 0.16967 | 0.00246 | 0.03036 | 0.00054 | 0.10727 | 0.01910 | 0.01910 | 0.00055 | 0.07646 | 0.01348 | 0.01349 |
| 0.75000 | 0.00069 | 0.11496 | 0.02262 | 0.02262 | 0.00022 | 0.16191 | 0.00260 | 0.03210 | 0.00054 | 0.10238 | 0.02020 | 0.02020 | 0.00056 | 0.07301 | 0.01427 | 0.01428 |
| 0.76603 | 0.00069 | 0.10918 | 0.02382 | 0.02382 | 0.00022 | 0.15372 | 0.00274 | 0.03376 | 0.00054 | 0.09723 | 0.02126 | 0.02126 | 0.00056 | 0.06936 | 0.01503 | 0.01504 |
| 0.80104 | 0.00066 | 0.09559 | 0.02625 | 0.02625 | 0.00021 | 0.13446 | 0.00301 | 0.03714 | 0.00052 | 0.08510 | 0.02341 | 0.02341 | 0.00054 | 0.06077 | 0.01660 | 0.01661 |
| 0.84884 | 0.00058 | 0.07503 | 0.02912 | 0.02912 | 0.00018 | 0.10543 | 0.00333 | 0.04107 | 0.00045 | 0.06678 | 0.02595 | 0.02595 | 0.00047 | 0.04775 | 0.01846 | 0.01847 |
| 0.90116 | 0.00042 | 0.05037 | 0.03155 | 0.03155 | 0.00013 | 0.07069 | 0.00359 | 0.04437 | 0.00033 | 0.04481 | 0.02809 | 0.02809 | 0.00034 | 0.03209 | 0.02005 | 0.02006 |
| 0.94896 | 0.00023 | 0.02640 | 0.03299 | 0.03299 | 0.00007 | 0.03703 | 0.00375 | 0.04629 | 0.00018 | 0.02348 | 0.02935 | 0.02935 | 0.00019 | 0.01683 | 0.02100 | 0.02101 |
| 0.98397 | 0.00007 | 0.00834 | 0.03349 | 0.03349 | 0.00002 | 0.01169 | 0.00380 | 0.04695 | 0.00006 | 0.00741 | 0.02979 | 0.02979 | 0.00006 | 0.00532 | 0.02134 | 0.02135 |
| 1.00000 | 0.00000 | 0.00000 | 0.03355 | 0.03355 | 0.00000 | 0.00000 | 0.00380 | 0.04703 | 0.00000 | 0.00000 | 0.02984 | 0.02984 | 0.00000 | 0.00000 | 0.02138 | 0.02139 |

Another interesting observation is that VTMBT is stiffer than NTMBT (above certain load) in term of transverse deflections for $N = 0.01$, while NTMBT is stiffer than VTMBT for $N = 0.5$. This can be explained by the definitions of nonlinearity in two theories. In NTMBT the nonlinearity

arises due to the strain definition:

$$e_{xx}^{T(s)} = \left( \frac{du_0^T}{dx} - \psi_y^T \frac{dw_0^T}{dx} \right) + z \frac{d\phi_x^T}{dx}$$

while in VTMBT the nonlinear strain is defined as:

$$\varepsilon_{xx}^{T(s)} = \frac{du_0^T}{dx} + \frac{1}{2} \left( \frac{dw_0^T}{dx} \right)^2 + z \frac{d\phi_x^T}{dx}$$

It is clear that nonlinearity in VTMBT is independent of the microrotations, while in NTMBT it is due the combination of both microrotations and the rotations of normals to the axis of the beam. Since for lower coupling number, $N = 0.01$, the microrotations are small in NTMBT, the effect of nonlinearity is not severe. However, the nonlinearity in VTMBT being independent of the microrotations and also microrotations being equal to macrorotations, the nonlinearity is severe compared to NTMBT and thus predict stiffer deflections. Towards the other end of coupling number spectrum, say $N = 0.5$, both theories predict $\psi_y^T \approx \omega^T$. However, NTMBT is stiffer than VTMBT at such conditions as is evident from factor $\frac{1}{2}$ in the nonlinear strain definitions of the two theories. This is further illustrated in Fig. 2.5, where nonlinearity in deflections for the two theories are compared to the deflections from linear Timoshenko micropolar beam theory (LTMBT). It also shows that nonlinearity begins sooner in NTMBT than in VTMBT with increasing load.

Lastly, Fig. 2.6 compares the transverse deflections, microrotations and macrorotations predicted by VTMBT and NTMBT for a range of coupling numbers. It can be clearly seen that at lower values of coupling number the bending stiffness predicted by VTMBT is higher than that predicted by NTMBT, while it is the other way around at higher values of coupling number. Further, Fig. 2.6b shows that the magnitude of microrotations is small compared to macrorotations for lower coupling numbers and increases with increasing coupling number when NTMBT is used to model the beam. However, when VTMBT is used, microrotations are equal to macrorotations irrespective of the coupling number. The behavior predicted by NTMBT concurs with theory micropolar elasticity even at lower values of coupling number, while this is not the case with VTMBT.

Thus, for materials with low micropolar coupling, NTMBT is more appropriate than VTMBT.

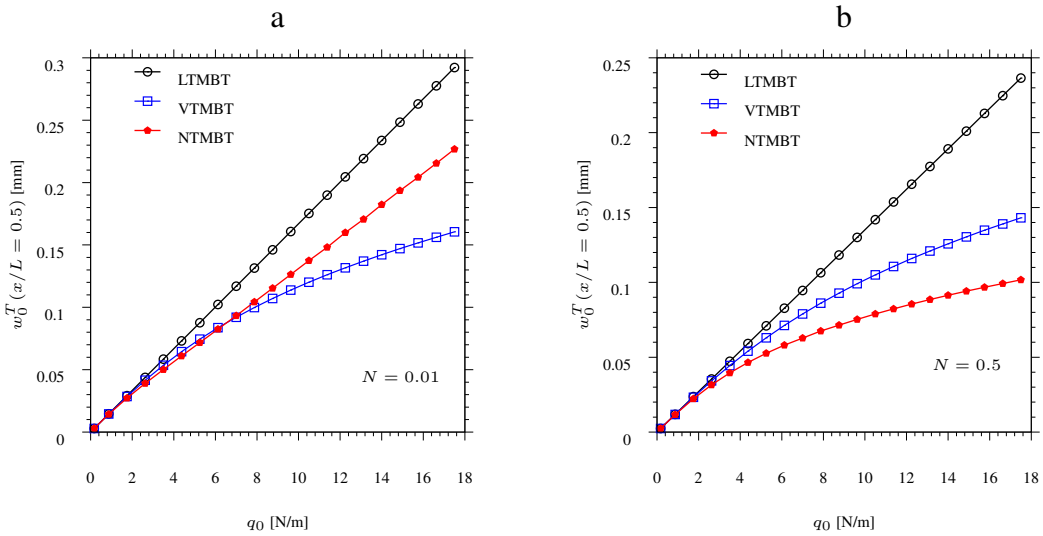


Figure 2.5: Load *vs* maximum transverse deflections of a beam with pin-pin boundary conditions subjected to uniformly distributed load on top ($H = 0.3099$ mm and $L/H = 50$). (a) $N = 0.01$ and (b) $N = 0.5$ [3].

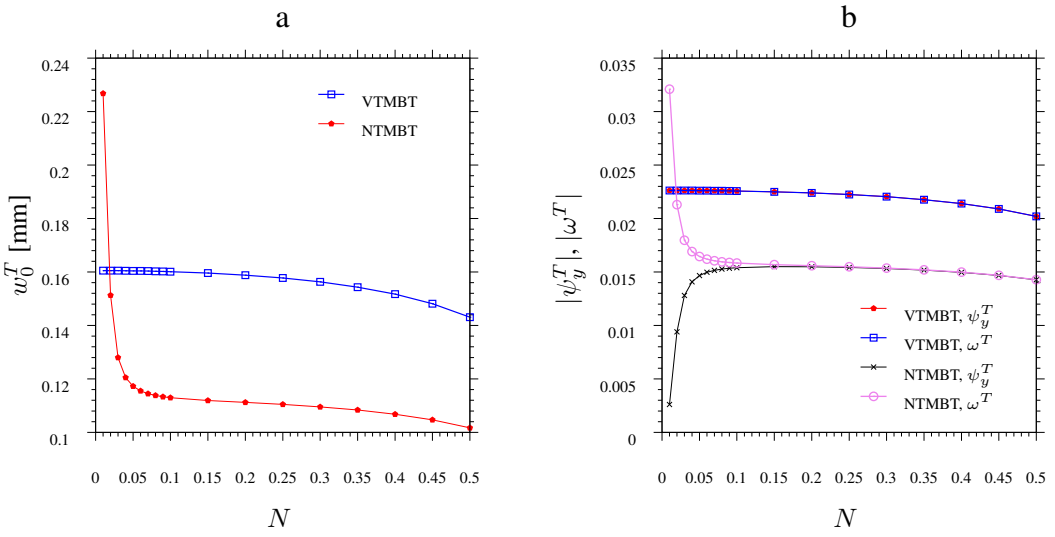


Figure 2.6: Comparison of VTMBT and NTMBT for a beam with pin-pin boundary conditions, subjected to uniformly distributed load, $q_0 = 17.5$ N/m, on the top ($H = 0.3099$ mm and $L/H = 50$). (a) $N$ *vs* $w_0^T(x/L = 0.5)$ and (b) $N$ *vs* $|\psi_y^T(x/L = 0.25)|$ and $N$ *vs* $|\omega^T(x/L = 0.25)|$ [3].

# 3. NONLINEAR MICROPOLAR PLATE THEORIES

## 3.1 Introduction

In this section we will utilize the *first order shear deformation* (FSD) plate theory of classical Cauchy continuum to construct the plate theory for micropolar continuum. Let the plate considered be such that its mid plane coincides with the $x$-$y$ plane of the coordinate system considered, while the $z$-axis will be pointing in downward direction. The length of the plate is $L$, breadth of the plate is $B$ and height of the plate is $H$. The displacement field of FSD micropolar plate theory is based on the same assumptions of FSD plate theory of classical continuum (i.e., the assumptions that the planes perpendicular to the axis of the plate remain plane after deformation and are in-extensible are still valid). Thus the displacement field is given by

$$\begin{aligned} u_1(x,y,z) &= u_0(x,y) + z\phi_x(x,y) \\ u_2(x,y,z) &= v_0(x,y) + z\phi_y(x,y) \\ u_3(x,y,z) &= w_0(x,y) \end{aligned} \tag{3.1.1}$$

We assume that only the $x$ and $y$ components of the microrotation are non-zero and that they only depend on $x$ and $y$ coordinates.

$$\begin{aligned} \psi_1(x,y,z) &= \psi_x(x,y) \\ \psi_2(x,y,z) &= \psi_y(x,y) \\ \psi_3(x,y,z) &= 0 \end{aligned} \tag{3.1.2}$$

This approximation implies that the planes normal to the mid-plane of the plate are made of particles which can only rotate about $x$ and $y$ axes. Thus $\phi_x$ and $\phi_y$ represent the rotation of these planes about $y$-axis and $x$-axis respectively, while $\psi_x$ and $\psi_y$ represents the rotations of the particles within this plane about $x$-axis and $y$-axis respectively.

### 3.2 von Kármán nonlinearity and corresponding governing equations

For a Cauchy continuum plate, to account for the moderate rotations while still considering displacement gradients to be small, the nonlinear terms of the Green-Lagrange strain tensor that correspond to the product of rotations of fibers perpendicular to the mid plane of the plate are retained. The resulting plate equations after this modification to the strains are called von-Kármán nonlinear plate theories of classical continuum [107]. In classical continuum the von-Kármán nonlinearity leads to the following nonlinear strains (of classical continuum):

$$\varepsilon_{xx} = \frac{\partial u_0}{\partial x} + \frac{1}{2}\left(\frac{\partial w_0}{\partial x}\right)^2 + z\frac{\partial \phi_x}{\partial x}$$
$$\varepsilon_{yy} = \frac{\partial v_0}{\partial y} + \frac{1}{2}\left(\frac{\partial w_0}{\partial y}\right)^2 + z\frac{\partial \phi_y}{\partial y}$$
$$2\varepsilon_{xy} = \frac{\partial u_0}{\partial y} + \frac{\partial v_0}{\partial x} + \frac{\partial w_0}{\partial x}\frac{\partial w_0}{\partial y} + z\left(\frac{\partial \phi_x}{\partial y} + \frac{\partial \phi_y}{\partial x}\right)$$

If we extend the same argument to micropolar plates, that is, the displacement gradients are small but the rotations of the fibers perpendicular to the mid plane of plate are moderate, we can extend the von Kármán approximation of classical continuum plate to micropolar plate (see [6]). This will result in the following modified strains of micropolar plate:

$$
\begin{aligned}
\varepsilon_{xx}^{(s)} &= \frac{\partial u_0}{\partial x} + \frac{1}{2}\left(\frac{\partial w_0}{\partial x}\right)^2 + z\frac{\partial \phi_x}{\partial x} \\
\varepsilon_{yy}^{(s)} &= \frac{\partial v_0}{\partial y} + \frac{1}{2}\left(\frac{\partial w_0}{\partial y}\right)^2 + z\frac{\partial \phi_y}{\partial y} \\
2\varepsilon_{xy}^{(s)} &= \left(\frac{\partial v_0}{\partial x} + \frac{\partial u_0}{\partial y} + \frac{\partial w_0}{\partial x}\frac{\partial w_0}{\partial y}\right) + z\left(\frac{\partial \phi_y}{\partial x} + \frac{\partial \phi_x}{\partial y}\right) \\
2\varepsilon_{xy}^{(a)} &= \left(\frac{\partial u_0}{\partial y} - \frac{\partial v_0}{\partial x}\right) + z\left(\frac{\partial \phi_x}{\partial y} - \frac{\partial \phi_y}{\partial x}\right) \\
2\varepsilon_{xz}^{(s)} &= \left(\phi_x + \frac{\partial w_0}{\partial x}\right) \\
2\varepsilon_{xz}^{(a)} &= \left(\phi_x - \frac{\partial w_0}{\partial x} - 2\psi_y\right) \\
2\varepsilon_{yz}^{(s)} &= \left(\phi_y + \frac{\partial w_0}{\partial y}\right) \\
2\varepsilon_{yz}^{(a)} &= \left(\phi_y - \frac{\partial w_0}{\partial y} + 2\psi_x\right)
\end{aligned}
\tag{3.2.1}
$$

$$
\begin{aligned}
\eta_{xx} &= \frac{\partial \psi_x}{\partial x}, \qquad & \eta_{xy} &= \frac{\partial \psi_x}{\partial y} \\
\eta_{yx} &= \frac{\partial \psi_y}{\partial x}, \qquad & \eta_{yy} &= \frac{\partial \psi_y}{\partial y}
\end{aligned}
\tag{3.2.2}
$$

If $\sigma_{ij}^{(s)}$, $\sigma_{ij}^{(a)}$ and $r_{ij}$ are the symmetric and anti-symmetric stresses and couple stresses conjugate to modified $\varepsilon_{ij}^{(s)}$, $\varepsilon_{ij}^{(a)}$ and $\eta_{ij}$ respectively, we definie the stress, moment and couple stress resultants acting on the plate as

$$
\begin{Bmatrix} N_{xx}^{(s)} \\ N_{yy}^{(s)} \\ N_{xy}^{(s)} \\ N_{xy}^{(a)} \end{Bmatrix} = \int_{-\frac{H}{2}}^{\frac{H}{2}} \begin{Bmatrix} \sigma_{xx}^{(s)} \\ \sigma_{yy}^{(s)} \\ \sigma_{xy}^{(s)} \\ \sigma_{xy}^{(a)} \end{Bmatrix} dz, \qquad \begin{Bmatrix} M_{xx}^{(s)} \\ M_{yy}^{(s)} \\ M_{xy}^{(s)} \\ M_{xy}^{(a)} \end{Bmatrix} = \int_{-\frac{H}{2}}^{\frac{H}{2}} \begin{Bmatrix} \sigma_{xx}^{(s)} \\ \sigma_{yy}^{(s)} \\ \sigma_{xy}^{(s)} \\ \sigma_{xy}^{(a)} \end{Bmatrix} z dz \tag{3.2.3}
$$

$$\begin{Bmatrix} Q_x^{(s)} \\ Q_x^{(a)} \\ Q_y^{(s)} \\ Q_y^{(a)} \end{Bmatrix} = \int_{-\frac{H}{2}}^{\frac{H}{2}} \begin{Bmatrix} \sigma_{xz}^{(s)} \\ \sigma_{xz}^{(a)} \\ \sigma_{yz}^{(s)} \\ \sigma_{yz}^{(a)} \end{Bmatrix} dz, \qquad \begin{Bmatrix} P_{xx} \\ P_{xy} \\ P_{yx} \\ P_{yy} \end{Bmatrix} = \int_{-\frac{H}{2}}^{\frac{H}{2}} \begin{Bmatrix} r_{xx} \\ r_{xy} \\ r_{yx} \\ r_{yy} \end{Bmatrix} dz \tag{3.2.4}$$

The principle of virtual work for the micropolar plate with a distributed transverse load $q_0$ can be written in terms of the resultants (3.2.3) and (3.2.4) as follows

$$\begin{aligned} \int_A \Bigg\{ & N_{xx}^{(s)} \left( \frac{\partial \delta u_0}{\partial x} + \frac{\partial \delta w_0}{\partial x} \frac{\partial w_0}{\partial x} \right) + M_{xx}^{(s)} \frac{\partial \delta \phi_x}{\partial x} + N_{yy}^{(s)} \left( \frac{\partial \delta v_0}{\partial y} + \frac{\partial \delta w_0}{\partial y} \frac{\partial w_0}{\partial y} \right) \\ & + M_{yy}^{(s)} \frac{\partial \delta \phi_y}{\partial y} + N_{xy}^{(s)} \left( \frac{\partial \delta u_0}{\partial y} + \frac{\partial \delta v_0}{\partial x} + \frac{\partial \delta w_0}{\partial x} \frac{\partial w_0}{\partial y} + \frac{\partial \delta w_0}{\partial y} \frac{\partial w_0}{\partial x} \right) \\ & + M_{xy}^{(s)} \left( \frac{\partial \delta \phi_y}{\partial x} + \frac{\partial \delta \phi_x}{\partial y} \right) + N_{xy}^{(a)} \left( \frac{\partial \delta u_0}{\partial y} - \frac{\partial \delta v_0}{\partial x} \right) + M_{xy}^{(a)} \left( \frac{\partial \delta \phi_x}{\partial y} - \frac{\partial \delta \phi_y}{\partial x} \right) \\ & + Q_x^{(s)} \left( \frac{\partial \delta w_0}{\partial x} + \delta \phi_x \right) + Q_y^{(s)} \left( \frac{\partial \delta w_0}{\partial y} + \delta \phi_y \right) + Q_x^{(a)} \left( \delta \phi_x - \frac{\partial \delta w_0}{\partial x} - 2 \delta \psi_y \right) \\ & + Q_y^{(a)} \left( \delta \phi_y - \frac{\partial \delta w_0}{\partial y} + 2 \delta \psi_x \right) + P_{xx} \frac{\partial \delta \psi_x}{\partial x} + P_{xy} \frac{\partial \delta \psi_x}{\partial y} + P_{yx} \frac{\partial \delta \psi_y}{\partial x} + P_{yy} \frac{\partial \delta \psi_y}{\partial y} \\ & - q_0 \delta w_0 \Bigg\} dx dy = 0 \end{aligned} \tag{3.2.5}$$

where $A$ is the area of the plate. The governing equations of von-Kármán micropolar plate theory

are obtained by taking the Euler equations of the above variational statement (3.2.5) as

$$\delta u_0: \quad \frac{\partial N_{xx}^{(s)}}{\partial x} + \frac{\partial}{\partial y}\left(N_{xy}^{(s)} + N_{xy}^{(a)}\right) = 0 \tag{3.2.6}$$

$$\delta v_0: \quad \frac{\partial}{\partial x}\left(N_{xy}^{(s)} - N_{xy}^{(a)}\right) + \frac{\partial N_{yy}^{(s)}}{\partial y} = 0 \tag{3.2.7}$$

$$\begin{aligned}\delta w_0: \quad & \frac{\partial}{\partial x}\left(\frac{\partial w_0}{\partial x}N_{xx}^{(s)} + \frac{\partial w_0}{\partial y}N_{xy}^{(s)}\right) + \frac{\partial}{\partial y}\left(\frac{\partial w_0}{\partial x}N_{xy}^{(s)} + \frac{\partial w_0}{\partial y}N_{yy}^{(s)}\right) \\ & + \frac{\partial}{\partial x}(Q_x^{(s)} - Q_x^{(a)}) + \frac{\partial}{\partial y}(Q_y^{(s)} - Q_y^{(a)}) + q_0 = 0\end{aligned} \tag{3.2.8}$$

$$\delta \phi_x: \quad \frac{\partial M_{xx}^{(s)}}{\partial x} + \frac{\partial}{\partial y}\left(M_{xy}^{(s)} + M_{xy}^{(a)}\right) - Q_x^{(s)} - Q_x^{(a)} = 0 \tag{3.2.9}$$

$$\delta \phi_y: \quad \frac{\partial}{\partial x}\left(M_{xy}^{(s)} - M_{xy}^{(a)}\right) + \frac{\partial M_{yy}^{(s)}}{\partial y} - Q_y^{(s)} - Q_y^{(a)} = 0 \tag{3.2.10}$$

$$\delta \psi_x: \quad \frac{\partial P_{xx}}{\partial x} + \frac{\partial P_{xy}}{\partial y} - 2Q_y^{(a)} = 0 \tag{3.2.11}$$

$$\delta \psi_y: \quad \frac{\partial P_{yx}}{\partial x} + \frac{\partial P_{yy}}{\partial y} + 2Q_x^{(a)} = 0 \tag{3.2.12}$$

with the following natural boundary conditions

$$\begin{aligned}
Q_1 &\equiv N_{xx}^{(s)} n_x + \left(N_{xy}^{(s)} + N_{xy}^{(a)}\right) n_y = 0 \\
Q_2 &\equiv \left(N_{xy}^{(s)} - N_{xy}^{(a)}\right) n_x + N_{yy}^{(s)} n_y = 0 \\
Q_3 &\equiv \left(Q_x^{(s)} - Q_x^{(a)} + \frac{\partial w_0}{\partial x}N_{xx}^{(s)} + \frac{\partial w_0}{\partial y}N_{xy}^{(s)}\right) n_x \\
&\quad + \left(Q_y^{(s)} - Q_y^{(a)} + \frac{\partial w_0}{\partial x}N_{xy}^{(s)} + \frac{\partial w_0}{\partial y}N_{yy}^{(s)}\right) n_y = 0 \\
Q_4 &\equiv M_{xx}^{(s)} n_x + \left(M_{xy}^{(s)} + M_{xy}^{(a)}\right) n_y = 0 \\
Q_5 &\equiv \left(M_{xy}^{(s)} - M_{xy}^{(a)}\right) n_x + M_{yy}^{(s)} n_y = 0 \\
Q_6 &\equiv P_{xx} n_x + P_{xy} n_y = 0 \\
Q_7 &\equiv P_{yx} n_x + P_{yy} n_y = 0
\end{aligned} \tag{3.2.13}$$

where $n_x$ and $n_y$ are the $x$ and $y$ components of the directions cosines of the boundary.

### 3.3 Micropolar nonlinearity and corresponding governing equations

In this section, rather than borrowing the von Kármán nonlinearity of classical continuum to account for the moderate rotations of the micropolar plate we will make appropriate approximations on the symmetric and anti-symmetric Cosserat deformation components of Eq. (1.1.12) to reflect the condition of moderate rotations of fibers normal to the mid plane of plate while still assuming the displacement gradients to be small. Since the displacement gradients are small, except for those that represent the rotations of fibers perpendicular to the mid plane of plate, we can make the following approximation on the magnitudes of various terms of Eqs. (1.1.12)

$$\begin{aligned} & u_{\alpha,i} = o(\rho), \qquad \psi_i = o(\sqrt{\rho}) \\ & u_{3,\alpha} = o(\sqrt{\rho}), \qquad \phi_y, \phi_x = o(\sqrt{\rho}) \\ & \text{where} \quad \rho << 1, \quad \alpha = 1,2 \quad \text{and} \quad i = 1,2,3 \end{aligned} \tag{3.3.1}$$

Neglecting terms of order $o(\rho)$ and higher in calculating the Cosserat deformation components of Eqs. (1.1.12) we will arrive at a nonlinear Cosserat deformation tensor which will represent the moderate rotations and small displacement gradients of the micropolar plate. The resulting

components of the Cosserat deformation gradient and wryness tensor are

$$
\begin{aligned}
e_{xx}^{(s)} &= \left(\frac{\partial u_0}{\partial x} - \psi_y \frac{\partial w_0}{\partial x}\right) + z\left(\frac{\partial \phi_x}{\partial x}\right) \\
e_{yy}^{(s)} &= \left(\frac{\partial v_0}{\partial y} + \psi_x \frac{\partial w_0}{\partial y}\right) + z\left(\frac{\partial \phi_y}{\partial y}\right) \\
2e_{xy}^{(s)} &= \left(\frac{\partial u_0}{\partial y} + \frac{\partial v_0}{\partial x} + \psi_x \frac{\partial w_0}{\partial x} - \psi_y \frac{\partial w_0}{\partial y}\right) + z\left(\frac{\partial \phi_x}{\partial y} + \frac{\partial \phi_y}{\partial x}\right) \\
2e_{xy}^{(a)} &= \left(\frac{\partial u_0}{\partial y} - \frac{\partial v_0}{\partial x} - \psi_x \frac{\partial w_0}{\partial x} - \psi_y \frac{\partial w_0}{\partial y}\right) + z\left(\frac{\partial \phi_x}{\partial y} - \frac{\partial \phi_y}{\partial x}\right) \\
2e_{xz}^{(s)} &= \left(\frac{\partial w_0}{\partial x} + \phi_x\right) \\
2e_{xz}^{(a)} &= \left(\phi_x - \frac{\partial w_0}{\partial x} - 2\psi_y\right) \\
2e_{yz}^{(s)} &= \left(\frac{\partial w_0}{\partial y} + \phi_y\right) \\
2e_{yz}^{(a)} &= \left(\phi_y - \frac{\partial w_0}{\partial y} + 2\psi_x\right)
\end{aligned}
\tag{3.3.2}
$$

$$
\begin{aligned}
\eta_{xx} &= \frac{\partial \psi_x}{\partial x}, \qquad \eta_{xy} = \frac{\partial \psi_x}{\partial y} \\
\eta_{yx} &= \frac{\partial \psi_y}{\partial x}, \qquad \eta_{yy} = \frac{\partial \psi_y}{\partial y}
\end{aligned}
\tag{3.3.3}
$$

If $\Sigma_{ij}^{(s)}$, $\Sigma_{ij}^{(a)}$ and $m_{ij}$ are the symmetric anti-symmetric stresses and couple stresses conjugate to $e_{ij}^{(s)}$, $e_{ij}^{(a)}$ and $\eta_{ij}$ after moderate rotation approximation, we define stress, moment and couple stress resultants acting on the plate as

$$
\begin{Bmatrix} \mathfrak{N}_{xx}^{(s)} \\ \mathfrak{N}_{yy}^{(s)} \\ \mathfrak{N}_{xy}^{(s)} \\ \mathfrak{N}_{xy}^{(a)} \end{Bmatrix} = \int_{-\frac{H}{2}}^{\frac{H}{2}} \begin{Bmatrix} \Sigma_{xx}^{(s)} \\ \Sigma_{yy}^{(s)} \\ \Sigma_{xy}^{(s)} \\ \Sigma_{xy}^{(a)} \end{Bmatrix} dz, \qquad \begin{Bmatrix} \mathfrak{Q}_{x}^{(s)} \\ \mathfrak{Q}_{x}^{(a)} \\ \mathfrak{Q}_{y}^{(s)} \\ \mathfrak{Q}_{y}^{(a)} \end{Bmatrix} = \int_{-\frac{H}{2}}^{\frac{H}{2}} \begin{Bmatrix} \Sigma_{xz}^{(s)} \\ \Sigma_{xz}^{(a)} \\ \Sigma_{yz}^{(s)} \\ \Sigma_{yz}^{(a)} \end{Bmatrix} dz \tag{3.3.4}
$$

$$\begin{Bmatrix} \mathfrak{M}_{xx}^{(s)} \\ \mathfrak{M}_{yy}^{(s)} \\ \mathfrak{M}_{xy}^{(s)} \\ \mathfrak{M}_{xy}^{(a)} \end{Bmatrix} = \int_{-\frac{H}{2}}^{\frac{H}{2}} \begin{Bmatrix} \Sigma_{xx}^{(s)} \\ \Sigma_{yy}^{(s)} \\ \Sigma_{xy}^{(s)} \\ \Sigma_{xy}^{(a)} \end{Bmatrix} z dz, \qquad \begin{Bmatrix} \mathfrak{P}_{xx} \\ \mathfrak{P}_{xy} \\ \mathfrak{P}_{yx} \\ \mathfrak{P}_{yy} \end{Bmatrix} = \int_{-\frac{H}{2}}^{\frac{H}{2}} \begin{Bmatrix} m_{xx} \\ m_{xy} \\ m_{yx} \\ m_{yy} \end{Bmatrix} dz \tag{3.3.5}$$

The principle of virtual work for the micropolar plate with transverse distributed load $q_0$ can be written in terms of the resultants (3.3.4) and (3.3.5) as follows

$$\begin{aligned}
\int_A \Bigg\{ & \mathfrak{N}_{xx}^{(s)} \left( \frac{\partial \delta u_0}{\partial x} - \delta\psi_y \frac{\partial w_0}{\partial x} - \psi_y \frac{\partial \delta w_0}{\partial x} \right) + \mathfrak{M}_{xx}^{(s)} \frac{\partial \delta \phi_x}{\partial x} + \mathfrak{M}_{yy}^{(s)} \frac{\partial \delta \phi_y}{\partial y} \\
& + \mathfrak{N}_{yy}^{(s)} \left( \frac{\partial \delta v_0}{\partial y} + \delta\psi_x \frac{\partial w_0}{\partial y} + \psi_x \frac{\partial \delta w_0}{\partial y} \right) + \mathfrak{M}_{xy}^{(s)} \left( \frac{\partial \delta \phi_x}{\partial y} + \frac{\partial \delta \phi_y}{\partial x} \right) \\
& + \mathfrak{N}_{xy}^{(s)} \left( \frac{\partial \delta u_0}{\partial y} + \frac{\partial \delta v_0}{\partial x} + \delta\psi_x \frac{\partial w_0}{\partial x} + \psi_x \frac{\partial \delta w_0}{\partial x} - \delta\psi_y \frac{\partial w_0}{\partial y} - \psi_y \frac{\partial \delta w_0}{\partial y} \right) \\
& + \mathfrak{N}_{xy}^{(a)} \left( \frac{\partial \delta u_0}{\partial y} - \frac{\partial \delta v_0}{\partial x} - \delta\psi_x \frac{\partial w_0}{\partial x} - \psi_x \frac{\partial \delta w_0}{\partial x} - \delta\psi_y \frac{\partial w_0}{\partial y} - \psi_y \frac{\partial \delta w_0}{\partial y} \right) \\
& + \mathfrak{M}_{xy}^{(a)} \left( \frac{\partial \delta \phi_x}{\partial y} - \frac{\partial \delta \phi_y}{\partial x} \right) + \mathfrak{Q}_x^{(s)} \left( \delta\phi_x + \frac{\partial \delta w_0}{\partial x} \right) + \mathfrak{Q}_x^{(a)} \left( \delta\phi_x - \frac{\partial \delta w_0}{\partial x} - 2\delta\psi_y \right) \\
& + \mathfrak{Q}_y^{(s)} \left( \frac{\partial \delta w_0}{\partial y} + \delta\phi_y \right) + \mathfrak{Q}_y^{(a)} \left( \delta\phi_y - \frac{\partial \delta w_0}{\partial y} + 2\delta\psi_x \right) + \mathfrak{P}_{xx} \frac{\partial \delta \psi_x}{\partial x} \\
& + \mathfrak{P}_{xy} \frac{\partial \delta \psi_x}{\partial y} + \mathfrak{P}_{yx} \frac{\partial \delta \psi_y}{\partial x} + \mathfrak{P}_{yy} \frac{\partial \delta \psi_y}{\partial y} - q_0 \delta w_0 \Bigg\} dx dy = 0
\end{aligned} \tag{3.3.6}$$

where $A$ is the area of the plate. The governing equations of nonlinear micropolar plate theory are

obtained by taking the Euler equations of the above variational statement (3.3.6) as

$$\delta u_0: \quad \frac{\partial \mathfrak{N}_{xx}^{(s)}}{\partial x} + \frac{\partial}{\partial y}\left(\mathfrak{N}_{xy}^{(s)} + \mathfrak{N}_{xy}^{(a)}\right) = 0 \tag{3.3.7}$$

$$\delta v_0: \quad \frac{\partial}{\partial x}\left(\mathfrak{N}_{xy}^{(s)} - \mathfrak{N}_{xy}^{(a)}\right) + \frac{\partial \mathfrak{N}_{yy}^{(s)}}{\partial y} = 0 \tag{3.3.8}$$

$$\begin{aligned}\delta w_0: \quad & \frac{\partial}{\partial x}\left(\psi_y \mathfrak{N}_{xx}^{(s)} - \psi_x\left(\mathfrak{N}_{xy}^{(s)} - \mathfrak{N}_{xy}^{(a)}\right)\right) - \frac{\partial}{\partial y}\left(\psi_x \mathfrak{N}_{yy}^{(s)} - \psi_y\left(\mathfrak{N}_{xy}^{(s)} + \mathfrak{N}_{xy}^{(a)}\right)\right) \\ & - \frac{\partial}{\partial x}\left(\mathfrak{Q}_x^{(s)} - \mathfrak{Q}_x^{(a)}\right) - \frac{\partial}{\partial y}\left(\mathfrak{Q}_y^{(s)} - \mathfrak{Q}_y^{(a)}\right) - q_0 = 0\end{aligned} \tag{3.3.9}$$

$$\delta \phi_x: \quad \frac{\partial \mathfrak{M}_{xx}^{(s)}}{\partial x} + \frac{\partial}{\partial y}\left(\mathfrak{M}_{xy}^{(s)} + \mathfrak{M}_{xy}^{(a)}\right) - \mathfrak{Q}_x^{(s)} - \mathfrak{Q}_x^{(a)} = 0 \tag{3.3.10}$$

$$\delta \phi_y: \quad \frac{\partial}{\partial x}\left(\mathfrak{M}_{xy}^{(s)} - \mathfrak{M}_{xy}^{(a)}\right) + \frac{\partial \mathfrak{M}_{yy}^{(s)}}{\partial y} - \mathfrak{Q}_y^{(s)} - \mathfrak{Q}_y^{(a)} = 0 \tag{3.3.11}$$

$$\delta \psi_x: \quad \frac{\partial \mathfrak{P}_{xx}}{\partial x} + \frac{\partial \mathfrak{P}_{xy}}{\partial y} - \left(\mathfrak{N}_{xy}^{(s)} - \mathfrak{N}_{xy}^{(a)}\right)\frac{\partial w_0}{\partial x} - \mathfrak{N}_{yy}^{(s)}\frac{\partial w_0}{\partial y} - 2\mathfrak{Q}_y^{(a)} = 0 \tag{3.3.12}$$

$$\delta \psi_y: \quad \frac{\partial \mathfrak{P}_{yx}}{\partial x} + \frac{\partial \mathfrak{P}_{yy}}{\partial y} + \mathfrak{N}_{xx}^{(s)}\frac{\partial w_0}{\partial x} + \left(\mathfrak{N}_{xy}^{(s)} + \mathfrak{N}_{xy}^{(a)}\right)\frac{\partial w_0}{\partial y} + 2\mathfrak{Q}_x^{(a)} = 0 \tag{3.3.13}$$

with the following natural boundary conditions

$$\begin{aligned}
\mathfrak{Q}_1 &\equiv \mathfrak{N}_{xx}^{(s)} n_x + \left(\mathfrak{N}_{xy}^{(s)} + \mathfrak{N}_{xy}^{(a)}\right) n_y = 0 \\
\mathfrak{Q}_2 &\equiv \left(\mathfrak{N}_{xy}^{(s)} - \mathfrak{N}_{xy}^{(a)}\right) n_x + \mathfrak{N}_{yy}^{(s)} n_y = 0 \\
\mathfrak{Q}_3 &\equiv \left[\mathfrak{Q}_x^{(s)} - \mathfrak{Q}_x^{(a)} - \psi_y \mathfrak{N}_{xx}^{(s)} + \psi_x\left(\mathfrak{N}_{xy}^{(s)} - \mathfrak{N}_{xy}^{(a)}\right)\right] n_x \\
&\qquad + \left[\mathfrak{Q}_y^{(s)} - \mathfrak{Q}_y^{(a)} + \psi_x \mathfrak{N}_{yy}^{(s)} - \psi_y\left(\mathfrak{N}_{xy}^{(s)} + \mathfrak{N}_{xy}^{(a)}\right)\right] n_y = 0 \\
\mathfrak{Q}_4 &\equiv \mathfrak{M}_{xx}^{(s)} n_x + \left(\mathfrak{M}_{xy}^{(s)} + \mathfrak{M}_{xy}^{(a)}\right) n_y = 0 \\
\mathfrak{Q}_5 &\equiv \left(\mathfrak{M}_{xy}^{(s)} - \mathfrak{M}_{xy}^{(a)}\right) n_x + \mathfrak{M}_{yy}^{(s)} n_y = 0 \\
\mathfrak{Q}_6 &\equiv \mathfrak{P}_{xx} n_x + \mathfrak{P}_{xy} n_y = 0 \\
\mathfrak{Q}_7 &\equiv \mathfrak{P}_{yx} n_x + \mathfrak{P}_{yy} n_y = 0
\end{aligned} \tag{3.3.14}$$

where $n_x$ and $n_y$ are the $x$ and $y$ components of the directions cosines of the boundary.

### 3.4 Finite element models

In this section we develop the weak-form Galerkin finite element model of the governing equations derived in sections 3.2 and 3.3. For the plate theories considered in this paper the primary variables are $(u_0, v_0, w_0, \phi_x, \phi_y, \psi_x, \psi_y)$. These variables are approximated using 2-dimensional Lagrange interpolation functions $L_j^{(1)}, L_j^{(2)}, L_j^{(3)}, L_j^{(4)}, L_j^{(5)}, L_j^{(6)}$ and $L_j^{(7)}$, respectively. Here $j = \{1, 2, \ldots, n\}$ where $n$ is the number of nodes on a typical element. Since we are using weak-form Galerkin finite element formulation, the weight functions $w_1, w_2, w_3, w_4, w_5, w_6$ and $w_7$ used in the development of the weak-form equations are taken to be the same Lagrange interpolations functions used in approximating the primary variables [93]. Thus, we have,

$$
\begin{aligned}
u_0 &\approx \sum_{j=1}^{n} U_j L_j^{(1)}(x,y), & w_1(x,y) &= L_i^{(1)}(x,y) \\
v_0 &\approx \sum_{j=1}^{n} V_j L_j^{(2)}(x,y), & w_2(x,y) &= L_i^{(2)}(x,y) \\
w_0 &\approx \sum_{j=1}^{n} W_j L_j^{(3)}(x,y), & w_3(x,y) &= L_i^{(3)}(x,y) \\
\phi_x &\approx \sum_{j=1}^{n} \Phi x_j L_j^{(4)}(x,y), & w_4(x,y) &= L_i^{(4)}(x,y) \\
\phi_y &\approx \sum_{j=1}^{n} \Phi y_j L_j^{(5)}(x,y), & w_5(x,y) &= L_i^{(5)}(x,y) \\
\psi_x &\approx \sum_{j=1}^{n} \Psi x_j L_j^{(6)}(x,y), & w_6(x,y) &= L_i^{(6)}(x,y) \\
\psi_y &\approx \sum_{j=1}^{n} \Psi y_j L_j^{(7)}(x,y), & w_7(x,y) &= L_i^{(7)}(x,y)
\end{aligned}
\tag{3.4.1}
$$

where $i = \{1, 2, 3 \ldots n\}$. $U_j, V_j, W_j, \Phi x_j, \Phi y_j, \Psi x_j$ and $\Psi y_j$ are the nodal values of their respective primary variables on a typical finite element.

- von Kármán micropolar plate theory (VMPT)

  The weak-form equations of von Kármán micropolar plate theory on a typical finite element

$\Omega_e$ are

$$0 = \int_{\Omega_e} \left\{ \frac{\partial w_1}{\partial x} N_{xx}^{(s)} + \frac{\partial w_1}{\partial y} (N_{xy}^{(s)} + N_{xy}^{(a)}) \right\} dxdy - \oint_{\Gamma_e} w_1 Q_1^{(e)} ds \tag{3.4.2}$$

$$0 = \int_{\Omega_e} \left\{ \frac{\partial w_2}{\partial x} (N_{xy}^{(s)} - N_{xy}^{(a)}) + \frac{\partial w_2}{\partial y} N_{yy}^{(s)} \right\} dxdy - \oint_{\Gamma_e} w_2 Q_2^{(e)} ds \tag{3.4.3}$$

$$\begin{aligned} 0 = \int_{\Omega_e} \Bigg\{ & \frac{\partial w_3}{\partial x} \left( \frac{\partial w_0}{\partial x} N_{xx}^{(s)} + \frac{\partial w_0}{\partial y} N_{xy}^{(s)} + Q_x^{(s)} - Q_x^{(a)} \right) \\ & + \frac{\partial w_3}{\partial y} \left( \frac{\partial w_0}{\partial x} N_{xy}^{(s)} + \frac{\partial w_0}{\partial y} N_{yy}^{(s)} + Q_y^{(s)} - Q_y^{(a)} \right) - w_3 q_0 \Bigg\} dxdy \\ & - \oint_{\Gamma_e} w_3 Q_3^{(e)} ds \end{aligned} \tag{3.4.4}$$

$$\begin{aligned} 0 = \int_{\Omega_e} & \left\{ \frac{\partial w_4}{\partial x} M_{xx}^{(s)} + \frac{\partial w_4}{\partial y} (M_{xy}^{(s)} + M_{xy}^{(a)}) + w_4 Q_x^{(s)} + w_4 Q_x^{(a)} \right\} dxdy \\ & - \oint_{\Gamma_e} w_4 Q_4^{(e)} ds \end{aligned} \tag{3.4.5}$$

$$\begin{aligned} 0 = \int_{\Omega_e} & \left\{ \frac{\partial w_5}{\partial x} (M_{xy}^{(s)} - M_{xy}^{(a)}) + \frac{\partial w_5}{\partial y} M_{yy}^{(s)} + w_5 Q_y^{(s)} + w_5 Q_y^{(a)} \right\} dxdy \\ & - \oint_{\Gamma_e} w_5 Q_5^{(e)} ds \end{aligned} \tag{3.4.6}$$

$$0 = \int_{\Omega_e} \left\{ \frac{\partial w_6}{\partial x} P_{xx} + \frac{\partial w_6}{\partial y} P_{xy} + 2 w_6 Q_y^{(a)} \right\} dxdy - \oint_{\Gamma_e} w_6 Q_6^{(e)} ds \tag{3.4.7}$$

$$0 = \int_{\Omega_e} \left\{ \frac{\partial w_7}{\partial x} P_{yx} + \frac{\partial w_7}{\partial y} P_{yy} - 2 w_7 Q_x^{(a)} \right\} dxdy - \oint_{\Gamma_e} w_7 Q_7^{(e)} ds \tag{3.4.8}$$

where $Q_i^{(e)}$ $(i = 1, 2, \ldots, 7)$ are the secondary variables on the boundary $\Gamma_e$ of finite element $\Omega_e$. The definitions of the secondary variables are given in Eqs. (3.2.13). The stress, moment and couple stress resultants in the weak-form equations can be written in terms of the displacements, rotations and microrotations using the constitutive relations given in Appendix A.2.

- Nonlinear micropolar plate theory (NMPT)

  The weak-form equations of nonlinear micropolar plate theory on a typical finite element $\Omega_e$

are

$$0 = \int_{\Omega_e} \left\{ \frac{\partial w_1}{\partial x}\mathfrak{N}_{xx}^{(s)} + \frac{\partial w_1}{\partial y}(\mathfrak{N}_{xy}^{(s)} + \mathfrak{N}_{xy}^{(a)}) \right\} dxdy - \oint_{\Gamma_e} w_1 \mathfrak{Q}_1^{(e)} ds \tag{3.4.9}$$

$$0 = \int_{\Omega_e} \left\{ \frac{\partial w_2}{\partial x}(\mathfrak{N}_{xy}^{(s)} - \mathfrak{N}_{xy}^{(a)}) + \frac{\partial w_2}{\partial y}\mathfrak{N}_{yy}^{(s)} \right\} dxdy - \oint_{\Gamma_e} w_2 \mathfrak{Q}_2^{(e)} ds \tag{3.4.10}$$

$$\begin{aligned} 0 = \int_{\Omega_e} \Bigg\{ & \frac{\partial w_3}{\partial x}\left(\psi_x(\mathfrak{N}_{xy}^{(s)} - \mathfrak{N}_{xy}^{(a)}) - \psi_y \mathfrak{N}_{xx}^{(s)} + \mathfrak{Q}_x^{(s)} - \mathfrak{Q}_x^{(a)}\right) \\ & + \frac{\partial w_3}{\partial y}\left(\psi_x \mathfrak{N}_{yy}^{(s)} - \psi_y\left(\mathfrak{N}_{xy}^{(s)} + \mathfrak{N}_{xy}^{(a)}\right) + \mathfrak{Q}_y^{(s)} - \mathfrak{Q}_y^{(a)}\right) - w_3 q_0 \Bigg\} dxdy \\ & - \oint_{\Gamma_e} w_3 \mathfrak{Q}_3^{(e)} ds \end{aligned} \tag{3.4.11}$$

$$\begin{aligned} 0 = \int_{\Omega_e} & \left\{ \frac{\partial w_4}{\partial x}\mathfrak{M}_{xx}^{(s)} + \frac{\partial w_4}{\partial y}\left(\mathfrak{M}_{xy}^{(s)} + \mathfrak{M}_{xy}^{(a)}\right) + w_4 \mathfrak{Q}_x^{(s)} + w_4 \mathfrak{Q}_x^{(a)} \right\} dxdy \\ & - \oint_{\Gamma_e} w_4 \mathfrak{Q}_4^{(e)} ds \end{aligned} \tag{3.4.12}$$

$$\begin{aligned} 0 = \int_{\Omega_e} & \left\{ \frac{\partial w_5}{\partial x}\left(\mathfrak{M}_{xy}^{(s)} - \mathfrak{M}_{xy}^{(a)}\right) + \frac{\partial w_5}{\partial y}\mathfrak{M}_{yy}^{(s)} + w_5 \mathfrak{Q}_y^{(s)} + w_5 \mathfrak{Q}_y^{(a)} \right\} dxdy \\ & - \oint_{\Gamma_e} w_5 \mathfrak{Q}_5^{(e)} ds \end{aligned} \tag{3.4.13}$$

$$\begin{aligned} 0 = \int_{\Omega_e} & \left\{ \frac{\partial w_6}{\partial x}\mathfrak{P}_{xx} + \frac{\partial w_6}{\partial y}\mathfrak{P}_{xy} + w_6 \frac{\partial w_0}{\partial x}\left(\mathfrak{N}_{xy}^{(s)} - \mathfrak{N}_{xy}^{(a)}\right) + w_6 \frac{\partial w_0}{\partial y}\mathfrak{N}_{yy}^{(s)} \right. \\ & \left. + 2w_6 \mathfrak{Q}_y^{(a)} \right\} dxdy - \oint_{\Gamma_e} w_6 \mathfrak{Q}_6^{(e)} ds \end{aligned} \tag{3.4.14}$$

$$\begin{aligned} 0 = \int_{\Omega_e} & \left\{ \frac{\partial w_7}{\partial x}\mathfrak{P}_{yx} + \frac{\partial w_7}{\partial y}\mathfrak{P}_{yy} - w_7 \frac{\partial w_0}{\partial x}\mathfrak{N}_{xx}^{(s)} - w_7 \frac{\partial w_0}{\partial y}\left(\mathfrak{N}_{xy}^{(s)} + \mathfrak{N}_{xy}^{(a)}\right) \right. \\ & \left. -2w_7 \mathfrak{Q}_x^{(a)} \right\} dxdy - \oint_{\Gamma_e} w_7 \mathfrak{Q}_7^{(e)} ds \end{aligned} \tag{3.4.15}$$

where $\mathfrak{Q}_i^{(e)}$ $(i = 1, 2, \ldots, 7)$ are the secondary variables on the boundary $\Gamma_e$ of finite element $\Omega_e$. The definitions of the secondary variables are give in Eqs. (3.3.14). The stress, moment and couple stress resultants in the weak-form equations can be written in terms of the displacements, rotations and microrotations using the constitutive relations given in Appendix A.2.

After using the approximations of the primary variables given in Eqs. (3.4.1) in the weak-form equations (3.4.2)-(3.4.8) and (3.4.9)-(3.4.15) respectively, the nonlinear finite element equations

on a typical element for both nonlinear theories can be written in the form

$$\mathbf{K}^{(\mathbf{e})}\mathfrak{U}^{(\mathbf{e})} = \mathbf{F}^{(\mathbf{e})} \tag{3.4.16}$$

where,

$$\mathbf{K}^{(\mathbf{e})} = \begin{bmatrix} \mathbf{K^{11}} & \mathbf{K^{12}} & \mathbf{K^{13}} & \mathbf{K^{14}} & \mathbf{K^{15}} & \mathbf{K^{16}} & \mathbf{K^{17}} \\ \mathbf{K^{21}} & \mathbf{K^{22}} & \mathbf{K^{23}} & \mathbf{K^{24}} & \mathbf{K^{25}} & \mathbf{K^{26}} & \mathbf{K^{27}} \\ \mathbf{K^{31}} & \mathbf{K^{32}} & \mathbf{K^{33}} & \mathbf{K^{34}} & \mathbf{K^{35}} & \mathbf{K^{36}} & \mathbf{K^{37}} \\ \mathbf{K^{41}} & \mathbf{K^{42}} & \mathbf{K^{43}} & \mathbf{K^{44}} & \mathbf{K^{45}} & \mathbf{K^{46}} & \mathbf{K^{47}} \\ \mathbf{K^{51}} & \mathbf{K^{52}} & \mathbf{K^{53}} & \mathbf{K^{54}} & \mathbf{K^{55}} & \mathbf{K^{56}} & \mathbf{K^{57}} \\ \mathbf{K^{61}} & \mathbf{K^{62}} & \mathbf{K^{63}} & \mathbf{K^{64}} & \mathbf{K^{65}} & \mathbf{K^{66}} & \mathbf{K^{67}} \\ \mathbf{K^{71}} & \mathbf{K^{72}} & \mathbf{K^{73}} & \mathbf{K^{74}} & \mathbf{K^{75}} & \mathbf{K^{76}} & \mathbf{K^{77}} \end{bmatrix}^{(e)} \tag{3.4.17}$$

$$\mathfrak{U}^{(\mathbf{e})} = \begin{Bmatrix} \mathbf{U} \\ \mathbf{V} \\ \mathbf{W} \\ \boldsymbol{\Phi x} \\ \boldsymbol{\Phi y} \\ \boldsymbol{\Psi y} \\ \boldsymbol{\Psi y} \end{Bmatrix}^{(e)} \qquad \mathbf{F}^{(\mathbf{e})} = \begin{Bmatrix} \mathbf{F^1} \\ \mathbf{F^2} \\ \mathbf{F^3} \\ \mathbf{F^4} \\ \mathbf{F^5} \\ \mathbf{F^6} \\ \mathbf{F^7} \end{Bmatrix}^{(e)} \tag{3.4.18}$$

The non-zero components of the coefficient matrix (3.4.16) are given in Appendix B.2, for both VMPT and NMPT.

### 3.4.1 Higher order finite elements

It is well known that lower order displacement finite elements for plates are prone to locking [100, 103, 108] when quadrature rules that result in exact integration of element coefficient matrix

are employed. Such locking phenomena are usually eliminated using selective full and reduced integration techniques. In place of such numerical remedies, we employ higher order polynomials in approximating the primary variables within an element. For such higher-order polynomials of order $n-1$ on a typical element, there are $n$ nodes. However, when these nodes are equally spaced the polynomial interpolations exhibit oscillations near the end points of the standard interval. This phenomenon is called *Runge effect*. To overcome the Runge effect the use of an unequal spacing of the nodes within each 1-D element was discussed in chapter 2. Similarly, we can obtain the corresponding higher order elements in 2-D using tensor product of the vectors containing 1-D interpolation functions in $x$ and $y$ directions (see [93]).

### 3.4.2 Solutions of nonlinear equations

The nonlinear finite element equations of (3.4.16) are solved using Newton's iterative procedure [100], by constructing the tangent stiffness matrix of a typical element at the beginning of $r^{th}$ iteration as

$$\mathbf{T}^{(\mathbf{e})(r)} = \left[\frac{\partial \mathbf{R}^{(\mathbf{e})}}{\partial \mathfrak{U}^{(\mathbf{e})}}\right]^{(r-1)} \tag{3.4.19}$$

such that

$$\mathbf{T}^{(\mathbf{e})(r)} \Delta \mathfrak{U}^{\mathbf{e}} = -\mathbf{R}^{(\mathbf{e})(r-1)} \tag{3.4.20}$$

where

$$\mathbf{R}^{(\mathbf{e})} = \mathbf{K}^{(\mathbf{e})}(\mathfrak{U}^{(\mathbf{e})})\mathfrak{U}^{(\mathbf{e})} - \mathbf{F}^{(\mathbf{e})} \quad \text{and} \quad \Delta \mathfrak{U}^{(\mathbf{e})} = \mathfrak{U}^{(\mathbf{e})(r)} - \mathfrak{U}^{(\mathbf{e})(r-1)}$$

The explicit expressions of the components of the element tangent stiffness matrix for all the nonlinear theories considered in this chapter are given in Appendix B.2.

When the normalized difference between solution vectors from two consecutive iterations

(measured with Euclidean norm) is less than a pre-selected tolerance, convergence is declared and further iterations are terminated [100].

### 3.5 Numerical results

For the purpose of numerical analysis we consider a rectangular micropolar plate with the following material properties:

$$\begin{aligned} &\lambda = 2.25 \times 10^6 \text{ psi (15513.20 MPa)}, \quad \mu = 10^6 \text{ psi (6894.76 MPa)} \\ &\alpha = 100 \text{ lb (444.82 N)}, \quad \beta = 100 \text{ lb (444.82 N)}, \quad \gamma = 600 \text{ lb (2668.93 N)} \end{aligned} \tag{3.5.1}$$

For a given value of $\mu$, the material constant $\kappa$ plays an important role in determining the degree of micropolarity exhibited by the material [105]. A dimensionless parameter called *coupling number* $(N)$ is usually defined to quantify the level of shear stress asymmetry, there by reflecting the degree of micropolarity exhibited by the material [23, 106]. The coupling number is bounded below by the classical elasticity and above by the so-called constrained Cosserat elasticity (or couple stress theory), where in the microrotation is equal to the conventional rotation (macrorotation) [106]. To bring out the effect of coupling number on the plate theories considered in this chapter, we consider a range of coupling numbers and the corresponding value of $\kappa$ is calculated using the formula:

$$\kappa = \frac{2\mu N^2}{1 - 2N^2} \tag{3.5.2}$$

The length $(L)$ of the micropolar plate is taken to be twice the breadth $(B)$. Two different boundary conditions are considered under the action of a uniformly distributed load $q_0$: (a) simply supported on all sides (SSSS) (b) clamped on all sides (CCCC). Since the boundary and loading conditions considered here result in symmetry about $x$- and $y$-axes, we consider only the quarter plate lying in the first quadrant as the computational domain (see Fig. 3.1). For such a computational domain the considered boundary conditions after symmetry arguments are listed in Table 3.1. Unless stated otherwise all the loads listed are on full plate.

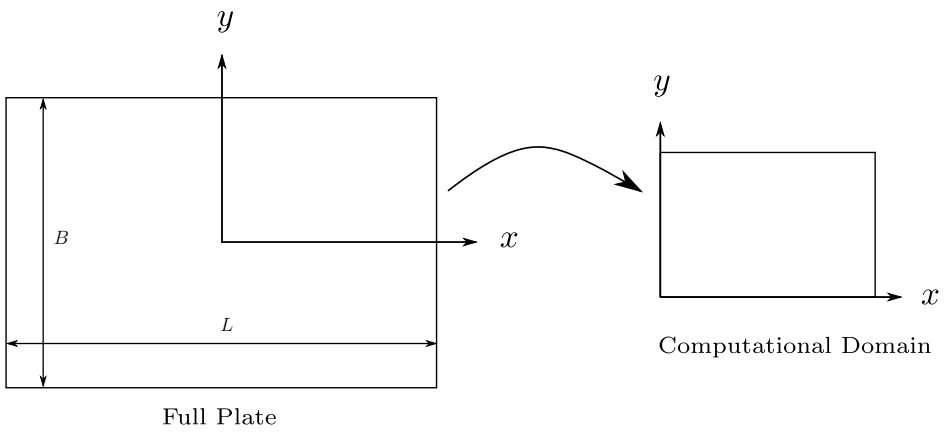


Figure 3.1: Choice of computational domain for the bending analysis under considered boundary and loading conditions.

Table 3.1: Various boundary conditions on the computational domain for bending analysis.

| | SSSS | CCCC |
|---|---|---|
| $y = 0$ | $v_0 = \phi_y = \psi_x = 0$ | $v_0 = \phi_y = \psi_x = 0$ |
| $y = B/2$ | $u_0 = w_0 = \phi_x = \psi_y = 0$ | $u_0 = v_0 = w_0 = \phi_x = \psi_y = \phi_y = \psi_x = 0$ |
| $x = 0$ | $u_0 = \phi_x = \psi_y = 0$ | $u_0 = \phi_x = \psi_y = 0$ |
| $x = L/2$ | $v_0 = w_0 = \phi_y = \psi_x = 0$ | $u_0 = v_0 = w_0 = \phi_x = \psi_y = \phi_y = \psi_x = 0$ |
| $(0, 0)$ | $u_0 = v_0 = \phi_x = \psi_y = \phi_y = \psi_x = 0$ | $u_0 = v_0 = \phi_x = \psi_y = \phi_y = \psi_x = 0$ |
| $(L/2, 0)$ | $v_0 = w_0 = \phi_y = \psi_x = 0$ | $u_0 = v_0 = w_0 = \phi_x = \psi_y = \phi_y = \psi_x = 0$ |
| $(0, B/2)$ | $u_0 = w_0 = \phi_x = \psi_y = 0$ | $u_0 = v_0 = w_0 = \phi_x = \psi_y = \phi_y = \psi_x = 0$ |
| $(L/2, B/2)$ | $u_0 = v_0 = w_0 = \phi_x = \psi_y = \phi_y = \psi_x = 0$ | $u_0 = v_0 = w_0 = \phi_x = \psi_y = \phi_y = \psi_x = 0$ |

### 3.5.1 Effect of coupling number

Consider a rectangular micropolar plate, with material properties given in Eq. (3.5.1), of thickness $H = 0.01220$ in (0.3099 cm), length $L = 50H$ and breadth $B = L/2$ under the action of a distributed load $q_0 = 5.0$ lb/in$^2$ (34473.7 N/m$^2$) on the top face. To analyze this plate we use 16 elements of equal size on the computational domain. 4 elements along the $x$-axis and 4 elements along the $y - axis$ are used, with each element having 81 nodes, 9 along $x$-axis and 9 along $y$-axis of the element. Further, we shall define the following dimensionless quantities:

$$\begin{aligned} \overline{w}(x,y) = w_0(x,y)\frac{\lambda H^3}{q_0 L^4}, \quad \overline{u}(x,y) = u_0(x,y)\frac{\lambda}{q_0 L}, \quad \chi = \frac{2\sqrt{x^2+y^2}}{\sqrt{L^2+B^2}} \\ \overline{\sigma}^{(s)}_{xy} = \sigma^{(s)}_{xy}\frac{H}{q_0 L}, \quad \overline{\sigma}^{(a)}_{xy} = \sigma^{(a)}_{xy}\frac{H}{q_0 L} \end{aligned} \tag{3.5.3}$$

Fig. 3.2a shows the dimensionless transverse deflection of a clamped micropolar plate along the line $y = 0$ for various values of coupling number $N$. Further, a comparison between the NMPT and VMPT is also given. Similarly, Fig. 3.2b presents the dimensionless transverse deflection simply supported micropolar plate along the line $y = 0$ for various values of coupling number. A comparison between NMPT and VMPT for simply supported boundary conditions is also presented in Fig. 3.2b. It can be seen that an increase in coupling number is also causing an increasing the bending stiffness of the micropolar plate as evident by the magnitude if the transverse deflections for both NMPT and VMPT. Fig. 3.2 also tells us that for lower values of coupling numbers VMPT predicts stiffer results compared to NMPT, while at higher values of coupling numbers the difference between the two theories is not significant in terms of transverse deflections. It should also be noted that the difference between NMPT and VMPT does not only depend on the coupling number but also on the type of the boundary conditions the plate is subjected as evident from Fig. 3.2.

Next, we examine the effect of coupling number on the in-plane displacement $u_0(x, y)$. Fig. 3.3a presents the comparison between the dimensionless in-plane displacement $\overline{u}$ along the line $y = 0$, of a simply supported micropolar plate modeled using VMPT for various values of coupling number. It can be seen that the magnitude of the in-plane displacement $u_0$ decreases with increase in $N$

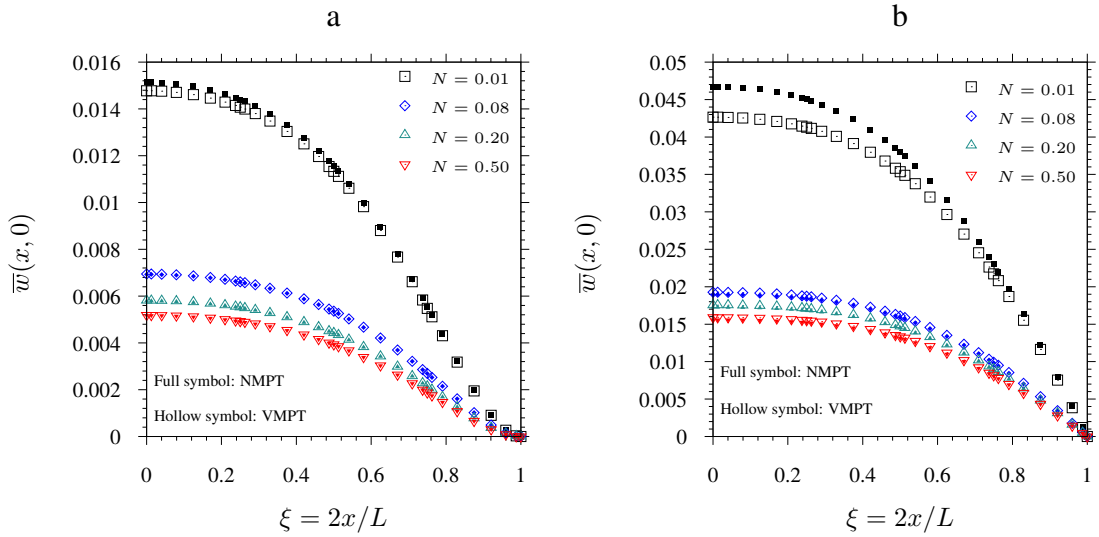


Figure 3.2: (a) Dimensionless transverse deflection along the line $y = 0$ for CCCC boundary conditions for various values of $N$. (b) Dimensionless transverse deflection along the line $y = 0$ for SSSS boundary conditions for various values of $N$.

when VMPT is used to model the plate. However, when the same plate is modeled using NMPT, the magnitude of in-plane dimensionless displacement $\overline{u}$ first increases and then again starts to decrease as evident by Fig. 3.3b.

Finally, we consider the in-plane symmetric and anti-symmetric shear stresses on the top face of the micropolar plate. The stresses can be post-computed once the displacement filed is obtained from the finite element solutions. Fig. 3.4a presents the comparison between the values of dimensionless in-plane symmetric shear stress $\overline{\sigma}^{(s)}_{xy}$ as obtained from VMPT and NMPT for various values of coupling number $N$, while Fig. 3.4b presents the comparison between the values of dimensionless in-plane anti-symmetric shear stress $\overline{\sigma}^{(a)}_{xy}$ as obtained from VMPT and NMPT for various values of coupling number $N$. It can be seen that the magnitude of in-plane symmetric shear stress decreases with increase in coupling number for both VMPT and NMPT (see Fig. 3.4a). However, the magnitude of in-plane anti-symmetric shear stress increases with increase in coupling number for both VMPT and NMPT (see Fig. 3.4b). Further, note that the magnitude of in-plane anti-symmetric shear stress predicted by VMPT is less than the magnitude predicted by NMPT for

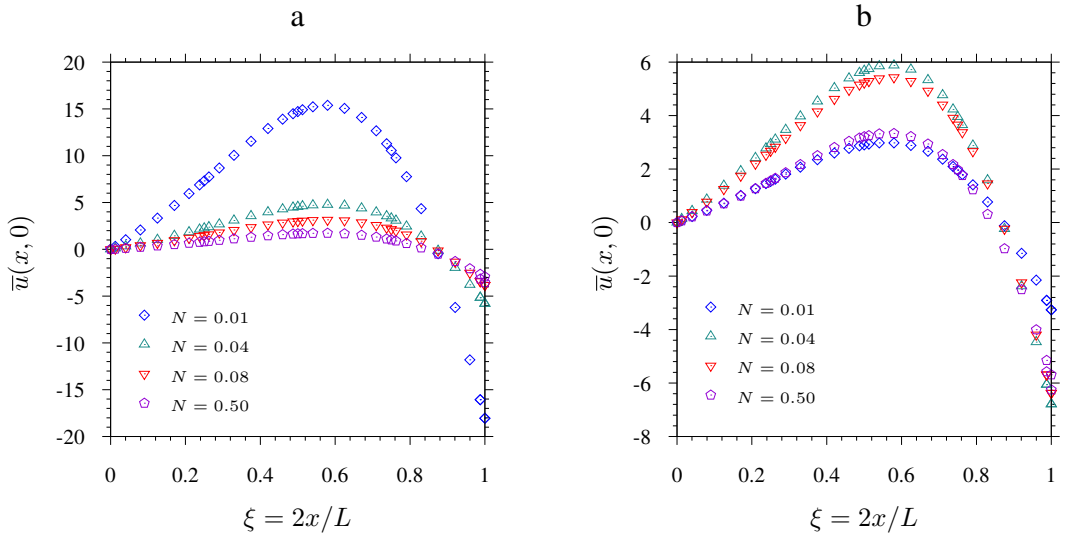


Figure 3.3: (a) Dimensionless deflection $\overline{u}$ of VMPT along the line $y = 0$ for SSSS boundary conditions for various values of $N$. (b) Dimensionless deflection $\overline{u}$ of NMPT along the line $y = 0$ for SSSS boundary conditions for various values of $N$.

higher values of coupling number, while for lower values of coupling number ($N = 0.01$) the magnitude of in-plane anti-symmetric shear stress predicted by VMPT is greater than the magnitude predicted by NMPT.

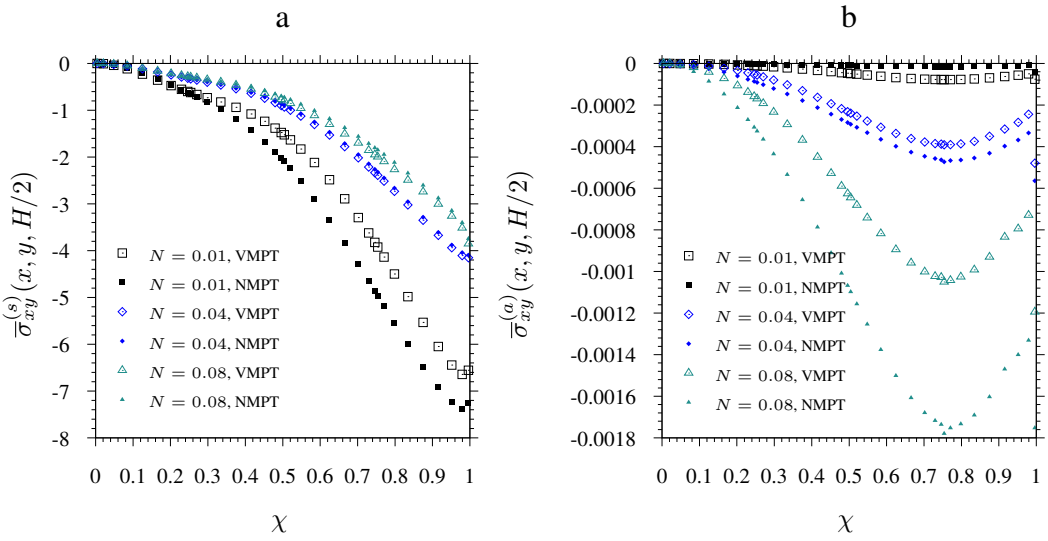


Figure 3.4: (a) Dimensionless in-plane symmetric shear stress $\overline{\sigma}^{(s)}_{xy}$ on the top face of micropolar plate along the line $x = y$ for SSSS boundary conditions. (b) Dimensionless in-plane antisymmetric shear stress $\overline{\sigma}^{(a)}_{xy}$ on the top face of micropolar plate along the line $x = y$ for SSSS boundary conditions.

# 4. NONLINEAR FINITE ELEMENT ANALYSIS OF LATTICE CORE SANDWICH BEAMS*

## 4.1 Introduction

In this chapter we will consider lattice core sandwich beams and their modeling using von Kármán Timoshenko micropolar beam theory discussed in chapter 2. We will review the kinematics of the micropolar beam and then discuss the constitutive modeling of lattice core sandwich beams as micropolar beams [1, 4]. Then the corresponding governing equations and the finite element equations are derived. Finally, numerical results are presented to illustrate the accuracy of the constitutive model and the corresponding finite element model.

## 4.2 Kinematics of micropolar beam

In this section we will review the Timoshenko micropolar beam kinematics considered in chapter 2. The 3-D displacements and microrotations of the a micropolar beam are given in terms of the center line variables $(u_0, w_0, \phi_x, \psi_y)$ such that

$$\begin{aligned} u_1(x,y,z) &= u_0(x) + z\phi_x(x) \\ u_2(x,y,z) &= 0 \\ u_3(x,y,z) &= w_0(x) \\ \psi_1(x,y,z) &= 0 \\ \psi_2(x,y,z) &= \psi_y(x) \\ \psi_3(x,y,z) &= 0 \end{aligned} \tag{4.2.1}$$

Here $(u_0, w_0)$ represent the axial and transverse displacements of the center line of the beam, while $\phi_x$ is the rotations of the fibers normal to the center line and $\psi_y$ is the microrotations about $y$-axis.

*Part of this chapter is reprinted with permission from "Nonlinear finite element analysis of lattice core sandwich beams" by P. Nampally, A. T. Karttunen, and J. N. Reddy, 2019. European Journal of Mechanics - A/Solids, vol. 74, pp. 431–439, Copyright (2018) Elsevier Masson SAS.

The corresponding linear strains and wryness tensor components are given by [44]

$$\begin{aligned} \varepsilon_{xx} &= \frac{du_0}{dx} + z\frac{d\phi_x}{dx} = \varepsilon^0_{xx} + z\kappa_{xx}, \qquad & \chi_{xy} &= \frac{d\psi_y}{dx} \\ \varepsilon_{xz} &= \frac{dw_0}{dx} + \psi_y, & \varepsilon_{zx} &= \phi_x - \psi_y \end{aligned} \tag{4.2.2}$$

Further we define the symmetric and anti-symmetric shear strains as follows

$$\begin{aligned} \gamma^s_x &= \varepsilon_{xz} + \varepsilon_{zx} = \frac{dw_0}{dx} + \phi_x \\ \gamma^a_x &= \varepsilon_{xz} - \varepsilon_{zx} = \frac{dw_0}{dx} - \phi_x + 2\psi_y \end{aligned} \tag{4.2.3}$$

We will be using von Kármán nonlinearity in modeling the lattice core sandwich beams. Hence the nonlinear strains would be given by

$$\begin{aligned} \varepsilon_{xx} &= \frac{du_0}{dx} + \frac{1}{2}\left(\frac{dw_0}{dx}\right)^2 + z\frac{d\phi_x}{dx} = \hat{\varepsilon}^0_{xx} + z\kappa_{xx} \\ \varepsilon_{xz} &= \frac{dw_0}{dx} + \psi_y \\ \varepsilon_{zx} &= \phi_x - \psi_y \\ \chi_{xy} &= \frac{d\psi_y}{dx} \end{aligned} \tag{4.2.4}$$

## 4.3 Two-scale constitutive modeling of lattice beams

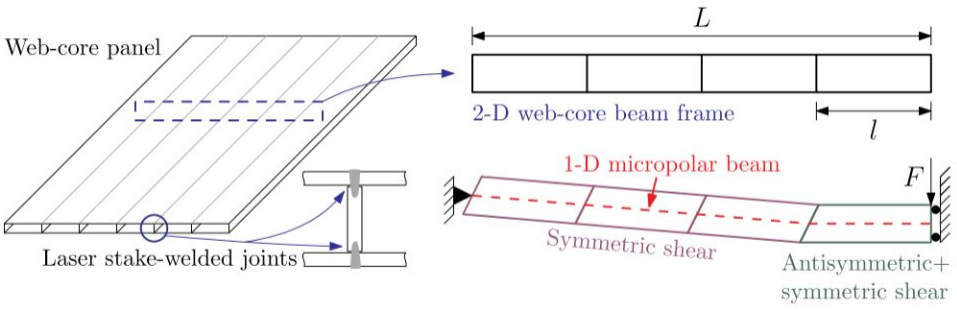


Figure 4.1: Web-core lattice beam (Reprinted with permission from [4]).

In this section we shall describe the two-scale constitutive model proposed in [1, 4] for web-core lattice beams. Let us consider a web-core beam frame as shown in Fig. 4.1. The idea is to replace this beam with a micropolar beam which will serve as Equivalent Single Layer (ESL) beam model of the original web-core lattice beam. To achieve this, a unit cell of the web-core beam is isolated and this unit cell is considered energetically equivalent to continuum point of the micropolar beam. Fig. 4.2 shows the unit cell of web-core lattice beam along with the micropolar beam (red line) which is intended to be ESL beam. The unit cell which is of length $l$ and height $h$ represent the periodic microstructure of the macro-structural beam (web-core beam frame) of length $L$ ($l \leq L$).

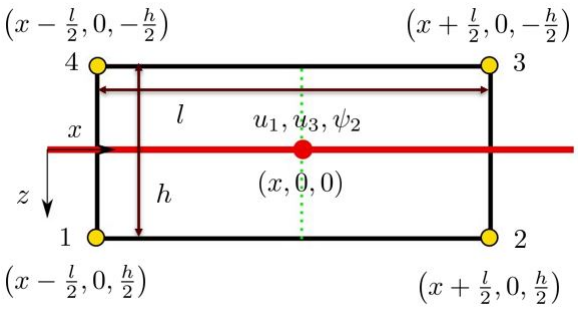


Figure 4.2: Web-core lattice beam unit cell.

The red circle at the center of Fig. 4.2 is assumed to be point within the micropolar beam whose strain energy is assumed to be equivalent to that of the strain energy stored in the unit cell. The first step in establishing this equivalence of energy is to write the displacements and rotations of nodes 1, 2, 3 and 4 shown in Fig. 4.2 in terms of the displacements and microrotations at point $(x, 0, 0)$ of the micropolar beam. To achieve this we shall use Taylor series expansion up to order one on each of the functions $u_1$, $u_3$ and $\psi_2$ about the point $(x, 0, 0)$. Thus, if $(X, Y, Z)$ is considered as the coordinates of the nodes 1, 2, 3 and 4 of the unit cell, we can write the Taylor series expansion of

a displacement component, say $u_1$, of the micropolar beam as

$$u_1(X,Y,Z) = u_1(x,0,0) + (X-x)\left.\frac{\partial u_1}{\partial X}\right|_{(x,0,0)} + (Z-0)\left.\frac{\partial u_1}{\partial Z}\right|_{(x,0,0)} \tag{4.3.1}$$

The coordinates $(X,Y,Z)$ take the following values depending on the node considered.

$$\begin{aligned} &\text{Node 1:} \quad (X,Y,Z) = \left(x - \frac{l}{2}, 0, \frac{h}{2}\right), \qquad \text{Node 2:} \quad (X,Y,Z) = \left(x + \frac{l}{2}, 0, \frac{h}{2}\right) \\ &\text{Node 3:} \quad (X,Y,Z) = \left(x + \frac{l}{2}, 0, -\frac{h}{2}\right), \quad \text{Node 4:} \quad (X,Y,Z) = \left(x - \frac{l}{2}, 0, -\frac{h}{2}\right) \end{aligned} \tag{4.3.2}$$

Thus, for noode 1 Eq. (4.3.1) can be written as

$$u_1(x - l/2, 0, h/2) = u_0(x) - \frac{l}{2}\left(\frac{\partial u_0}{\partial X} + \frac{h}{2}\frac{\partial \phi_x}{\partial X}\right)\Bigg|_{(x,0,0)} + \frac{h}{2}\phi_x\Bigg|_{(x,0,0)} \tag{4.3.3}$$

Now we shall us the strain-displacement relations of Eqs. (4.2.2)-(4.2.3) in the above equation to obtain

$$u_1(x - l/2, 0, h/2) = u_0(x) - \frac{l}{2}\left(\varepsilon^0_{xx} + \frac{h}{2}\kappa_{xx}\right) + \frac{h}{2}\left[\frac{1}{2}(\gamma^s_x - \gamma^a_x) + \psi_y\right] \tag{4.3.4}$$

In a similar fashion as explained above we can obtain the displacements and rotations of all the four nodes of the unit cell using the Taylor series expansion. These can be compactly written as

$$u^{(i)}_1\left(x \pm l/2, 0, \pm h/2\right) = u_0(x) \pm \frac{l}{2}\left(\varepsilon^0_{xx} \pm \frac{h}{2}\kappa_{xx}\right) \pm \frac{h}{2}\left[\frac{1}{2}\left(\gamma^s_x - \gamma^a_x\right) + \psi_y(x)\right] \tag{4.3.5}$$

$$u^{(i)}_3\left(x \pm l/2, 0, \pm h/2\right) = w_0(x) \pm \frac{l}{2}\left[\frac{1}{2}\left(\gamma^s_x + \gamma^a_x\right) - \psi_y(x)\right] \tag{4.3.6}$$

$$\psi^{(i)}_2\left(x \pm l/2, 0, \pm h/2\right) = \psi_y(x) \pm \frac{l}{2}\chi_{xy} \tag{4.3.7}$$

where the superscript $(i)$ on $u_1$, $u_3$ and $\psi_2$ represent the node number of the unit cell. For example, $u^{(1)}_1$ represents the displacement $u_1$ at node 1. The displacements of the unit cell nodes can be

written in a vector form as follows:

$$\mathbf{d} = \begin{Bmatrix} u_1^{(1)} & u_3^{(1)} & \psi_2^{(1)} & u_1^{(2)} & u_3^{(2)} & \psi_2^{(2)} & u_1^{(3)} & u_3^{(3)} & \psi_2^{(3)} & u_1^{(4)} & u_3^{(4)} & \psi_2^{(4)} \end{Bmatrix}^T \tag{4.3.8}$$

The vector $\mathbf{d}$ can be further broken into two parts, one corresponding to micropolar beam displacements and microrotations, while the other corresponding to the strains of micropolar beam as given in Eqs. (4.2.2)-(4.2.3).

$$\mathbf{d} = \mathbf{d}_u + \mathbf{d}_\epsilon = \mathbf{T}_u \mathbf{u} + \mathbf{T}_\epsilon \boldsymbol{\epsilon} \tag{4.3.9}$$

where

$$\mathbf{T}_\epsilon = \begin{bmatrix} -\frac{l}{2} & 0 & 0 & \frac{l}{2} & 0 & 0 & \frac{l}{2} & 0 & 0 & -\frac{l}{2} & 0 & 0 \\ -\frac{hl}{4} & 0 & 0 & \frac{hl}{4} & 0 & 0 & -\frac{hl}{4} & 0 & 0 & \frac{hl}{4} & 0 & 0 \\ \frac{h}{4} & -\frac{l}{4} & 0 & \frac{h}{4} & \frac{l}{4} & 0 & -\frac{h}{4} & \frac{l}{4} & 0 & -\frac{h}{4} & -\frac{l}{4} & 0 \\ -\frac{h}{4} & -\frac{l}{4} & 0 & -\frac{h}{4} & \frac{l}{4} & 0 & \frac{h}{4} & \frac{l}{4} & 0 & \frac{h}{4} & -\frac{l}{4} & 0 \\ 0 & 0 & -\frac{l}{2} & 0 & 0 & \frac{l}{2} & 0 & 0 & \frac{l}{2} & 0 & 0 & -\frac{l}{2} \end{bmatrix}^{\mathrm{T}} \tag{4.3.10}$$

$$\mathbf{T}_u = \begin{bmatrix} 1 & 0 & 0 & 1 & 0 & 0 & 1 & 0 & 0 & 1 & 0 & 0 \\ 0 & 1 & 0 & 0 & 1 & 0 & 0 & 1 & 0 & 0 & 1 & 0 \\ 0 & 0 & 0 & 0 & 0 & 0 & 0 & 0 & 0 & 0 & 0 & 0 \\ \frac{h}{2} & \frac{l}{2} & 1 & \frac{h}{2} & -\frac{l}{2} & 1 & -\frac{h}{2} & -\frac{l}{2} & 1 & -\frac{h}{2} & \frac{l}{2} & 1 \end{bmatrix}^{\mathrm{T}} \tag{4.3.11}$$

$$\boldsymbol{\epsilon} = \begin{Bmatrix} \varepsilon_{xx}^0 & \kappa_{xx} & \gamma_x^s & \gamma_x^a & \chi_{xy} \end{Bmatrix}^{\mathrm{T}} \tag{4.3.12}$$

$$\mathbf{u} = \begin{Bmatrix} u_0 & w_0 & \phi_x & \psi_y \end{Bmatrix}^T \tag{4.3.13}$$

If the unit cell is considered as a beam frame made of four classical Euler-Bernoulli beam elements, we can attribute the displacements and microrotations $u_1^{(i)}$, $u_3^{(i)}$ and $\psi_2^{(i)}$ at the nodes of the unit cell as the displacements and rotations of the Euler-Bernoulli beams of the beam frame at these points (nodes). Thus, the microrotations of the ESL micropolar beam are being mapped as rotations (slopes) of the Euler-Bernoulli beam elements which the unit cell is assumed to be made of. The four Euler-Bernoulli beam elements are as follows:

| | | | |
|---|---|---|---|
| EB-Beam 1: | Node 1 to Node 2, | Young's modulus $= E_f$, | Second area moment $= I_f$ |
| EB-Beam 2: | Node 2 to Node 3, | Young's modulus $= E_w$, | Second area moment $= I_w$ |
| EB-Beam 3: | Node 3 to Node 4, | Young's modulus $= E_f$, | Second area moment $= I_f$ |
| EB-Beam 4: | Node 4 to Node 1, | Young's modulus $= E_w$, | Second area moment $= I_w$ |

Here, EB-Beam 1 and EB-Beam 3 are of the same material as the face sheets of the lattice panel while EB-Beam 2 and EB-Beam 4 are of the same material as the core of the lattice panel.

Now that we have the displacements of the unit cell nodes in terms of the strains, displacements and microrotations of the ESL micropolar beam, we seek to write the stiffness matrix of the unit cell so that the total strain energy stored in the unit cell can be written as

$$W = \frac{1}{2}\mathbf{d}^T\mathbf{K}\mathbf{d} \tag{4.3.14}$$

To achieve this we first write the displacement finite element stiffness matrix of each of the Euler-Bernoulli beam element (see [93]) of the unit cell. For example, if we consider EB-Beam 1 and EB-Beam 3 without any additional rotational stiffening [4, 1], we have the following stiffness

matrix

$$\mathbf{K}_f = \frac{2E_f I_f}{l^3}\begin{bmatrix} \frac{A_f l^2}{2I_f} & 0 & 0 & -\frac{A_f l^2}{2I_f} & 0 & 0 \\ 0 & 6 & -3l & 0 & -6 & -3l \\ 0 & -3l & 2l^2 & 0 & 3l & l^2 \\ -\frac{A_f l^2}{2I_f} & 0 & 0 & \frac{A_f l^2}{2I_f} & 0 & 0 \\ 0 & -6 & 3l & 0 & 6 & 3l \\ 0 & -3l & l^2 & 0 & 3l & 2l^2 \end{bmatrix} \tag{4.3.15}$$

where $A_f$ is the are of cross section of EB-Beam 1 and EB-Beam 3. Now the total stiffness matrix of the unit cell can be obtained by assembly of Euler-Bernoulli beam elements of unit cell (see [93]). Substituting the total stiffness matrix $\mathbf{K}$ and displacement $\mathbf{d}$ from Eq. (4.3.9) it can be easily seen that

$$W = \frac{1}{2}\mathbf{d}^T\mathbf{K}\mathbf{d} = \frac{1}{2}\mathbf{d}_\epsilon^T\mathbf{K}\mathbf{d}_\epsilon = \frac{1}{2}\boldsymbol{\epsilon}^T\mathbf{T}_\epsilon^T\mathbf{K}\mathbf{T}_\epsilon\boldsymbol{\epsilon} \tag{4.3.16}$$

Let us now define the strain energy density (per length of unit cell) as

$$W_l^0 = \frac{W}{l} = \frac{1}{2}\boldsymbol{\epsilon}^T\mathbf{C}\boldsymbol{\epsilon}; \qquad \mathbf{C} = \frac{1}{l}\mathbf{T}_\epsilon^T\mathbf{K}\mathbf{T}_\epsilon \tag{4.3.17}$$

Since the web-core beam frame and ESL micropolar beam are assumed to be energetically equivalent, the strain energy density of unit cell given in Eq. (4.3.17) is equal to the strain energy density of the ESL micropolar beam. Assuming hyper elastic constitutive behavior of ESL micropolar beam we can write the constitutive relations of the micropolar beam as relations for the micropolar beam as

$$\mathbf{S} \equiv \frac{\partial W_0^l}{\partial \hat{\boldsymbol{\epsilon}}} = \frac{1}{2}\frac{\partial}{\partial \boldsymbol{\epsilon}}\left(\boldsymbol{\epsilon}^{\mathrm{T}}\mathbf{C}\hat{\boldsymbol{\epsilon}}\right) = \mathbf{C}\boldsymbol{\epsilon}, \tag{4.3.18}$$

where $\mathbf{S}$ is now the stress resultant vector of the 1-D micropolar beam and for the lattice structures

considered here (web-core, hexagonal, Y-frame, corrugated) Eq. (4.3.18) takes the following form:

$$\begin{Bmatrix} N_{xx} \\ M_{xx} \\ Q_x^s \\ Q_x^a \\ P_{xy} \end{Bmatrix} = \begin{bmatrix} C_{11} & C_{12} & 0 & 0 & C_{15} \\ C_{12} & C_{22} & 0 & 0 & C_{25} \\ 0 & 0 & C_{33} & C_{34} & 0 \\ 0 & 0 & C_{34} & C_{44} & 0 \\ C_{15} & C_{25} & 0 & 0 & C_{55} \end{bmatrix} \begin{Bmatrix} \varepsilon_{xx}^0 \\ \kappa_{xx} \\ \gamma_x^s \\ \gamma_s^a \\ \chi_{xy} \end{Bmatrix}, \tag{4.3.19}$$

where $N_{xx}$ is the axial force, $M_{xx}$ and $P_{xy}$ are the bending and couple-stress moments, respectively, and $Q_x^s$ and $Q_x^a$ are the symmetric and anti-symmetric shear forces.

If the web-core of the lattice structure are laser welded to the lattice structure faces, then the Euler-Bernoulli beam elements of unit cell EB-Beam 2 and EB-Beam 4 may have additional rotational stiffness. This can be modeled by adding rotational springs (of some known stiffness $k_\theta$) to these two beam elements, there by increasing their rotational stiffness [4, 1]. For one such web-core lattice structure with the properties $E_f = 212$ GPa, $E_w = 200$ GPa, $k_\theta = 2675$ Nm and $\nu = 0.3$ for the face and web Young's moduli, rotational joint stiffness and Poisson ratio respectively, we can write the constitutive relation (4.3.19) as follows

$$\begin{Bmatrix} N_{xx} \\ M_{xx} \\ Q_x^s \\ Q_x^a \\ P_{xy} \end{Bmatrix} = \begin{bmatrix} 2E_fA_f & 0 & 0 & 0 & 0 \\ & \frac{E_fA_fh^2}{2} + \Theta & 0 & 0 & \Theta \\ & & \frac{6E_fI_f+\Theta}{l^2} & \frac{6E_fI_f-\Theta}{l^2} & 0 \\ & \text{SYM} & & \frac{6E_fI_f+\Theta}{l^2} & 0 \\ & & & & 2E_fI_f + \Theta \end{bmatrix} \begin{Bmatrix} \varepsilon_{xx}^0 \\ \kappa_{xx} \\ \gamma_s \\ \gamma_a \\ \chi_{xy} \end{Bmatrix} \tag{4.3.20}$$

where

$$\Theta = \frac{3E_wI_wk_\theta l}{6E_wI_w + k_\theta h} \tag{4.3.21}$$

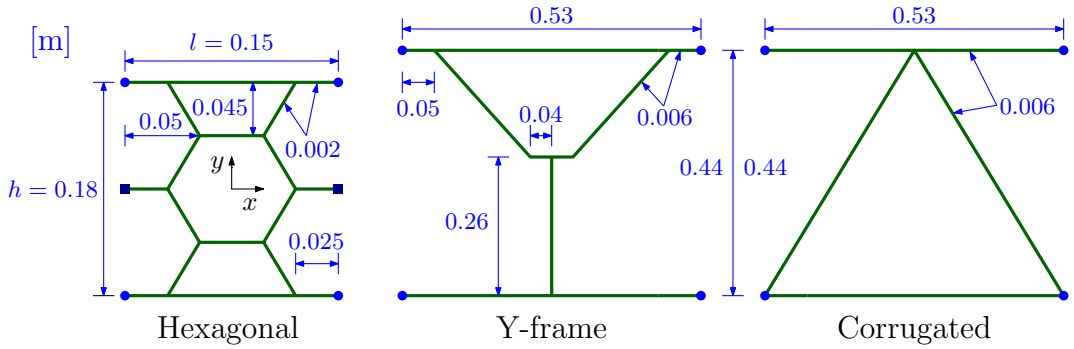


Figure 4.3: Unit cells of hexagonal, Y-frame and corrugated lattice core sandwich beams. The latter two are modeled according to [5].

For the other cores displayed in Fig. 4.3, Young's modulus and Poisson ratio are $E = 210$ GPa and $\nu = 0.3$, respectively. Other relevant parameters are given in Fig. 4.3. The hexagonal core includes two mid-nodes in addition to the four corner nodes that need to be taken into account essentially to ensure connectivity between neighboring unit cells on the micropolar continuum level. Static condensation is applied at the inner nodes of the unit cell. It is difficult to obtain a meaningful symbolic form for the hexagonal constitutive matrix, in numerical form we have

$$\mathbf{C}_{\text{hex}} = \begin{bmatrix} 4.26438 \times 10^7 & 0 & 0 & 0 & 0 \\ 0 & 340740 & 0 & 0 & 27.1761 \\ 0 & 0 & 94735.4 & 8319.08 & 0 \\ 0 & 0 & 8319.08 & 3315.25 & 0 \\ 0 & 27.1761 & 0 & 0 & 44.3467 \end{bmatrix} \tag{4.3.22}$$

The constitutive matrix (4.3.22) is of the same form as that of the web-core with the exception that

for the hexagonal core $C_{33} \neq C_{44}$. For the Y-frame and corrugated cores we obtain

$$\mathbf{C}_{\mathrm{Y}} = \begin{bmatrix} 1.26053 \times 10^8 & 11696.2 & 0 & 0 & 5292.50 \\ 11696.2 & 6.10097 \times 10^6 & 0 & 0 & 1164.35 \\ 0 & 0 & 42094.9 & 9541.42 & 0 \\ 0 & 0 & 9541.42 & 5302.30 & 0 \\ 5292.50 & 1164.35 & 0 & 0 & 1012.92 \end{bmatrix} \tag{4.3.23}$$

and

$$\mathbf{C}_{\text{corr}} = \begin{bmatrix} 1.26018 \times 10^8 & -3902.45 & 0 & 0 & -3902.45 \\ -3902.45 & 6.09926 \times 10^6 & 0 & 0 & 858.539 \\ 0 & 0 & 2.09792 \times 10^7 & 3734.96 & 0 \\ 0 & 0 & 3734.96 & 5078.42 & 0 \\ -3902.45 & 858.539 & 0 & 0 & 1334.05 \end{bmatrix}, \tag{4.3.24}$$

respectively. The axial and classical sandwich bending stiffnesses in Eqs. (4.3.22)–(4.3.24) are practically given by $C_{11} \approx 2EA_f$ and $C_{22} \approx EA_f h^2/2$, respectively. We see that due to the lack of symmetry about the $x$-axis, the coupling terms $C_{12}$ and $C_{15}$ appear in the constitutive matrices of the Y-frame and corrugated cores. In addition, the symmetric shear stiffness $C_{33}$ of the corrugated core is very high in comparison to that of the other cores because the corrugated lattice core has a stretch-dominated shear-carrying mechanism while the others cores are bending-dominated. In other words, when bent, the constituents of the corrugated lattice core act as axial rods without significant bending so that the core is very stiff. Finally, it is easy verify that all eigenvalues of each constitutive matrix above are positive which means that the matrices are positive definite. It follows that each lattice core material is stable in the conventional sense (i.e., strain energy is positive for nonzero strains).

## 4.4 Governing differential equations

The governing differential equations of geometrically nonlinear micropolar beams and plates are derived using the principle of virtual work [102], which can be stated as follows:

$$\delta W = \delta W_I - \delta W_E = 0 \tag{4.4.1}$$

where $W_I$ is the potential energy due to internal forces (force stresses and couple stresses) and $W_E$ is the potential energy due to the externally applied forces. Writing Eq. (4.4.1) in terms of the stress resultants and virtual strains, we get:

$$\int_0^L [N_{xx}\delta\hat{\varepsilon}^0_{xx} + M_{xx}\delta\kappa_{xx} + Q^s_x\delta\gamma^s_x + Q^a_x\delta\gamma^a_x + P_{xy}\delta\chi_{xy}]dx - \int_0^L q_0\delta w_0 dx = 0 \tag{4.4.2}$$

The virtual strains can be written in terms of the virtual displacement using the strain displacement relations of Eq. (4.2.3) and Eq. (4.2.4). After expressing Eq.(4.4.2) in terms of the virtual displacements and virtual microrotations, the governing differential equations of equivalent single layer micropolar beam are obtained by taking the Euler-Lagrange equations of Eq. (4.4.2). These are listed below.

$$\delta u_0 : \quad \frac{dN_{xx}}{dx} = 0 \tag{4.4.3}$$

$$\delta w_0 : \quad \frac{d}{dx}\left(\frac{dw_0}{dx}N_{xx}\right) + \frac{d(Q^s_x + Q^a_x)}{dx} + q_0 = 0 \tag{4.4.4}$$

$$\delta \phi_x : \quad \frac{dM_{xx}}{dx} - Q^s_x + Q^a_x = 0 \tag{4.4.5}$$

$$\delta \psi_y : \quad \frac{dP_{xy}}{dx} - 2Q^a_x = 0 \tag{4.4.6}$$

Here $q_0(x)$ is the distributed load acting on the top of the beam. The governing equations (4.4.3)-(4.4.6) can be further expressed in terms of the displacements and microrotations by using the general constitutive relation Eq. (4.3.19).

## 4.5 Finite element formulation

To develop the weak form Galerkin finite element model we construct the weak form equations of (4.4.3)-(4.4.6) on a typical element of the beam, $\Omega_e = (x_a, x_b)$. The primary variables $(u_0, w_0, \phi_x, \psi_y)$ are approximated using 1-D linear Lagrange interpolations functions $L_j^{(\alpha)}$ [93], where $(\alpha = 1, 2, 3, 4)$. Since we are developing weak form Galerkin finite elements, the weight functions $w_i$ $(i = 1, 2, 3, 4)$, used in constructing the weak form equations are taken to be 1-D linear Lagrange interpolation functions used in approximating the primary variables [93]. Thus we have

$$\begin{aligned}
u_0 &\approx \sum_{j=1}^{4} U_j L_j^{(1)}(x), \qquad w_1(x) = L_i^{(1)}(x) \\
w_0 &\approx \sum_{j=1}^{4} W_j L_j^{(2)}(x), \qquad w_2(x) = L_i^{(2)}(x) \\
\phi_x &= \sum_{j=1}^{4} \Phi x_j L_j^{(3)}(x), \qquad w_3(x) = L_i^{(3)}(x) \\
\psi_y &\approx \sum_{j=1}^{4} \Psi y_j L_j^{(4)}(x), \qquad w_4(x) = L_i^{(4)}(x)
\end{aligned} \tag{4.5.1}$$

Now we write the weak form equations of the micropolar plate governing equations (4.4.3)-(4.4.6) on a typical element $\Omega_e = (x_a, x_b)$ as

$$\int_{x_a}^{x_b} \left[\frac{dw_1}{dx} N_{xx}\right] dx - w_1(x_a)Q_1 - w_2(x_b)Q_5 = 0 \tag{4.5.2}$$

$$\begin{aligned}
\int_{x_a}^{x_b} \left[\frac{dw_2}{dx}\left(N_{xx}\frac{dw_0}{dx}\right) + \frac{dw_2}{dx}(Q_x^s + Q_x^a)\right] dx \\
- \int_{x_a}^{x_b} q_0 w_2 dx - w_2(x_a)Q_2 - w_2(x_b)Q_6 = 0
\end{aligned} \tag{4.5.3}$$

$$\int_{x_a}^{x_b} \left[\frac{dw_3}{dx} M_{xx} + w_3(Q_x^s - Q_x^a)\right] dx - w_3(x_a)Q_3 - w_3(x_b)Q_7 = 0 \tag{4.5.4}$$

$$\int_{x_a}^{x_b} \left[\frac{dw_4}{dx} P_{xy} + 2w_4 Q_x^a\right] dx - w_4(x_a)Q_4 - w_4(x_b)Q_8 = 0 \tag{4.5.5}$$

After using the general constitutive relation of Eq. (4.3.19) in the above equations to express the stress and couple stress resultants in term of the displacements and microrotations, the finite ele-

ment equations for typical beam element can be expressed as

$$\mathbf{K^{(e)}}\mathfrak{U}^{\mathbf{(e)}} = \mathbf{F^{(e)}} \tag{4.5.6}$$

where

$$\mathbf{K^{(e)}} = \begin{bmatrix} \mathbf{K^{11}} & \mathbf{K^{12}} & \mathbf{K^{13}} & \mathbf{K^{14}} \\ \mathbf{K^{21}} & \mathbf{K^{22}} & \mathbf{K^{23}} & \mathbf{K^{24}} \\ \mathbf{K^{31}} & \mathbf{K^{32}} & \mathbf{K^{33}} & \mathbf{K^{34}} \\ \mathbf{K^{41}} & \mathbf{K^{42}} & \mathbf{K^{43}} & \mathbf{K^{44}} \end{bmatrix}^{(e)}, \quad \mathfrak{U}^{\mathbf{(e)}} = \begin{Bmatrix} \mathbf{U} \\ \mathbf{W} \\ \boldsymbol{\Phi x} \\ \boldsymbol{\Psi y} \end{Bmatrix}^{(e)}, \quad \mathbf{F^{(e)}} = \begin{Bmatrix} \mathbf{F^1} \\ \mathbf{F^2} \\ \mathbf{F^3} \\ \mathbf{F^4} \end{Bmatrix}^{(e)} \tag{4.5.7}$$

The stiffness coefficients $K_{ij}^{\alpha\beta}$ and force coefficients $F_i^{\alpha}$ ($\alpha, \beta = 1, 2, 3, 4$ and $i, j = 1, 2$) are defined as

$$K_{ij}^{11} = \int_{x_a}^{x_b} \left\{ C_{11} \frac{dL_i^{(1)}}{dx} \frac{dL_j^{(1)}}{dx} \right\} dx$$

$$K_{ij}^{12} = \frac{1}{2} \int_{x_a}^{x_b} \left\{ C_{11} \left( \frac{dw_0}{dx} \right) \frac{dL_i^{(1)}}{dx} \frac{dL_j^{(2)}}{dx} \right\} dx$$

$$K_{ij}^{13} = \int_{x_a}^{x_b} \left\{ C_{12} \frac{dL_i^{(1)}}{dx} \frac{dL_j^{(3)}}{dx} \right\} dx$$

$$K_{ij}^{14} = \int_{x_a}^{x_b} \left\{ C_{15} \frac{dL_i^{(1)}}{dx} \frac{dL_j^{(4)}}{dx} \right\} dx$$

$$K_{ij}^{21} = \int_{x_a}^{x_b} \left\{ C_{11} \left( \frac{dw_0}{dx} \right) \frac{dL_i^{(2)}}{dx} \frac{dL_j^{(1)}}{dx} \right\} dx$$

$$K_{ij}^{22} = \frac{1}{2} \int_{x_a}^{x_b} \left\{ C_{11} \left( \frac{dw_0}{dx} \right)^2 \frac{dL_i^{(2)}}{dx} \frac{dL_j^{(2)}}{dx} \right\} dx + \int_{x_a}^{x_b} \left\{ (C_{33} + 2C_{34} + C_{44}) \frac{dL_i^{(2)}}{dx} \frac{dL_j^{(2)}}{dx} \right\} dx$$

$$K_{ij}^{23} = \int_{x_a}^{x_b} \left\{ C_{12} \left( \frac{dw_0}{dx} \right) \frac{dL_i^{(2)}}{dx} \frac{dL_j^{(3)}}{dx} \right\} dx + \int_{x_a}^{x_b} \left\{ (C_{33} - C_{44}) \frac{dL_i^{(2)}}{dx} L_j^{(3)} \right\} dx$$

$$K_{ij}^{24} = \int_{x_a}^{x_b} \left\{ C_{15} \left( \frac{dw_0}{dx} \right) \frac{dL_i^{(2)}}{dx} \frac{dL_j^{(4)}}{dx} \right\} dx + 2 \int_{x_a}^{x_b} \left\{ (C_{34} + C_{44}) \frac{dL_i^{(2)}}{dx} L_j^{(4)} \right\} dx$$

$$K_{ij}^{31} = \int_{x_a}^{x_b} \left\{ C_{12} \frac{dL_i^{(3)}}{dx} \frac{dL_j^{(1)}}{dx} \right\} dx$$

$$K_{ij}^{32} = \frac{1}{2} \int_{x_a}^{x_b} \left\{ C_{12} \left( \frac{dw_0}{dx} \right) \frac{dL_i^{(3)}}{dx} \frac{dL_j^{(2)}}{dx} \right\} dx + \int_{x_a}^{x_b} \left\{ (C_{33} - C_{44}) L_i^{(3)} \frac{dL_j^{(2)}}{dx} \right\} dx$$

$$K_{ij}^{33} = \int_{x_a}^{x_b} \left\{ C_{22} \frac{dL_i^{(3)}}{dx} \frac{dL_j^{(3)}}{dx} \right\} dx + \int_{x_a}^{x_b} \left\{ (C_{33} + C_{44}) L_i^{(3)} L_j^{(3)} \right\} dx$$

$$K_{ij}^{34} = \int_{x_a}^{x_b} \left\{ C_{25} \frac{dL_i^{(3)}}{dx} \frac{dL_j^{(4)}}{dx} \right\} dx + 2 \int_{x_a}^{x_b} \left\{ (C_{34} - C_{44}) L_i^{(3)} L_j^{(4)} \right\} dx$$

$$K_{ij}^{41} = \int_{x_a}^{x_b} \left\{ C_{15} \frac{dL_i^{(4)}}{dx} \frac{dL_j^{(1)}}{dx} \right\} dx$$

$$K_{ij}^{42} = \frac{1}{2}\int_{x_a}^{x_b}\left\{C_{15}\left(\frac{dw_0}{dx}\right)\frac{dL_i^{(4)}}{dx}\frac{dL_j^{(2)}}{dx}\right\}dx + 2\int_{x_a}^{x_b}\left\{\left(C_{34}+C_{44}\right)L_i^{(4)}\frac{dL_j^{(2)}}{dx}\right\}dx$$

$$K_{ij}^{43} = \int_{x_a}^{x_b}\left\{C_{25}\frac{dL_i^{(4)}}{dx}\frac{dL_j^{(3)}}{dx}\right\}dx + 2\int_{x_a}^{x_b}\left\{(C_{34}-C_{44})L_i^{(4)}L_j^{(3)}\right\}dx$$

$$K_{ij}^{44} = \int_{x_a}^{x_b}\left\{C_{55}\frac{dL_i^{(4)}}{dx}\frac{dL_j^{(4)}}{dx}\right\}dx + 4\int_{x_a}^{x_b}\left\{C_{44}L_i^{(4)}L_j^{(4)}\right\}dx$$

$$F_i^1 = Q_1 L_i^{(1)}(x_a) + Q_5 L_i^{(1)}(x_b)$$

$$F_i^2 = \int_{x_a}^{x_b} q_0(x)L_i^{(2)}dx + Q_2 L_i^{(1)}(x_a) + Q_6 L_i^{(1)}(x_b)$$

$$F_i^3 = Q_3 L_i^{(1)}(x_a) + Q_7 L_i^{(1)}(x_b)$$

$$F_i^4 = Q_4 L_i^{(1)}(x_a) + Q_8 L_i^{(1)}(x_b)$$

### 4.5.1 Solution of nonlinear equations

The nonlinear finite element equations (4.5.1) are solved iteratively using the Newton's iteration procedure (see [100]). The linearized element equation at the beginning of the $r^{th}$ iteration will take the form:

$$\mathbf{T}^{(\mathbf{e})(r)} = \left[\frac{\partial \mathbf{R}^{(\mathbf{e})}}{\partial \mathfrak{U}^{(\mathbf{e})}}\right]^{(r-1)} \tag{4.5.8}$$

such that

$$\mathbf{T}^{(\mathbf{e})(r)}\Delta\mathfrak{U}^{\mathbf{e}} = -\mathbf{R}^{(\mathbf{e})^{(r-1)}} \tag{4.5.9}$$

where

$$\mathbf{R}^{(\mathbf{e})} = \mathbf{K}^{(\mathbf{e})}(\mathfrak{U}^{(\mathbf{e})})\mathfrak{U}^{(\mathbf{e})} - \mathbf{F}^{(\mathbf{e})} \quad \text{and} \quad \Delta\mathfrak{U}^{(\mathbf{e})} = \mathfrak{U}^{(\mathbf{e})^{(r)}} - \mathfrak{U}^{(\mathbf{e})^{(r-1)}}$$

The explicit expressions of the components of the element tangent stiffness matrix are

$$T_{ij}^{\alpha\beta} = K_{ij}^{\alpha\beta}$$

except for the following terms

$$T_{ij}^{12} = K_{ij}^{12} + \frac{1}{2}\int_{x_a}^{x_b}\left\{C_{11}\frac{dw_0}{dx}\frac{dL_i^{(1)}}{dx}\frac{dL_j^{(2)}}{dx}\right\}dx$$

$$T_{ij}^{32} = K_{ij}^{32} + \frac{1}{2}\int_{x_a}^{x_b}\left\{C_{12}\frac{dw_0}{dx}\frac{dL_i^{(3)}}{dx}\frac{dL_j^{(2)}}{dx}\right\}dx$$

$$T_{ij}^{42} = K_{ij}^{42} + \frac{1}{2}\int_{x_a}^{x_b}\left\{C_{15}\frac{dw_0}{dx}\frac{dL_i^{(4)}}{dx}\frac{dL_j^{(2)}}{dx}\right\}dx$$

$$T_{ij}^{22} = K_{ij}^{22} + \int_{x_a}^{x_b}\left\{C_{11}\frac{du_0}{dx}\frac{dL_i^{(2)}}{dx}\frac{dL_j^{(2)}}{dx}\right\}dx + \int_{x_a}^{x_b}\left\{C_{11}\left(\frac{dw_0}{dx}\right)^2\frac{dL_i^{(2)}}{dx}\frac{dL_j^{(2)}}{dx}\right\}dx$$
$$+ \int_{x_a}^{x_b}\left\{C_{12}\frac{d\phi_x}{dx}\frac{dL_i^{(2)}}{dx}\frac{dL_j^{(2)}}{dx}\right\}dx + \int_{x_a}^{x_b}\left\{C_{15}\frac{d\psi_y}{dx}\frac{dL_i^{(2)}}{dx}\frac{dL_j^{(2)}}{dx}\right\}dx$$

After the element equations are computed, they can be assembled according to the nodal connectivity of the mesh to obtain global equations. Boundary conditions are imposed on the global equations and subsequent equations are solved to obtain the global incremental generalized displacement vector $\Delta\mathfrak{U}$ at the end of $r^{th}$ iteration. The normalized difference between solution vectors from two consecutive iterations, measured with Euclidean norm, is computed at the end of each iteration. If the value computed is less than a preselected tolerance '$tol$' further iterations are terminated and nonlinear convergence is assumed (for all the nonlinear cases considered we chose $tol = 10^{-3}$)

$$\sqrt{\frac{\Delta\mathfrak{U}\cdot\Delta\mathfrak{U}}{\mathfrak{U}^{(r)}\cdot\mathfrak{U}^{(r)}}} \leqslant tol$$

Once the nonlinear convergence is attained, the final global generalized displacement vector is

obtained using

$$\mathfrak{U}^{(r)} = \Delta\mathfrak{U} + \mathfrak{U}^{(r-1)} \tag{4.5.10}$$

### 4.5.2 Shear and membrane locking

In chapter 2 we considered higher order interpolation functions to eliminate shear and membrane locking. In this chapter we shall use linear Lagrange interpolation functions on all the primary variables and employ reduced integration technique to eliminate locking. In the thin beam limit, when linear interpolation is used for $w_0$, the cross-sectional rotation $\phi_x$ should approach $-(dw_0/dx)$, which is necessarily constant. But since $\phi_x$ is also interpolated as linear, it can never be constant. This inconsistency causes what is known as shear locking (see [100]). To avoid this inconsistency, we may use equal interpolation on both $w_0$ and $\phi_x$ but treat $\phi_x$ as constant while evaluating the symmetric $\gamma_x^s$ and anti-symmetric $\gamma_x^a$ shear strains. This amounts to using reduced Gauss quadrature rule in evaluating the integrals containing constants $C_{33}$, $C_{34}$ and $C_{44}$ while computing the element coefficient matrices of Eq. (4.5.6) and Eq. (4.5.9).

When von Kármán nonlinearity is included, there is coupling between $u_0$ and $w_0$ which causes the beam to undergo axial displacement even when there are no axial forces. But in the case of hinged-hinged beam, there are no constraints on $u_0$ at the boundaries, thus causing the beam to roll over freely without axial strain, i.e,

$$\hat{\varepsilon}_x^0 = \frac{du_0}{dx} + \frac{1}{2}\left(\frac{dw_0}{dx}\right)^2 = 0$$

In order to satisfy this we need

$$-\frac{du_0}{dx} \sim \left(\frac{dw_0}{dx}\right)^2$$

In essence, we need to have the same degree of polynomial variation on both $(du_0/dx)$ and $(dw_0/dx)^2$. But when equal interpolation of degree greater than one is used for both $u_0$ and $w_0$

this criteria cannot be satisfied and leads to what is known as membrane locking (see [100]). To overcome this we have to treat $(dw_0/dx)^2$ as same order as $(du_0/dx)$. This is achieved using reduced integration while evaluating all the nonlinear terms of the element coefficients matrices of Eqs. (4.5.2) and (4.5.3).

## 4.6 Numerical bending examples

### 4.6.1 General Setup

The developed micropolar beam finite element model is used for bending analysis of lattice core sandwich beams. The four structural cores considered in section 4.3 are used in the calculations. Both geometrically linear and nonlinear cases are analyzed using the 1-D beam model. 2-D reference solutions are computed using Euler–Bernoulli FE beam frames modeled by Abaqus; the pins in simply-supported cases are at the central axis of the 2-D frame so that the model corresponds to 1-D cases.

### 4.6.2 Bending of a web-core beam

A beam consisting of 24 web-core unit cells is considered first. The length of each web-core unit cell is $l = 0.12$ m resulting in a total beam length of $L = 2.88$ m. The beam is analyzed for two different boundary conditions, namely, a fixed-fixed case and a three-point-bending setup. For the fixed-fixed case the boundaries are subjected to the following conditions:

$$\begin{aligned} x = 0 &: u_0 = 0, w_0 = 0, \phi_x = 0, \psi_y = 0 \\ x = L &: u_0 = 0, w_0 = 0, \phi_x = 0, \psi_y = 0 \end{aligned} \tag{4.6.1}$$

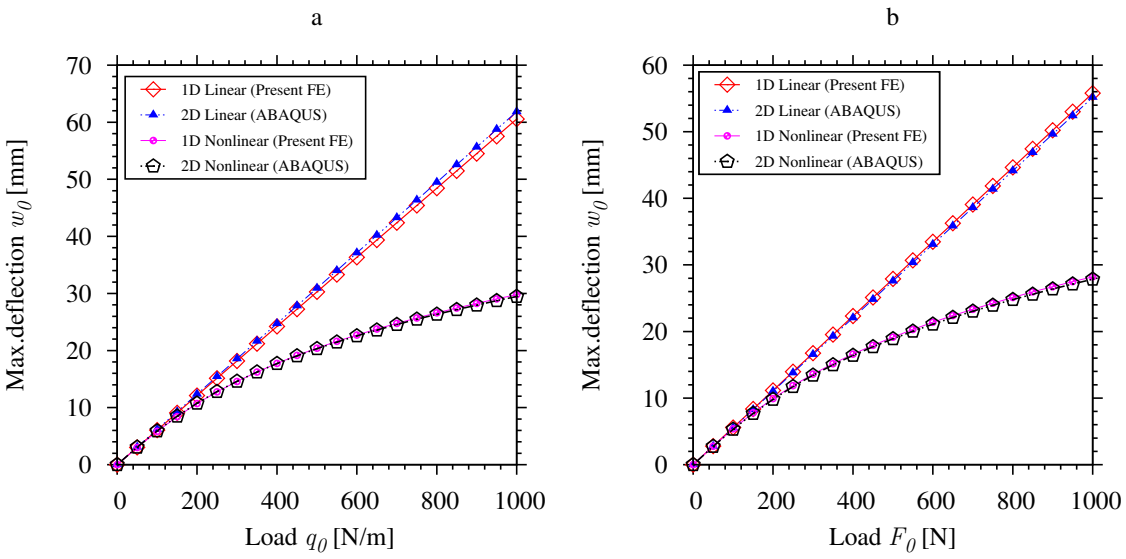


Figure 4.4: (a) Maximum transverse deflection of a fixed-fixed web-core beam subjected to a uniformly distributed load. (b) Maximum transverse deflection of a web-core beam under three-point-bending [5].

A uniformly distributed load $q_0$ is exerted on the beam. The load is applied in increments of $\Delta q_0 = 50$ N/m until a maximum load of $1000$ N/m is reached. The maximum deflection, which occurs at the center of the beam, is recorded against the corresponding applied load. The results for both linear and nonlinear cases are plotted in Fig. 4.4a. The nonlinear deflections are smaller than the linear deflections at large loads because, as the load increases, the internal forces resisting the deformation increase in a nonlinear fashion.

For the three-point-bending case the boundaries are subjected to the following conditions:

$$\begin{aligned} x = 0 &: u_0 = 0, w_0 = 0, M_{xx} = 0, P_{xy} = 0 \\ x = L &: u_0 = 0, w_0 = 0, M_{xx} = 0, P_{xy} = 0 \end{aligned} \tag{4.6.2}$$

Here, instead of a uniformly distributed load, a point load $F_0$ is applied at the center of the beam. The point load is applied in increments of $\Delta F_0 = 50$ N until a maximum load of $1000$ N is reached. The maximum deflection, which occurs at the center of the beam, is recorded against

the corresponding applied load. The results from the finite element model developed here for the 1-D equivalent single layer beam are compared with the 2-D FE results (see Fig. 4.4b). Note that ABAQUS uses a more complete Green-Lagrange strain tensor for the geometrically nonlinear beam element, whereas in the present finite element model developed in this study the nonlinearity is included in the form of von Kármán strains.

### 4.6.3 Fixed-fixed hexagonal and Y-frame core beams

Here we consider two beams, one made of 48 hexagonal core unit cells and the other made of 30 Y-frame unit cells (see Fig. 4.3). Thus, the total length of the hexagonal core beam is $L = 7.2$ m and the length of Y-frame core beam is $L = 15.9$ m. Both the beams are subjected to a uniformly distributed load $q_0$. Fixed-fixed boundary conditions (4.6.1) are applied at the beam ends. For the hexagonal core beam the load is applied in increments of $\Delta q_0 = 75$ N/m until a maximum load of $1500$ N/m is reached, while for the Y-frame core beam the load is applied in increments of $\Delta q_0 = 5$ N/m until a maximum load of $100$ N/m is reached. The maximum transverse deflections, which occur at the beam centers, are recorded and plotted against the corresponding applied load in Figs. 4.5a and 4.5b.

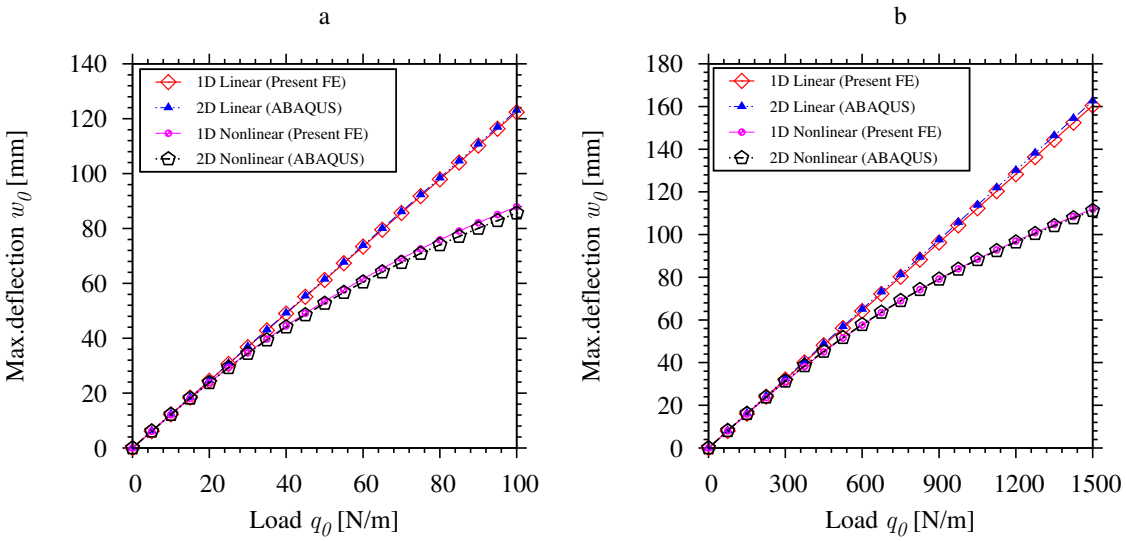


Figure 4.5: Maximum deflection of a (a) Y-frame and (b) hexagonal core sandwich beams subjected to a uniformly distributed load under fixed-fixed boundary conditions [5].

### 4.6.4 Fixed-fixed corrugated core beam

A beam consisting of 30 corrugated core unit cells is considered. Since the length of each corrugated unit cell is $l = 0.53$ m, the total length of the beam is $L = 15.9$ m (see Fig. 4.3). The beam is subjected to fixed-fixed boundary conditions (4.6.1). A uniformly distributed load $q_0$ is applied on the beam. The load is applied in increments of $\Delta q_0 = 50$ N/m until a maximum load of $1000$ N/m is reached. The maximum vertical deflection of the beam is plotted against the corresponding applied load in Fig. 4.6a. The error in the maximum vertical deflection is calculated using,

$$\Delta w_0 = 100 \times \left( \frac{w_0^{1-D \text{ micropolar}} - w_0^{2-D \text{ beam frame}}}{w_0^{2-D \text{ beam frame}}} \right) \tag{4.6.3}$$

and is plotted against the applied load for both the linear and nonlinear cases in Fig. 4.6b.

Unlike the other structural cores, we see that the nonlinear deflections of the corrugated core beam, calculated using the finite element model developed for the 1-D equivalent single layer

beam, are not in good agreement with the 2-D beam frame results all the way. This is due to the local buckling of the stretch-dominated corrugated core that occurs in the 2-D model. The 1-D equivalent single layer model cannot account for this local buckling.

We also note that even though the lengths and heights of both corrugated core and Y-frame core beams are equal, the corrugated core beam is much stiffer than the Y-frame core beam. The maximum nonlinear deflection for the Y-frame core beam subjected to fixed-fixed boundary conditions is $88$ mm at a uniformly distributed load of $100$ N/m (see Fig. 4.5a), while for the corrugated core beam the maximum deflection for a uniformly distributed load of $100$ N/m is only $2.9$ mm (see Fig. 4.6a). The high stiffness of the corrugated core beam is attributed to its stretch-dominated behavior unlike Y-frame core which is bending-dominated. The corrugated core has a very high shear stiffness because of the fact that the elements (the Euler-Bernoulli beam elements within the core structure) of the corrugated core act essentially like rods and do not bend much, where as this is not the case in the Y-frame core. Although the elements of the part which resemble the corrugated core (the upper 'V' part of 'Y') in the Y-frame core do not exhibit lot of bending, the remaining part, consisting of lower element, undergoes significant bending.

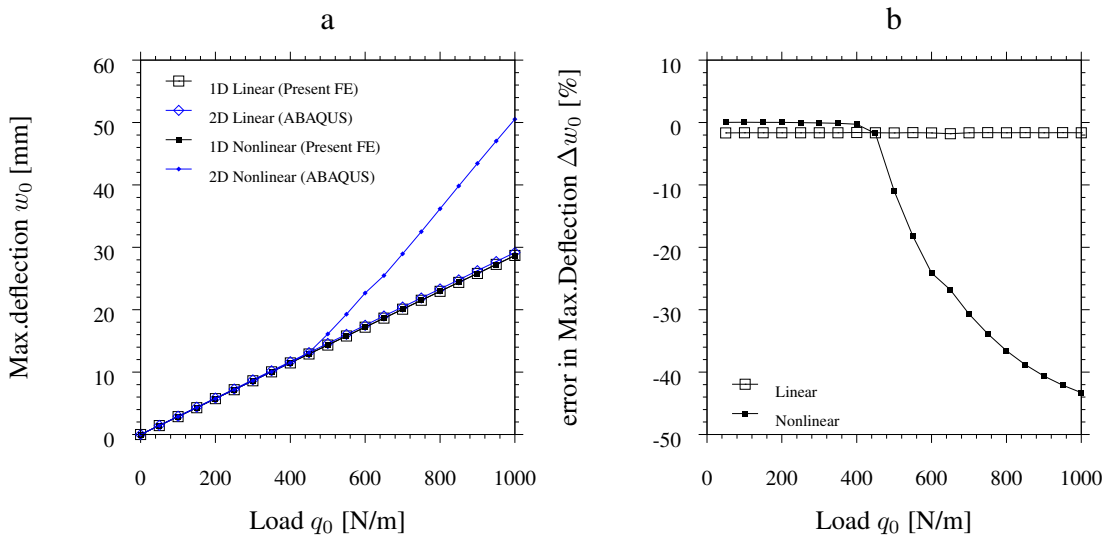


Figure 4.6: (a) Maximum deflection of a corrugated core sandwich beam subjected a uniformly distributed load under fixed-fixed boundary conditions. Local buckling occurs in the 2-D reference model near $q = 500$ N/m which cannot be accounted for by the micropolar 1-D model. (b) Percentage error of 1D beam model developed, in terms of maximum vertical deflection relative to 2D-beam frame solution (face sheet deflection) calculated using ABAQUS [5].

# 5. NONLINEAR FINITE ELEMENT ANALYSIS OF LATTICE CORE SANDWICH PLATES*

## 5.1 Introduction

In this chapter will consider lattice core sandwich plates and their modeling using von Kármán micropolar plate theory discussed in chapter 3. We will first review the kinematics of the micropolar plate and then we give the constitutive models of web core lattice plates and pyramid core lattice plates modeled as micropolar plate [9, 6]. Then the corresponding governing equations and finite element equations are derived. Finally numerical results are presented to illustrate the accuracy of the constitutive modeling and the corresponding finite element formulation.

## 5.2 Kinematics of micropolar plate

In this section we will review the micropolar plate kinematics considered in chapter 3. The 3-D displacements and microrotations of a micropolar plate can be approximated by 2-D midsurface kinematic variables $(u_0, v_0, w_0, \phi_x, \phi_y, \psi_x, \psi_y)$ so that

$$\begin{aligned} u_1(x,y,z,t) &= u_0(x,y,t) + z\phi_x(x,y,t) \\ u_2(x,y,z,t) &= v_0(x,y,t) + z\phi_y(x,y,t) \\ u_3(x,y,z,t) &= w_0(x,y,t) \\ \psi_1(x,y,z,t) &= \psi_x(x,y,t) \\ \psi_2(x,y,z,t) &= \psi_y(x,y,t) \\ \psi_3(x,y,z,t) &= 0 \end{aligned} \tag{5.2.1}$$

where $t$ is time, $(u_0, v_0, w_0)$ denote the displacements of a point on the plane $z = 0$, and $(\phi_x, \phi_y)$ are the rotations of a transverse normal about the $y$- and $x$-axes, respectively, whereas $(\psi_x, \psi_y)$ are

*Reprinted with permission from "Nonlinear finite element analysis of lattice core sandwich plates" by P. Nampally, A. T. Karttunen, and J. N. Reddy, 2020. International Journal of Non-Linear Mechanics, vol. 121, p. 103423, Copyright (2020) Elsevier Ltd.

microrotations about the $x$- and $y$-axes, respectively. The corresponding linear strains and wryness tensor components developed in the micropolar plate are [44]

$$\varepsilon_{kl} = u_{l,k} + \epsilon_{lkm}\psi_m \tag{5.2.2}$$

$$\chi_{kl} = \psi_{l,k} \tag{5.2.3}$$

Following the displacements and microrotations given in Eq. (5.2.1), the nonzero strains in Cartesian coordinates are

$$\begin{aligned}
&\varepsilon_{xx} = \frac{\partial u_0}{\partial x} + z\frac{\partial \phi_x}{\partial x} = \varepsilon^0_{xx} + z\kappa_{xx}, && \varepsilon_{yy} = \frac{\partial v_0}{\partial y} + z\frac{\partial \phi_y}{\partial y} = \varepsilon^0_{yy} + z\kappa_{yy} \\
&\varepsilon_{xy} = \frac{\partial v_0}{\partial x} + z\frac{\partial \phi_y}{\partial x} = \varepsilon^0_{xy} + z\kappa_{xy}, && \varepsilon_{yx} = \frac{\partial u_0}{\partial y} + z\frac{\partial \phi_x}{\partial y} = \varepsilon^0_{yx} + z\kappa_{yx} \\
&\varepsilon_{xz} = \frac{\partial w_0}{\partial x} + \psi_y, && \varepsilon_{zx} = \phi_x - \psi_y \\
&\varepsilon_{yz} = \frac{\partial w_0}{\partial y} - \psi_x, && \varepsilon_{zy} = \phi_y + \psi_x \\
&\chi_{xx} = \frac{\partial \psi_x}{\partial x}, \quad \chi_{yy} = \frac{\partial \psi_y}{\partial y}, && \chi_{xy} = \frac{\partial \psi_y}{\partial x}, \quad \chi_{yx} = \frac{\partial \psi_x}{\partial y}
\end{aligned} \tag{5.2.4}$$

With the inclusion of von Kármán type geometric nonlinearities [100] into the vector $\boldsymbol{\epsilon}^0$ below, we write the strains in the form

$$\boldsymbol{\epsilon}^0 = \begin{Bmatrix} \varepsilon^0_{xx} \\ \varepsilon^0_{yy} \\ \varepsilon^0_{xy} \\ \varepsilon^0_{yx} \end{Bmatrix} = \begin{Bmatrix} \frac{\partial u_0}{\partial x} + \frac{1}{2}\left(\frac{\partial w_0}{\partial x}\right)^2 \\ \frac{\partial v_0}{\partial y} + \frac{1}{2}\left(\frac{\partial w_0}{\partial y}\right)^2 \\ \frac{\partial v_0}{\partial x} + \frac{1}{2}\frac{\partial w_0}{\partial x}\frac{\partial w_0}{\partial y} \\ \frac{\partial u_0}{\partial y} + \frac{1}{2}\frac{\partial w_0}{\partial x}\frac{\partial w_0}{\partial y} \end{Bmatrix} \qquad \boldsymbol{\kappa} = \begin{Bmatrix} \kappa_{xx} \\ \kappa_{yy} \\ \kappa_{xy} \\ \kappa_{yx} \end{Bmatrix} = \begin{Bmatrix} \frac{\partial \phi_x}{\partial x} \\ \frac{\partial \phi_y}{\partial y} \\ \frac{\partial \phi_y}{\partial x} \\ \frac{\partial \phi_x}{\partial y} \end{Bmatrix} \tag{5.2.5}$$

$$\boldsymbol{\gamma} = \begin{Bmatrix} \gamma_x^s \\ \gamma_x^a \\ \gamma_y^s \\ \gamma_y^a \end{Bmatrix} = \begin{Bmatrix} \frac{\partial w_0}{\partial x} + \phi_x \\ \frac{\partial w_0}{\partial x} - \phi_x + 2\psi_y \\ \frac{\partial w_0}{\partial y} + \phi_y \\ \frac{\partial w_0}{\partial y} - \phi_y - 2\psi_x \end{Bmatrix} \qquad \boldsymbol{\chi} = \begin{Bmatrix} \chi_{xx} \\ \chi_{yy} \\ \chi_{xy} \\ \chi_{yx} \end{Bmatrix} = \begin{Bmatrix} \frac{\partial \psi_x}{\partial x} \\ \frac{\partial \psi_y}{\partial y} \\ \frac{\partial \psi_y}{\partial x} \\ \frac{\partial \psi_x}{\partial y} \end{Bmatrix} \tag{5.2.6}$$

where the symmetric shear strains are defined as

$$\begin{aligned} \gamma_x^s &= \epsilon_{xz} + \epsilon_{zx} = \frac{\partial w_0}{\partial x} + \phi_x \\ \gamma_y^s &= \epsilon_{yz} + \epsilon_{zy} = \frac{\partial w_0}{\partial y} + \phi_y \end{aligned} \tag{5.2.7}$$

and the antisymmetric shear strains are

$$\begin{aligned} \gamma_x^a &= \epsilon_{xz} - \epsilon_{zx} = \frac{\partial w_0}{\partial x} - \phi_x + 2\psi_y = 2(\psi_y - \omega_2) \\ \gamma_y^a &= \epsilon_{yz} - \epsilon_{zy} = \frac{\partial w_0}{\partial y} - \phi_y - 2\psi_x = 2(\omega_1 - \psi_x) \end{aligned} \tag{5.2.8}$$

where $(\omega_1, \omega_2)$ are the macrorotations. The symmetric shear strains $(\gamma_x^s, \gamma_y^s)$ are of the same form as the shear strains in the conventional FSDT plate theory based on classical elasticity. However, the antisymmetric parts are defined in terms both macrorotations and microrotations.

## 5.3 Two-scale constitutive modeling of lattice core sandwich plates

The unit cells for the web-core and pyramid core are shown in Fig. 5.1. The unit cells represent lattice materials of which the 2-D micropolar ESL-FSDT plate is made of. Two-scale, energy-based constitutive modeling was carried out in detail in [9] for the web-core unit cell presented in Fig. 5.1. This approach was also applied to the pyramid core in [6]. The procedure to arrive at the constitutive equations of lattice core sandwich plates is similar to the one described for lattice core sandwich beams in chapter 4.

The derivation of the constitutive equations of the lattice core sandwich plate is based on the same concept of energy equivalence of unit cell and a continuum point of the equivalent single

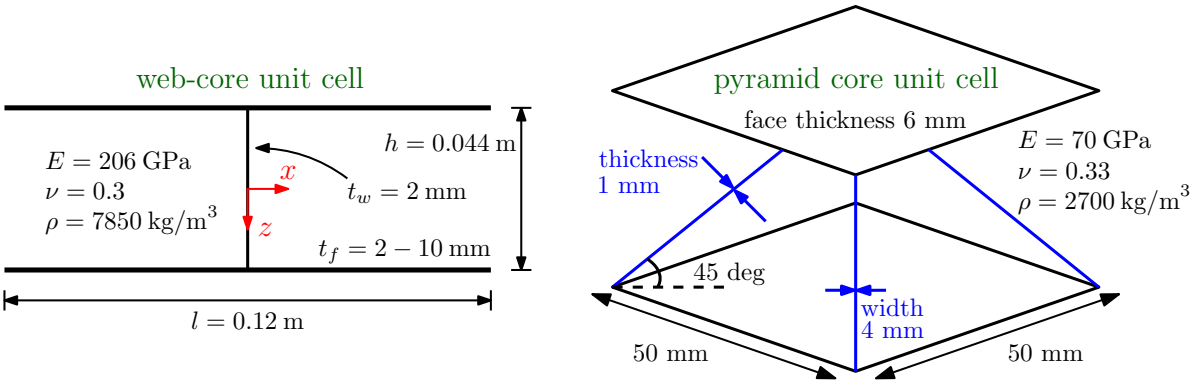


Figure 5.1: Parameters of web-core and pyramid core unit cells made of steel and aluminium, respectively. All face sheet edges of both cores are taken to be of equal length so that, e.g., the web-core planform area is $A = l^2 = 0.0144$ m$^2$. The struts (beams) in the pyramid core have rectangular cross sections [6].

layer micropolar plate. The only difference being that in calculating the energy of the plate unit cell, the numerical values of the element stiffness matrix are used instead of analytical expressions. Further details of the constitutive models of the lattice plates with unit cell shown in Fig. 5.1 are given in [9, 6]. As the outcome of the constitutive modeling, we have for the 2-D micropolar plate continuum

$$\mathbf{S} = \mathbf{C}\boldsymbol{\epsilon} \tag{5.3.1}$$

where $\mathbf{S}$ is the stress resultant vector and $\mathbf{C}$ is the constitutive matrix. The explicit matrix form of Eq. (5.3.1) is

$$\begin{Bmatrix} \mathbf{N} \\ \mathbf{M} \\ \mathbf{Q} \\ \mathbf{P} \end{Bmatrix} = \begin{bmatrix} \mathbf{A} & \mathbf{0} & \mathbf{0} & \mathbf{0} \\ \mathbf{0} & \mathbf{D} & \mathbf{0} & \mathbf{0} \\ \mathbf{0} & \mathbf{0} & \mathbf{G} & \mathbf{0} \\ \mathbf{0} & \mathbf{0} & \mathbf{0} & \mathbf{H} \end{bmatrix} \begin{Bmatrix} \boldsymbol{\epsilon}^0 \\ \boldsymbol{\kappa} \\ \boldsymbol{\gamma} \\ \boldsymbol{\chi} \end{Bmatrix} \tag{5.3.2}$$

where the vectors for the membrane $\mathbf{N}$, global bending and twisting $\mathbf{M}$, symmetric and antisym-

metric shear $\mathbf{Q}$ and local (couple-stress related) bending and twisting $\mathbf{P}$ resultants read

$$\begin{aligned}
\mathbf{N} &= \{N_{xx} \;\; N_{yy} \;\; N_{xy} \;\; N_{yx}\}^{\mathrm{T}} \\
\mathbf{M} &= \{M_{xx} \;\; M_{yy} \;\; M_{xy} \;\; M_{yx}\}^{\mathrm{T}} \\
\mathbf{Q} &= \left\{Q_x^s \;\; Q_x^a \;\; Q_y^s \;\; Q_y^a\right\}^{\mathrm{T}} \\
\mathbf{P} &= \{P_{xx} \;\; P_{yy} \;\; P_{xy} \;\; P_{yx}\}^{\mathrm{T}}
\end{aligned} \tag{5.3.3}$$

respectively. The submatrices for the constitutive parameters of the web-core and pyramid will take the following form.

$$\begin{aligned}
\mathbf{A} &= \begin{bmatrix} A_{11} & A_{12} & 0 & 0 \\ A_{12} & A_{22} & 0 & 0 \\ 0 & 0 & A_{33} & A_{34} \\ 0 & 0 & A_{34} & A_{44} \end{bmatrix}, \quad \mathbf{D} = \begin{bmatrix} D_{11} & D_{12} & 0 & 0 \\ D_{12} & D_{22} & 0 & 0 \\ 0 & 0 & D_{33} & D_{34} \\ 0 & 0 & D_{34} & D_{44} \end{bmatrix} \\
\mathbf{G} &= \begin{bmatrix} G_{11} & G_{12} & 0 & 0 \\ G_{12} & G_{22} & 0 & 0 \\ 0 & 0 & G_{33} & G_{34} \\ 0 & 0 & G_{34} & G_{44} \end{bmatrix}, \quad \mathbf{H} = \begin{bmatrix} H_{11} & H_{12} & 0 & 0 \\ H_{12} & H_{22} & 0 & 0 \\ 0 & 0 & H_{33} & H_{34} \\ 0 & 0 & H_{34} & H_{44} \end{bmatrix}
\end{aligned} \tag{5.3.4}$$

The matrices include 24 constitutive parameters and are symmetric for both web-core and pyramid core. The constitutive parameters for the web-core are derived in [9] and are given in Table 5.1 and Table 5.2, while the constitutive parameters for pyramid core are derived in [6] and are given in Table 5.3. Similarly, the inertial coefficients, which are the components of the matrix $\mathbf{M}$ given in Eq. (5.3.5), for web-core and pyramid core are given in Table 5.4 and Table 5.5 which are derived in [9] and [6] respectively.

$$\mathbf{M} = \begin{bmatrix} m_{11} & 0 & 0 & 0 & 0 & 0 & 0 \\ 0 & m_{22} & 0 & 0 & 0 & 0 & 0 \\ 0 & 0 & m_{33} & 0 & 0 & 0 & 0 \\ 0 & 0 & 0 & m_{44} & m_{45} & 0 & 0 \\ 0 & 0 & 0 & m_{45} & m_{55} & 0 & 0 \\ 0 & 0 & 0 & 0 & 0 & m_{66} & m_{67} \\ 0 & 0 & 0 & 0 & 0 & m_{67} & m_{77} \end{bmatrix} \tag{5.3.5}$$

Table 5.1: Constitutive parameters **A** and **D** for the web-core shown in Fig. 5.1 (Reprinted with permission from [9]).

| **A**[MN/m] | $t_f$ = 2 mm | 4 mm | 6 mm | 8 mm | 10 mm |
|---|---|---|---|---|---|
| $A_{11}$ | 905.495 | 1810.99 | 2716.48 | 3621.98 | 4527.47 |
| $A_{12}$ | 271.648 | 543.297 | 814.945 | 1086.59 | 1358.24 |
| $A_{22}$ | 997.277 | 1907.18 | 2814.44 | 3720.98 | 4627.24 |
| $A_{33}$ | 316.923 | 633.846 | 950.769 | 1267.69 | 1584.62 |
| **D**[MNm] | $t_f$ = 2 mm | 4 mm | 6 mm | 8 mm | 10 mm |
| $D_{11}$ | 0.43826 | 0.87652 | 1.31478 | 1.75304 | 2.19130 |
| $D_{12}$ | 0.13148 | 0.26296 | 0.39443 | 0.52591 | 0.65739 |
| $D_{22}$ | 0.46020 | 0.90585 | 1.35350 | 1.80011 | 2.24 4 48 |
| $D_{33}$ | 0.15339 | 0.30678 | 0.46017 | 0.61356 | 0.76695 |

Table 5.2: Constitutive parameters **G** and **H** for the web-core shown in Fig. 5.1 (Reprinted with permission from [9]).

| **G**[MN/m] | $t_f$ = 2 mm | 4 mm | 6 mm | 8 mm | 10 mm |
|---|---|---|---|---|---|
| $G_{11}$ | 1.16557 | 4.26884 | 9.82709 | 18.1926 | 29.5600 |
| $G_{12}$ | 0.93837 | 3.92462 | 9.46343 | 17.8250 | 29.1924 |
| $G_{22}$ | 0.91865 | 3.89135 | 9.42900 | 17.7917 | 29.1609 |
| $G_{33}$ | 34.9111 | 45.7777 | 55.5037 | 66.3705 | 79.3196 |
| $G_{34}$ | 1.32756 | 5.01625 | 11.1895 | 20.0058 | 31.6599 |
| $G_{44}$ | 0.98325 | 4.17269 | 9.96295 | 18.5242 | 30.0194 |
| **H**[Nm] | $t_f$ = 2 mm | 4 mm | 6 mm | 8 mm | 10 mm |
| $H_{11}$ | 190.167 | 1416.73 | 4647.49 | 10763.7 | 20571.6 |
| $H_{12}$ | 23.8172 | 211.894 | 712.203 | 1656.92 | 3155.87 |
| $H_{22}$ | 181.960 | 1407.22 | 4638.13 | 10754.7 | 20563.1 |
| $H_{33}$ | 301.832 | 2414.65 | 8149.45 | 19317.2 | 37728.9 |
| $H_{34}$ | -90.5495 | -724.396 | -2444.84 | -5795.16 | -11318.7 |
| $H_{44}$ | 1317.40 | 7712.00 | 20232.4 | 38648.9 | 63268.3 |

Table 5.3: Constitutive parameters for the pyramid core shown in Fig. 5.1 [6]

| | **A** [MN/m] | | **D** [kN/m] | | **G** [MN/m] | | **H** [Nm] |
|---|---|---|---|---|---|---|---|
| $A_{11}$ | 943.83 | $D_{11}$ | 294.96 | $G_{11}$ | 11.907 | $H_{11}$ | 1603.5 |
| $A_{12}$ | 312.24 | $D_{12}$ | 97.579 | $G_{12}$ | 9.1773 | $H_{12}$ | 18.615 |
| $A_{22}$ | 943.83 | $D_{22}$ | 294.96 | $G_{22}$ | 9.1770 | $H_{22}$ | 1603.5 |
| $A_{33}$ | 317.19 | $D_{33}$ | 99.126 | $G_{33}$ | 11.907 | $H_{33}$ | 2829.5 |
| $A_{34}$ | 317.19 | $D_{34}$ | 99.126 | $G_{34}$ | 9.1773 | $H_{34}$ | -933.59 |
| $A_{44}$ | 317.19 | $D_{44}$ | 99.126 | $G_{44}$ | 9.1770 | $H_{44}$ | 2829.5 |

Table 5.4: Inertia coefficients for the web-core shown in Fig. 5.1 (Reprinted with permission from [9]).

| **M**[kg/m$^3$] | $t_f$ = 2 mm | 4 mm | 6 mm | 8 mm | 10 mm |
|---|---|---|---|---|---|
| $m_{11}$ | 37.1567 | 68.5567 | 99.9567 | 131.357 | 162.757 |
| $m_{22}$ | 37.1567 | 68.5567 | 99.9567 | 131.357 | 162.757 |
| $m_{33}$ | 37.1567 | 68.5567 | 99.9567 | 131.357 | 162.757 |
| **M**[kg] | $t_f$ = 2 mm | 4 mm | 6 mm | 8 mm | 10 mm |
| $m_{44}$ | 0.016476 | 0.031692 | 0.046904 | 0.062107 | 0.077307 |
| $m_{45}$ | -0.000208 | -0.000071 | -0.000014 | 0.000007 | 0.000015 |
| $m_{55}$ | 0.000759 | 0.001776 | 0.002730 | 0.003637 | 0.004498 |
| $m_{66}$ | 0.014032 | 0.028606 | 0.043443 | 0.058422 | 0.073481 |
| $m_{67}$ | 0.000152 | 0.000345 | 0.000489 | 0.000567 | 0.000596 |
| $m_{77}$ | 0.000244 | 0.000685 | 0.001429 | 0.002399 | 0.003434 |

Table 5.5: Inertia coefficients for the pyramid core shown in Fig. 5.1 [6].

| | M [kg/m$^2$] | | M [kg] |
|---|---|---|---|
| $m_{11}$ | 33.264 | $m_{44}$ | 0.0102 |
| $m_{22}$ | 33.264 | $m_{45}$ | 0 |
| $m_{33}$ | 33.264 | $m_{55}$ | $0.1715\times10^{-3}$ |
| | | $m_{66}$ | 0.0102 |
| | | $m_{67}$ | 0 |
| | | $m_{77}$ | $0.1715\times10^{-3}$ |

## 5.4 Governing differential equations

Using the constitutive relations derived for lattice core sandwich plates in the previous section, the strain energy for the 2-D micropolar plate can be written as

$$U = \frac{1}{2}\int_{\Omega} \boldsymbol{\epsilon}^{\mathrm{T}}\mathbf{C}\boldsymbol{\epsilon}\, dxdy \tag{5.4.1}$$

while the total kinetic energy of the plate is

$$K = \frac{1}{2}\int_{\Omega} \dot{\mathbf{u}}^{\mathrm{T}}\mathbf{M}\dot{\mathbf{u}}\, dxdy \tag{5.4.2}$$

where

$$\mathbf{u} = \{u_0 \;\; v_0 \;\; w_0 \;\; \phi_x \;\; \psi_y \;\; \phi_y \;\; \psi_x\}^{\mathrm{T}} \tag{5.4.3}$$

and the over dot on $\mathbf{u}$ represents derivative with respect to time. Finally, the potential energy contribution due to a distributed transverse load is given by

$$V = -\int_{\Omega} qw_0\, dxdy \tag{5.4.4}$$

By substituting expressions (5.4.1), (5.4.2) and (5.4.4) into Hamilton's principle [102], we have

$$\delta \int_0^T \left[K - (U + V)\right] dt = 0 \tag{5.4.5}$$

which we can be written as

$$\int_0^T \int_\Omega \left(\delta \dot{\mathbf{u}}^{\mathrm{T}} \mathbf{M} \dot{\mathbf{u}} - \delta \boldsymbol{\epsilon}^{\mathrm{T}} \mathbf{C} \boldsymbol{\epsilon} + q \delta w_0\right) dx dy dt = 0 \tag{5.4.6}$$

where we can use Eq. (5.3.1), that is, $\mathbf{S} = \mathbf{C}\boldsymbol{\epsilon}$. The governing equations of the ESL-FSDT micropolar plate used for modeling the lattice core sandwich plates are obtained by writing the Euler-Lagrange equations of the variational statement (5.4.6). These are listed below.

$$\delta u_0 : \quad \frac{\partial N_{xx}}{\partial x} + \frac{\partial N_{yx}}{\partial y} = m_{11} \frac{\partial^2 u_0}{\partial t^2} \tag{5.4.7}$$

$$\delta v_0 : \quad \frac{\partial N_{xy}}{\partial x} + \frac{\partial N_{yy}}{\partial y} = m_{22} \frac{\partial^2 v_0}{\partial t^2} \tag{5.4.8}$$

$$\delta w_0 : \quad \frac{\partial (Q_x^s + Q_x^a)}{\partial x} + \frac{\partial (Q_y^s + Q_y^a)}{\partial y} + \mathscr{N} + q_0 = m_{33} \frac{\partial^2 w_0}{\partial t^2} \tag{5.4.9}$$

$$\delta \phi_x : \quad \frac{\partial M_{xx}}{\partial x} + \frac{\partial M_{yx}}{\partial y} - Q_x^s + Q_x^a = m_{44} \frac{\partial^2 \phi_x}{\partial t^2} + m_{45} \frac{\partial^2 \psi_y}{\partial t^2} \tag{5.4.10}$$

$$\delta \psi_y : \quad \frac{\partial P_{xy}}{\partial x} + \frac{\partial P_{yy}}{\partial y} - 2Q_x^a = m_{55} \frac{\partial^2 \psi_y}{\partial t^2} + m_{45} \frac{\partial^2 \phi_x}{\partial t^2} \tag{5.4.11}$$

$$\delta \phi_y : \quad \frac{\partial M_{xy}}{\partial x} + \frac{\partial M_{yy}}{\partial y} - Q_y^s + Q_y^a = m_{66} \frac{\partial^2 \phi_y}{\partial t^2} + m_{67} \frac{\partial^2 \psi_x}{\partial t^2} \tag{5.4.12}$$

$$\delta \psi_x : \quad \frac{\partial P_{xx}}{\partial x} + \frac{\partial P_{yx}}{\partial y} + 2Q_y^a = m_{77} \frac{\partial^2 \psi_x}{\partial t^2} + m_{67} \frac{\partial^2 \phi_y}{\partial t^2} \tag{5.4.13}$$

where

$$\mathscr{N} = \frac{\partial}{\partial x}\left[N_{xx} \frac{\partial w_0}{\partial x} + \frac{1}{2}\left(N_{xy} + N_{yx}\right) \frac{\partial w_0}{\partial y}\right] + \frac{\partial}{\partial y}\left[N_{yy} \frac{\partial w_0}{\partial y} + \frac{1}{2}\left(N_{xy} + N_{yx}\right) \frac{\partial w_0}{\partial x}\right] \tag{5.4.14}$$

## 5.5 Finite element formulation

In this section, we develop the weak form Galerkin finite element model for the governing equations (5.4.7)-(5.4.13) of the 2-D micropolar ESL-FSDT plate. In the finite element formulation the mid-surface kinematic variables $(u_0, v_0, w_0, \phi_x, \phi_y, \psi_x, \psi_y)$ are taken as the primary variables. These variables are approximated using linear Lagrange interpolation functions $L_j^{(J)}$ [93], where $(J = 1, 2, 3, 4, 5, 6, 7)$. Since we are using weak-form Galerkin finite element formulation, the weight functions $w_i$ $(i = 1, 2, 3, 4, 5, 6, 7)$ are taken to be the same as the Lagrange interpolation functions used in approximating the primary variables. Thus, we have,

$$
\begin{aligned}
u_0 &\approx \sum_{j=1}^{4} U_j(t) L_j^{(1)}(x,y), \qquad w_1(x,y) = L_i^{(1)}(x,y) \\
v_0 &\approx \sum_{j=1}^{4} V_j(t) L_j^{(2)}(x,y), \qquad w_2(x,y) = L_i^{(2)}(x,y) \\
w_0 &= \sum_{j=1}^{4} W_j(t) L_j^{(3)}(x,y), \qquad w_3(x,y) = L_i^{(3)}(x,y) \\
\phi_x &\approx \sum_{j=1}^{4} \Phi x_j(t) L_j^{(4)}(x,y), \qquad w_4(x,y) = L_i^{(4)}(x,y) \\
\psi_y &\approx \sum_{j=1}^{4} \Psi y_j(t) L_j^{(5)}(x,y), \qquad w_5(x,y) = L_i^{(5)}(x,y) \\
\phi_y &\approx \sum_{j=1}^{4} \Phi y_j(t) L_j^{(6)}(x,y), \qquad w_6(x,y) = L_i^{(6)}(x,y) \\
\psi_x &\approx \sum_{j=1}^{4} \Psi x_j(t) L_j^{(7)}(x,y), \qquad w_7(x,y) = L_i^{(7)}(x,y)
\end{aligned}
\tag{5.5.1}
$$

Now we write the weak form equations of the micropolar plate governing equations (5.4.7)-(5.4.13) on a typical element $\Omega_e$ as

$$0 = \int_{\Omega_e} \left\{ w_1 m_{11} \frac{\partial^2 u_0}{\partial t^2} + \frac{\partial w_1}{\partial x} N_{xx} + \frac{\partial w_1}{\partial y} N_{yx} \right\} dxdy - \int_{\tau_e} w_1 Q_1 ds \tag{5.5.2}$$

$$0 = \int_{\Omega_e} \left\{ w_2 m_{22} \frac{\partial^2 v_0}{\partial t^2} + \frac{\partial w_2}{\partial x} N_{xy} + \frac{\partial w_2}{\partial y} N_{yy} \right\} dxdy - \int_{\tau_e} w_2 Q_2 ds \tag{5.5.3}$$

$$\begin{aligned} 0 = \int_{\Omega_e} \Bigg\{ & w_3 m_{33} \frac{\partial^2 w_0}{\partial t^2} + \frac{\partial w_3}{\partial x} \left( Q_x^s + Q_x^a \right) + \frac{\partial w_3}{\partial y} \left( Q_y^s + Q_y^a \right) \\ & + \frac{\partial w_3}{\partial x} \left[ N_{xx} \frac{\partial w_0}{\partial x} + \frac{1}{2} \left( N_{xy} + N_{yx} \right) \frac{\partial w_0}{\partial y} \right] + \frac{\partial w_3}{\partial y} \left[ N_{yy} \frac{\partial w_0}{\partial y} + \frac{1}{2} \left( N_{xy} + N_{yx} \right) \frac{\partial w_0}{\partial x} \right] \\ & - w_3 q_0 \Bigg\} dxdy - \int_{\tau_e} w_3 Q_3 ds \end{aligned} \tag{5.5.4}$$

$$0 = \int_{\Omega_e} \left\{ w_4 m_{44} \frac{\partial^2 \phi_x}{\partial t^2} + w_4 m_{45} \frac{\partial^2 \psi_y}{\partial t^2} + \frac{\partial w_4}{\partial x} M_{xx} + \frac{\partial w_4}{\partial y} M_{yx} + w_4 (Q_x^s - Q_x^a) \right\} dxdy - \int_{\tau_e} w_4 Q_4 ds \tag{5.5.5}$$

$$0 = \int_{\Omega_e} \left\{ w_5 m_{55} \frac{\partial^2 \psi_y}{\partial t^2} + w_5 m_{45} \frac{\partial^2 \phi_x}{\partial t^2} + \frac{\partial w_5}{\partial x} P_{xy} + \frac{\partial w_5}{\partial y} P_{yy} + 2 w_5 Q_x^a \right\} dxdy - \int_{\tau_e} w_5 Q_5 ds \tag{5.5.6}$$

$$0 = \int_{\Omega_e} \left\{ w_6 m_{66} \frac{\partial^2 \phi_y}{\partial t^2} + w_6 m_{67} \frac{\partial^2 \psi_x}{\partial t^2} + \frac{\partial w_6}{\partial x} M_{xy} + \frac{\partial w_6}{\partial y} M_{yy} + w_6 (Q_y^s - Q_y^a) \right\} dxdy - \int_{\tau_e} w_6 Q_6 ds \tag{5.5.7}$$

$$0 = \int_{\Omega_e} \left\{ w_7 m_{77} \frac{\partial^2 \psi_x}{\partial t^2} + w_7 m_{67} \frac{\partial^2 \phi_y}{\partial t^2} + \frac{\partial w_7}{\partial x} P_{xx} + \frac{\partial w_7}{\partial y} P_{yx} - 2 w_7 Q_y^a \right\} dxdy - \int_{\tau_e} w_7 Q_7 ds \tag{5.5.8}$$

After using the constitutive equations (12) and (13) along with the interpolations of the primary variables and weight functions (5.5.1) in the above equations, we have the following finite element formulation on a typical element:

$$\mathbf{M}^{(\mathbf{e})}\ddot{\mathfrak{U}}^{(\mathbf{e})} + \mathbf{K}^{(\mathbf{e})}\mathfrak{U}^{(\mathbf{e})} = \mathbf{F}^{(\mathbf{e})} \tag{5.5.9}$$

where,

$$\mathbf{M}^{(\mathbf{e})} = \begin{bmatrix} \mathbf{M^{11}} & \mathbf{M^{12}} & \mathbf{M^{13}} & \mathbf{M^{14}} & \mathbf{M^{15}} & \mathbf{M^{16}} & \mathbf{M^{17}} \\ \mathbf{M^{21}} & \mathbf{M^{22}} & \mathbf{M^{23}} & \mathbf{M^{24}} & \mathbf{M^{25}} & \mathbf{M^{26}} & \mathbf{M^{27}} \\ \mathbf{M^{31}} & \mathbf{M^{32}} & \mathbf{M^{33}} & \mathbf{M^{34}} & \mathbf{M^{35}} & \mathbf{M^{36}} & \mathbf{M^{37}} \\ \mathbf{M^{41}} & \mathbf{M^{42}} & \mathbf{M^{43}} & \mathbf{M^{44}} & \mathbf{M^{45}} & \mathbf{M^{46}} & \mathbf{M^{47}} \\ \mathbf{M^{51}} & \mathbf{M^{52}} & \mathbf{M^{53}} & \mathbf{M^{54}} & \mathbf{M^{55}} & \mathbf{M^{56}} & \mathbf{M^{57}} \\ \mathbf{M^{61}} & \mathbf{M^{62}} & \mathbf{M^{63}} & \mathbf{M^{64}} & \mathbf{M^{65}} & \mathbf{M^{66}} & \mathbf{M^{67}} \\ \mathbf{M^{71}} & \mathbf{M^{72}} & \mathbf{M^{73}} & \mathbf{M^{74}} & \mathbf{M^{75}} & \mathbf{M^{76}} & \mathbf{M^{77}} \end{bmatrix}^{(e)} \tag{5.5.10}$$

$$\mathbf{K}^{(\mathbf{e})} = \begin{bmatrix} \mathbf{K^{11}} & \mathbf{K^{12}} & \mathbf{K^{13}} & \mathbf{K^{14}} & \mathbf{K^{15}} & \mathbf{K^{16}} & \mathbf{K^{17}} \\ \mathbf{K^{21}} & \mathbf{K^{22}} & \mathbf{K^{23}} & \mathbf{K^{24}} & \mathbf{K^{25}} & \mathbf{K^{26}} & \mathbf{K^{27}} \\ \mathbf{K^{31}} & \mathbf{K^{32}} & \mathbf{K^{33}} & \mathbf{K^{34}} & \mathbf{K^{35}} & \mathbf{K^{36}} & \mathbf{K^{37}} \\ \mathbf{K^{41}} & \mathbf{K^{42}} & \mathbf{K^{43}} & \mathbf{K^{44}} & \mathbf{K^{45}} & \mathbf{K^{46}} & \mathbf{K^{47}} \\ \mathbf{K^{51}} & \mathbf{K^{52}} & \mathbf{K^{53}} & \mathbf{K^{54}} & \mathbf{K^{55}} & \mathbf{K^{56}} & \mathbf{K^{57}} \\ \mathbf{K^{61}} & \mathbf{K^{62}} & \mathbf{K^{63}} & \mathbf{K^{64}} & \mathbf{K^{65}} & \mathbf{K^{66}} & \mathbf{K^{67}} \\ \mathbf{K^{71}} & \mathbf{K^{72}} & \mathbf{K^{73}} & \mathbf{K^{74}} & \mathbf{K^{75}} & \mathbf{K^{76}} & \mathbf{K^{77}} \end{bmatrix}^{(e)} \tag{5.5.11}$$

$$\ddot{\mathfrak{U}}^{(\mathbf{e})} = \begin{Bmatrix} \ddot{\mathbf{U}} \\ \ddot{\mathbf{V}} \\ \ddot{\mathbf{W}} \\ \ddot{\boldsymbol{\Phi}}\boldsymbol{x} \\ \ddot{\boldsymbol{\Psi}}\boldsymbol{y} \\ \ddot{\boldsymbol{\Phi}}\boldsymbol{y} \\ \ddot{\boldsymbol{\Psi}}\boldsymbol{x} \end{Bmatrix}^{(e)} \qquad \mathfrak{U}^{(\mathbf{e})} = \begin{Bmatrix} \mathbf{U} \\ \mathbf{V} \\ \mathbf{W} \\ \boldsymbol{\Phi}\boldsymbol{x} \\ \boldsymbol{\Psi}\boldsymbol{y} \\ \boldsymbol{\Phi}\boldsymbol{y} \\ \boldsymbol{\Psi}\boldsymbol{x} \end{Bmatrix}^{(e)} \qquad \mathbf{F}^{(\mathbf{e})} = \begin{Bmatrix} \mathbf{F^1} \\ \mathbf{F^2} \\ \mathbf{F^3} \\ \mathbf{F^4} \\ \mathbf{F^5} \\ \mathbf{F^6} \\ \mathbf{F^7} \end{Bmatrix}^{(e)} \tag{5.5.12}$$

The non-zero components of the above matrices are

$$K_{ij}^{11} = \int_{\Omega_e} \left( A_{11}\, {}^{11}S_{ij}^{xx} + A_{44}\, {}^{11}S_{ij}^{yy} \right) d\Omega, \qquad K_{ij}^{12} = \int_{\Omega_e} \left( A_{12}\, {}^{12}S_{ij}^{xy} + A_{34}\, {}^{12}S_{ij}^{yx} \right) d\Omega$$

$$K_{ij}^{13} = \int_{\Omega_e} \left\{ \frac{A_{11}}{2} \frac{\partial w_0}{\partial x}\, {}^{13}S_{ij}^{xx} + \frac{A_{12}}{2} \frac{\partial w_0}{\partial y}\, {}^{13}S_{ij}^{xy} + \left( \frac{A_{34} + A_{44}}{4} \right) \left( \frac{\partial w_0}{\partial x}\, {}^{13}S_{ij}^{xy} + \frac{\partial w_0}{\partial y}\, {}^{13}S_{ij}^{yx} \right) \right\} d\Omega$$

$$K_{ij}^{21} = \int_{\Omega_e} \left( A_{34}\, {}^{21}S_{ij}^{xy} + A_{12}\, {}^{21}S_{ij}^{yx} \right) d\Omega, \qquad K_{ij}^{22} = \int_{\Omega_e} \left( A_{33}\, {}^{22}S_{ij}^{xx} + A_{22}\, {}^{22}S_{ij}^{yy} \right) d\Omega$$

$$K_{ij}^{23} = \int_{\Omega_e} \left\{ \frac{A_{12}}{2} \frac{\partial w_0}{\partial x}\, {}^{23}S_{ij}^{yx} + \frac{A_{22}}{2} \frac{\partial w_0}{\partial y}\, {}^{23}S_{ij}^{yy} + \left( \frac{A_{33} + A_{34}}{4} \right) \left( \frac{\partial w_0}{\partial x}\, {}^{23}S_{ij}^{xy} + \frac{\partial w_0}{\partial y}\, {}^{23}S_{ij}^{xx} \right) \right\} d\Omega$$

$$K_{ij}^{31} = \int_{\Omega_e} \left\{ A_{11} \frac{\partial w_0}{\partial x}\, {}^{31}S_{ij}^{xx} + A_{12} \frac{\partial w_0}{\partial y}\, {}^{31}S_{ij}^{yx} + \left( \frac{A_{34} + A_{44}}{2} \right) \left( \frac{\partial w_0}{\partial x}\, {}^{31}S_{ij}^{yy} + \frac{\partial w_0}{\partial y}\, {}^{31}S_{ij}^{xy} \right) \right\} d\Omega$$

$$K_{ij}^{32} = \int_{\Omega_e} \left\{ A_{12} \frac{\partial w_0}{\partial x}\, {}^{32}S_{ij}^{xy} + A_{22} \frac{\partial w_0}{\partial y}\, {}^{32}S_{ij}^{yy} + \left( \frac{A_{33} + A_{34}}{2} \right) \left( \frac{\partial w_0}{\partial x}\, {}^{32}S_{ij}^{yx} + \frac{\partial w_0}{\partial y}\, {}^{32}S_{ij}^{xx} \right) \right\} d\Omega$$

$$\begin{aligned} K_{ij}^{33} = \int_{\Omega_e} \Bigg\{ & \left( G_{11} + 2G_{12} + G_{22} \right) {}^{33}S_{ij}^{xx} + \left( G_{33} + 2G_{34} + G_{44} \right) {}^{33}S_{ij}^{yy} \\ & + \frac{A_{11}}{2} \left( \frac{\partial w_0}{\partial x} \right)^2 {}^{33}S_{ij}^{xx} + \frac{A_{22}}{2} \left( \frac{\partial w_0}{\partial y} \right)^2 {}^{33}S_{ij}^{yy} \\ & + \frac{A_{12}}{4} \left[ \left( \frac{\partial w_0}{\partial x} \right)^2 {}^{33}S_{ij}^{yy} + \left( \frac{\partial w_0}{\partial y} \right)^2 {}^{33}S_{ij}^{xx} + \frac{\partial w_0}{\partial y} \frac{\partial w_0}{\partial x} \left( {}^{33}S_{ij}^{xy} + {}^{33}S_{ij}^{yx} \right) \right] \\ & + \left( \frac{A_{33} + A_{34}}{8} \right) \left[ \frac{\partial w_0}{\partial x} \frac{\partial w_0}{\partial y} \left( {}^{33}S_{ij}^{xy} + {}^{33}S_{ij}^{yx} \right) + \left( \frac{\partial w_0}{\partial y} \right)^2 {}^{33}S_{ij}^{xx} + \left( \frac{\partial w_0}{\partial x} \right)^2 {}^{33}S_{ij}^{yy} \right] \\ & + \left( \frac{A_{34} + A_{44}}{8} \right) \left[ \frac{\partial w_0}{\partial x} \frac{\partial w_0}{\partial y} \left( {}^{33}S_{ij}^{xy} + {}^{33}S_{ij}^{yx} \right) + \left( \frac{\partial w_0}{\partial y} \right)^2 {}^{33}S_{ij}^{yy} + \left( \frac{\partial w_0}{\partial x} \right)^2 {}^{33}S_{ij}^{xx} \right] \Bigg\} d\Omega \end{aligned}$$

$$K_{ij}^{34} = \int_{\Omega_e} \left( G_{11} - G_{22} \right) {}^{34}S_{ij}^{x0} d\Omega, \qquad K_{ij}^{35} = 2 \int_{\Omega_e} \left( G_{12} + G_{22} \right) {}^{35}S_{ij}^{x0} d\Omega$$

$$K_{ij}^{36} = \int_{\Omega_e} \left( G_{33} - G_{44} \right) {}^{36}S_{ij}^{y0} d\Omega, \qquad K_{ij}^{37} = -2 \int_{\Omega_e} \left( G_{34} + G_{44} \right) {}^{37}S_{ij}^{y0} d\Omega$$

$$K_{ij}^{43} = \int_{\Omega_e} \left( G_{11} - G_{22} \right) {}^{43}S_{ij}^{0x} d\Omega$$

$$K_{ij}^{44} = \int_{\Omega_e} \left( D_{11}\, {}^{44}S_{ij}^{xx} + D_{44}\, {}^{44}S_{ij}^{yy} + \left( G_{11} - 2G_{12} + G_{22} \right) {}^{44}S_{ij}^{00} \right) d\Omega$$

$$K_{ij}^{45} = 2\int_{\Omega_e} (G_{12} - G_{22})\, {}^{44}S_{ij}^{00} d\Omega, \qquad K_{ij}^{46} = \int_{\Omega_e} \left( D_{12}\, {}^{45}S_{ij}^{xy} + D_{34}\, {}^{45}S_{ij}^{yx} \right) d\Omega$$

$$K_{ij}^{53} = 2\int_{\Omega_e} (G_{12} + G_{22})\, {}^{53}S_{ij}^{0x} d\Omega \qquad K_{ij}^{54} = 2\int_{\Omega_e} (G_{12} - G_{22})\, {}^{54}S_{ij}^{00} d\Omega$$

$$K_{ij}^{55} = \int_{\Omega_e} \left( H_{33}\, {}^{55}S_{ij}^{xx} + H_{22}\, {}^{55}S_{ij}^{yy} + 4G_{22}\, {}^{55}S_{ij}^{00} \right) d\Omega, \qquad K_{ij}^{57} = \int_{\Omega_e} \left( H_{34}\, {}^{57}S_{ij}^{xy} + H_{12}\, {}^{57}S_{ij}^{yx} \right) d\Omega$$

$$K_{ij}^{63} = \int_{\Omega_e} (G_{33} - G_{44})\, {}^{63}S_{ij}^{0y} d\Omega, \qquad K_{ij}^{64} = \int_{\Omega_e} \left( D_{34}\, {}^{64}S_{ij}^{xy} + D_{12}\, {}^{64}S_{ij}^{yx} \right) d\Omega$$

$$K_{ij}^{66} = \int_{\Omega_e} \left( D_{33}\, {}^{66}S_{ij}^{xx} + D_{22}\, {}^{66}S_{ij}^{yy} + (G_{33} - 2G_{34} + G_{44})\, {}^{66}S_{ij}^{00} \right) d\Omega$$

$$K_{ij}^{67} = 2\int_{\Omega_e} (G_{44} - G_{34})\, {}^{67}S_{ij}^{00} d\Omega, \quad K_{ij}^{73} = -2\int_{\Omega_e} (G_{34} + G_{44})\, {}^{73}S_{ij}^{0y} d\Omega$$

$$K_{ij}^{75} = \int_{\Omega_e} \left( H_{12}\, {}^{75}S_{ij}^{xy} + H_{34}\frac{\partial L_i^{(7)}}{\partial y}\, {}^{75}S_{ij}^{yx} \right) d\Omega$$

$$K_{ij}^{76} = 2\int_{\Omega_e} (G_{44} - G_{34})\, {}^{76}S_{ij}^{00} d\Omega, \qquad K_{ij}^{77} = \int_{\Omega_e} \left( H_{11}\, {}^{77}S_{ij}^{xx} + H_{44}\, {}^{77}S_{ij}^{yy} + 4G_{44}\, {}^{77}S_{ij}^{00} \right) d\Omega$$

Similarly the non-zero components of element mass matrix (5.5.10) are given by

$$M_{ij}^{11} = \int_{\Omega_e} m_{11}\, {}^{11}S_{ij}^{00} d\Omega, \quad M_{ij}^{22} = \int_{\Omega_e} m_{22}\, {}^{22}S_{ij}^{00} d\Omega, \quad M_{ij}^{33} = \int_{\Omega_e} m_{33}\, {}^{33}S_{ij}^{00} d\Omega$$

$$M_{ij}^{44} = \int_{\Omega_e} m_{44}\, {}^{44}S_{ij}^{00} d\Omega, \quad M_{ij}^{45} = \int_{\Omega_e} m_{45}\, {}^{45}S_{ij}^{00} d\Omega, \quad M_{ij}^{54} = \int_{\Omega_e} m_{45}\, {}^{54}S_{ij}^{00} d\Omega$$

$$M_{ij}^{55} = \int_{\Omega_e} m_{55}\, {}^{55}S_{ij}^{00} d\Omega, \quad M_{ij}^{66} = \int_{\Omega_e} m_{66}\, {}^{66}S_{ij}^{00} d\Omega, \quad M_{ij}^{67} = \int_{\Omega_e} m_{67}\, {}^{67}S_{ij}^{00} d\Omega$$

$$M_{ij}^{76} = \int_{\Omega_e} m_{67}\, {}^{76}S_{ij}^{00} d\Omega, \quad M_{ij}^{77} = \int_{\Omega_e} m_{77}\, {}^{77}S_{ij}^{00} d\Omega$$

where we have used the notation

$$ {}^{IJ}S_{ij}^{ab} = \frac{\partial L_i^{(I)}}{\partial a}\frac{\partial L_j^{(J)}}{\partial b}, \quad {}^{IJ}S_{ij}^{0b} = L_i^{(I)}\frac{\partial L_j^{(J)}}{\partial b}, \quad {}^{IJ}S_{ij}^{a0} = \frac{\partial L_i^{(I)}}{\partial a}L_j^{(J)}, \quad {}^{IJ}S_{ij}^{00} = L_i^{(I)}L_j^{(J)} $$

where $I, J = \{1, 2, 3, 4, 5, 6, 7\}$, $i, j = \{1, 2, 3, 4\}$ and $a, b = \{x, y\}$.

### 5.5.1 Solution of nonlinear equations

Although the nonlinear finite element equations (5.5.9) can be used to solve time-dependent cases with appropriate time discretization schemes, in the present study we only consider time-independent nonlinear cases. For the time-independent nonlinear case the finite element equations (5.5.9) are solved using Newton's iterative procedure [100], by constructing the tangent stiffness of a typical element at the beginning of $r^{th}$ iteration as

$$ \mathbf{T}^{(\mathbf{e})(r)} = \left[\frac{\partial \mathbf{R}^{(\mathbf{e})}}{\partial \mathfrak{U}^{(\mathbf{e})}}\right]^{(r-1)} \tag{5.5.13} $$

such that

$$ \mathbf{T}^{(\mathbf{e})(r)}\Delta\mathfrak{U}^{\mathbf{e}} = -\mathbf{R}^{(\mathbf{e})(r-1)} \tag{5.5.14} $$

where

$$ \mathbf{R}^{(\mathbf{e})} = \mathbf{K}^{(\mathbf{e})}(\mathfrak{U}^{(\mathbf{e})})\mathfrak{U}^{(\mathbf{e})} - \mathbf{F}^{(\mathbf{e})} \quad \text{and} \quad \Delta\mathfrak{U}^{(\mathbf{e})} = \mathfrak{U}^{(\mathbf{e})(r)} - \mathfrak{U}^{(\mathbf{e})(r-1)} $$

The explicit expressions of the components of the element tangent stiffness matrix are

$$ T_{ij}^{IJ} = K_{ij}^{IJ} $$

except for the following terms

$$T_{ij}^{13} = 2K_{ij}^{13}, \quad T_{ij}^{23} = 2K_{ij}^{23}$$

$$\begin{aligned}
T_{ij}^{33} &= K_{ij}^{33} \\
&+ \int_{\Omega_e} \left\{ A_{11} \frac{\partial u_0}{\partial x} {}^{33}S_{ij}^{xx} + A_{12} \frac{\partial u_0}{\partial x} {}^{33}S_{ij}^{yy} + \left( \frac{A_{34} + A_{44}}{2} \right) \left( \frac{\partial u_0}{\partial y} {}^{33}S_{ij}^{xy} + \frac{\partial u_0}{\partial y} {}^{33}S_{ij}^{yx} \right) \right\} d\Omega \\
&+ \int_{\Omega_e} \left\{ A_{12} \frac{\partial v_0}{\partial y} {}^{33}S_{ij}^{xx} + A_{22} \frac{\partial v_0}{\partial y} {}^{33}S_{ij}^{yy} + \left( \frac{A_{33} + A_{34}}{2} \right) \left( \frac{\partial v_0}{\partial x} {}^{33}S_{ij}^{xy} + \frac{\partial v_0}{\partial x} {}^{33}S_{ij}^{yx} \right) \right\} d\Omega \\
&+ \int_{\Omega_e} \left\{ A_{11} \left( \frac{\partial w_0}{\partial x} \right)^2 {}^{33}S_{ij}^{xx} + A_{22} \left( \frac{\partial w_0}{\partial y} \right)^2 {}^{33}S_{ij}^{yy} \right. \\
&+ \left( \frac{A_{12} + A_{34}}{4} + \frac{A_{33} + A_{44}}{8} \right) \left[ \left( \frac{\partial w_0}{\partial x} \right)^2 {}^{33}S_{ij}^{yy} + \left( \frac{\partial w_0}{\partial y} \right)^2 {}^{33}S_{ij}^{xx} \right] \\
&\left. + \left( \frac{A_{12} + A_{34}}{4} + \frac{A_{33} + A_{44}}{8} \right) \left[ 3 \frac{\partial w_0}{\partial y} \frac{\partial w_0}{\partial x} \left( {}^{33}S_{ij}^{xy} + {}^{33}S_{ij}^{yx} \right) \right] \right\} d\Omega
\end{aligned}$$

After the element equations are computed, they can be assembled according to the nodal connectivity of the mesh to obtain global equations. Boundary conditions are imposed on the global equations and subsequent equations are solved to obtain the global incremental generalized displacement vector $\Delta\mathfrak{U}$ at the end of $r^{th}$ iteration. The normalized difference between solution vectors from two consecutive iterations, measured with Euclidean norm, is computed at the end of each iteration. If the value computed is less than a preselected tolerance '$tol$' further iterations are terminated and nonlinear convergence is assumed (for all the nonlinear cases considered we chose $tol = 10^{-3}$)

$$\sqrt{\frac{\Delta\mathfrak{U} \cdot \Delta\mathfrak{U}}{\mathfrak{U}^{(r)} \cdot \mathfrak{U}^{(r)}}} \leqslant tol$$

Once the nonlinear convergence is attained, the final global generalized displacement vector is obtained using

$$\mathfrak{U}^{(r)} = \Delta\mathfrak{U} + \mathfrak{U}^{(r-1)} \tag{5.5.15}$$

### 5.5.2 Natural vibration frequencies

In the present study we will only consider the natural frequencies of the lattice plates undergoing linear free vibrations. The natural frequencies can be calculated by solving the eigenvalue problem obtained by substituting $\mathfrak{U}(x, y, t) = \mathfrak{U}_\circ(x, y)e^{j\lambda t}$ (where $j = \sqrt{-1}$) into the assembled linear global equations (i.e., nonlinear terms in coefficient matrices are ignored) after the imposition of boundary conditions. Here $\mathfrak{U}_\circ$ is the global mode shape corresponding to the eigenvalue $\lambda^2$. Once the eigenvalues are obtained the natural frequencies [Hz] are calculated using

$$f_i = \frac{\lambda}{2\pi} \tag{5.5.16}$$

It should be noted that the number of eigenvalues obtained will be equal to the number of degrees of freedom in the problem. Thus for the convergence of higher mode shapes a finer mesh is required compared to the lower mode shapes.

### 5.5.3 Shear and membrane locking

In chapter 3 we used higher order interpolation functions on all the primary variables to eliminate locking in micropolar plates. In this chapter we shall use linear interpolation on all the primary variables and employ reduced integration technique to eliminate shear and membrane locking. Since linear Lagrange interpolation functions are used in the approximation of all the primary variables, the elements become excessively stiff in the thin plate limit because of spurious constraints imposed on the bending energy due to this inconsistent interpolation, resulting in a phenomenon known as *shear locking* [108, 100, 93]. Consider a plate of dimensions $(a \times b)$ being modeled by a single rectangular element. Since linear interpolations are used on both $w_0$ and $\phi_x$,

if $(w_{01}, w_{02}, w_{03}, w_{04})$ and $(\phi_{x1}, \phi_{x2}, \phi_{x3}, \phi_{x4})$ are the nodal values of $w_0$ and $\phi_x$ respectively, we have

$$w_0 = w_{01}\left(1-\frac{x}{a}\right)\left(1-\frac{y}{b}\right) + w_{02}\frac{x}{a}\left(1-\frac{y}{b}\right) + w_{03}\frac{x}{a}\frac{y}{b} + w_{04}\left(1-\frac{x}{a}\right)\frac{y}{b}$$
$$\phi_x = \phi_{x1}\left(1-\frac{x}{a}\right)\left(1-\frac{y}{b}\right) + \phi_{x2}\frac{x}{a}\left(1-\frac{y}{b}\right) + \phi_{x3}\frac{x}{a}\frac{y}{b} + \phi_{x4}\left(1-\frac{x}{a}\right)\frac{y}{b}$$

$$\gamma_x^s = \left(\frac{w_{02}-w_{01}+a\phi_{x1}}{a}\right) + \left(\frac{\phi_{x1}-\phi_{x2}+\phi_{x3}-\phi_{x4}}{ab}\right)xy + \left(\frac{\phi_{x2}-\phi_{x1}}{a}\right)x + \left(\frac{w_{01}-w_{02}+w_{03}-w_{04}+a\phi_{x4}-a\phi_{x1}}{ab}\right)y$$

In the thin plate limit $\gamma_x^{(s)}$ approaches zero and this only possible when the constant terms and coefficients of $x$, $y$ and $xy$ of $\gamma_x^{(s)}$ are all zero. That is,

$$\frac{w_{01}-w_{02}}{a} = \phi_{x1} \tag{5.5.17}$$
$$\frac{w_{03}-w_{04}}{a} = \phi_{x4} \tag{5.5.18}$$
$$\phi_{x1} = \phi_{x2}, \qquad \phi_{x3} = \phi_{x4} \tag{5.5.19}$$

However, Eq. (5.5.19) implies that $\phi_x$ is constant with respect to $x$ and this will pose an unnecessary restriction on bending energy which will manifest as shear locking. A similar argument can be extended to antisymmetric shear strains as well. Various remedies have been proposed in the literature to overcome shear locking, see, for example, [108, 109] and [103]. In the present finite element formulation we use selective reduced integration to overcome the shear locking. That is, we will evaluate the stiffness coefficient terms corresponding to symmetric and antisymmetric shear strains using reduced Gauss quadrature rule [93, 100].

With the addition of von Kármán nonlinearity, bending-stretching coupling is introduced into the plate thereby predicting membrane strain even when only bending forces are applied. But in the cases where the membrane (axial) strains are not physically possible in the plate (example, when

all the edges are hinge-supported) the theory will still predict membrane strains. This phenomenon is called *membrane locking* [100]. To overcome this we will use reduced integration on all the nonlinear terms of the element coefficient matrices.

## 5.6 Numerical examples

3-D finite element models for web-core and pyramid core sandwich panels are discussed in Section 4.1. These FE models are built using Abaqus 2019 to provide reference solutions to which the 2-D results can be compared.

In section 5.6.2, we first study the convergence of the finite element calculations by considering the linear static bending of a simply-supported web-core sandwich panel under line and uniformly distributed loads. Second, the nonlinear bending of simply-supported web-core panels is investigated for the same loads. Third, we consider the nonlinear bending of web-core panels that have clamped and free edges as well.

The web-core lattice is bending-dominated, whereas the pyramid core is stretch-dominated, meaning that the struts of the core do not essentially bend but carry only axial loads, that is, they behave as axial rods. It has been shown earlier for lattice core beams that stretch-dominated cores do not exhibit global nonlinear bending but rather go straight from linear bending to local buckling where individual unit cells basically collapse near supports or point loads [5]. This type of local buckling behavior is not captured by the current plate model, or by any other 2-D ESL-FSDT plate model to the best of our knowledge. In conclusion, in the case of the pyramid core sandwich panels, we focus only the linear natural vibration frequency calculations in this study. The natural frequencies of both the pyramid core and web-core plate are studied in section 5.6.3.

### 5.6.1 Plate dimensions and 3-D FE reference models

For the web-core plate two different size plates will be considered; the plate planform area is $(a \times b)$ m$^2$ and the studied sizes are $(5.4 \times 3.6)$ m$^2$ for bending and $(1.8 \times 1.2)$ m$^2$ for natural frequency calculations. The other relevant dimensions are given in Fig. 5.1. The corresponding 3-D FE reference model for the larger plate consists of 453600 shell elements of type S8R5 and

the smaller one contains 141000 shell elements of type S4R. A pyramid core plate of size $(1 \times 1)$ $m^2$ is considered in the natural frequency calculations. The corresponding 3-D FE reference model consists of 9600 linear beam elements of type B33, 33885 quadrilateral shell elements of type S8R5 and 1002 triangular elements of type STRI65. All the 3-D FE models are convergent.

The 3-D boundary conditions are imposed in a similar manner as in classical simply-supported, clamped and free edge 3-D solid plate problems. For simply-supported edges, for all nodes $i = 1, 2, \ldots, n$ of the shell elements on edges $x = (-a/2, a/2)$ (see Fig. 2) we use $U_z^i = U_y^i = Rot_x^i = 0$ with reference to the global coordinate system. Analogously, for all nodes on edges $y = (-b/2, b/2)$ we use $U_z^i = U_x^i = Rot_y^i = 0$. For clamped edges we have $U_x^i = U_y^i = U_z^i = Rot_x^i = Rot_y^i = Rot_z^i = 0$. No boundary conditions are set on free edges.

### 5.6.2 Bending analysis

For the bending analysis of the 2-D micropolar ESL-FSDT plates the coordinate system is chosen such that the center of the plate coincides with the origin as shown in Fig. 5.2. For the web-core plates the webs are parallel to the $y-$axis. Four sets of boundary conditions are considered:

1. Simply-supported on all edges (SSSS).

2. Edges parallel to $x$-axis are clamped and edges parallel to $y$-axis are simply supported (CSCS).

3. All edges are clamped (CCCC).

4. Edges parallel to $x$-axis are free and edges parallel to $y$-axis are clamped (CFCF).

Furthermore, for each boundary condition case the plate is subjected to two different loadings, a uniformly distributed load and a line load along the $y$-axis at the center of the plate. Since the boundary and loading conditions considered here result in symmetry about $x$- and $y$-axes, we consider only the quarter plate lying in the first quadrant as the computational domain (see Fig. 5.2). For such a computational domain the considered boundary conditions after symmetry arguments are listed in Table 5.6. It should be noted that for web-core plates the center web is along $y$-axis

and for the line load case only half of the total load intensity on the full plate is to be considered on the computational domain. Unless stated otherwise all the loads listed in this study are on full plate.

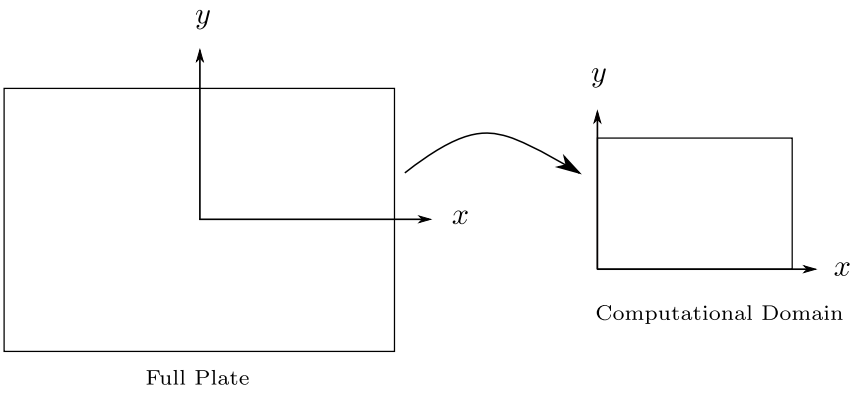


Figure 5.2: Choice of computational domain for the bending analysis under considered boundary and loading conditions.

Table 5.6: Various boundary conditions on the computational domain for bending analysis.

| | SSSS | CSCS | CCCC | CFCF |
|---|---|---|---|---|
| $y = 0$ | $v_0 = \phi_y = \psi_x = 0$ | $v_0 = \phi_y = \psi_x = 0$ | $v_0 = \phi_y = \psi_x = 0$ | $v_0 = \phi_y = \psi_x = 0$ |
| $y = b/2$ | $u_0 = w_0 = \phi_x = \psi_y = 0$ | $u_0 = v_0 = w_0 = \phi_x = \psi_y = \phi_y = \psi_x = 0$ | $u_0 = v_0 = w_0 = \phi_x = \psi_y = \phi_y = \psi_x = 0$ | $N_{yx} = N_{yy} = Q_y^{(s)} + Q_y^{(a)} = M_{yx} = P_{yy} = M_{yy} = P_{yx} = 0$ |
| $x = 0$ | $u_0 = \phi_x = \psi_y = 0$ | $u_0 = \phi_x = \psi_y = 0$ | $u_0 = \phi_x = \psi_y = 0$ | $u_0 = \phi_x = \psi_y = 0$ |
| $x = a/2$ | $v_0 = w_0 = \phi_y = \psi_x = 0$ | $v_0 = w_0 = \phi_y = \psi_x = 0$ | $u_0 = v_0 = w_0 = \phi_x = \psi_y = \phi_y = \psi_x = 0$ | $u_0 = v_0 = w_0 = \phi_x = \psi_y = \phi_y = \psi_x = 0$ |
| $(0, 0)$ | $u_0 = v_0 = \phi_x = \psi_y = \phi_y = \psi_x = 0$ | $u_0 = v_0 = \phi_x = \psi_y = \phi_y = \psi_x = 0$ | $u_0 = v_0 = \phi_x = \psi_y = \phi_y = \psi_x = 0$ | $u_0 = v_0 = \phi_x = \psi_y = \phi_y = \psi_x = 0$ |
| $(a/2, 0)$ | $v_0 = w_0 = \phi_y = \psi_x = 0$ | $v_0 = w_0 = \phi_y = \psi_x = 0$ | $u_0 = v_0 = w_0 = \phi_x = \psi_y = \phi_y = \psi_x = 0$ | $u_0 = v_0 = w_0 = \phi_x = \psi_y = \phi_y = \psi_x = 0$ |
| $(0, b/2)$ | $u_0 = w_0 = \phi_x = \psi_y = 0$ | $u_0 = v_0 = w_0 = \phi_x = \psi_y = \phi_y = \psi_x = 0$ | $u_0 = v_0 = w_0 = \phi_x = \psi_y = \phi_y = \psi_x = 0$ | $u_0 = \phi_x = \psi_y = 0$ |
| $(a/2, b/2)$ | $u_0 = v_0 = w_0 = \phi_x = \psi_y = \phi_y = \psi_x = 0$ | $u_0 = v_0 = w_0 = \phi_x = \psi_y = \phi_y = \psi_x = 0$ | $u_0 = v_0 = w_0 = \phi_x = \psi_y = \phi_y = \psi_x = 0$ | $u_0 = v_0 = w_0 = \phi_x = \psi_y = \phi_y = \psi_x = 0$ |

A mesh of $32 \times 32$ equal sized rectangular elements on the computational domain was found to give convergent results with respect to the transverse deflection. The mesh convergence results with respect to the linear transverse deflections of web-core lattice plates of size $(5.4 \times 3.6)$ m$^2$ and for various face thickness, $t_f$, subjected to SSSS boundary conditions are given in Fig. 5.3. The error in maximum transverse deflection is calculated using

$$\Delta w_0^{max} = 100 \times \left( \frac{w_0^{max(\text{Nav})} - w_0^{max(\text{present FE})}}{w_0^{max(\text{Nav})}} \right),$$

where $w_0^{max(\text{Nav})}$ is the Navier solution to the 2-D micropolar ESL-FSDT plate [9].

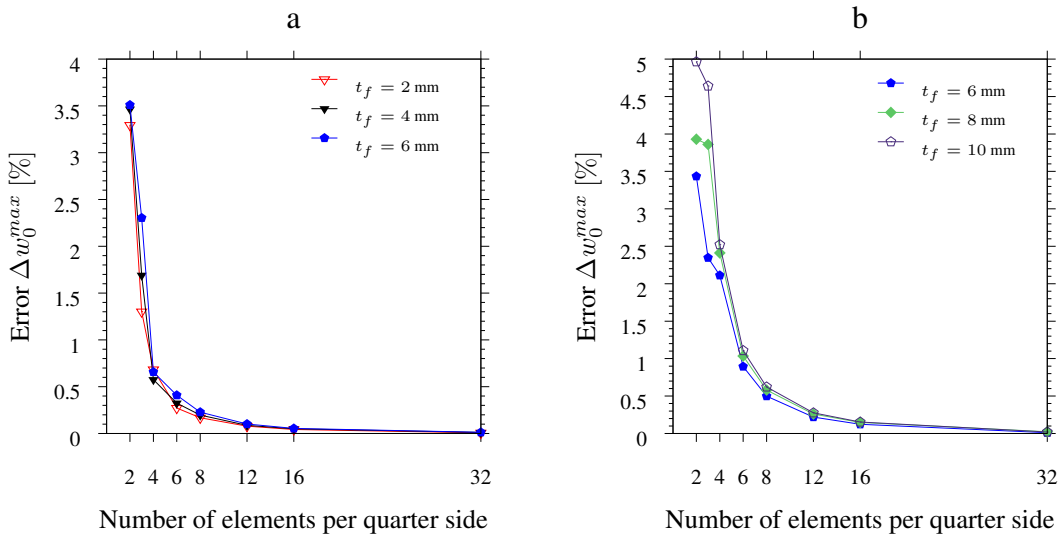


Figure 5.3: Mesh convergence with respect to maximum transverse deflection $w_0^{max}$ for linear analysis on quarter domain of $(5.4 \times 3.6)$ m$^2$ web-core plates subjected to SSSS boundary conditions. (a) Uniformly distributed load of $10000$ N/m$^2$ (b) Line load of $10000$ N/m along the $y-$axis [6].

Fig. 5.4(a) gives a comparison between the linear transverse deflections of a $(5.4 \times 3.6)$ m$^2$ web-core plate having face thickness $t_f = 6$ mm, modeled as ESL-FSDT plate based on micropolar elasticity and ESL-FSDT plate based on classical elasticity for uniformly distributed load, while Fig. 5.4(b) shows the comparison for a line load along $y$-axis. The linear transverse deflections are obtained using the Navier solution [9, 107]. It can be seen that for the uniformly distributed load the two ESL theories give almost the same transverse deflections but for the line load they deviate from each other. It was shown by [9] that the micropolar model predicts the transverse deflections of a line-loaded web-core plate accurately, whereas the classical ESL-FSDT plate yielded displacement errors of 34–175% for face thicknesses of 2–10 mm. Further, Fig. 5.4 also shows the comparison between the nonlinear transverse deflections of the 3-D FE web-core

plate (Abaqus) and the corresponding 2-D micropolar plate (present finite element). It can be seen that the present finite element model is able to accurately predict the transverse deflections in both uniformly distributed and line load cases.

To further test the reliability of micropolar ESL-FSDT plate model and the nonlinear finite element formulation based on it, linear and nonlinear transverse deflections of a $(5.4 \times 3.6)$ m$^2$ web-core plate having face thickness $t_f = 4$ mm subjected to CSCS boundary conditions and a $(5.4 \times 3.6)$ m$^2$ web-core plate having face thickness $t_f = 6$ mm subjected to CCCC boundary conditions are presented in Fig. 5.5 for both uniformly distributed load and line load cases. Moreover, the nonlinear results are compared with the nonlinear results obtained from the 3-D FE analysis of these web-core plates in Abaqus. Excellent agreement between the 2-D micropolar and 3-D reference solutions is observed.

Finally, we consider the $(5.4 \times 3.6)$ m$^2$ web-core plate with CFCF boundary conditions. In Fig. 5.6(a), web-core plates with face thicknesses $t_f = 6$ mm and $t_f = 10$ mm subjected to a uniformly distributed load are considered, while in Fig. 5.6(b) the same plates are under a line load along y-axis (cf. Fig. 2). The present 2-D nonlinear finite element model slightly underpredicts the deflections at high load intensities in this case. This maybe due to the fact that Abaqus uses complete Green strain tensor while in the present nonlinear formulation we only considered von Kármán nonlinear terms. Thus at very high load intensities the von Kármán nonlinearity may not be an adequate choice for estimating the global deflections.

It is worth noting that only 1024 isoparametric linear rectangular elements based on Lagrange interpolation functions are used on the computational domain in the 2-D micropolar bending analysis of the $(5.4 \times 3.6)$ m$^2$ web-core lattice plate, while the complete 3-D FE analysis uses 453600 shell elements of type S8R5 as pointed out earlier. Thus, the present finite element model is computationally very efficient in obtaining the global response of lattice plates.

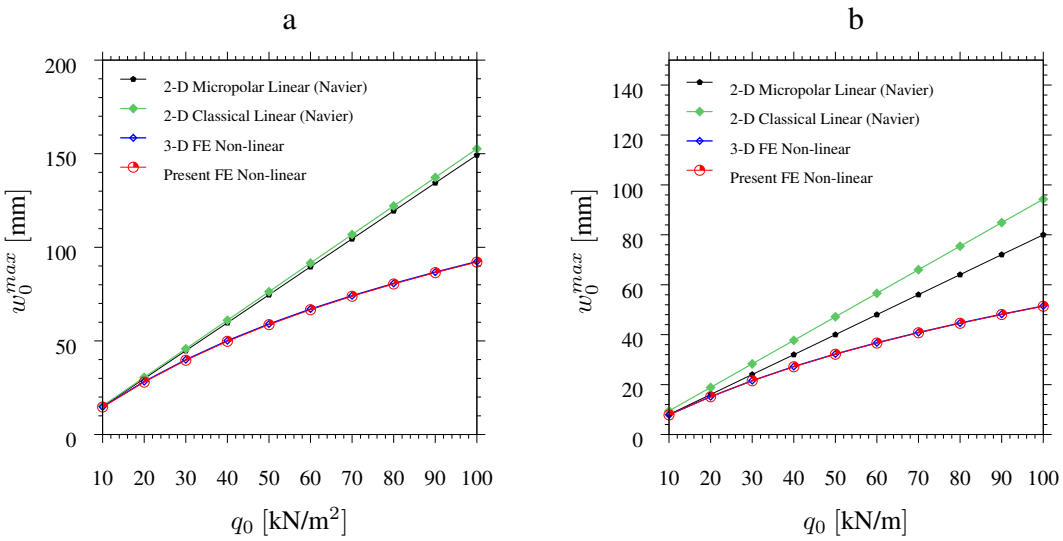


Figure 5.4: Load vs maximum deflection of $(5.4 \times 3.6)$ m$^2$ web-core plate ($t_f = 6$ mm) under SSSS boundary conditions. The linear solutions are computed using Navier solution. (a) Uniformly distributed load (b) Line load along y-axis [6].

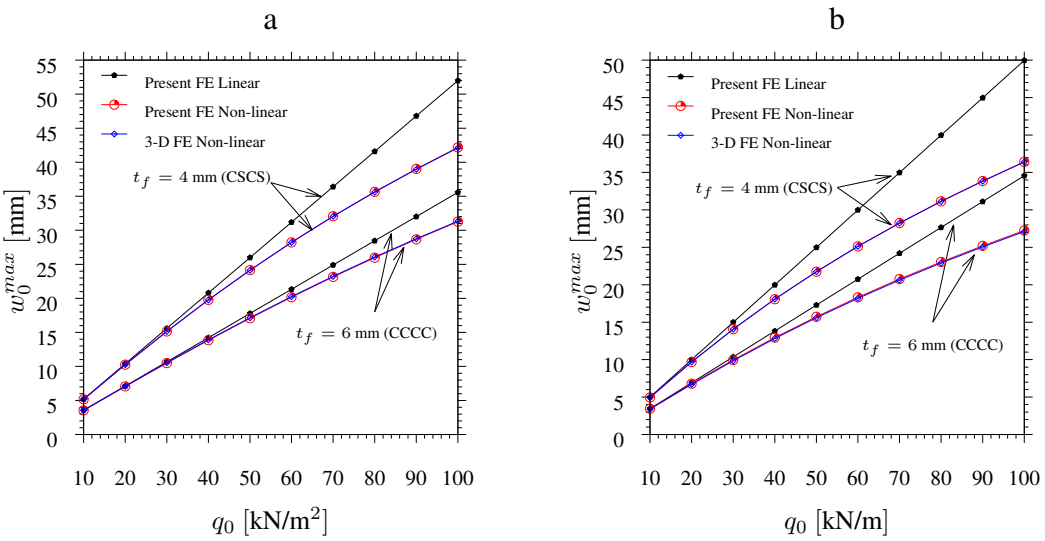


Figure 5.5: Load vs maximum deflections of $(5.4 \times 3.6)$ m$^2$ web-core plates with $t_f = 4$ mm subjected to CSCS boundary conditions and $t_f = 6$ mm subjected to CCCC boundary conditions. (a) Uniformly distributed load (a) Line load along y-axis [6].

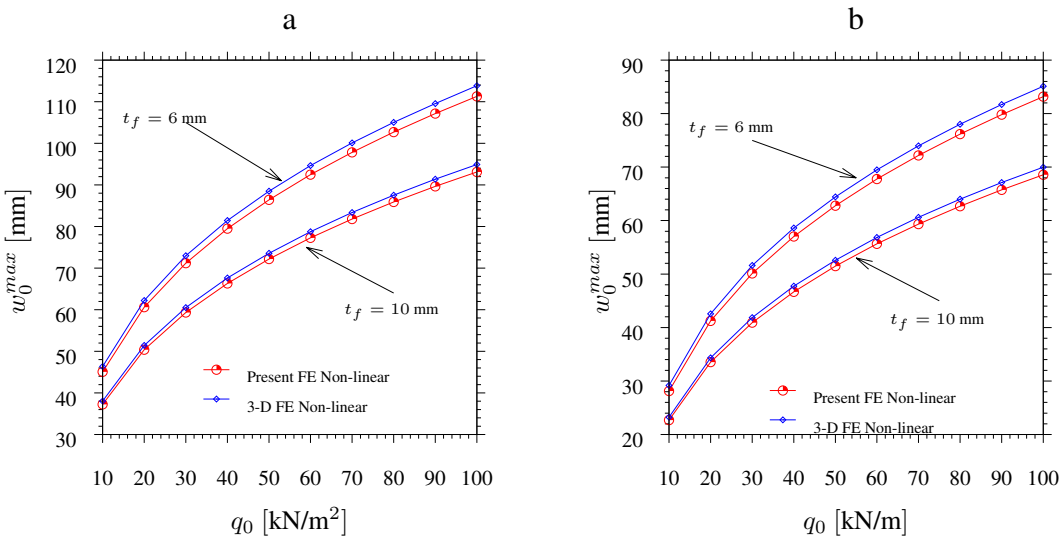


Figure 5.6: Load vs maximum deflections of $(5.4 \times 3.6)$ m$^2$ web-core plates with $t_f = 6$ mm and $t_f = 10$ mm subjected to CFCF boundary conditions. (a) Uniformly distributed load (b) Line load along y-axis[6].

### 5.6.3 Natural vibration frequencies

Here we will consider the free linear vibration analysis of both web-core and pyramid core lattice plates subjected to the same boundary conditions listed for the bending analysis. But it should be noted that the argument of symmetry cannot be used for the frequency analysis and, thus, the full plate has to be taken as the computational domain. For the linear free vibration analysis using the present finite element model, we ignore the nonlinear terms and consider only the linear terms in evaluating the element coefficient matrices.

In Figure 5.7, a comparison between the 3-D FE analysis and 2-D ESL-FSDT plates based on both classical and micropolar elasticity for the lowest eight natural frequencies of a pyramid core lattice plate of size $(1.0 \times 1.0)$ m$^2$ subjected to SSSS boundary conditions is given. The frequencies from ESL-FSDT micropolar plate model are obtained from the present finite element model while the frequencies of the 2-D classical ESL-FSDT plate are obtained using the Navier solution [9].

Both ESL-FSDT plate models provide accurate estimates for the fundamental vibration frequency $f_{1,1}$. However, as the mode number increases, the ESL-FSDT plate based on classical elasticity begins to under predict the frequencies while the ESL-FSDT plate based on micropolar elasticity still continues to predict the natural frequencies accurately.

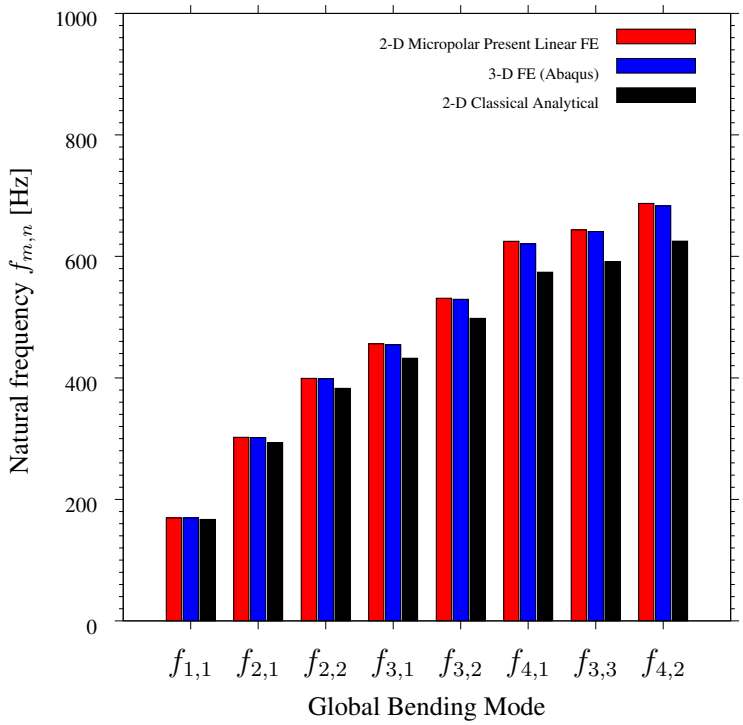


Figure 5.7: Eight lowest natural vibration frequencies of pyramid core plate of size $(1.0 \times 1.0)$ m$^2$ subjected to SSSS boundary conditions. In $f_{m,n}$, $m$ refers to the number of half waves in $x$-direction and $n$ gives the same for $y$-direction [6].

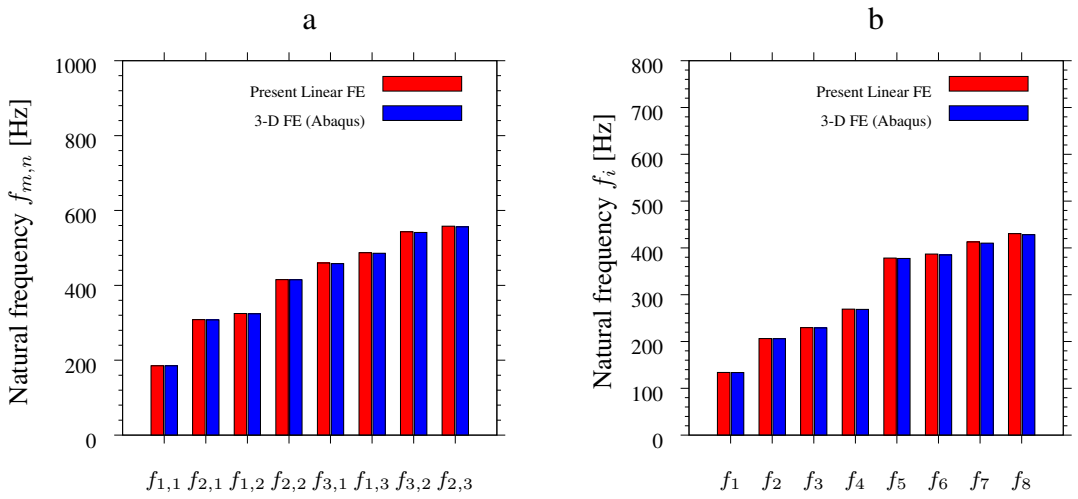


Figure 5.8: Eight lowest natural vibration frequencies of pyramid core plate of size $(1.0 \times 1.0)$ m$^2$. (a) CSCS boundary condition (b) all edges free (FFFF) [6].

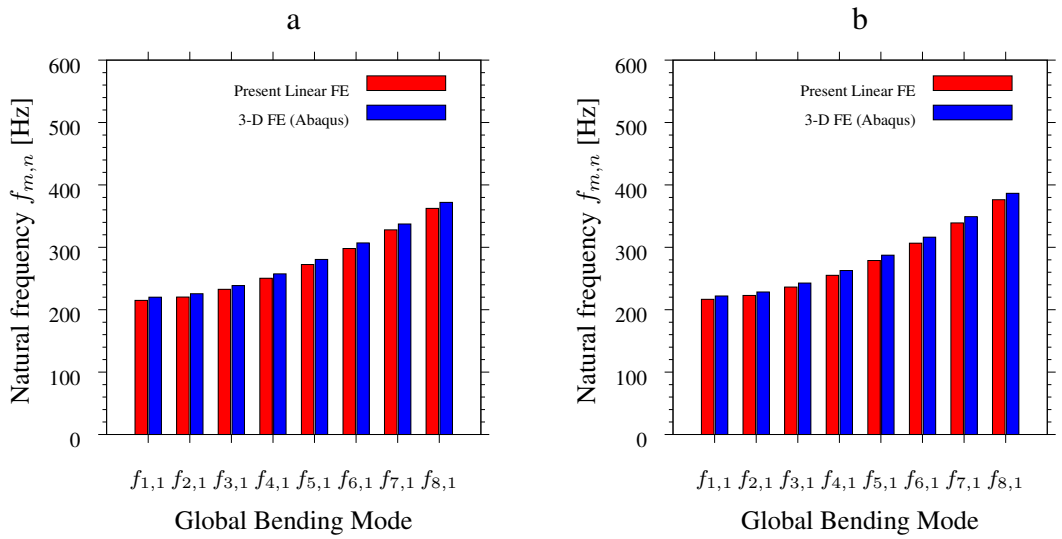


Figure 5.9: Eight lowest natural vibration frequencies of web-core ($t_f = 4$ mm) plate of size $(1.8 \times 1.2)$ m$^2$. (a) CSCS boundary condition (b) CCCC boundary condition [6].

A comparison between natural frequency results from 3-D FE analysis and from the present finite element formulation of pyramid core lattice plates of size $(1.0 \times 1.0)$ m$^2$ is given in Fig. 5.8 for CSCS boundary conditions and an unconstrained plate. Fig. 5.9 shows a comparison of 3-D FE results and results from the present finite element formulation for a web-core lattice plate of size $(1.8 \times 1.2)$ m$^2$ having face thickness $t_f = 4$ mm, subjected to CSCS and CCCC boundary conditions. The 2-D and 3-D results are in good agreement and the 2-D plate provides computationally efficient means for computing the global bending modes of both pyramid core and web-core sandwich panels.

# 6. DUAL MESH CONTROL DOMAIN METHOD FOR BENDING ANALYSIS OF FUNCTIONALLY GRADED BEAMS*

## 6.1 Introduction

In chapter 1 we introduced the dual mesh control domain method (DMCDM) and applied it to study 1-D axial bar. In this chapter we will apply the DMCDM to Euler-Bernoulli and Timoshenko beam theories. While for the bar problem each node of the mesh has only one degree of freedom, for the beam theories we have three degrees of freedom at each node. These degrees of freedom are axial displacement, transverse displacement and cross-sectional rotation for displacement models while axial displacement, transverse displacement and moment are the degrees of freedom for mixed models.

We consider through thickness functionally graded beams with constant Poisson's ration while the Young's modulus is assumed to vary with the thickness coordinate $z$ given by the following power-law variation [85, 110, 111]:

$$E(z) = (E_1 - E_2)f(z) + E_2, \quad f(z) = \left(\frac{1}{2} + \frac{z}{H}\right)^n \tag{6.1.1}$$

Here $E_1$ is the Young's modulus on the top face of the beam while $E_2$ is the Young's modulus on the bottom face of the beam. The thickness of the beam is $H$, while $n$ denote the power-law index which governs the material distribution through the thickness of the beam.

## 6.2 Governing equations of functionally graded beams

In this section we will review the governing equations Euler-Bernoulli beam theory and Timoshenko beam theory. Then we cast the governing equations in terms of axial displacement, transverse displacement and moment to facilitate the development of mixed dual mesh control domain

*Reprinted with permission from "A dual mesh finite domain method for the analysis of functionally graded beams" by J. N. Reddy and P. Nampally, 2020. Composite Structures, vol. 251, p. 112648, Copyright (2020) Elsevier Ltd.

method [10, 7]. The coordinate system used for the analysis of the beam is shown in Fig. 6.1

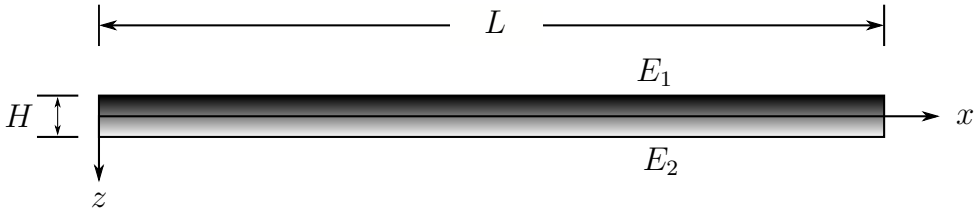


Figure 6.1: Functionally graded beam with the chosen coordinate system.

### 6.2.1 Euler-Bernoulli beam theory

The displacement filed of the Euler-Bernoulli beam theory is given by

$$\begin{aligned} u_1(x,y,z) &= u(x) - z\frac{dw}{dx} \\ u_2(x,y,z) &= 0 \\ u_3(x,y,z) &= w(x) \end{aligned} \tag{6.2.1}$$

The non-zero linear strains corresponding to this displacement field is given by

$$\varepsilon_{xx} = \frac{du}{dx} - z\frac{d^2w}{dx^2} = \varepsilon^0_{xx} + z\varepsilon^1_{xx} \tag{6.2.2}$$

while the constitutive relation for functionally graded beam with power-law variation of Young's modulus and constant Poisson's ration is given by

$$\sigma_{xx} = E(z)\varepsilon_{xx} \tag{6.2.3}$$

We further define the stress and moment resultant acting on the beam as follows:

$$N_{xx} = \int_A \sigma_{xx} dA = A_{xx}\frac{du}{dx} - B_{xx}\frac{d^2w}{dx^2} \tag{6.2.4a}$$

$$M_{xx} = \int_A \sigma_{xx} z dA = B_{xx}\frac{du}{dx} - D_{xx}\frac{d^2w}{dx^2} \tag{6.2.4b}$$

Here $A_{xx}$, $B_{xx}$, and $D_{xx}$ are the extensional, extensional-bending, and bending stiffness coefficients

$$(A_{xx}, B_{xx}, D_{xx}) = \int_A (1, z, z^2) E(z)\, dA \tag{6.2.5}$$

The governing differential equations of the beam can be obtained from the principle of virtual work, which for the functionally graded Euler-Bernoulli beam can be expressed as:

$$\int_0^L [N_{xx}\delta\varepsilon^0_{xx} + M_{xx}\delta\varepsilon^1_{xx}]dx - \int_0^L (f\delta u + q\delta w)dx = 0 \tag{6.2.6}$$

Taking the Euler-Lagrange equations of the variational statement (6.2.6) we obtain the governing differential equations of functionally graded Euler-Bernoulli beam as follows:

$$-\frac{dN_{xx}}{dx} - f = 0 \tag{6.2.7}$$

$$-\frac{d^2M_{xx}}{dx^2} - q = 0 \tag{6.2.8}$$

Now using the expressions for stress and moment resultants from Eqs. (6.2.4a)-(6.2.4b), we can write the governing equations as

$$-\frac{d}{dx}\left(A_{xx}\frac{du}{dx} - B_{xx}\frac{d^2w}{dx^2}\right) - f = 0 \tag{6.2.9}$$

$$-\frac{d^2}{dx^2}\left(B_{xx}\frac{du}{dx} - D_{xx}\frac{d^2w}{dx^2}\right) - q = 0 \tag{6.2.10}$$

The governing equations (6.2.9) and (6.2.10) are fourth-order differential equations and are not

suitable for the development of dual mesh control domain method. Hence we will recast these equations in terms of the axial and transverse displacements $u$ and $w$ respectively and the bending moment $M_{xx}$. To do so, we eliminate $\frac{d^2w}{dx^2}$ from Eq. (6.2.4a) using Eq. (6.2.4b) to get

$$N_{xx} = \bar{A}_{xx}\frac{du}{dx} + \bar{B}_{xx}M_{xx} \tag{6.2.11}$$

and express Eq. (6.2.4b) as

$$-\frac{d^2w}{dx^2} = -\bar{B}_{xx}\frac{du}{dx} + \frac{1}{D_{xx}}M_{xx} \tag{6.2.12}$$

where

$$D^*_{xx} \equiv D_{xx}A_{xx} - B^2_{xx}, \;\; \bar{A}_{xx} \equiv \frac{D^*_{xx}}{D_{xx}}, \;\; \bar{B}_{xx} \equiv \frac{B_{xx}}{D_{xx}} \tag{6.2.13}$$

Now the governing equations in terms of displacements and moment are given by Eqs. (6.2.7),(6.2.8) and (6.2.12) where the expression for $N_{xx}$ is taken from Eq. (6.2.11). These equations are listed bellow.

$$-\frac{d}{dx}\left(\bar{A}_{xx}\,\frac{du}{dx} + \bar{B}_{xx}\,M_{xx}\right) = f \tag{6.2.14}$$

$$-\frac{d^2M_{xx}}{dx^2} = q \tag{6.2.15}$$

$$-\frac{d^2w}{dx^2} - \frac{1}{D_{xx}}M_{xx} + \bar{B}_{xx}\,\frac{du}{dx} = 0 \tag{6.2.16}$$

### 6.2.2 Timoshenko beam theory

The displacement filed of the Timoshenko beam theory is given by

$$\begin{aligned} u_1(x,y,z) &= u(x) + z\phi_x(x) \\ u_2(x,y,z) &= 0 \\ u_3(x,y,z) &= w(x) \end{aligned} \tag{6.2.17}$$

The non-zero linear strains corresponding to this displacement field is given by

$$\varepsilon_{xx} = \frac{du}{dx} + z\frac{d\phi_x}{dx} = \varepsilon^0_{xx} + z\varepsilon^1_{xx} \tag{6.2.18a}$$

$$\gamma_{xz} = \phi_x + \frac{dw}{dx} \tag{6.2.18b}$$

while the constitutive relation for functionally graded beam with power-law variation of Young's modulus and constant Poisson's ration is given by

$$\sigma_{xx} = E(z)\varepsilon_{xx}, \quad \sigma_{xz} = \frac{E(x)}{2(1+\nu)}\gamma_{xz} \tag{6.2.19}$$

We further define the stress and moment resultant acting on the beam as follows:

$$N_{xx} = \int_A \sigma_{xx} dA = A_{xx}\frac{du}{dx} + B_{xx}\frac{d\phi_x}{dx} \tag{6.2.20a}$$

$$M_{xx} = \int_A \sigma_{xx} z dA = B_{xx}\frac{du}{dx} + D_{xx}\frac{d\phi_x}{dx} \tag{6.2.20b}$$

$$Q_x = K_s \int_A \sigma_{xz}\, dA = S_{xz}\left(\phi_x + \frac{dw}{dx}\right), \;\; S_{xz} = \frac{K_s}{2(1+\nu)}\int_A E(z)\, dA \tag{6.2.20c}$$

Here $A_{xx}$, $B_{xx}$, and $D_{xx}$ are the extensional, extensional-bending, and bending stiffness coefficients and are given in Eq. (6.2.5). $K_s$ is the shear correction factor and is taken to be 5/6 for beams with rectangular cross-section. The governing differential equations of the beam can be obtained from the principle of virtual work, which for the functionally graded Timoshenko beam can be expressed as:

$$\int_0^L [N_{xx}\delta\varepsilon^0_{xx} + M_{xx}\delta\varepsilon^1_{xx} + Q_x\delta\gamma_{xz}]dx - \int_0^L (f\delta u + q\delta w)dx = 0 \tag{6.2.21}$$

Taking the Euler-Lagrange equations of the variational statement (6.2.21) we obtain the governing differential equations of functionally graded Timoshenko beam as follows:

$$-\frac{dN_{xx}}{dx} - f = 0 \tag{6.2.22}$$

$$-\frac{dQ_x}{dx} - q = 0 \tag{6.2.23}$$

$$-\frac{dM_{xx}}{dx} + Q_x = 0 \tag{6.2.24}$$

Now using the expressions for stress and moment resultants from Eqs. (6.2.20a)-(6.2.20c), we can write the governing equations as

$$-\frac{d}{dx}\left(A_{xx}\frac{du}{dx} + B_{xx}\frac{d\phi_x}{dx}\right) - f = 0 \tag{6.2.25}$$

$$-\frac{d}{dx}\left[S_{xz}\left(\phi_x + \frac{dw}{dx}\right)\right] - q = 0 \tag{6.2.26}$$

$$-\frac{d}{dx}\left(B_{xx}\frac{du}{dx} + D_{xx}\frac{d\phi_x}{dx}\right) + S_{xz}\left(\phi_x + \frac{dw}{dx}\right) = 0 \tag{6.2.27}$$

To express the governing equations in terms of displacements and moments we first write $N_{xx}$ in terms of $u$ and $M_{xx}$ using Eq. (6.2.20a) and Eq. (6.2.20b) to get

$$N_{xx} = \bar{A}_{xx}\frac{du}{dx} + \bar{B}_{xx}M_{xx} \tag{6.2.28}$$

and Eq. (6.2.20b) can be written as

$$\frac{d\phi_x}{dx} = -\bar{B}_{xx}\frac{du}{dx} + \frac{1}{D_{xx}}M_{xx} \tag{6.2.29}$$

and Eq. (6.2.24) can be written as

$$\frac{d\phi_x}{dx} = -\frac{d^2w}{dx^2} + \frac{1}{S_{xz}}\frac{d^2M_{xx}}{dx^2} \tag{6.2.30}$$

Now eliminating $\frac{d\phi_x}{dx}$ from Eq. (6.2.29) and Eq. (6.2.30) we get

$$-\frac{d^2w}{dx^2} = -\frac{1}{S_{xz}}\frac{d^2M_{xx}}{dx^2} - \bar{B}_{xx}\frac{du}{dx} + \frac{1}{D_{xx}}M_{xx} \tag{6.2.31}$$

Finally the governing equations of Timoshenko beam in terms of displacements and moment are given by

$$-\frac{d}{dx}\left(\bar{A}_{xx}\frac{du}{dx} + \bar{B}_{xx}M_{xx}\right) - f = 0 \tag{6.2.32}$$

$$-\frac{d^2M_{xx}}{dx^2} - q = 0 \tag{6.2.33}$$

$$-\frac{d}{dx}\left(\frac{dw}{dx} - \frac{1}{S_{xz}}\frac{dM_{xx}}{dx}\right) + \bar{B}_{xx}\frac{du}{dx} - \frac{1}{D_{xx}}M_{xx} = 0 \tag{6.2.34}$$

while the effective rotation $\phi_x$ is given in terms of $w$ and $M_{xx}$ as

$$\phi_x = -\frac{dw}{dx} + \frac{1}{S_{xz}}\frac{dM_{xx}}{dx} \tag{6.2.35}$$

## 6.3 Dual mesh control domain formulation

### 6.3.1 Euler-Bernoulli beam

The dual mesh control domain method is best suited for solving first or second-order differential equations. Since the governing equations of the Euler-Bernoulli beam when expressed in term of displacements alone result in forth-order differential equations (see Eqs. (6.2.9)-(6.2.10)), we shall use the differential equations which are given in terms of displacements and moment (see Eqs. (6.2.14)-(6.2.16)) to formulate the dual mesh control domain method. The resulting formulation is called mixed dual mesh control domain method since the primary variables of the formulation consists of displacements and force like terms (i.e., moment).

#### 6.3.1.1 Mixed DMCDM

In the DMCDM, we divide the domain $\Omega = (0, L)$ into a set of $N$ primal mesh elements separated by nodes, as shown in Fig. 6.2, with each node having its own control domain (a dual mesh). The nodes are numbered sequentially from the left to the right. We consider two adjacent primal mesh elements connected at a typical interior node $I$ and control domain associated with that node (see Fig. 6.2).

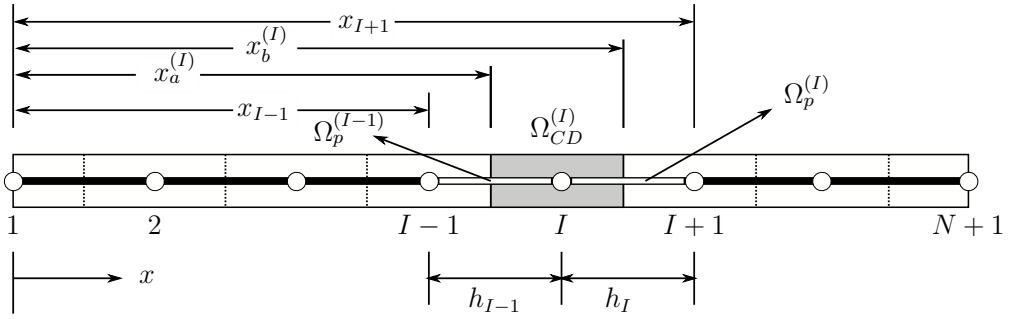


Figure 6.2: Primal and dual mesh discretization of the beam. The primal mesh elements $\Omega_p^{(I-1)}$ and $\Omega_p^{(I)}$ and control domain $\Omega_{CD}^{(I)}$ associated with and internal node $I$ are indicated.

Next, we derive the discretized equations associated with Eqs. (6.2.32)–(6.2.34). The complete steps of the DMCDM are presented by considering Eq. (6.2.32) and then summarize results for the remaining equations and also for the other models described here.

The first step is to set up the integral statement of Eq. (6.2.32) over an interior control domain, say $\Omega_{CD}^{(I)}$ associated with node $I$:

$$0 = \int_{x_a^{(I)}}^{x_b^{(I)}} \left[ -\frac{d}{dx}\left( \bar{A}_{xx} \frac{du}{dx} + \bar{B}_{xx} M_{xx} \right) - f \right] dx \tag{6.3.1}$$

Unlike in a weighted-residual method (or weak form), we weaken the differentiability on $u$ by

carrying out the indicated integration and obtain

$$0 = \int_{x_a^{(I)}}^{x_b^{(I)}} \left[ -\frac{d}{dx}\left( \bar{A}_{xx}\,\frac{du}{dx} + \bar{B}_{xx}\,M_{xx} \right) - f \right] dx$$
$$= \left[ \bar{A}_{xx}\,\frac{du}{dx} + \bar{B}_{xx}\,M_{xx} \right]_{x_a^{(I)}} - \left[ \bar{A}_{xx}\,\frac{du}{dx} + \bar{B}_{xx}\,M_{xx} \right]_{x_b^{(I)}} - \int_{x_a^{(I)}}^{x_b^{(I)}} f\,dx \tag{6.3.2}$$

or

$$0 = -N_1^{(I)} - N_2^{(I)} - \int_{x_a^{(I)}}^{x_b^{(I)}} f\,dx \tag{6.3.3a}$$

where

$$N_1^{(I)} \equiv -\left[ \bar{A}_{xx}\,\frac{du}{dx} + \bar{B}_{xx}\,M_{xx} \right]_{x_a^{(I)}}, \quad N_2^{(I)} \equiv \left[ \bar{A}_{xx}\,\frac{du}{dx} + \bar{B}_{xx}\,M_{xx} \right]_{x_b^{(I)}} \tag{6.3.3b}$$

Here $N_1^{(I)}$ and $N_2^{(I)}$ denote the secondary variables (axial forces) at the left and right interfaces of the control domain centered at node $I$. The minus sign in the definition of $N_1^{(I)}$ indicates that it a compressive force, and both $N_1^{(I)}$ and $N_2^{(I)}$ are axial forces in the positive $x$ direction (see Fig. 6.3).

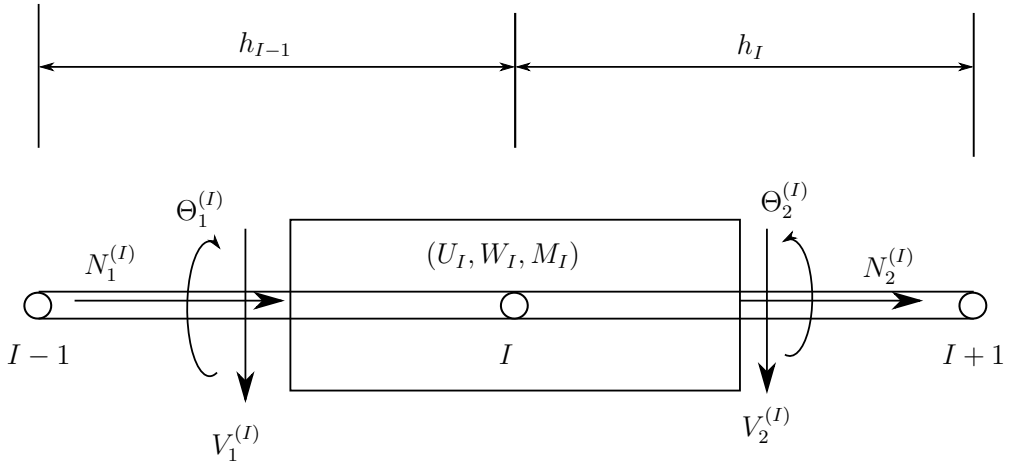


Figure 6.3: Primary and secondary variables associated with the control domain of an interior node $I$.

Next, we use finite element approximations of $u(x)$, $w(x)$, and $M_{xx}(x)$ over a typical primal

mesh element, $\Omega_p^{(I)} = (x_I, x_{I+1})$. For example, $u(x)$ is approximated using linear interpolation

$$u(x) \approx u_h(x) \equiv U_I \psi_1^{(I)}(x) + U_{I+1} \psi_2^{(I)}(x) \tag{6.3.4}$$

where $U_I$ is the value of $u$ at node $I$ (i.e., $U_I \approx u(x_I)$) and $\psi_i^{(I)}(x)$ $(i = 1, 2)$ are linear Lagrange interpolation functions of element $\Omega_p^{(I)}$ for $I = 1, 2, \ldots, N$:

$$\psi_1^{(I)}(x) = \frac{x_{I+1} - x}{h_I}, \quad \psi_2^{(I)}(x) = \frac{x - x_I}{h_I} \tag{6.3.5}$$

Hence, we can calculate parts of $N_1^{(I)}$ and $N_2^{(I)}$ in Eq. (6.3.3b) using the interpolation of the type in Eq. (6.3.5) for each of the dependent variable of the formulation (note $N_1^{(I)}$ is in primal mesh element $\Omega_p^{(I-1)}$ and $N_2^{(I)}$ is in primal mesh element $\Omega_p^{(I)}$; see Fig. 6.3 ) as follows:

$$\begin{aligned}\left[\bar{A}_{xx}\frac{du}{dx} + \bar{B}_{xx}\, M_{xx}\right]_{x_a^{(I)}}^{x_b^{(I)}} &= \frac{\bar{A}_{I-1}}{h_{I-1}}\, U_{I-1} - \left(\frac{\bar{A}_{I-1}}{h_{I-1}} + \frac{\bar{A}_I}{h_I}\right) U_I + \frac{\bar{A}_I}{h_I}\, U_{I+1} \\ &\quad + 0.5\left[-\bar{B}_{I-1} M_{I-1} + \left(\bar{B}_{I-1} - \bar{B}_I\right) M_I + \bar{B}_I M_{I+1}\right]\end{aligned} \tag{6.3.6}$$

where $\bar{A}_{I-1} = \bar{A}_{xx}(x_a^{(I)})$ at the left interface and $\bar{A}_I = \bar{A}_{xx}(x_b^{(I)})$ at the right interface of the control domain centered around node $I$. Similar meaning applies to $\bar{B}_{I-1}$ and $\bar{B}_I$; $M_I$ denotes the nodal value of $M_{xx}$ at node $I$.

Substituting the representations in Eqs. (6.3.6) into Eq. (6.3.3a), we obtain (for $I = 2, 3, \ldots, N$)

$$\begin{aligned}&-\frac{\bar{A}_{I-1}}{h_{I-1}} U_{I-1} + \left(\frac{\bar{A}_{I-1}}{h_{I-1}} + \frac{\bar{A}_I}{h_I}\right) U_I - \frac{\bar{A}_I}{h_I} U_{I+1} + 0.5\bar{B}_{I-1} M_{I-1} \\ &\qquad + 0.5\left(\bar{B}_{I-1} - \bar{B}_I\right) M_I - 0.5\bar{B}_I M_{I+1} - \int_{x_a^{(I)}}^{x_b^{(I)}} f(x)\, dx = 0\end{aligned} \tag{6.3.7}$$

where

$$\bar{A}_{I-1} = \left.\frac{D_{xx}^*}{D_{xx}}\right|_{x_a^{(I)}}, \quad \bar{A}_I = \left.\frac{D_{xx}^*}{D_{xx}}\right|_{x_b^{(I)}}, \quad \bar{B}_{I-1} = \left.\frac{B_{xx}}{D_{xx}}\right|_{x_a^{(I)}}, \quad \bar{B}_I = \left.\frac{B_{xx}}{D_{xx}}\right|_{x_b^{(I)}} \tag{6.3.8}$$

The integral of a function $f(x)$ over the control domain $(x_a^{(I)}, x_b^{(I)})$ can be evaluated using either

exact integration or numerical integration (e.g., trapezoidal rule, Gauss quadrature rule).

Lastly, we write the discretized equations for the boundary nodes [see Fig. 6.4]:

$$0 = -N_1^{(1)} + \frac{\bar{A}_1}{h_1}U_1 - \frac{\bar{A}_1}{h_1}U_2 + 0.5\bar{B}_1\, M_1 + 0.5\bar{B}_1\, M_2 - \int_0^{0.5h_1} f\, dx \tag{6.3.9}$$

$$0 = -N_2^{(N+1)} - \frac{\bar{A}_N}{h_N}U_N + \frac{\bar{A}_N}{h_N}U_{N+1} + 0.5\bar{B}_N\, M_N + 0.5\bar{B}_N\, M_{N+1} - \int_0^{0.5h_N} f(\bar{x})\, d\bar{x} \tag{6.3.10}$$

where $\bar{x}$ is the local coordinate with origin at node 1 of primal mesh element and $N_1^{(1)}$ and $N_2^{(N+1)}$ are the boundary forces (at nodes 1 and $N+1$, respectively), which are either specified or their duality counter parts, namely, the displacements $U_1$ and $U_{(N+1)}$, are specified. This completes the discretization of Eq. (6.2.14).

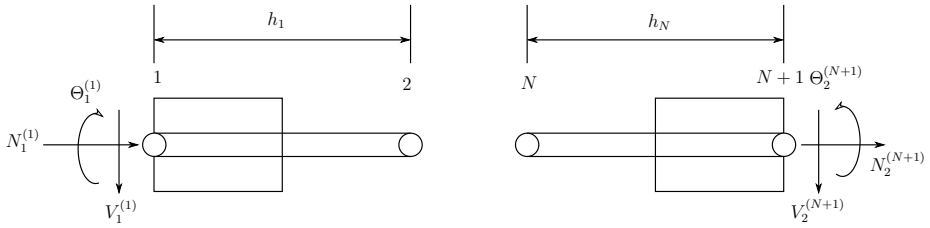


Figure 6.4: Control domains corresponding to boundary nodes.

The same procedure can be applied to Eqs. (6.2.15) and (6.2.16) to obtain the discretized equations for the interior and boundary nodes. We have the following integral statements of Eqs. (6.2.15) and (6.2.16):

$$0 = -V_1^{(I)} - V_2^{(I)} - \int_{x_a^{(I)}}^{x_b^{(I)}} q\, dx \tag{6.3.11}$$

$$0 = -\Theta_1^{(I)} - \Theta_2^{(I)} + \int_{x_a^{(I)}}^{x_b^{(I)}} \left(-\frac{1}{D_{xx}}M_{xx} + \bar{B}_{xx}\frac{du}{dx}\right) dx \tag{6.3.12}$$

where $V_1^{(I)}$ and $V_2^{(I)}$ denote the secondary variables (shear forces acting upward positive) at the

left and right interfaces of the control domain centered at node $I$,

$$V_1^{(I)} \equiv -\left[\frac{dM_{xx}}{dx}\right]_{x_a^{(I)}} = -\frac{M_I - M_{I-1}}{h_{I-1}}, \;\; V_2^{(I)} \equiv \left[\frac{dM_{xx}}{dx}\right]_{x_b^{(I)}} = \frac{M_{I+1} - M_I}{h_I} \tag{6.3.13}$$

and $\Theta_1^{(I)}$ and $\Theta_2^{(I)}$ denote the secondary variables (rotations in counterclock direction) at the left and right interfaces of the control domain centered at node $I$,

$$\Theta_1^{(I)} \equiv -\left[\frac{dw}{dx}\right]_{x_a^{(I)}} = \frac{W_{I-1} - W_I}{h_{I-1}}, \;\; \Theta_2^{(I)} \equiv \left[\frac{dw}{dx}\right]_{x_b^{(I)}} = \frac{W_{I+1} - W_I}{h_I} \tag{6.3.14}$$

The discretized equations associated with Eq. (6.2.15) at an interior node are:

$$-\frac{1}{h_{I-1}} M_{I-1} + \left(\frac{1}{h_{I-1}} + \frac{1}{h_I}\right) M_I - \frac{1}{h_I} M_{I+1} = \int_{x_a^{(I)}}^{x_b^{(I)}} q \, dx \tag{6.3.15}$$

For the boundary nodes 1 and $N+1$, we have

$$0 = -V_1^{(1)} + \frac{1}{h_1} M_1 - \frac{1}{h_1} M_2 - \int_0^{0.5h_1} q \, dx \tag{6.3.16}$$

$$0 = -V_2^{(N+1)} - \frac{1}{h_N} M_N + \frac{1}{h_N} M_{N+1} - \int_0^{0.5h_N} q(\bar{x}) \, d\bar{x} \tag{6.3.17}$$

The discretized equations associated with Eq. (6.2.16) are

$$\begin{aligned} -\frac{1}{h_{I-1}} W_{I-1} + \left(\frac{1}{h_{I-1}} + \frac{1}{h_I}\right) W_I - \frac{1}{h_I} W_{I+1} - \frac{1}{8}\frac{h_{I-1}}{D_{I-1}} M_{I-1} \\ - \frac{3}{8}\left(\frac{h_{I-1}}{D_{I-1}} + \frac{h_I}{D_I}\right) M_I - \frac{1}{8}\frac{h_I}{D_I} M_{I+1} \\ - 0.5\bar{B}_{I-1} U_{I-1} + 0.5\left(\bar{B}_{I-1} - \bar{B}_I\right) U_I + 0.5\bar{B}_I U_{I+1} = 0 \end{aligned} \tag{6.3.18}$$

for an interior node. Here $D_I$ denotes the value of $D_{xx}$ in primal mesh element $I$ and $\bar{B}_I$ denotes

the value of $B_{xx}/D_{xx}$ in primal mesh element $I$. For the boundary nodes 1 and $N+1$, we have

$$0 = -\Theta_1^{(1)} + \frac{1}{h_1}W_1 - \frac{1}{h_1}W_2 - \frac{3}{8}\frac{h_1}{D_1}M_1 - \frac{1}{8}\frac{h_1}{D_1}M_2 + 0.5\bar{B}_1\left(U_2 - U_1\right) \tag{6.3.19}$$

$$0 = -\Theta_2^{(N+1)} - \frac{1}{h_N}W_N + \frac{1}{h_N}W_{N+1} - \frac{1}{8}\frac{h_N}{D_N}M_N - \frac{3}{8}\frac{h_N}{D_N}M_{N+1} + 0.5\bar{B}_N\left(U_{N+1} - U_N\right) \tag{6.3.20}$$

This completes the development of the discretized equations based on the DMCDM for the mixed formulation of the Euler–Bernoulli beam theory.

### 6.3.2 Timoshenko beam

#### *6.3.2.1 Displacement DMCDM*

The displacement based DMCDM of Timoshenko beam is developed using Eqs. (6.2.25)–(6.2.27). In order to derive the discretized equations associated with Eqs. (6.2.25)–(6.2.27), we follow the same procedure as described for the EBT. The integral statements over the $I$th control domain centered around node $I$ (see Fig. 6.5 for the nodal degrees of freedom) for each of these three equations are:

$$0 = -N_1^{(I)} - N_2^{(I)} - \int_{x_a^{(I)}}^{x_b^{(I)}} f\,dx \tag{6.3.21a}$$

$$N_1^{(I)} \equiv -\left[A_{xx}\frac{du}{dx} + B_{xx}\frac{d\phi_x}{dx}\right]_{x_a^{(I)}}, \qquad N_2^{(I)} \equiv \left[A_{xx}\frac{du}{dx} + B_{xx}\frac{d\phi_x}{dx}\right]_{x_b^{(I)}} \tag{6.3.21b}$$

$$0 = -V_1^{(I)} - V_2^{(I)} - \int_{x_a^{(I)}}^{x_b^{(I)}} q dx \tag{6.3.22a}$$

$$V_1^{(I)} \equiv -\left[S_{xz}\left(\phi_x + \frac{dw}{dx}\right)\right]_{x_a^{(I)}}, \qquad V_2^{(I)} \equiv \left[S_{xz}\left(\phi_x + \frac{dw}{dx}\right)\right]_{x_b^{(I)}} \tag{6.3.22b}$$

$$0 = -M_1^{(I)} - M_2^{(I)} + \int_{x_a^{(I)}}^{x_b^{(I)}} S_{xz}\left(\phi_x + \frac{dw}{dx}\right) dx \tag{6.3.23a}$$

$$M_1^{(I)} \equiv -\left[B_{xx}\frac{du}{dx} + D_{xx}\frac{d\phi_x}{dx}\right]_{x_a^{(I)}}, \qquad M_2^{(I)} \equiv \left[B_{xx}\frac{du}{dx} + D_{xx}\frac{d\phi_x}{dx}\right]_{x_b^{(I)}} \tag{6.3.23b}$$

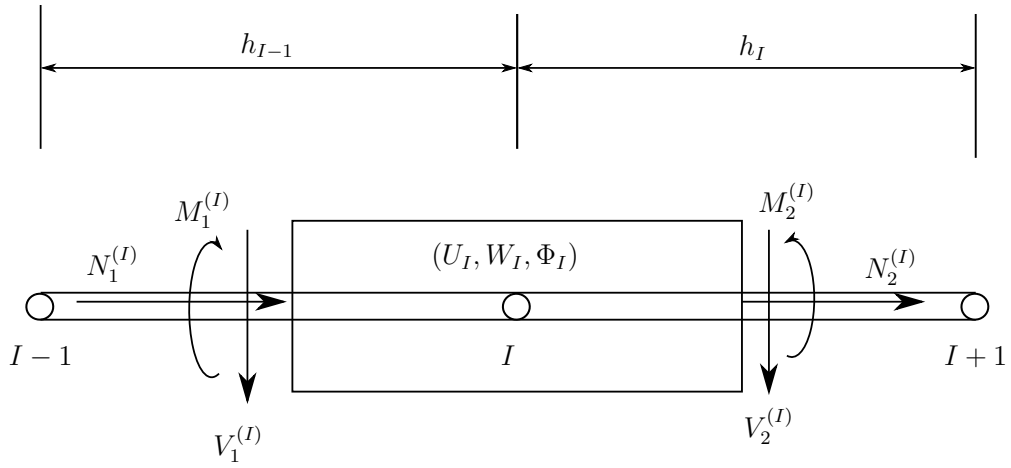


Figure 6.5: Primary and secondary variables associated with the control domain of an interior node $I$ of displacement DMCDM of TBT.

Here ($N_1^{(I)}$, $V_1^{(I)}$, $M_1^{(I)}$) and ($N_2^{(I)}$, $V_2^{(I)}$, $M_2^{(I)}$) denote the axial forces, shear forces, and bending moments at the left and right interfaces, respectively, of the control domain centered at node $I$ (see Fig. 6.5). Since the displacement model of the TBT suffers from shear locking, we evaluate the integral appearing in Eq. (6.3.23a) (i.e., the shear force) as a constant to avoid shear locking:

$$\int_{x_a^{(I)}}^{x_b^{(I)}} S_{xz}\left(\phi_x + \frac{dw}{dx}\right) dx = \tfrac{1}{2} S_{I-1}\left(\Phi_{I-1} + \Phi_I\right)\frac{h_{I-1}}{2} + \tfrac{1}{2} S_I\left(\Phi_I + \Phi_{I+1}\right)\frac{h_I}{2} + S_{I-1}\frac{W_I - W_{I-1}}{h_{I-1}}\frac{h_{I-1}}{2} + S_I\frac{W_{I+1} - W_I}{h_I}\frac{h_I}{2} \tag{6.3.24}$$

The discretized equations associated with Eqs. (6.2.25)–(6.2.27) for an interior node $I$ are

$$
\begin{aligned}
0 = &-\frac{A_{I-1}}{h_{I-1}}U_{I-1} + \left(\frac{A_{I-1}}{h_{I-1}} + \frac{A_I}{h_I}\right)U_I - \frac{A_I}{h_I}U_{I+1} \\
&- \frac{B_{I-1}}{h_{I-1}}\Phi_{I-1} + \left(\frac{B_{I-1}}{h_{I-1}} + \frac{B_I}{h_I}\right)\Phi_I - \frac{B_I}{h_I}\Phi_{I+1} - \int_{x_a^{(I)}}^{x_b^{(I)}} f\,dx \qquad (6.3.25a) \\
0 = &-\frac{S_{I-1}}{h_{I-1}}W_{I-1} + \left(\frac{S_{I-1}}{h_{I-1}} + \frac{S_I}{h_I}\right)W_I - \frac{S_I}{h_I}W_{I+1} \\
&+ 0.5S_{I-1}\Phi_{I-1} + 0.5\left(S_{I-1} - S_I\right)\Phi_I - 0.5S_I\Phi_{I+1} - \int_{x_a^{(I)}}^{x_b^{(I)}} q\,dx \qquad (6.3.25b) \\
0 = &-\frac{B_{I-1}}{h_{I-1}}U_{I-1} + \left(\frac{B_{I-1}}{h_{I-1}} + \frac{B_I}{h_I}\right)U_I - \frac{B_I}{h_I}U_{I+1} - 0.5S_{I-1}W_{I-1} \\
&+ 0.5\left(S_{I-1} - S_I\right)W_I + 0.5S_IW_{I+1} - \frac{D_{I-1}}{h_{I-1}}\Phi_{I-1} + \left(\frac{D_{I-1}}{h_{I-1}} + \frac{D_I}{h_I}\right)\Phi_I \\
&- \frac{D_I}{h_I}\Phi_{I+1} + 0.25S_{I-1}h_{I-1}\Phi_{I-1} + 0.25\left(S_{I-1}h_{I-1} + S_Ih_I\right)\Phi_I \\
&+ 0.25S_Ih_I\Phi_{I+1} \qquad (6.3.25c)
\end{aligned}
$$

The discretized equations of the left boundary node are

$$
\begin{aligned}
0 &= -N_1^{(1)} + \frac{A_1}{h_1}U_1 - \frac{A_1}{h_1}U_2 + \frac{B_1}{h_1}\Phi_1 - \frac{B_1}{h_1}\Phi_2 - \int_0^{0.5h_1} f\,dx \qquad (6.3.26a) \\
0 &= -V_1^{(1)} + \frac{S_1}{h_1}W_1 - \frac{S_1}{h_1}W_2 - 0.5S_1\Phi_1 - 0.5S_1\Phi_2 - \int_0^{0.5h_1} q\,dx \qquad (6.3.26b) \\
0 &= -M_1^{(1)} - \frac{B_1}{h_1}\left(U_2 - U_1\right) + 0.5S_1(W_2 - W_1) - \frac{D_1}{h_1}\left(\Phi_2 - \Phi_1\right) \\
&\quad + 0.25S_1h_1\left(\Phi_1 + \Phi_2\right) \qquad (6.3.26c)
\end{aligned}
$$

For the node on the right boundary, we have

$$0 = -N_1^{(N+1)} + \frac{A_N}{h_N}U_{N+1} - \frac{A_N}{h_1}U_N + \frac{B_N}{h_N}\Phi_{N+1} - \frac{B_N}{h_N}\Phi_N - \int_0^{0.5h_N} f(\bar{x})\, d\bar{x} \tag{6.3.27a}$$

$$0 = -V_2^{(N+1)} + \frac{S_N}{h_N}\left(W_{N+1} - W_N\right) + 0.5S_N(\Phi_{N+1} + \Phi_N) - \int_0^{0.5h_N} q(\bar{x})\, d\bar{x} \tag{6.3.27b}$$

$$0 = -M_2^{(N+1)} + \frac{B_N}{h_N}\left(U_{N+1} - U_N\right) + 0.5S_N(W_{N+1} - W_N) + \frac{D_N}{h_N}\left(\Phi_{N+1} - \Phi_N\right) + 0.25S_N h_N\left(\Phi_N + \Phi_{N+1}\right) \tag{6.3.27c}$$

### *6.3.2.2 Mixed DMCDM*

Although the displacement DMCDM of Timoshenko beam with reduced integration of shear force (see Eq. (6.3.24)) gives locking free solutions, this is not the only way to eliminate shear locking. It is known in finite element literature that mixed formulations (with displacements and moments as primary variables) can also successfully eliminate locking without any resort to any reduced integration of shear terms. Following the same idea, here we develop mixed dual mesh control domain method for Timoshenko beam. We use the Eqs. (6.2.32)–(6.2.34) to formulate the mixed dual mesh control domain method for Timoshenko beam. Discretization of these equations follows the same procedure described in the previous sections for mixed DMCDM of Euler-Bernoulli beam and displacement DMCDM of Timoshenko beam. The final discretized equations associated with Eq. (6.2.32) at the $I$th node, node 1, and node $N+1$ are given by

$$-\frac{\bar{A}_{I-1}}{h_{I-1}}U_{I-1} + \left(\frac{\bar{A}_{I-1}}{h_{I-1}} + \frac{\bar{A}_I}{h_I}\right)U_I - \frac{\bar{A}_I}{h_I}U_{I+1} + 0.5\bar{B}_{I-1}M_{I-1} + 0.5\left(\bar{B}_{I-1} - \bar{B}_I\right)M_I - 0.5\bar{B}_I M_{I+1} - \int_{x_a^{(I)}}^{x_b^{(I)}} f\, dx = 0 \tag{6.3.28a}$$

$$0 = -N_1^{(1)} + \frac{\bar{A}_1}{h_1}U_1 - \frac{\bar{A}_1}{h_1}U_2 + 0.5\bar{B}_1\, M_1 + 0.5\bar{B}_1\, M_2 - \int_0^{0.5h_1} f\, dx \tag{6.3.28b}$$

$$0 = -N_2^{(N+1)} - \frac{\bar{A}_N}{h_N}U_N + \frac{\bar{A}_N}{h_N}U_{N+1} + 0.5\bar{B}_N\, M_N + 0.5\bar{B}_N\, M_{N+1} - \int_0^{0.5h_N} f(\bar{x})\, d\bar{x} \tag{6.3.28c}$$

The discretized equations associated with Eq. (6.2.33) are:

$$0 = -\frac{M_{I+1} - M_I}{h_I} + \frac{M_I - M_{I-1}}{h_{I-1}} - \int_{x_a^{(I)}}^{x_b^{(I)}} q\, dx \tag{6.3.29a}$$

$$0 = -V_1^{(1)} + \frac{1}{h_1} M_1 - \frac{1}{h_1} M_2 - \int_0^{0.5h_1} q\, dx \tag{6.3.29b}$$

$$0 = -V_2^{(N+1)} + \frac{1}{h_N} M_{N+1} - \frac{1}{h_N} M_N - \int_0^{0.5h_N} q(\bar{x})\, d\bar{x} \tag{6.3.29c}$$

Finally, the discretized equations associated with Eq. (6.2.34) at the $I$th node, node 1, and node $N+1$ are:

$$\begin{aligned} 0 = & -0.5\bar{B}_{I-1} U_{I-1} + 0.5\left(\bar{B}_{I-1} - \bar{B}_I\right) U_I + 0.5\bar{B}_I U_{I+1} \\ & - \frac{1}{h_{I-1}} W_{I-1} + \left(\frac{1}{h_{I-1}} + \frac{1}{h_I}\right) W_I - \frac{1}{h_I} W_{I+1} \\ & + \frac{1}{h_{I-1}} \frac{1}{S_{I-1}} M_{I-1} - \left(\frac{1}{h_{I-1}} \frac{1}{S_{I-1}} + \frac{1}{h_I} \frac{1}{S_I}\right) M_I + \frac{1}{h_I} \frac{1}{S_I} M_{I+1} \\ & - \tfrac{1}{8} \frac{h_{I-1}}{D_{I-1}} M_{I-1} - \tfrac{3}{8} \left(\frac{h_{I-1}}{D_{I-1}} + \frac{h_I}{D_I}\right) M_I - \tfrac{1}{8} \frac{h_I}{D_I} M_{I+1} \end{aligned} \tag{6.3.30a}$$

$$\begin{aligned} 0 = & -\Theta_1^{(1)} + 0.5\bar{B}_1 \left(U_2 - U_1\right) - \frac{W_2 - W_1}{h_1} + \frac{1}{S_1} \frac{M_2 - M_1}{h_1} \\ & - \frac{1}{8} \frac{h_1}{D_1} \left(3M_1 + M_2\right) \end{aligned} \tag{6.3.30b}$$

$$\begin{aligned} 0 = & -\Theta_2^{(N+1)} + 0.5\bar{B}_N U_{N+1} - 0.5\bar{B}_N U_N - \frac{1}{h_N} W_N + \frac{1}{h_N} W_{N+1} \\ & + \frac{1}{S_N h_N} M_N - \frac{1}{S_N h_N} M_{N+1} - \frac{1}{8} \frac{h_N}{D_N} \left(M_N + 3M_{N+1}\right) \end{aligned} \tag{6.3.30c}$$

## 6.4 Numerical examples

To illustrate the working of DMCDM we consider two different examples, namely, pinned-pinned and clamped-clamped beams with uniformly distributed load (UDL) of intensity $q_0$. Due to symmetry about the center of the beam, only a half beam, $0 \leq x \leq L/2$, is considered as the computational domain. Further, the results obtained from DMCDM are compared with those obtained from FEM. For functionally graded beams the effect of power-law index $n$ (see Eq. (6.1.1)), which

dictates the material distribution through the beam thickness, on the deflections is also studied. In addition to the dual mesh control domain methods described in the previous sections, we also consider four different finite element models. All these models are briefly summarized below:

- **FE-EB(D)** - Displacement finite element model of the EBT
- **FE-EB(M)** - Mixed finite element model of the EBT
- **FE-TB(D)** - Displacement finite element model of the TBT
- **FE-TB(M)** - Mixed finite element model of the TBT
- **DM-EB(M)** - Mixed dual mesh finite domain model of the EBT
- **DM-TB(D)** - Displacement dual mesh finite domain model of the TBT
- **DM-TB(M)** - Mixed dual mesh finite domain model of the TBT

It should be noted that in the displacement finite element model of Euler-Bernoulli beam (FE-EB(D)) the transverse deflections are interpolated using Hermite cubic interpolation functions [93] while the axial deflection is interpolated using linear Lagrange interpolation functions. However, for the rest of the finite element models and dual mesh control domain models all the primary variables are interpolated using linear Lagrange interpolation functions.

We investigate the effect of mesh and the power-law index $n$ on the deflections and stresses. We consider a beam of length $L = 100$ in, $W \times H = 1 \times 1$ in$^2$ cross-sectional dimensions, functionally graded through the height ($h$) ($E_1 = 30 \times 10^6$ psi, $E_2 = 3 \times 10^6$ psi, and $\nu = 0.3$), and subjected to uniformly distributed transverse load of intensity $q_0$ lb/in. For the pinned-pinned and clamped-clamped boundary conditions, we can exploit the symmetry about $x = L/2$, and use the left half of the beam as the computational domain.

First, we consider the beam with both ends pinned. The boundary conditions on the *primary*

*variables* in various models for this problem are as follows:

$$\begin{aligned}\text{Displacement models}: &\quad u(0)=w(0)=u(\tfrac{L}{2})=0,\ \ \tfrac{dw}{dx}(\tfrac{L}{2})=0 \text{ or } \phi_x(\tfrac{L}{2})=0\\ \text{Mixed models}: &\quad u(0)=w(0)=M(0)=0,\ \ u(\tfrac{L}{2})=0\end{aligned} \tag{6.4.1}$$

The boundary conditions on the *secondary variables* (satisfied in an integral sense) are:

$$\begin{aligned}\text{Displacement models}: &\quad M(0)=0,\ \ V(\tfrac{L}{2})=0\\ \text{Mixed models}: &\quad V(\tfrac{L}{2})=0,\ \ \tfrac{dw}{dx}(\tfrac{L}{2})=0 \text{ or } \phi_x(\tfrac{L}{2})=0\end{aligned} \tag{6.4.2}$$

The exact solutions of pinned-pinned functionally graded beams, with the power-law given in Eq. (6.1.1), are given by

$$\begin{aligned}\bar{D}_{xx}\,u(x)&=\frac{q_0L^3}{12}\left(2\xi-3\xi^2+2\xi^3\right),\ \ \hat{D}_{xx}\,\phi_x(x)=-\frac{q_0L^4}{24}\left(1-6\xi^2-4\xi^3\right)\\ \hat{D}_{xx}\,w(x)&=\frac{q_0L^4}{24}\left(\xi-2\xi^3+\xi^4\right)+\tilde{D}_{xx}\frac{q_0L^2}{2}\xi(1-\xi)-\hat{B}_{xx}\frac{q_0L^2}{24}\xi(1-\xi)\\ M_{xx}(x)&=D^*_{xx}\frac{d\phi_x}{dx}=\frac{q_0L^2}{2}\xi(1-\xi),\ \ V(x)=\frac{dM_{xx}}{dx}=\frac{q_0L}{2}(1-2\xi)\\ \sigma(x,0.5h)&=\frac{M_{xx}(x)h}{2I}=\frac{hq_0L^2}{4I}\xi(1-\xi)\end{aligned} \tag{6.4.3}$$

where $\xi = x/L$ and

$$\hat{D}_{xx}=\frac{D^*_{xx}}{A_{xx}},\ \ \bar{D}_{xx}=\frac{D^*_{xx}}{B_{xx}},\ \ \hat{B}_{xx}=\frac{B^2_{xx}}{D_{xx}A_{xx}},\ \ \tilde{D}_{xx}=\frac{D^*_{xx}}{A_{xx}S_{xz}} \tag{6.4.4}$$

We note that for homogeneous beams $u(x) = 0$ everywhere. The EBT solutions are obtained from Eq. (6.4.3) by setting $\tilde{D}_{xx} = 0$ and replacing $\phi_x$ with $-dw/dx$. The bending stress, $\sigma(x, z)$, is computed at $x = L/2$ (where the bending moment is the maximum) and $z = h/2$, $h$ being the beam height. The stress is post-computed in the displacement models at the element center using

the relation

$$\sigma(x,z) = -E(z)\, z \frac{d^2 w}{dx^2} \;\text{ for EBT;}\;\; \sigma(x,z) = E(z)\, z \frac{d\phi_x}{dx} \;\text{ for TBT} \tag{6.4.5}$$

On the other hand, the stress in the mixed models is computed using the bending moment $M_{xx}(x)$ according to the formula

$$\sigma(x,z) = \frac{M_{xx}(x)\, z}{I} \tag{6.4.6}$$

where $M_{xx}(x)$ is the calculated from the finite element interpolation (i.e., $\sigma(L/2, h/2) = M(L/2)h/2I$, and $M(L/2)$ is the nodal value).

Tables 6.1 and 6.2 contain the normalized center deflection and stress, respectively, for homogeneous ($\hat{D}_{xx} = D_{xx} = EI$ and $\hat{B}_{xx} = B_{xx} = 0$) pinned-pinned (P-P) beams for different number of elements in the half beam. The tabulated deflections and stresses are normalized as follows (with $K_s = 5/6$):

$$\bar{w} = w\, \frac{\hat{D}_{xx}}{q_0 L^4}, \qquad \bar{\sigma} = \sigma\, \frac{I}{H\, q_0 L^2} \tag{6.4.7}$$

where $I$ is the moment of inertia. From the results it is clear that the mixed dual mesh control domain models are accurate in predicting the displacements and stresses. In fact, all mixed models and the displacement model of the DMCDM give the exact stress for any number of elements. The shear locking is alleviated in the displacement finite element model and DMCDM of the TBT by the use of reduced integration. No such trick is used in the mixed FEM and mixed DMCDM.

Table 6.1: The center transverse deflection $\bar{w}(L/2) \times 10$ of homogeneous P-P beams predicted by various models [10].

| **Mesh** | **FE-EB(D)** | **FE-EB(M)** | **FE-TB(D)** | **FE-TB(M)** | **DM-EB(M)** | **DM-TB(D)** | **DM-TB(M)** |
|---|---|---|---|---|---|---|---|
| 4 | 0.1302 | 0.1286 | 0.1270 | 0.1285 | 0.1294 | 0.1270 | 0.1294 |
| 8 | 0.1302 | 0.1298 | 0.1294 | 0.1298 | 0.1300 | 0.1294 | 0.1300 |
| 16 | 0.1302 | 0.1301 | 0.1300 | 0.1301 | 0.1302 | 0.1300 | 0.1302 |
| 32 | 0.1302 | 0.1302 | 0.1302 | 0.1302 | 0.1302 | 0.1302 | 0.1302 |
| 64 | 0.1302 | 0.1302 | 0.1302 | 0.1302 | 0.1302 | 0.1302 | 0.1302 |
| **Exact** | 0.1302 | 0.1302 | 0.1302 | 0.1302 | 0.1302 | 0.1302 | 0.1302 |

The DMCDM always gives the exact value of the moment at $x = L/2$. We also note that for this slender beam ($L/h = 100$), the effect of shear deformation is negligible and the EBT and TBT solutions for $\bar{w}$ are the same upto the fourth decimal point.

Table 6.2: The center stress $\bar{\sigma}(L/2) \times 10$ for homogeneous P-P beams predicted by various models [10].

| **Mesh** | **FE-EB(D)** | **FE-EB(M)** | **FE-TB(D)** | **FE-TB(M)** | **DM-EB(M)** | **DM-TB(D)** | **DM-TB(M)** |
|---|---|---|---|---|---|---|---|
| 4 | 0.6120 | 0.6250 | 0.6055 | 0.6250 | 0.6250 | 0.6250 | 0.6250 |
| 8 | 0.6218 | 0.6250 | 0.6201 | 0.6250 | 0.6250 | 0.6250 | 0.6250 |
| 16 | 0.6242 | 0.6250 | 0.6238 | 0.6250 | 0.6250 | 0.6250 | 0.6250 |
| 32 | 0.6248 | 0.6250 | 0.6250 | 0.6250 | 0.6250 | 0.6250 | 0.6250 |
| 64 | 0.6249 | 0.6250 | 0.6250 | 0.6250 | 0.6250 | 0.6250 | 0.6250 |
| **Exact** | 0.6250 | 0.6250 | 0.6250 | 0.6250 | 0.6250 | 0.6250 | 0.6250 |

Table 6.3 contains the normalized center deflection for functionally graded pinned-pinned (P-P) beams for different values of the power-law index $n$. All of the results are obtained using 16 elements in the half beam. All models predict solutions that match the exact solutions upto the fourth decimal point. The stresses in the FGM beams are exactly the same as those in the homogeneous beams, because the bending moment is independent of the stiffness coefficients.

Table 6.3: The center transverse deflection $\bar{w}(L/2) \times 10$ of FGM P-P beams predicted by various models [10].

| n | **FE-EB(D)** | **FE-TB(D)** | **FE-EB(M)** | **FE-TB(M)** | **DM-EB(M)** | **DM-TB(D)** | **DM-TB(M)** |
|---|---|---|---|---|---|---|---|
| 0.0 | 0.1302 | 0.1302 | 0.1302 | 0.1302 | 0.1302 | 0.1300 | 0.1302 |
| 1.0 | 0.1069 | 0.1068 | 0.1067 | 0.1069 | 0.1069 | 0.1068 | 0.1069 |
| 2.0 | 0.0919 | 0.0918 | 0.0919 | 0.0919 | 0.0919 | 0.0918 | 0.0919 |
| 3.0 | 0.0879 | 0.0878 | 0.0879 | 0.0879 | 0.0879 | 0.0878 | 0.0879 |
| 5.0 | 0.0900 | 0.0899 | 0.0899 | 0.0900 | 0.0900 | 0.0899 | 0.0900 |
| 7.5 | 0.0959 | 0.0958 | 0.0958 | 0.0958 | 0.0958 | 0.0958 | 0.0959 |
| 10.0 | 0.1012 | 0.1011 | 0.1012 | 0.1012 | 0.1012 | 0.1011 | 0.1012 |
| 12.0 | 0.1048 | 0.1047 | 0.1047 | 0.1048 | 0.1048 | 0.1047 | 0.1048 |
| 15.0 | 0.1091 | 0.1090 | 0.1090 | 0.1090 | 0.1090 | 0.1090 | 0.1091 |
| 20.0 | 0.1142 | 0.1140 | 0.1141 | 0.1141 | 0.1141 | 0.1140 | 0.1142 |

It is interesting to note that the effect of the power-law index $n$ on the deflections is *not* monotonic. As $n$ goes from zero to a value of about $n = 2$, the deflection decreases and then increases for $n > 2$. This is due to the fact that $B_{xx}$ is not a monotonically increasing or decreasing function of $n$, as can be seen from Fig. 6.6 (see [100]). Figure 6.7 shows the variation of the normalized center deflection $\bar{w}$ with the power-law index $n$.

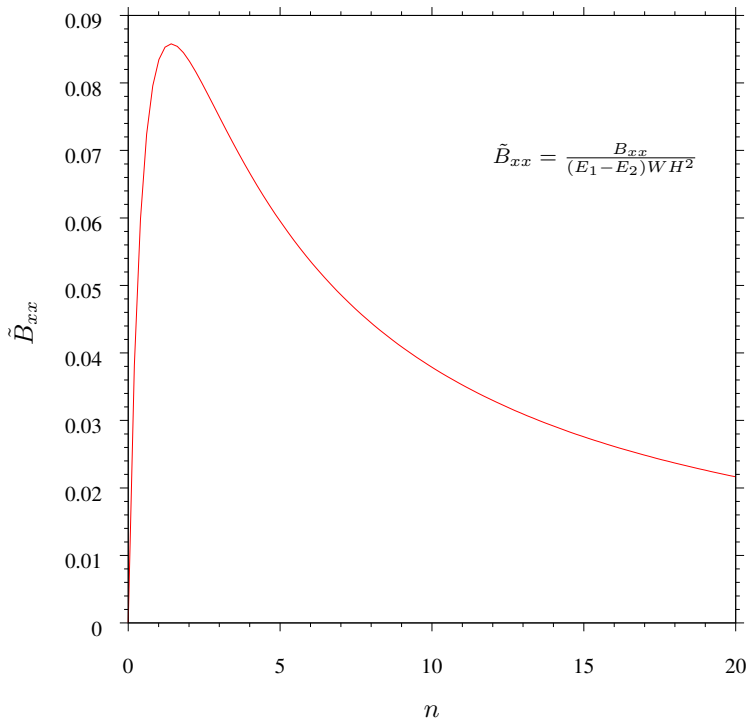


Figure 6.6: Variation of $B_{xx}$ with $n$ for given values of $E_1$ and $E_2$ and given cross-section of beam.

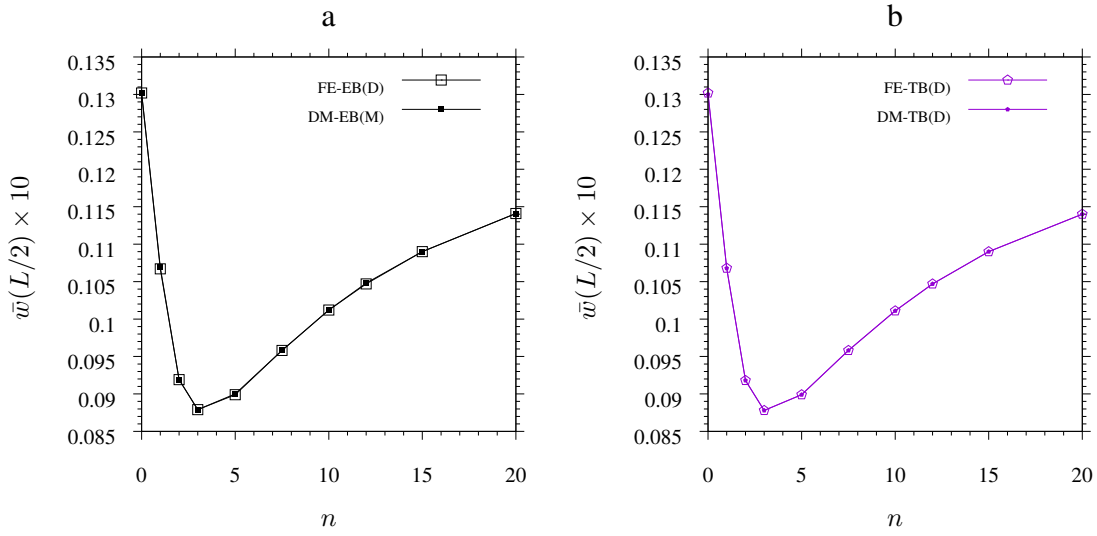


Figure 6.7: Center deflections of pin-pin functionally graded beams (a) Euler-Bernoulli beam theory (b) Timoshenko beam theory.

Next, we consider a beam *clamped* (C-C) at both ends. The boundary conditions on the primary variables in various models for this problem are as follows (replace $dw/dx$ with $\phi_x$ for the TBT:

$$\begin{aligned} \text{Displacement models}: \quad & u(0) = w(0) = 0, \;\; \frac{dw}{dx}(0) = 0, \;\; u(L/2) = \frac{dw}{dx}(\tfrac{L}{2}) = 0 \\ \text{Mixed models}: \quad & u(0) = w(0) = 0, \;\; u(L/2) = 0 \end{aligned} \tag{6.4.8}$$

The boundary conditions on the secondary variables in various models for this problem (satisfied in an integral sense) are as follows:

$$\begin{aligned} \text{Displacement models}: \quad & V(\tfrac{L}{2}) = 0 \\ \text{Mixed models}: \quad & \frac{dw}{dx}(0) = 0, \;\; \frac{dw}{dx}(\tfrac{L}{2}) = 0 \end{aligned} \tag{6.4.9}$$

The exact solutions for clamped-clamped beams are given by ($\xi = x/L$)

$$\begin{aligned} u(x) &= \frac{q_0 L^4}{12\bar{D}_{xx}}\left(\xi - 3\xi^2 + 2\xi^3\right), \;\; w(x) = \frac{q_0 L^4}{24EI}\xi^2\left(1-\xi\right)^2 \\ \phi_x(x) = -\frac{dw}{dx} &= -\frac{q_0 L^3}{12EI}\left(\xi - 3\xi^2 + 2\xi^3\right), \;\; M(x) = -EI\frac{d^2w}{dx^2} = \frac{q_0 L^2}{12}\left(1 - 6\xi + 6\xi^2\right) \\ V(x) &= \frac{q_0 L}{2}\left(2\xi - 1\right), \;\; \sigma(x, 0.5h) = \frac{q_0 L^2}{24I}\left(1 - 6\xi + 6\xi^2\right) \end{aligned} \tag{6.4.10}$$

Tables 6.4 and 6.5 contain the normalized center deflection and stress, respectively, for the clamped-clamped (C-C) homogeneous beam. From the results it is clear that the mixed dual mesh finite domain models and finite element results are very close, if not identical. The displacement finite element model is the most accurate by virtue of the higher (Hermite cubic) approximation of the deflection.

Table 6.4: The center transverse deflection $\bar{w}(L/2) \times 10$ predicted by various models for homogeneous beams [10].

| **Mesh** | **FE-EB(D)** | **FE-EB(M)** | **FE-TB(D)** | **FE-TB(M)** | **DM-EB(M)** | **DM-TB(D)** | **DM-TB(M)** |
|---|---|---|---|---|---|---|---|
| 4 | 0.2604 | 0.2604 | 0.2445 | 0.2601 | 0.2685 | 0.2445 | 0.2688 |
| 8 | 0.2604 | 0.2604 | 0.2567 | 0.2601 | 0.2624 | 0.2567 | 0.2627 |
| 16 | 0.2604 | 0.2604 | 0.2597 | 0.2601 | 0.2609 | 0.2597 | 0.2612 |
| 32 | 0.2604 | 0.2604 | 0.2605 | 0.2601 | 0.2606 | 0.2605 | 0.2608 |
| 64 | 0.2604 | 0.2604 | 0.2607 | 0.2601 | 0.2604 | 0.2607 | 0.2608 |
| **Exact** | 0.2604 | 0.2604 | 0.2607 | 0.2607 | 0.2604 | 0.2607 | 0.2607 |

Table 6.5: The center stress $\bar{\sigma}(L/2) \times 10$ predicted by various models for homogeneous C-C beams [10].

| **Mesh** | **FE-EB(D)** | **FE-EB(M)** | **FE-TB(D)** | **FE-TB(M)** | **DM-EB(M)** | **DM-TB(D)** | **DM-TB(M)** |
|---|---|---|---|---|---|---|---|
| 4 | 0.1953 | 0.1953 | 0.1953 | 0.1953 | 0.2148 | 0.2148 | 0.2149 |
| 8 | 0.2051 | 0.2051 | 0.2051 | 0.2051 | 0.2100 | 0.2100 | 0.2100 |
| 16 | 0.2075 | 0.2075 | 0.2075 | 0.2075 | 0.2087 | 0.2087 | 0.2087 |
| 32 | 0.2082 | 0.2082 | 0.2082 | 0.2082 | 0.2084 | 0.2084 | 0.2084 |
| 64 | 0.2083 | 0.2083 | 0.2083 | 0.2083 | 0.2083 | 0.2083 | 0.2083 |
| **Exact** | 0.2083 | 0.2083 | 0.2083 | 0.2083 | 0.2083 | 0.2083 | 0.2083 |

Table 6.6 contains the normalized center deflection for the functionally graded clamped-clamped beam for different values of $n$. All of the results were obtained with 16 elements in half beam. For the C-C beams the normalized delfections do not deviate significantly from each other (they differ only in the fourth or fifth decimal point).

Table 6.6: The center transverse deflection $\bar{w}(L/2) \times 10^2$ of FGM C-C beams predicted by various models [10].

| n | **FE-EB(D)** | **FE-TB(D)** | **FE-EB(M)** | **FE-TB(M)** | **DM-EB(M)** | **DM-TB(D)** | **DM-TB(M)** |
|---|---|---|---|---|---|---|---|
| 0.0 | 0.26040 | 0.26070 | 0.26040 | 0.26070 | 0.26093 | 0.25972 | 0.26125 |
| 1.0 | 0.26019 | 0.25965 | 0.26019 | 0.26044 | 0.26058 | 0.25965 | 0.26084 |
| 2.0 | 0.26004 | 0.25964 | 0.26004 | 0.26028 | 0.26037 | 0.25964 | 0.26060 |
| 3.0 | 0.26000 | 0.25965 | 0.26000 | 0.26025 | 0.26031 | 0.25965 | 0.26055 |
| 5.0 | 0.26002 | 0.25968 | 0.26002 | 0.26031 | 0.26034 | 0.25968 | 0.26062 |
| 10.0 | 0.26013 | 0.25976 | 0.26013 | 0.26049 | 0.26050 | 0.25976 | 0.26086 |
| 15.0 | 0.26021 | 0.25979 | 0.26021 | 0.26060 | 0.26062 | 0.25979 | 0.26100 |
| 20.0 | 0.26026 | 0.25980 | 0.26026 | 0.26066 | 0.26069 | 0.25980 | 0 .26109 |

# 7. DUAL MESH CONTROL DOMAIN METHOD FOR BENDING ANALYSIS OF FUNCTIONALLY GRADED PLATES *

## 7.1 Introduction

In this chapter we consider the bending analysis of functionally graded axisymmetric circular plates and functionally graded rectangular plates. Dual mesh control domain formulations based on both both classical plate theory and first-order shear deformation theory are considered for axisymmetric circular plates while for rectangular plates only dual mesh control domain formulation based on first-order shear deformation is considered. Two constituent through-thickness functionally graded plates, with power-law variation of modulus of elasticity while keeping the Poisson's ratio constant, are considered. If the $z$-coordinate is taken along the thickness of the plate then the variation of Young's modulus is then given by (see Reddy [85])

$$E(z) = (E_1 - E_2)f(z) + E_2, \qquad f(z) = \left(\frac{1}{2} + \frac{z}{H}\right)^n \tag{7.1.1}$$

where $E_1$ and $E_2$ are the material properties of the top and bottom faces of the plate, respectively, $n$ is the power-law index, and $H$ is the plate thickness. Note that when $n = 0$, we obtain the single-material plate (with modulus $E_1$).

## 7.2 Governing equations of functionally graded axisymmetric circular plates

Consider a through-thickness functionally graded circular plate of thickness $H$ and radius $R$ subjected to axisymmetric distributed load $q$ (i.e., independent of the angular coordinate, $\theta$) on the top face. If further, the boundary conditions are also selected to be axisymmetric, then the plate can be considered as functionally graded axisymmetric circular plate. We select the cylindrical

*Parts of this chapter are reprinted with permission from "Bending Analysis of Functionally Graded Axisymmetric Circular Plates using the Dual Mesh Finite Domain Method," by P. Nampally and J. N. Reddy, 2020, Latin American Journal of Solids and Structures, vol. 17, no. 7, e302, Copyright (2020) Praneeth Nampally and "Bending analysis of functionally graded rectangular plates using the dual mesh control domain method," by P. Nampally, E. Ruocco, and J. N. Reddy, 2021. International Journal for Computational Methods in Engineering Science and Mechanics, vol. 0, no. 0, pp. 1–14, Copyright (2021) Taylor & Francis .

coordinate system $(r, \theta, z)$ to analyze the plate, where $r$ is the radial coordinate outward form the center of the plate $(0 \leq r \leq R)$, $z$ denotes the transverse coordinate $(-H/2 \leq z \leq H/2)$, and $\theta$ is the angular coordinate $(0 \leq \theta \leq 2\pi)$ (see figure 7.1). The displacement field of such a circular plate based on the first-order shear deformation plate theory (FSDT) are given by

$$u_r(r, \theta, z) = u(r) + z\phi(r) \tag{7.2.1a}$$

$$u_\theta(r, \theta, z) = 0 \tag{7.2.1b}$$

$$u_z(r, \theta, z) = w(r) \tag{7.2.1c}$$

The non-zero linear strains based on the above displacements would then be

$$\varepsilon_{rr} = \frac{du}{dr} + z\frac{d\phi}{dr} \tag{7.2.2a}$$

$$\varepsilon_{\theta\theta} = \frac{u}{r} + \frac{z}{r}\phi \tag{7.2.2b}$$

$$\varepsilon_{rz} = \frac{1}{2}\left(\phi + \frac{dw}{dr}\right) \tag{7.2.2c}$$

while the constitutive relations of the functionally graded axisymmetric circular plate are given by

$$\begin{Bmatrix} \sigma_{rr} \\ \sigma_{\theta\theta} \\ \sigma_{rz} \end{Bmatrix} = \frac{E(z)}{1-\nu^2} \begin{bmatrix} 1 & \nu & 0 \\ \nu & 1 & 0 \\ 0 & 0 & 1-\nu \end{bmatrix} \begin{Bmatrix} \varepsilon_{rr} \\ \varepsilon_{\theta\theta} \\ \varepsilon_{rz} \end{Bmatrix} \tag{7.2.3}$$

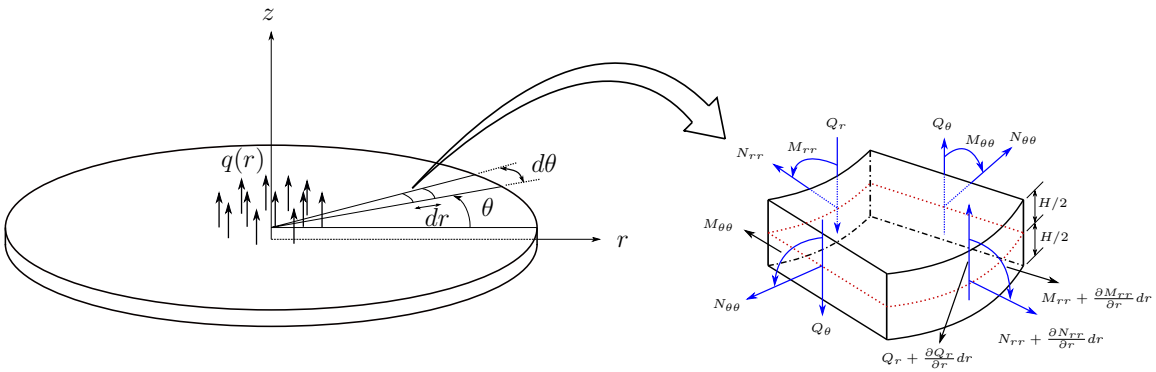


Figure 7.1: Schematic representation of the axisymmetric circular plate and various stress resultants acting on a differential element of the axisymmetric circular plate [7].

We further define the stress and moment resultants on the circular plate (see figure 7.1) as follows:

$$N_{rr} = \int_{-H/2}^{H/2} \sigma_{rr} dz = A\left[\frac{du}{dr} + \nu\frac{u}{r}\right] + B\left[\frac{d\phi}{dr} + \frac{\nu}{r}\phi\right] \tag{7.2.4a}$$

$$M_{rr} = \int_{-H/2}^{H/2} \sigma_{rr} z dz = B\left[\frac{du}{dr} + \nu\frac{u}{r}\right] + D\left[\frac{d\phi}{dr} + \frac{\nu}{r}\phi\right] \tag{7.2.4b}$$

$$N_{\theta\theta} = \int_{-H/2}^{H/2} \sigma_{\theta\theta} dz = A\left[\nu\frac{du}{dr} + \frac{u}{r}\right] + B\left[\nu\frac{d\phi}{dr} + \frac{1}{r}\phi\right] \tag{7.2.4c}$$

$$M_{\theta\theta} = \int_{-H/2}^{H/2} \sigma_{\theta\theta} z dz = B\left[\nu\frac{du}{dr} + \frac{u}{r}\right] + D\left[\nu\frac{d\phi}{dr} + \frac{1}{r}\phi\right] \tag{7.2.4d}$$

$$Q_r = \int_{-H/2}^{H/2} \sigma_{rz} dz = S\left(\phi + \frac{dw}{dr}\right) \tag{7.2.4e}$$

where

$$\begin{aligned} A &= \int_{-H/2}^{H/2} \frac{E(z)}{1-\nu^2} dz, \quad B = \int_{-H/2}^{H/2} \frac{E(z)z}{1-\nu^2} dz \\ D &= \int_{-H/2}^{H/2} \frac{E(z)z^2}{1-\nu^2} dz, \quad S = \int_{-H/2}^{H/2} \frac{K_s E(z)}{2(1+\nu)} dz \end{aligned} \tag{7.2.5}$$

The explicit expressions of the above integrals for the power-law variation of $E(z)$ (see Eq. (7.1.1))

are given as

$$
\begin{aligned}
A &= \frac{(E_1 - E_2)H}{(n+1)(1-\nu^2)} + \frac{E_2 H}{1-\nu^2} \\
B &= \frac{(E_1 - E_2)H^2}{1-\nu^2}\left[\frac{1}{n+2} - \frac{1}{2(n+1)}\right] \\
D &= \frac{(E_1 - E_2)H^3}{1-\nu^2}\left[\frac{1}{n+3} + \frac{1}{4(n+1)} - \frac{1}{n+2}\right] + \frac{E_2 H^3}{12(1-\nu^2)} \\
S &= \frac{K_s(E_1 - E_2)H}{2(n+1)(1+\nu)} + \frac{K_s E_2 H}{2(1+\nu)}
\end{aligned}
\tag{7.2.6}
$$

The equations of equilibrium of the functionally graded (FG) axisymmetric circular plate can be obtained using the principle of virtual work. The virtual work statement for FG axisymmetric circular plate is

$$
\int_0^{2\pi}\int_0^R\int_{-H/2}^{H/2} \left(\sigma_{rr}\delta\varepsilon_{rr} + \sigma_{\theta\theta}\delta\varepsilon_{\theta\theta} + 2\sigma_{rz}\delta\varepsilon_{rz}\right) r dz dr d\theta - \int_0^{2\pi}\int_0^R q\delta w r dr d\theta = 0 \tag{7.2.7}
$$

Now using the stress and moment resultant definitions of Eqs. (7.2.4a)-(7.2.4e) and strain definition of Eqs. (7.2.2a)-(7.2.2c) we can rewrite the virtual work statement as

$$
\int_0^R \left[N_{rr}\left(\frac{d\delta u}{dr}\right) + M_{rr}\left(\frac{d\delta\phi}{dr}\right) + \frac{N_{\theta\theta}}{r}\delta u + \frac{M_{\theta\theta}}{r}\delta\phi + Q_r\left(\delta\phi + \frac{d\delta w}{dr}\right) - q\delta w\right] r dr = 0 \tag{7.2.8}
$$

The governing differential equations of the FG axisymmetric circular plate are obtained by taking the Euler-Lagrange equations of the above variational statement. The resulting governing equations read

$$
-\frac{1}{r}\frac{d}{dr}\left(rN_{rr}\right) + \frac{N_{\theta\theta}}{r} = 0 \tag{7.2.9}
$$

$$
-\frac{1}{r}\frac{d}{dr}(rQ_r) - q = 0 \tag{7.2.10}
$$

$$
-\frac{1}{r}\left[\frac{d}{dr}\left(rM_{rr}\right) - M_{\theta\theta}\right] + Q_r = 0 \tag{7.2.11}
$$

The governing equations derived above are based on the first-order shear deformation theory, where the transverse shear strain is non-zero and assumes a constant value (and hence require the shear correction factor, $K_s$ in Eq. (7.2.5)). However, as the radius to thickness ratio of the circular plate increases the shear strains are known to tend to zero. In such cases we may also use classical plate theory (i.e., based on Kirchhoff hypothesis) to predict the plate behavior. To accommodate zero transverse shear strains the value of $\phi$ in FSDT is taken to be $-\frac{dw}{dr}$ and hence the displacement field of FG axisymmetric circular plate based on classical plate theory (CPT) would become

$$u_r(r,\theta,z) = u(r) - z\frac{dw}{dr} \tag{7.2.12a}$$

$$u_\theta(r,\theta,z) = 0 \tag{7.2.12b}$$

$$u_z(r,\theta,z) = w(r) \tag{7.2.12c}$$

The stress and moment resultants on the FG axisymmetric circular plate based on the classical plate theory would then be

$$N_{rr} = \int_{-H/2}^{H/2} \sigma_{rr} dz = A\left[\frac{du}{dr} + \nu\frac{u}{r}\right] - B\left[\frac{d^2w}{dr^2} + \frac{\nu}{r}\frac{dw}{dr}\right] \tag{7.2.13a}$$

$$M_{rr} = \int_{-H/2}^{H/2} \sigma_{rr} z dz = B\left[\frac{du}{dr} + \nu\frac{u}{r}\right] - D\left[\frac{d^2w}{dr^2} + \frac{\nu}{r}\frac{dw}{dr}\right] \tag{7.2.13b}$$

$$N_{\theta\theta} = \int_{-H/2}^{H/2} \sigma_{\theta\theta} dz = A\left[\nu\frac{du}{dr} + \frac{u}{r}\right] - B\left[\nu\frac{d^2w}{dr^2} + \frac{1}{r}\frac{dw}{dr}\right] \tag{7.2.13c}$$

$$M_{\theta\theta} = \int_{-H/2}^{H/2} \sigma_{\theta\theta} z dz = B\left[\nu\frac{du}{dr} + \frac{u}{r}\right] - D\left[\nu\frac{d^2w}{dr^2} + \frac{1}{r}\frac{dw}{dr}\right] \tag{7.2.13d}$$

In this case the transverse shear strain vanishes; however, the governing equations remain the same as those listed in Eqs. (7.2.9)-(7.2.11) with the exception that the shear stress resultant $Q_r$ can only be expressed in terms of the moments $M_{rr}$ and $M_{\theta\theta}$ as given by Eq. (7.2.11) rather than directly computing in terms of shear strain (which is zero in this case).

The governing differential equations of FG axisymmetric circular plate based on the FSDT can be expressed in terms of the generalized displacements ($u$, $w$, $\phi$) by substituting the expressions

of stress and moment resultants of Eqs. (7.2.4a)-(7.2.4e) into Eqs. (7.2.9)-(7.2.11). The resulting equations are listed below.

$$-\frac{1}{r}\frac{d}{dr}\left[rA\left(\frac{du}{dr}+\nu\frac{u}{r}\right)+rB\left(\frac{d\phi}{dr}+\frac{\nu}{r}\phi\right)\right] + \frac{A}{r}\left(\nu\frac{du}{dr}+\frac{u}{r}\right)+\frac{B}{r}\left(\nu\frac{d\phi}{dr}+\frac{1}{r}\phi\right)=0 \tag{7.2.14}$$

$$-\frac{1}{r}\frac{d}{dr}\left[rS\left(\phi+\frac{dw}{dr}\right)\right]-q=0 \tag{7.2.15}$$

$$-\frac{1}{r}\frac{d}{dr}\left[rB\left(\frac{du}{dr}+\nu\frac{u}{r}\right)+rD\left(\frac{d\phi}{dr}+\frac{\nu}{r}\phi\right)\right] + \frac{B}{r}\left(\nu\frac{du}{dr}+\frac{u}{r}\right)+\frac{D}{r}\left(\nu\frac{d\phi}{dr}+\frac{1}{r}\phi\right)+S\left(\phi+\frac{dw}{dr}\right)=0 \tag{7.2.16}$$

Similarly, the governing differential equations of FG axisymmetric circular plate based on CPT can be expressed in terms of the displacements $u$ and $w$ by first expressing Eq. (7.2.10) in terms of moments $M_{rr}$ and $M_{\theta\theta}$ using Eq. (7.2.11) as

$$-\frac{1}{r}\left[\frac{d}{dr}(rM_{rr})-M_{\theta\theta}\right]-q=0 \tag{7.2.17}$$

and then substituting the stress and moment resultants of Eqs. (7.2.13a)-(7.2.13d) into the above equation and Eq. (7.2.9) to give

$$-\frac{1}{r}\frac{d}{dr}\left[rA\left(\frac{du}{dr}+\nu\frac{u}{r}\right)-rB\left(\frac{d^2w}{dr^2}+\frac{\nu}{r}\frac{dw}{dr}\right)\right] +\frac{A}{r}\left(\nu\frac{du}{dr}+\frac{u}{r}\right)-\frac{B}{r}\left(\nu\frac{d^2w}{dr^2}+\frac{1}{r}\frac{dw}{dr}\right)=0 \tag{7.2.18}$$

$$-\frac{1}{r}\frac{d}{dr}\left[\frac{d}{dr}\left[rB\left(\frac{du}{dr}+\nu\frac{u}{r}\right)-rD\left(\frac{d^2w}{dr^2}+\frac{\nu}{r}\frac{dw}{dr}\right)\right] -B\left(\nu\frac{du}{dr}+\frac{u}{r}\right)+D\left(\nu\frac{d^2w}{dr^2}+\frac{1}{r}\frac{dw}{dr}\right)\right]-q=0 \tag{7.2.19}$$

## 7.3 DMCDM for axisymmetric circular plates

In this section we will derive the dual mesh control domain equations of axisymmetric circular plates based on classical plate theory and first-order shear deformation theory. Mixed dual mesh control domain method is derived for classical plate theory and displacement dual mesh control domain method is derived for first-order shear deformation theory.

### 7.3.1 Mixed DMCDM for axisymmetric circular plates based on classical plate theory

The governing equations FG axisymmetric circular plate based on the classical plate theory when expressed in terms of the displacements, $u$ and $w$, would result in fourth order differential equations. However, since the dual mesh control domain method is applicable only for first-order or second-order differential equations, we will recast the governing equations (7.2.9)-(7.2.11) as second-order differential equations such that the primary variables of the resulting equations are $\{u, w, M_{rr}\}$. First, we will consider the equations (7.2.13a) and (7.2.13b). From these two equations we can write an expression of $N_{rr}$ in terms of $u$ and $M_{rr}$. Similarly, $N_{\theta\theta}$ can be expressed in terms of $u$ and $M_{\theta\theta}$ using the equations (7.2.13c) and (7.2.13d). In the following we list the resulting equations after some algebraic manipulations.

$$N_{rr} = \overline{A}\left(\frac{du}{dr} + \nu\frac{u}{r}\right) + \overline{B}M_{rr} \tag{7.3.1}$$

$$N_{\theta\theta} = \overline{A}\left(\nu\frac{du}{dr} + \frac{u}{r}\right) + \overline{B}M_{\theta\theta} \tag{7.3.2}$$

where

$$\overline{A} = \frac{D^*}{D} = \frac{AD - B^2}{D}, \quad \overline{B} = \frac{B}{D}$$

To eliminate $M_{\theta\theta}$ from Eq. (7.3.2) we use Eq. (7.2.13b) and Eq. (7.2.13d) to obtain

$$M_{\theta\theta} = \nu M_{rr} + B(1-\nu^2)\frac{u}{r} - \frac{D(1-\nu^2)}{r}\frac{dw}{dr} \tag{7.3.3}$$

Thus $N_{\theta\theta}$ can be written as

$$N_{\theta\theta} = \overline{A}\left(\nu\frac{du}{dr} + \frac{u}{r}\right) + \overline{B}\nu M_{rr} + \frac{B^2(1-\nu^2)}{D}\frac{u}{r} - \frac{B(1-\nu^2)}{r}\frac{dw}{dr} \tag{7.3.4}$$

Finally, Eq. (7.2.13b) can be expressed as

$$-\left(\frac{d^2w}{dr^2} + \frac{\nu}{r}\frac{dw}{dr}\right) + \overline{B}\left(\frac{du}{dr} + \nu\frac{u}{r}\right) - \frac{1}{D}M_{rr} = 0 \tag{7.3.5}$$

The governing equations of FG axisymmetric circular plate based on classical plate theory in terms of $\{u, w, M_{rr}\}$ would then be given by Eq. (7.2.9), Eq. (7.2.17) and Eq. (7.3.5); wherein the expressions for $N_{rr}$, $N_{\theta\theta}$ and $M_{\theta\theta}$ are obtained from Eqs. (7.3.1), (7.3.4) and (7.3.3) respectively. The resulting final equations are as follows:

$$\begin{aligned} -\frac{1}{r}\frac{d}{dr}\left[r\overline{A}\left(\frac{du}{dr} + \nu\frac{u}{r}\right) + r\overline{B}M_{rr}\right] + \frac{\overline{A}}{r}\left(\nu\frac{du}{dr} + \frac{u}{r}\right) \\ + \frac{\overline{B}\nu}{r}M_{rr} - \frac{B(1-\nu^2)}{r^2}\frac{dw}{dr} + \frac{B^2(1-\nu^2)}{Dr^2}u = 0 \end{aligned} \tag{7.3.6}$$

$$-\frac{1}{r}\frac{d}{dr}\left[r\frac{dM_{rr}}{dr} + (1-\nu)M_{rr} - \frac{B(1-\nu^2)}{r}u + \frac{D(1-\nu^2)}{r}\frac{dw}{dr}\right] - q = 0 \tag{7.3.7}$$

$$-\frac{1}{r}\frac{d}{dr}\left(r\frac{dw}{dr}\right) + \frac{(1-\nu)}{r}\frac{dw}{dr} + \overline{B}\left(\frac{du}{dr} + \nu\frac{u}{r}\right) - \frac{1}{D}M_{rr} = 0 \tag{7.3.8}$$

As noted earlier, the dual mesh control domain method is only applicable to equations of second order or less. Thus we develop dual mesh control domain formulation of the FG axisymmetric circular plate based on classical plate theory using the governing equations (7.3.6)-(7.3.8). The resulting formulation is called mixed dual mesh control domain method (see [10]) since the formulation has both generalized displacements $(u, w)$ and the moment $(M_{rr})$ as the primary variables. This is similar to the mixed formulations of finite element method.

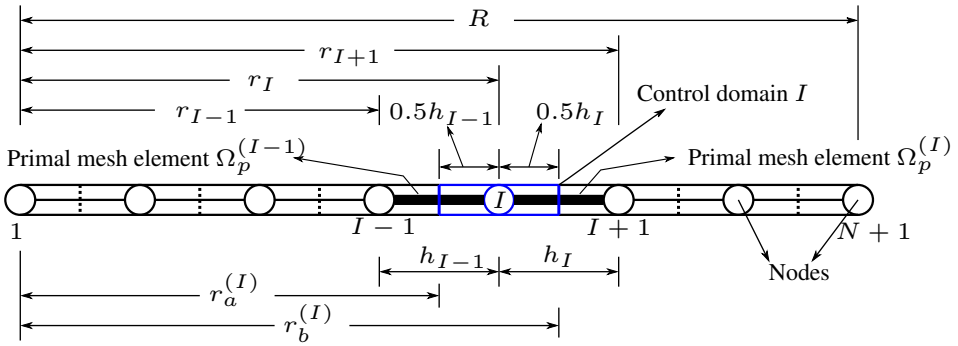


Figure 7.2: Primal mesh (primal mesh elements) and dual mesh (control domains) on the computational domain [7].

To obtain the discretized equations, we consider the computational domain $\Omega = (0, R)$ and divide it into $N$ primal mesh elements (primal mesh) such that each node has its associated control domain (dual mesh). Except for the control domains corresponding to the boundary nodes, all the interior control domains encompass two primal mesh elements (primal mesh) such that one half of each of these two primal mesh elements lie within the control domain (see figure 7.2). Thus, for a uniform primal mesh the interior nodes lie at the center of their corresponding control domains.

The dependent variables are approximated on each primal mesh element using Lagrange interpolation functions (see figure 7.3). Although different sets of interpolation functions can be used for different primary variables, in the present study we use same set of linear 1-D Lagrange interpolation functions for all the primary variables. For a typical primal mesh element $\Omega_p^{(I)} = (r_I, r_{I+1})$, the primary variables can thus be approximated using the set of linear 1-D Lagrange interpolation functions $\{\psi_1^{(I)}, \psi_2^{(I)}\}$ as

$$\begin{aligned} u(r) &\approx U_I \psi_1^{(I)}(r) + U_{I+1} \psi_2^{(I)}(r), \\ w(r) &\approx W_I \psi_1^{(I)}(r) + W_{I+1} \psi_2^{(I)}(r) \\ M_{rr}(r) &\approx M_{rr_I} \psi_1^{(I)}(r) + M_{rr_{I+1}} \psi_2^{(I)}(r) \end{aligned} \tag{7.3.9}$$

Here $U_I$, $W_I$, $M_{rr_I}$ represent the values of $u$, $w$ and $M_{rr}$ respectively at node $I$, while $U_{I+1}$, $W_{I+1}$, $M_{rr_{I+1}}$ represent the values of $u$, $w$ and $M_{rr}$ respectively at node $I+1$. It should be noted that when

Eq. (7.2.18) and Eq. (7.2.19) are used in developing finite element equations, a minimum of cubic Hermite interpolation is needed on the transverse deflection $w$ and linear Lagrange interpolation is needed on $u$ [93]. However, for the mixed formulations, akin to the one considered here, a minimum of linear Lagrange interpolations on all the primary variables would suffice [10]. The linear Lagrange interpolation functions $\psi_1^{(I)}$ and $\psi_2^{(I)}$ on a typical primal mesh element $\Omega_p^{(I)}$ are given by

$$\psi_1^{(I)} = \frac{r_{I+1} - r}{h_I}, \qquad \psi_1^{(I)} = \frac{r - r_I}{h_I} \quad \text{where} \quad h_I = r_{I+1} - r_I$$

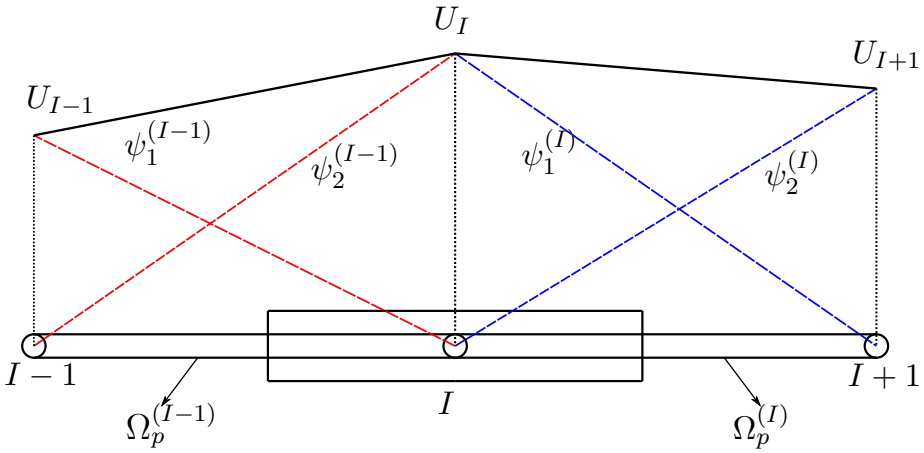


Figure 7.3: Lagrange interpolation functions on the primal mesh elements $\Omega_p^{(I-1)}$ and $\Omega_p^{(I)}$ for variable $u$ [7].

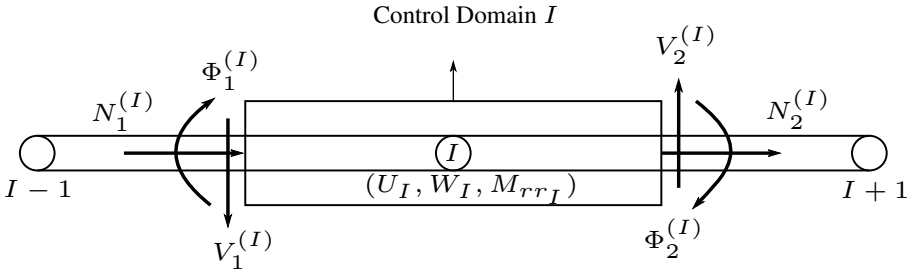


Figure 7.4: A typical control domain for the mixed model of CPT with the secondary variables at the faces and the primary variables at the node associated with the control domain [7].

Now we proceed to develop the discretized equations corresponding to Eqs. (7.3.6)-(7.3.8) by writing their integral statements on a typical interior control domain $(r_a^{(I)}, r_b^{(I)})$, associated with node $I$ (see figure 7.4).

$$\int_{r_a^{(I)}}^{r_b^{(I)}} \left\{ -\frac{1}{r}\frac{d}{dr}\left[ r\overline{A}\left(\frac{du}{dr}+\nu\frac{u}{r}\right) + r\overline{B}M_{rr}\right] + \frac{\overline{A}}{r}\left(\nu\frac{du}{dr}+\frac{u}{r}\right) + \frac{\overline{B}\nu}{r}M_{rr} - \frac{B(1-\nu^2)}{r^2}\frac{dw}{dr} + \frac{B^2(1-\nu^2)}{Dr^2}u \right\} r dr = 0 \quad (7.3.10)$$

$$\int_{r_a^{(I)}}^{r_b^{(I)}} \left\{ -\frac{1}{r}\frac{d}{dr}\left[ \frac{d}{dr}(rM_{rr}) - \nu M_{rr} - \frac{B(1-\nu^2)}{r}u + \frac{D(1-\nu^2)}{r}\frac{dw}{dr}\right] - q \right\} r dr = 0 \quad (7.3.11)$$

$$\int_{r_a^{(I)}}^{r_b^{(I)}} \left\{ -\left(\frac{d^2w}{dr^2}+\frac{\nu}{r}\frac{dw}{dr}\right) + \overline{B}\left(\frac{du}{dr}+\nu\frac{u}{r}\right) - \frac{1}{D}M_{rr} \right\} r dr = 0 \quad (7.3.12)$$

The first step in developing the discritized equations is to carry out the indicated integration of Eqs. (7.3.10)-(7.3.12) such that the resulting boundary terms represent physically meaningful secondary variables which are dual to the primary variables. Eqs. (7.3.10)-(7.3.12) after such

integration are listed below.

$$-N_1^{(I)} - N_2^{(I)} + \int_{r_a^{(I)}}^{r_b^{(I)}} \left\{ \frac{\overline{A}}{r}\left(\nu\frac{du}{dr} + \frac{u}{r}\right) + \frac{\overline{B}\nu}{r}M_{rr} - \frac{B(1-\nu^2)}{r^2}\frac{dw}{dr} + \frac{B^2(1-\nu^2)}{Dr^2}u \right\} rdr = 0 \tag{7.3.13}$$

$$-V_1^{(I)} - V_2^{(I)} - \int_{r_a^{(I)}}^{r_b^{(I)}} qrdr = 0 \tag{7.3.14}$$

$$-\Phi_1^{(I)} - \Phi_2^{(I)} + \int_{r_a^{(I)}}^{r_b^{(I)}} \left\{ \frac{1-\nu}{r}\frac{dw}{dr} + \overline{B}\left(\frac{du}{dr} + \frac{\nu}{r}u\right) - \frac{1}{D}M_{rr} \right\} rdr = 0 \tag{7.3.15}$$

In the above equations the secondary variables are defined as follows

$$N_1^{(I)} = -\left[ r\overline{A}\left(\frac{du}{dr} + \frac{\nu}{r}u\right) + r\overline{B}M_{rr} \right]_{r=r_a^{(I)}} \tag{7.3.16a}$$

$$N_2^{(I)} = \left[ r\overline{A}\left(\frac{du}{dr} + \frac{\nu}{r}u\right) + r\overline{B}M_{rr} \right]_{r=r_b^{(I)}} \tag{7.3.16b}$$

$$V_1^{(I)} = -\left[ \frac{d}{dr}\left(rM_{rr}\right) - \nu M_{rr} - \frac{B(1-\nu^2)}{r}u + \frac{D(1-\nu^2)}{r}\frac{dw}{dr} \right]_{r=r_a^{(I)}} \tag{7.3.17a}$$

$$V_2^{(I)} = \left[ \frac{d}{dr}\left(rM_{rr}\right) - \nu M_{rr} - \frac{B(1-\nu^2)}{r}u + \frac{D(1-\nu^2)}{r}\frac{dw}{dr} \right]_{r=r_b^{(I)}} \tag{7.3.17b}$$

$$\Phi_1^{(I)} = \left[ -r\frac{dw}{dr} \right]_{r=r_a^{(I)}} \tag{7.3.18a}$$

$$\Phi_2^{(I)} = \left[ r\frac{dw}{dr} \right]_{r=r_b^{(I)}} \tag{7.3.18b}$$

Here ($N_1^{(I)}$, $V_1^{(I)}$, $\Phi_1^{(I)}$) represent the axial force, shear force and rotation respectively at the left face of the control domain numbered $I$ (i.e., $r = r_a^{(I)}$), while ($N_2^{(I)}$, $V_2^{(I)}$, $\Phi_2^{(I)}$) represent axial force, shear force and rotation respectively at right face of the control domain numbered $I$ (i.e.,

$r = r_b^{(I)}$) (see figure 7.4). Since all the primary variables are approximated using linear Lagrange interpolation functions on each finite element, the boundary terms given in Eqs. (7.3.16a)-(7.3.18b) can be easily evaluated (see Appendix C), while the integrations of Eqs. (7.3.13)-(7.3.15) can be either evaluated numerically (see, e.g., Gauss quadrature rule) or exactly. In the present study we use Gauss quadrature to evaluate the integral expressions. Thus for an interior node $I$ associated with interior control domain numbered $I$ the discretized equations would read

$$
\begin{aligned}
&U_{I-1}\left[-\frac{r_a^{(I)}\overline{A}_{I-1}}{h_{I-1}}+\frac{\overline{A}_{I-1}\nu_{I-1}}{2}+\int_{r_a^{(I)}}^{r_I}\left(\overline{A}_{I-1}\nu_{I-1}\frac{d\psi_1^{(I-1)}}{dr}+\frac{\overline{A}_{I-1}}{r}\psi_1^{(I-1)}\right.\right.\\
&\left.\left.+\frac{B_{I-1}^2(1-\nu_{I-1}^2)}{rD_{I-1}}\psi_1^{(I-1)}\right)dr\right]+W_{I-1}\left[\int_{r_a^{(I)}}^{r_I}\left(\frac{B_{I-1}(\nu_{I-1}^2-1)}{r}\frac{d\psi_1^{(I-1)}}{dr}\right)dr\right]\\
&+M_{rr_{I-1}}\left[\frac{r_a^{(I)}\overline{B}_{I-1}}{2}+\int_{r_a^{(I)}}^{r_I}\left(\overline{B}_{I-1}\nu_{I-1}\psi_1^{(I-1)}\right)dr\right]+U_I\left[\frac{r_a^{(I)}\overline{A}_{I-1}}{h_{I-1}}+\frac{r_b^{(I)}\overline{A_I}}{h_I}\right.\\
&\left.-\frac{\overline{A}_I\nu_I-\overline{A}_{I-1}\nu_{I-1}}{2}+\int_{r_a^{(I)}}^{r_I}\left(\overline{A}_{I-1}\nu_{I-1}\frac{d\psi_2^{(I-1)}}{dr}+\frac{\overline{A}_{I-1}}{r}\psi_2^{(I-1)}\right)dr\right.\\
&+\int_{r_I}^{r_b^{(I)}}\left(\overline{A}_I\nu_I\frac{d\psi_1^{(I)}}{dr}+\frac{\overline{A}_I}{r}\psi_1^{(I)}\right)dr+\int_{r_a^{(I)}}^{r_I}\left(\frac{B_{I-1}^2(1-\nu_{I-1}^2)}{rD_{I-1}}\psi_2^{(I-1)}\right)dr\\
&+\int_{r_I}^{r_b^{(I)}}\left(\frac{B_I^2(1-\nu_I^2)}{rD_I}\psi_1^{(I)}\right)dr\Bigg]+W_I\left[\int_{r_a^{(I)}}^{r_I}\left(\frac{B_{I-1}(\nu_{I-1}^2-1)}{r}\frac{d\psi_2^{(I-1)}}{dr}\right)dr\right.\\
&+\int_{r_I}^{r_b^{(I)}}\left(\frac{B_I(\nu_I^2-1)}{r}\frac{d\psi_1^{(I)}}{dr}\right)dr\Bigg]+M_{rr_I}\left[\int_{r_a^{(I)}}^{r_I}\left(\overline{B}_{I-1}\nu_{I-1}\psi_2^{(I-1)}\right)dr\right.\\
&\left.+\int_{r_I}^{r_b^{(I)}}\left(\overline{B}_I\nu_I\psi_1^{(I)}\right)dr-\frac{r_b^{(I)}\overline{B}_I-r_a^{(I)}\overline{B}_{I-1}}{2}\right]\\
&+U_{I+1}\left[-\frac{r_b^{(I)}\overline{A}_I}{h_I}-\frac{\overline{A}_I\nu_I}{2}+\int_{r_I}^{r_b^{(I)}}\left(\overline{A}_I\nu_I\frac{d\psi_2^{(I)}}{dr}+\frac{\overline{A}_I}{r}\psi_2^{(I)}\right)dr\right.\\
&+\int_{r_I}^{r_b^{(I)}}\left(\frac{B_I^2(1-\nu_I^2)}{rD_I}\psi_2^{(I)}\right)dr\Bigg]+W_{I+1}\left[\int_{r_I}^{r_b^{(I)}}\left(\frac{B_I(\nu_I^2-1)}{r}\frac{d\psi_2^{(I)}}{dr}\right)dr\right]\\
&+M_{rr_{I+1}}\left[\int_{r_I}^{r_b^{(I)}}\left(\overline{B}_I\nu_I\psi_2^{(I)}\right)dr-\frac{r_b^{(I)}\overline{B}_I}{2}\right]=0
\end{aligned}
\tag{7.3.19}
$$

$$U_{I-1}\left[-\frac{B_{I-1}(1-\nu_{I-1}^2)}{2r_a^{(I)}}\right]+W_{I-1}\left[-\frac{D_{I-1}(1-\nu_{I-1}^2)}{r_a^{(I)}h_{I-1}}\right]+M_{rr_{I-1}}\left[\frac{1}{2}-\frac{r_a^{(I)}}{h_{I-1}}-\frac{\nu_{I-1}}{2}\right]$$
$$+U_I\left[\frac{B_I(1-\nu_I^2)}{2r_b^{(I)}}-\frac{B_{I-1}(1-\nu_{I-1}^2)}{2r_a^{(I)}}\right]+W_I\left[\frac{D_{I-1}(1-\nu_{I-1}^2)}{r_a^{(I)}h_{I-1}}+\frac{D_I(1-\nu_I^2)}{r_b^{(I)}h_I}\right]$$
$$+M_{rr_I}\left[\frac{r_a^{(I)}}{h_{I-1}}+\frac{r_b^{(I)}}{h_I}+\frac{\nu_I-\nu_{I-1}}{2}\right]+U_{I+1}\left[\frac{B_I(1-\nu_I^2)}{2r_b^{(I)}}\right]+W_{I+1}\left[-\frac{D_I(1-\nu_I^2)}{r_b^{(I)}h_I}\right]$$
$$+M_{rr_{I+1}}\left[-\frac{1}{2}-\frac{r_b^{(I)}}{h_I}+\frac{\nu_I}{2}\right]-\int_{r_a^{(I)}}^{r_b^{(I)}}qrdr=0 \tag{7.3.20}$$

$$U_{I-1}\left[\int_{r_a^{(I)}}^{r_I}\left(\overline{B}_{I-1}r\frac{d\psi_1^{(I-1)}}{dr}+\overline{B}_{I-1}\nu_{I-1}\psi_1^{(I-1)}\right)dr\right]+W_{I-1}\left[-\frac{r_a^{(I)}}{h_{I-1}}\right.$$
$$\left.+\int_{r_a^{(I)}}^{r_I}\left((1-\nu_{I-1})\frac{d\psi_1^{(I-1)}}{dr}\right)dr\right]-M_{rr_{I-1}}\left[\int_{r_a^{(I)}}^{r_I}\left(\frac{r}{D_{I-1}}\psi_1^{(I-1)}\right)dr\right]$$
$$+U_I\left[\int_{r_a^{(I)}}^{r_I}\left(\overline{B}_{I-1}r\frac{d\psi_2^{(I-1)}}{dr}+\overline{B}_{I-1}\nu_{I-1}\psi_2^{(I-1)}\right)dr\right.$$
$$\left.+\int_{r_I}^{r_b^{(I)}}\left(\overline{B}_Ir\frac{d\psi_1^{(I)}}{dr}+\overline{B}_I\nu_I\psi_1^{(I)}\right)dr\right]+W_I\left[\frac{r_a^{(I)}}{h_{I-1}}+\int_{r_a^{(I)}}^{r_I}\left((1-\nu_{I-1})\frac{d\psi_2^{(I-1)}}{dr}\right)dr\right.$$
$$\left.+\frac{r_b^{(I)}}{h_I}+\int_{r_I}^{r_b^{(I)}}\left((1-\nu_I)\frac{d\psi_1^{(I)}}{dr}\right)dr\right]-M_{rr_I}\left[\int_{r_a^{(I)}}^{r_I}\left(\frac{r}{D_{I-1}}\psi_2^{(I-1)}\right)dr\right.$$
$$\left.+\int_{r_I}^{r_b^{(I)}}\left(\frac{r}{D_I}\psi_1^{(I)}\right)dr\right]+U_{I+1}\left[\int_{r_I}^{r_b^{(I)}}\left(\overline{B}_Ir\frac{d\psi_2^{(I)}}{dr}+\overline{B}_I\nu_I\psi_2^{(I)}\right)dr\right]$$
$$+W_{I+1}\left[-\frac{r_b^{(I)}}{h_I}+\int_{r_I}^{r_b^{(I)}}\left((1-\nu_I)\frac{d\psi_2^{(I)}}{dr}\right)dr\right]-M_{rr_{I+1}}\left[\int_{r_I}^{r_b^{(I)}}\left(\frac{r}{D_I}\psi_2^{(I)}\right)dr\right]=0 \tag{7.3.21}$$

In the above equations $\overline{B}_{I-1}$ represents the value of $\overline{B}$ in the primal mesh element $\Omega_p^{(I-1)}$ and $\overline{B}_I$ represents the value of $\overline{B}$ in the primal mesh element $\Omega_p^{(I)}$. Similar meaning applies to other coefficients $\overline{A}$, $\nu$, $B$ and $D$.

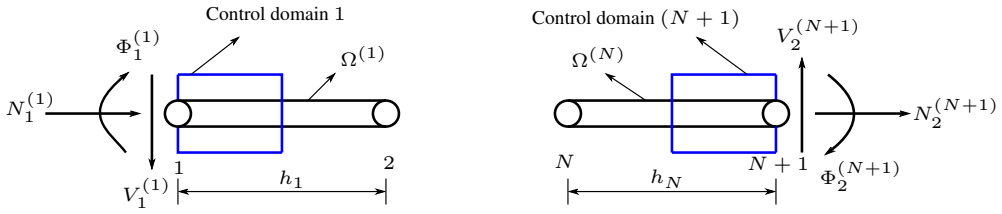


Figure 7.5: Secondary variables on the boundary control domains [7].

In a similar fashion, the discretized equations for the control domain 1 (see figure 7.5) would be

$$
\begin{aligned}
&-N_1^{(1)} + U_1\left[\frac{\overline{A}_1(1-\nu_1)}{2} + \int_0^{0.5h_1}\left(\overline{A}_1\nu_1\frac{d\psi_1^{(1)}}{dr} + \frac{\overline{A}_1}{r}\psi_1^{(1)} + \frac{B_1^2(1-\nu_1^2)}{rD_1}\psi_1^{(1)}\right)dr\right] \\
&+ W_1\left[\int_0^{0.5h_1}\left(\frac{B_1(\nu_1^2-1)}{r}\frac{d\psi_1^{(1)}}{dr}\right)dr\right] + M_{rr_1}\left[\int_0^{0.5h_1}\overline{B}_1\nu_1\psi_1^{(1)}dr - \frac{\overline{B}_1h_1}{4}\right] \\
&+ U_2\left[-\frac{\overline{A}_1(1+\nu_1)}{2} + \int_0^{0.5h_1}\left(\overline{A}_1\nu_1\frac{d\psi_2^{(1)}}{dr} + \frac{\overline{A}_1}{r}\psi_2^{(1)} + \frac{B_1^2(1-\nu_1^2)}{rD_1}\psi_2^{(1)}\right)dr\right] \\
&+ W_2\left[\int_0^{0.5h_1}\left(\frac{B_1(\nu_1^2-1)}{r}\frac{d\psi_2^{(1)}}{dr}\right)dr\right] + M_{rr_2}\left[\int_0^{0.5h_1}\overline{B}_1\nu_1\psi_2^{(1)}dr - \frac{\overline{B}_1h_1}{4}\right] = 0 \quad (7.3.22)
\end{aligned}
$$

$$
\begin{aligned}
&-V_1^{(1)} + U_1\left[\frac{B_1(1-\nu_1^2)}{h_1}\right] + W_1\left[\frac{2D_1(1-\nu_1^2)}{h_1^2}\right] + M_{rr_1}\left[\frac{\nu_1}{2}\right] \\
&+ U_2\left[\frac{B_1(1-\nu_1^2)}{h_1}\right] + W_2\left[-\frac{2D_1(1-\nu_1^2)}{h_1^2}\right] + M_{rr_2}\left[-1+\frac{\nu_1}{2}\right] - \int_0^{0.5h_1} qrdr = 0 \quad (7.3.23)
\end{aligned}
$$

$$
\begin{aligned}
&-\Phi_1^{(1)} + U_1\left[\int_0^{0.5h_1}\left(\overline{B}_1r\frac{d\psi_1^{(1)}}{dr} + \overline{B}_1\nu_1\psi_1^{(1)}\right)dr\right] + W_1\left[\frac{1}{2} + \int_0^{0.5h_1}\left((1-\nu_1)\frac{d\psi_1^{(1)}}{dr}\right)dr\right] \\
&+ U_2\left[\int_0^{0.5h_1}\left(\overline{B}_1r\frac{d\psi_2^{(1)}}{dr} + \overline{B}_1\nu_1\psi_2^{(1)}\right)dr\right] + W_2\left[-\frac{1}{2} + \int_0^{0.5h_1}\left((1-\nu_1)\frac{d\psi_2^{(1)}}{dr}\right)dr\right] \\
&- M_{rr_1}\left[\int_0^{0.5h_1}\left(\frac{r}{D_1}\psi_1^{(1)}\right)dr\right] - M_{rr_2}\left[\int_0^{0.5h_1}\left(\frac{r}{D_1}\psi_2^{(1)}\right)dr\right] = 0 \quad (7.3.24)
\end{aligned}
$$

Finally, the discretized equations on $(N+1)^{th}$ control domain (see figure 7.5) would be

$$
\begin{aligned}
&-N_2^{(N+1)} + U_N \left[ -\frac{(R-0.5h_N)\overline{A}_N}{h_N} + \frac{\overline{A}_N \nu_N}{2} \right. \\
&\left. + \int_{R-0.5h_N}^{R} \left( \overline{A}_N \nu_N \frac{d\psi_1^{(N)}}{dr} + \frac{\overline{A}_N}{r}\psi_1^{(N)} + \frac{B_N^2(1-\nu_N^2)}{rD_N}\psi_1^{(N)} \right) dr \right] \\
&+ W_N \left[ \int_{R-0.5h_N}^{R} \left( \frac{B_N(\nu_N^2-1)}{r} \frac{d\psi_1^{(N)}}{dr} \right) dr \right] \\
&+ M_{rr_N} \left[ \int_{R-0.5h_N}^{R} \overline{B}_N \nu_N \psi_1^{(N)} dr + \frac{\overline{B}_N(R-0.5h_N)}{2} \right] + U_{N+1} \left[ \frac{(R-0.5h_N)\overline{A}_N}{h_N} \right. \\
&\left. + \frac{\overline{A}_N \nu_N}{2} + \int_{R-0.5h_N}^{R} \left( \overline{A}_N \nu_N \frac{d\psi_2^{(N)}}{dr} + \frac{\overline{A}_N}{r}\psi_2^{(N)} + \frac{B_N^2(1-\nu_N^2)}{rD_N}\psi_2^{(N)} \right) dr \right] \\
&+ W_{N+1} \left[ \int_{R-0.5h_N}^{R} \left( \frac{B_N(\nu_N^2-1)}{r} \frac{d\psi_2^{(N)}}{dr} \right) dr \right] \\
&+ M_{rr_{N+1}} \left[ \int_{R-0.5h_N}^{R} \overline{B}_N \nu_N \psi_2^{(N)} dr + \frac{\overline{B}_N(R-0.5h_N)}{2} \right] = 0
\end{aligned} \tag{7.3.25}
$$

$$
\begin{aligned}
&-V_2^{(N+1)} + U_N \left[ -\frac{B_N(1-\nu_N^2)}{2(R-0.5h_N)} \right] + W_N \left[ -\frac{D_N(1-\nu_N^2)}{h_N(R-0.5h_N)} \right] \\
&+ M_{rr_N} \left[ 1 - \frac{R}{h_N} - \frac{\nu_N}{2} \right] + U_{N+1} \left[ -\frac{B_N(1-\nu_N^2)}{2(R-0.5h_N)} \right] + W_{N+1} \left[ \frac{D_N(1-\nu_N^2)}{h_N(R-0.5h_N)} \right] \\
&+ M_{rr_{N+1}} \left[ \frac{R}{h_N} - \frac{\nu_N}{2} \right] - \int_{R-0.5h_N}^{R} qr dr = 0
\end{aligned} \tag{7.3.26}
$$

$$
\begin{aligned}
&-\Phi_2^{(N+1)} + U_N \left[ \int_{R-0.5h_N}^{R} \left( \overline{B}_N r \frac{d\psi_1^{(N)}}{dr} + \overline{B}_N \nu_N \psi_1^{(N)} \right) dr \right] \\
&+ W_N \left[ -\frac{R-0.5h_N}{h_N} + \int_{R-0.5h_N}^{R} \left( (1-\nu_N) \frac{d\psi_1^{(N)}}{dr} dr \right) \right] - M_{rr_N} \left[ \int_{R-0.5h_N}^{R} \frac{r}{D_N} \psi_1^{(N)} dr \right] \\
&+ U_{N+1} \left[ \int_{R-0.5h_N}^{R} \left( \overline{B}_N r \frac{d\psi_2^{(N)}}{dr} + \overline{B}_N \nu_N \psi_2^{(N)} \right) dr \right] + W_{N+1} \left[ \frac{R-0.5h_N}{h_N} \right. \\
&\left. + \int_{R-0.5h_N}^{R} \left( (1-\nu_N) \frac{d\psi_2^{(N)}}{dr} \right) dr \right] - M_{rr_{N+1}} \left[ \int_{R-0.5h_N}^{R} \frac{r}{D_N} \psi_2^{(N)} dr \right] = 0
\end{aligned} \tag{7.3.27}
$$

This completes the *mixed dual mesh control domain* formulation of FG axisymmetric circular plate based on CPT.

### 7.3.2 Displacement DMCDM for axisymmetric circular plates based FSDT

Since the governing differential equations of axisymmetric circular plate based on FSDT in terms of generalized displacements are second-order differential equations, we can developed dual mesh control domain method directly from the equations (7.2.14)-(7.2.16). The integral statements of the governing equations on a typical interior control domain $(r_a^{(I)}, r_b^{(I)})$, associated with node $I$, would be

$$0 = \int_{r_a^{(I)}}^{r_b^{(I)}} \left\{ -\frac{1}{r}\frac{d}{dr}\left[ Ar\left(\frac{du}{dr} + \nu\frac{u}{r}\right) + Br\left(\frac{d\phi}{dr} + \frac{\nu}{r}\phi\right)\right] + \frac{A}{r}\left(\nu\frac{du}{dr} + \frac{u}{r}\right) + \frac{B}{r}\left(\nu\frac{d\phi}{dr} + \frac{1}{r}\phi\right)\right\} rdr \tag{7.3.28}$$

$$0 = \int_{r_a^{(I)}}^{r_b^{(I)}} \left\{ -\frac{1}{r}\frac{d}{dr}\left[ rS\left(\phi + \frac{dw}{dr}\right)\right] - q\right\} rdr \tag{7.3.29}$$

$$0 = \int_{r_a^{(I)}}^{r_b^{(I)}} \left\{ -\frac{1}{r}\frac{d}{dr}\left[ rB\left(\frac{du}{dr} + \nu\frac{u}{r}\right) + rD\left(\frac{d\phi}{dr} + \frac{\nu}{r}\phi\right)\right] + \frac{B}{r}\left(\nu\frac{du}{dr} + \frac{u}{r}\right) + \frac{D}{r}\left(\nu\frac{d\phi}{dr} + \frac{1}{r}\phi\right) + S\left(\phi + \frac{dw}{dr}\right)\right\} rdr \tag{7.3.30}$$

The indicated integration in the above equations is carried out such that the resulting boundary terms constitute the secondary variable, dual to the primary variable of the equation considered.

$$-N_1^{(I)} - N_2^{(I)} + \int_{r_a^{(I)}}^{r_b^{(I)}} \left\{ \frac{A}{r} \left( \nu \frac{du}{dr} + \frac{u}{r} \right) + \frac{B}{r} \left( \nu \frac{d\phi}{dr} + \frac{1}{r}\phi \right) \right\} r dr = 0 \tag{7.3.31}$$

$$-V_1^{(I)} - V_2^{(I)} - \int_{r_a^{(I)}}^{r_b^{(I)}} q r dr = 0 \tag{7.3.32}$$

$$-M_1^{(I)} - M_2^{(I)} + \int_{r_a^{(I)}}^{r_b^{(I)}} \left\{ \frac{B}{r} \left( \nu \frac{du}{dr} + \frac{u}{r} \right) + \frac{D}{r} \left( \nu \frac{d\phi}{dr} + \frac{1}{r}\phi \right) + S \left( \phi + \frac{dw}{dr} \right) \right\} r dr = 0 \tag{7.3.33}$$

where

$$N_1^{(I)} = - \left[ rA \left( \frac{du}{dr} + \nu \frac{u}{r} \right) + rB \left( \frac{d\phi}{dr} + \frac{\nu}{r}\phi \right) \right]_{r=r_a^{(I)}} \tag{7.3.34a}$$

$$N_2^{(I)} = \left[ rA \left( \frac{du}{dr} + \nu \frac{u}{r} \right) + rB \left( \frac{d\phi}{dr} + \frac{\nu}{r}\phi \right) \right]_{r=r_b^{(I)}} \tag{7.3.34b}$$

$$V_1^{(I)} = - \left[ rS \left( \phi + \frac{dw}{dr} \right) \right]_{r=r_a^{(I)}} \tag{7.3.35a}$$

$$V_2^{(I)} = \left[ rS \left( \phi + \frac{dw}{dr} \right) \right]_{r=r_b^{(I)}} \tag{7.3.35b}$$

$$M_1^{(I)} = - \left[ rB \left( \frac{du}{dr} + \nu \frac{u}{r} \right) + rD \left( \frac{d\phi}{dr} + \frac{\nu}{r}\phi \right) \right]_{r=r_a^{(I)}} \tag{7.3.36a}$$

$$M_2^{(I)} = \left[ rB \left( \frac{du}{dr} + \nu \frac{u}{r} \right) + rD \left( \frac{d\phi}{dr} + \frac{\nu}{r}\phi \right) \right]_{r=r_b^{(I)}} \tag{7.3.36b}$$

Here ($N_1^{(I)}$, $V_1^{(I)}$, $M_1^{(I)}$) represent the axial force, shear force and moment respectively at the left face of the control domain numbered $I$ (i.e., $r = r_a^{(I)}$), while ($N_2^{(I)}$, $V_2^{(I)}$, $M_2^{(I)}$) represent axial force, shear force and moment respectively at right face of the control domain numbered $I$ (i.e., $r = r_b^{(I)}$) (see figure 7.6). Assuming linear Lagrange interpolations of the primary variables $\{u, w, \phi\}$ on the finite elements, Eqs. (7.3.31)-(7.3.33) on an interior control domain evaluate to

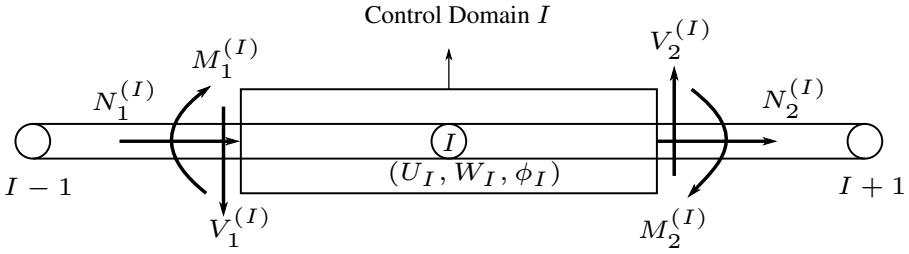


Figure 7.6: A typical control domain for the displacement model of FSDT with secondary variables at the faces and the primary variables at the node associated with the control domain [7].

$$
\begin{aligned}
&U_{I-1}\left[\frac{A_{I-1}\nu_{I-1}}{2}-\frac{A_{I-1}r_a^{(I)}}{h_{I-1}}+\int_{r_a^{(I)}}^{r_I}A_{I-1}\left(\nu_{I-1}\frac{d\psi_1^{(I-1)}}{dr}+\frac{\psi_1^{(I-1)}}{r}\right)dr\right]\\
&+\phi_{I-1}\left[\frac{B_{I-1}\nu_{I-1}}{2}-\frac{B_{I-1}r_a^{(I)}}{h_{I-1}}+\int_{r_a^{(I)}}^{r_I}B_{I-1}\left(\nu_{I-1}\frac{d\psi_1^{(I-1)}}{dr}+\frac{\psi_1^{(I-1)}}{r}\right)dr\right]\\
&+U_I\left[\frac{r_a^{(I)}A_{I-1}}{h_{I-1}}+\frac{r_b^{(I)}A_I}{h_I}+\frac{A_{I-1}\nu_{I-1}-A_I\nu_I}{2}+\int_{r_a^{(I)}}^{r_I}A_{I-1}\left(\nu_{I-1}\frac{d\psi_2^{(I-1)}}{dr}+\frac{\psi_2^{(I-1)}}{r}\right)dr\right.\\
&\left.+\int_{r_I}^{r_b^{(I)}}A_I\left(\nu_I\frac{d\psi_1^{(I)}}{dr}+\frac{\psi_1^{(I)}}{r}\right)dr\right]+\phi_I\left[\frac{r_a^{(I)}B_{I-1}}{h_{I-1}}+\frac{r_b^{(I)}B_I}{h_I}+\frac{B_{I-1}\nu_{I-1}-B_I\nu_I}{2}\right.\\
&\left.+\int_{r_a^{(I)}}^{r_I}B_{I-1}\left(\nu_{I-1}\frac{d\psi_2^{(I-1)}}{dr}+\frac{\psi_2^{(I-1)}}{r}\right)dr+\int_{r_I}^{r_b^{(I)}}B_I\left(\nu_I\frac{d\psi_1^{(I)}}{dr}+\frac{\psi_1^{(I)}}{r}\right)dr\right]\\
&+U_{I+1}\left[-\frac{A_I\nu_I}{2}-\frac{A_Ir_b^{(I)}}{h_I}+\int_{r_I}^{r_b^{(I)}}A_I\left(\nu_I\frac{d\psi_2^{(I)}}{dr}+\frac{\psi_2^{(I)}}{r}\right)dr\right]\\
&+\phi_{I+1}\left[-\frac{B_I\nu_I}{2}-\frac{B_Ir_b^{(I)}}{h_I}+\int_{r_I}^{r_b^{(I)}}B_I\left(\nu_I\frac{d\psi_2^{(I)}}{dr}+\frac{\psi_2^{(I)}}{r}\right)dr\right]=0 \qquad (7.3.37)
\end{aligned}
$$

$$
\begin{aligned}
&W_{I-1}\left[-\frac{r_a^{(I)}S_{I-1}}{h_{I-1}}\right]+\phi_{I-1}\left[\frac{r_a^{(I)}S_{I-1}}{2}\right]+W_I\left[\frac{r_a^{(I)}S_{I-1}}{h_{I-1}}+\frac{r_b^{(I)}S_I}{h_I}\right]\\
&+\phi_I\left[\frac{r_a^{(I)}S_{I-1}-r_b^{(I)}S_I}{2}\right]+W_{I+1}\left[-\frac{r_b^{(I)}S_I}{h_I}\right]+\phi_{I+1}\left[-\frac{r_b^{(I)}S_I}{2}\right]-\int_{r_a^{(I)}}^{r_b^{(I)}}qrdr=0 \qquad (7.3.38)
\end{aligned}
$$

$$
\begin{aligned}
&U_{I-1}\left[\frac{B_{I-1}\nu_{I-1}}{2}-\frac{B_{I-1}r_a^{(I)}}{h_{I-1}}+\int_{r_a^{(I)}}^{r_I}B_{I-1}\left(\nu_{I-1}\frac{d\psi_1^{(I-1)}}{dr}+\frac{\psi_1^{(I-1)}}{r}\right)dr\right]\\
&+\phi_{I-1}\left[\frac{D_{I-1}\nu_{I-1}}{2}-\frac{D_{I-1}r_a^{(I)}}{h_{I-1}}+\int_{r_a^{(I)}}^{r_I}D_{I-1}\left(\nu_{I-1}\frac{d\psi_1^{(I-1)}}{dr}+\frac{\psi_1^{(I-1)}}{r}\right)dr\right]\\
&+U_I\left[\frac{r_a^{(I)}B_{I-1}}{h_{I-1}}+\frac{r_b^{(I)}B_I}{h_I}+\frac{B_{I-1}\nu_{I-1}-B_I\nu_I}{2}+\int_{r_a^{(I)}}^{r_I}B_{I-1}\left(\nu_{I-1}\frac{d\psi_2^{(I-1)}}{dr}+\frac{\psi_2^{(I-1)}}{r}\right)dr\right.\\
&\left.+\int_{r_I}^{r_b^{(I)}}B_I\left(\nu_I\frac{d\psi_1^{(I)}}{dr}+\frac{\psi_1^{(I)}}{r}\right)dr\right]+\phi_I\left[\frac{r_a^{(I)}D_{I-1}}{h_{I-1}}+\frac{r_b^{(I)}D_I}{h_I}+\frac{D_{I-1}\nu_{I-1}-D_I\nu_I}{2}\right.\\
&\left.+\int_{r_a^{(I)}}^{r_I}D_{I-1}\left(\nu_{I-1}\frac{d\psi_2^{(I-1)}}{dr}+\frac{\psi_2^{(I-1)}}{r}\right)dr+\int_{r_I}^{r_b^{(I)}}D_I\left(\nu_I\frac{d\psi_1^{(I)}}{dr}+\frac{\psi_1^{(I)}}{r}\right)dr\right]\\
&+U_{I+1}\left[-\frac{B_I\nu_I}{2}-\frac{B_Ir_b^{(I)}}{h_I}+\int_{r_I}^{r_b^{(I)}}B_I\left(\nu_I\frac{d\psi_2^{(I)}}{dr}+\frac{\psi_2^{(I)}}{r}\right)dr\right]\\
&+\phi_{I+1}\left[-\frac{D_I\nu_I}{2}-\frac{D_Ir_b^{(I)}}{h_I}+\int_{r_I}^{r_b^{(I)}}D_I\left(\nu_I\frac{d\psi_2^{(I)}}{dr}+\frac{\psi_2^{(I)}}{r}\right)dr\right]\\
&+\left[\int_{r_a^{(I)}}^{r_I}\frac{S_{I-1}r}{2}dr\right]\phi_{I-1}+\left[\int_{r_a^{(I)}}^{r_I}\frac{S_{I-1}r}{2}dr\right]\phi_I+\left[\int_{r_I}^{r_b^{(I)}}\frac{S_Ir}{2}dr\right]\phi_I\\
&+\left[\int_{r_I}^{r_b^{(I)}}\frac{S_Ir}{2}dr\right]\phi_{I+1}+\left[\int_{r_a^{(I)}}^{r_I}S_{I-1}r\frac{d\psi_1^{(I-1)}}{dr}dr\right]W_{I-1}+\left[\int_{r_a^{(I)}}^{r_I}S_{I-1}r\frac{d\psi_2^{(I-1)}}{dr}dr\right]W_I\\
&+\left[\int_{r_I}^{r_b^{(I)}}S_Ir\frac{d\psi_1^{(I)}}{dr}dr\right]W_I+\left[\int_{r_I}^{r_b^{(I)}}S_Ir\frac{d\psi_2^{(I)}}{dr}dr\right]W_{I+1}=0
\end{aligned}
\tag{7.3.39}
$$

In evaluating Eq. (7.3.39), the coefficients of $\phi$ corresponding to the integral

$$\int_{r_a^{(I)}}^{r_b^{(I)}} rS\left(\phi+\frac{dw}{dr}\right)dr$$

are evaluated by considering $\phi$ to be constant within each element. Thus in element $\Omega^{(I-1)}$, $\phi=\frac{\phi_I+\phi_{I-1}}{2}$ while in the element $\Omega^{(I)}$, $\phi=\frac{\phi_{I+1}+\phi_I}{2}$. This is done to remedy the shear locking (see [93, 10]).

Similarly, the discretized equations on 1st control domain would be

$$
\begin{aligned}
&-N_1^{(1)} + U_1 \left[ \frac{A_1(1-\nu_1)}{2} + \int_0^{0.5h_1} A_1 \left( \nu_1 \frac{d\psi_1^{(1)}}{dr} + \frac{\psi_1^{(1)}}{r} \right) dr \right] \\
&+ \phi_1 \left[ \frac{B_1(1-\nu_1)}{2} + \int_0^{0.5h_1} B_1 \left( \nu_1 \frac{d\psi_1^{(1)}}{dr} + \frac{\psi_1^{(1)}}{r} \right) dr \right] \\
&+ U_2 \left[ -\frac{A_1(1+\nu_1)}{2} + \int_0^{0.5h_1} A_1 \left( \nu_1 \frac{d\psi_2^{(1)}}{dr} + \frac{\psi_2^{(1)}}{r} \right) dr \right] \\
&+ \phi_2 \left[ -\frac{B_1(1+\nu_1)}{2} + \int_0^{0.5h_1} B_1 \left( \nu_1 \frac{d\psi_2^{(1)}}{dr} + \frac{\psi_2^{(1)}}{r} \right) dr \right] = 0
\end{aligned} \tag{7.3.40}
$$

$$
-V_1^{(1)} + W_1 \left[ \frac{S_1}{2} \right] + \phi_1 \left[ -\frac{h_1 S_1}{4} \right] + W_2 \left[ \frac{-S_1}{2} \right] + \phi_2 \left[ -\frac{h_1 S_1}{4} \right] - \int_0^{0.5h_1} qr dr = 0 \tag{7.3.41}
$$

$$
\begin{aligned}
&-M_1^{(1)} + U_1 \left[ \frac{B_1(1-\nu_1)}{2} + \int_0^{0.5h_1} B_1 \left( \nu_1 \frac{d\psi_1^{(1)}}{dr} + \frac{\psi_1^{(1)}}{r} \right) dr \right] + W_1 \left[ \int_0^{0.5h_1} S_1 r \frac{d\psi_1^{(1)}}{dr} dr \right] \\
&+ \phi_1 \left[ \frac{D_1(1-\nu_1)}{2} + \int_0^{0.5h_1} D_1 \left( \nu_1 \frac{d\psi_1^{(1)}}{dr} + \frac{\psi_1^{(1)}}{r} \right) dr + \int_0^{0.5h_1} \frac{S_1 r}{2} dr \right] \\
&+ U_2 \left[ -\frac{B_1(1+\nu_1)}{2} + \int_0^{0.5h_1} B_1 \left( \nu_1 \frac{d\psi_2^{(1)}}{dr} + \frac{\psi_2^{(1)}}{r} \right) dr \right] + W_2 \left[ \int_0^{0.5h_1} S_1 r \frac{d\psi_2^{(1)}}{dr} dr \right] \\
&+ \phi_2 \left[ -\frac{D_1(1+\nu_1)}{2} + \int_0^{0.5h_1} D_1 \left( \nu_1 \frac{d\psi_2^{(1)}}{dr} + \frac{\psi_2^{(1)}}{r} \right) dr + \int_0^{0.5h_1} \frac{S_1 r}{2} dr \right] = 0
\end{aligned} \tag{7.3.42}
$$

while the discretized equations on $(N+1)^{th}$ control domain would be

$$-N_2^{(N+1)} + U_N \left[ \frac{A_N \nu_N}{2} - \frac{A_N(R-0.5h_N)}{h_N} + \int_{R-0.5h_N}^{R} A_N \left( \nu_N \frac{d\psi_1^{(N)}}{dr} + \frac{\psi_1^{(N)}}{r} \right) dr \right]$$
$$+ \phi_N \left[ \frac{B_N \nu_N}{2} - \frac{B_N(R-0.5h_N)}{h_N} + \int_{R-0.5h_N}^{R} B_N \left( \nu_N \frac{d\psi_1^{(N)}}{dr} + \frac{\psi_1^{(N)}}{r} \right) dr \right]$$
$$+ U_{N+1} \left[ \frac{A_N(R-0.5h_N)}{h_N} + \frac{A_N \nu_N}{2} + \int_{R-0.5h_N}^{R} A_N \left( \nu_N \frac{d\psi_2^{(N)}}{dr} + \frac{\psi_2^{(N)}}{r} \right) dr \right]$$
$$+ \phi_{N+1} \left[ \frac{B_N(R-0.5h_N)}{h_N} + \frac{B_N \nu_N}{2} + \int_{R-0.5h_N}^{R} B_N \left( \nu_N \frac{d\psi_2^{(N)}}{dr} + \frac{\psi_2^{(N)}}{r} \right) dr \right] = 0 \quad (7.3.43)$$

$$-V_2^{(N+1)} + W_N \left[ -\frac{(R-0.5h_N)S_N}{h_N} \right] + \phi_N \left[ \frac{(R-0.5h_N)S_N}{2} \right]$$
$$+ W_{N+1} \left[ \frac{(R-0.5h_N)S_N}{h_N} \right] + \phi_{N+1} \left[ \frac{(R-0.5h_N)S_N}{2} \right] - \int_{R-0.5h_N}^{R} q\, r dr = 0 \quad (7.3.44)$$

$$-M_2^{(N+1)} + U_N \left[ \frac{B_N \nu_N}{2} - \frac{B_N(R-0.5h_N)}{h_N} + \int_{R-0.5h_N}^{R} B_N \left( \nu_N \frac{d\psi_1^{(N)}}{dr} + \frac{\psi_1^{(N)}}{r} \right) dr \right]$$
$$+ \phi_N \left[ \frac{D_N \nu_N}{2} - \frac{D_N(R-0.5h_N)}{h_N} + \int_{R-0.5h_N}^{R} D_N \left( \nu_N \frac{d\psi_1^{(N)}}{dr} + \frac{\psi_1^{(N)}}{r} \right) dr \right]$$
$$+ U_{N+1} \left[ \frac{B_N(R-0.5h_N)}{h_N} + \frac{B_N \nu_N}{2} + \int_{R-0.5h_N}^{R} B_N \left( \nu_N \frac{d\psi_2^{(N)}}{dr} + \frac{\psi_2^{(N)}}{r} \right) dr \right]$$
$$+ \phi_{N+1} \left[ \frac{D_N(R-0.5h_N)}{h_N} + \frac{D_N \nu_N}{2} + \int_{R-0.5h_N}^{R} D_N \left( \nu_N \frac{d\psi_2^{(N)}}{dr} + \frac{\psi_2^{(N)}}{r} \right) dr \right]$$
$$+ W_N \left[ \int_{R-0.5h_N}^{R} S_N r \frac{d\psi_1^{(N)}}{dr} dr \right] + \phi_N \left[ \int_{R-0.5h_N}^{R} \frac{S_N r}{2} dr \right]$$
$$+ W_{N+1} \left[ \int_{R-0.5h_N}^{R} S_N r \frac{d\psi_2^{(N)}}{dr} dr \right] + \phi_{N+1} \left[ \int_{R-0.5h_N}^{R} \frac{S_N r}{2} dr \right] = 0 \quad (7.3.45)$$

## 7.4 Governing equations functionally graded rectangular plates

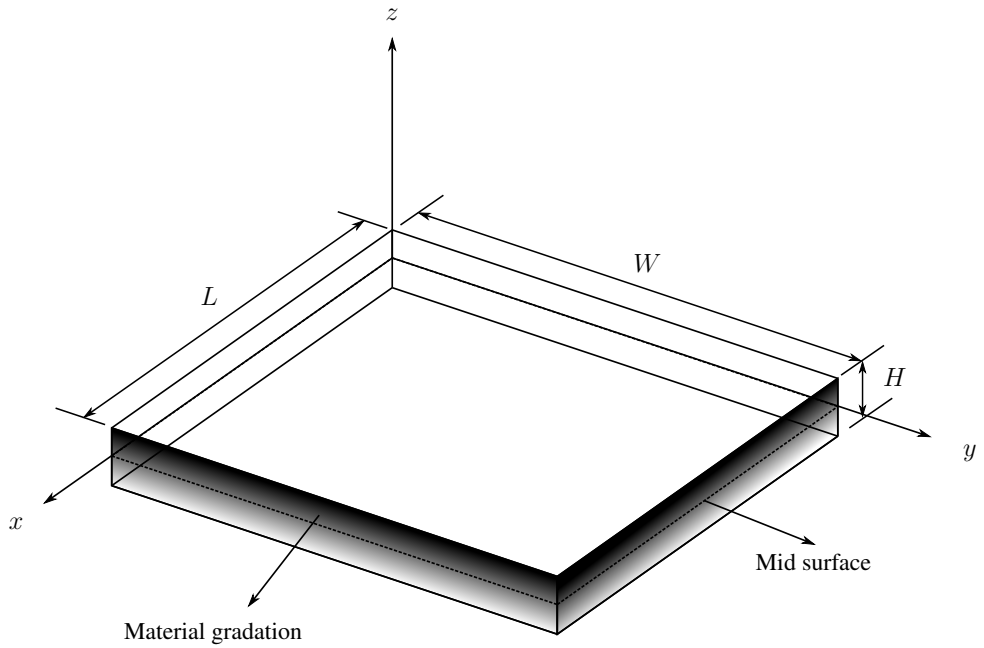


Figure 7.7: Functionally graded rectangular plate with coordinate system [8].

Consider a through-thickness functionally graded rectangular plate of length $L$, width $W$ and height $H$. The coordinate system used for the analysis is shown in Fig. (7.7). The displacement field of such a plate based on the *first-order shear deformation theory* (FSDT) is given by (see [107])

$$u_1(x, y, z) = u(x, y) + z\phi_x(x, y) \tag{7.4.1a}$$

$$u_2(x, y, z) = v(x, y) + z\phi_y(x, y) \tag{7.4.1b}$$

$$u_3(x, y, z) = w(x, y) \tag{7.4.1c}$$

The non-zero linear strains based on the above displacements would then be

$$\begin{Bmatrix} \varepsilon_{xx} \\ \varepsilon_{yy} \\ \gamma_{xz} \\ \gamma_{yz} \\ \gamma_{xy} \end{Bmatrix} = \begin{Bmatrix} \varepsilon^0_{xx} \\ \varepsilon^0_{yy} \\ \gamma^0_{xz} \\ \gamma^0_{yz} \\ \gamma^0_{xy} \end{Bmatrix} + z \begin{Bmatrix} \varepsilon^1_{xx} \\ \varepsilon^1_{yy} \\ \gamma^1_{xz} \\ \gamma^1_{yz} \\ \gamma^1_{xy} \end{Bmatrix} = \begin{Bmatrix} \frac{\partial u}{\partial x} \\ \frac{\partial v}{\partial y} \\ \phi_x + \frac{\partial w}{\partial x} \\ \phi_y + \frac{\partial w}{\partial y} \\ \frac{\partial u}{\partial y} + \frac{\partial v}{\partial x} \end{Bmatrix} + z \begin{Bmatrix} \frac{\partial \phi_x}{\partial x} \\ \frac{\partial \phi_y}{\partial y} \\ 0 \\ 0 \\ \frac{\partial \phi_x}{\partial y} + \frac{\partial \phi_y}{\partial x} \end{Bmatrix} \tag{7.4.2}$$

while the constitutive relations of the functionally graded plate are given by

$$\begin{Bmatrix} \sigma_{xx} \\ \sigma_{yy} \\ \sigma_{xz} \\ \sigma_{yz} \\ \sigma_{xy} \end{Bmatrix} = \frac{E(z)}{1-\nu^2} \begin{bmatrix} 1 & \nu & 0 & 0 & 0 \\ \nu & 1 & 0 & 0 & 0 \\ 0 & 0 & \frac{1-\nu}{2} & 0 & 0 \\ 0 & 0 & 0 & \frac{1-\nu}{2} & 0 \\ 0 & 0 & 0 & 0 & \frac{1-\nu}{2} \end{bmatrix} \begin{Bmatrix} \varepsilon_{xx} \\ \varepsilon_{yy} \\ \gamma_{xz} \\ \gamma_{yz} \\ \gamma_{xy} \end{Bmatrix} \tag{7.4.3}$$

Further, we define stress and moment resultants acting on the plate as follows:

$$N_{xx} = \int_{-H/2}^{H/2} \sigma_{xx} dz = A\left[\frac{\partial u}{\partial x} + \nu\frac{\partial v}{\partial y}\right] + B\left[\frac{\partial \phi_x}{\partial x} + \nu\frac{\partial \phi_y}{\partial y}\right] \tag{7.4.4a}$$

$$M_{xx} = \int_{-H/2}^{H/2} \sigma_{xx} z dz = B\left[\frac{\partial u}{\partial x} + \nu\frac{\partial v}{\partial y}\right] + D\left[\frac{\partial \phi_x}{\partial x} + \nu\frac{\partial \phi_y}{\partial y}\right] \tag{7.4.4b}$$

$$N_{yy} = \int_{-H/2}^{H/2} \sigma_{yy} dz = A\left[\nu\frac{\partial u}{\partial x} + \frac{\partial v}{\partial y}\right] + B\left[\nu\frac{\partial \phi_x}{\partial x} + \frac{\partial \phi_y}{\partial y}\right] \tag{7.4.4c}$$

$$M_{yy} = \int_{-H/2}^{H/2} \sigma_{yy} z dz = B\left[\nu\frac{\partial u}{\partial x} + \frac{\partial v}{\partial y}\right] + D\left[\nu\frac{\partial \phi_x}{\partial x} + \frac{\partial \phi_y}{\partial y}\right] \tag{7.4.4d}$$

$$N_{xy} = \int_{-H/2}^{H/2} \sigma_{xy} dz = \frac{A(1-\nu)}{2}\left[\frac{\partial u}{\partial y} + \frac{\partial v}{\partial x}\right] + \frac{B(1-\nu)}{2}\left[\frac{\partial \phi_x}{\partial y} + \frac{\partial \phi_y}{\partial x}\right] \tag{7.4.4e}$$

$$M_{xy} = \int_{-H/2}^{H/2} \sigma_{xy} z dz = \frac{B(1-\nu)}{2}\left[\frac{\partial u}{\partial y} + \frac{\partial v}{\partial x}\right] + \frac{D(1-\nu)}{2}\left[\frac{\partial \phi_x}{\partial y} + \frac{\partial \phi_y}{\partial x}\right] \tag{7.4.4f}$$

$$Q_x = \int_{-H/2}^{H/2} \sigma_{xz} dz = S\left(\phi_x + \frac{\partial w}{\partial x}\right) \tag{7.4.4g}$$

$$Q_y = \int_{-H/2}^{H/2} \sigma_{yz} dz = S\left(\phi_y + \frac{\partial w}{\partial y}\right) \tag{7.4.4h}$$

where

$$\begin{aligned} A &= \int_{-H/2}^{H/2} \frac{E(z)}{1-\nu^2} dz, \quad B = \int_{-H/2}^{H/2} \frac{E(z)z}{1-\nu^2} dz \\ D &= \int_{-H/2}^{H/2} \frac{E(z)z^2}{1-\nu^2} dz, \quad S = \int_{-H/2}^{H/2} \frac{K_s E(z)}{2(1+\nu)} dz \end{aligned} \tag{7.4.5}$$

The explicit expressions of the above integrals for the power-law variation of $E(z)$ (see Eq. (7.1.1)) are given in Eq. (7.2.6)

The equations of equilibrium of the functionally graded (FG) rectangular plate can be obtained

using the principle of virtual work [102]. The resulting governing equations are listed below.

$$\frac{\partial N_{xx}}{\partial x} + \frac{\partial N_{xy}}{\partial y} + f_x = 0 \tag{7.4.6}$$

$$\frac{\partial N_{xy}}{\partial x} + \frac{\partial N_{yy}}{\partial y} + f_y = 0 \tag{7.4.7}$$

$$\frac{\partial Q_x}{\partial x} + \frac{\partial Q_y}{\partial y} + q = 0 \tag{7.4.8}$$

$$\frac{\partial M_{xx}}{\partial x} + \frac{\partial M_{xy}}{\partial y} - Q_x = 0 \tag{7.4.9}$$

$$\frac{\partial M_{xy}}{\partial x} + \frac{\partial M_{yy}}{\partial y} - Q_y = 0 \tag{7.4.10}$$

The governing equations can be written in terms of displacements $u$, $v$, $w$ and rotations $\phi_x$, $\phi_y$ by substituting the stress and moment resultants of Eqs. (7.4.4a)-(7.4.4h) into the Eqs. (7.4.6)-(7.4.10). These are listed below.

$$\begin{aligned}\frac{\partial}{\partial x}\left[A\left(\frac{\partial u}{\partial x}+\nu\frac{\partial v}{\partial y}\right)+B\left(\frac{\partial \phi_x}{\partial x}+\nu\frac{\partial \phi_y}{\partial y}\right)\right]\\ +\frac{\partial}{\partial y}\left[\frac{A(1-\nu)}{2}\left(\frac{\partial u}{\partial y}+\frac{\partial v}{\partial x}\right)+\frac{B(1-\nu)}{2}\left(\frac{\partial \phi_x}{\partial y}+\frac{\partial \phi_y}{\partial x}\right)\right]=0\end{aligned} \tag{7.4.11}$$

$$\begin{aligned}\frac{\partial}{\partial x}\left[\frac{A(1-\nu)}{2}\left(\frac{\partial u}{\partial y}+\frac{\partial v}{\partial x}\right)+\frac{B(1-\nu)}{2}\left(\frac{\partial \phi_x}{\partial y}+\frac{\partial \phi_y}{\partial x}\right)\right]\\ +\frac{\partial}{\partial y}\left[A\left(\nu\frac{\partial u}{\partial x}+\frac{\partial v}{\partial y}\right)+B\left(\nu\frac{\partial \phi_x}{\partial x}+\frac{\partial \phi_y}{\partial y}\right)\right]=0\end{aligned} \tag{7.4.12}$$

$$\frac{\partial}{\partial x}\left[S\left(\phi_x+\frac{\partial w}{\partial x}\right)\right]+\frac{\partial}{\partial y}\left[S\left(\phi_y+\frac{\partial w}{\partial y}\right)\right]+q=0 \tag{7.4.13}$$

$$\begin{aligned}\frac{\partial}{\partial y}\left[\frac{B(1-\nu)}{2}\left(\frac{\partial u}{\partial y}+\frac{\partial v}{\partial x}\right)+\frac{D(1-\nu)}{2}\left(\frac{\partial \phi_x}{\partial y}+\frac{\partial \phi_y}{\partial x}\right)\right]\\ +\frac{\partial}{\partial x}\left[B\left(\frac{\partial u}{\partial x}+\nu\frac{\partial v}{\partial y}\right)+D\left(\frac{\partial \phi_x}{\partial x}+\nu\frac{\partial \phi_y}{\partial y}\right)\right]-S\left(\phi_x+\frac{\partial w}{\partial x}\right)=0\end{aligned} \tag{7.4.14}$$

$$\begin{aligned}\frac{\partial}{\partial x}\left[\frac{B(1-\nu)}{2}\left(\frac{\partial u}{\partial y}+\frac{\partial v}{\partial x}\right)+\frac{D(1-\nu)}{2}\left(\frac{\partial \phi_x}{\partial y}+\frac{\partial \phi_y}{\partial x}\right)\right]\\ +\frac{\partial}{\partial y}\left[B\left(\nu\frac{\partial u}{\partial x}+\frac{\partial v}{\partial y}\right)+D\left(\nu\frac{\partial \phi_x}{\partial x}+\frac{\partial \phi_y}{\partial y}\right)\right]-S\left(\phi_y+\frac{\partial w}{\partial y}\right)=0\end{aligned} \tag{7.4.15}$$

The governing equations (7.4.6)-(7.2.10) are derived based on the first-order shear deformation theory, where the transverse shear strain is non-zero and assumes a constant value throughout the plate thickness (rather than as a parabolic function) and hence require the shear correction factor, $K_s$ in Eq. (7.2.6). For rectangular plates $K_s = 5/6$.

## 7.5 Displacement DMCDM for rectangular plates based on FSDT

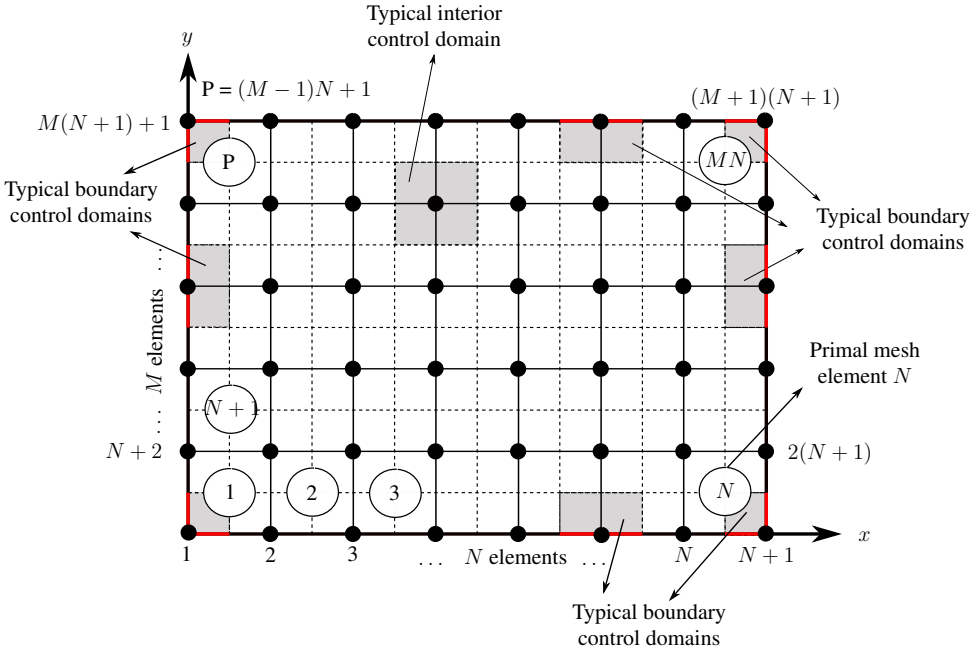


Figure 7.8: Dark lines represent primal mesh while dotted line represents dual mesh. Dark circles are the nodes of the mesh. Typical control domains are represented by shaded regions. The boundaries of control domains which coincide with the boundary of the computational domain are highlighted in red [8].

Fig. 7.8 shows a rectangular domain discretized by $N \times M$ primal mesh elements (i.e., $N$ elements along $x$-axis and $M$ elements along $y$-axis). On a typical primal mesh element $\Omega_p^{(e)}$ (here superscript $e$ represents the number assigned to a particular primal mesh element) of the primal mesh, the dependent variables are approximated using bilinear Lagrange interpolation functions. For a local coordinate system of $(\overline{x}, \overline{y})$ within each primal mesh element $\Omega_p^{(e)}$ (see Fig. 7.9b), a

dependent variable, say $u$, can be approximated as follows:

$$u(x,y) \approx \sum_{j=1}^{4} u_j^{(e)} \psi_j^{(e)}(\overline{x},\overline{y}), \qquad \overline{x} = x - x_1^{(e)}, \qquad \overline{y} = y - y_1^{(e)} \tag{7.5.1}$$

where $u_j^{(e)}$ denote the unknown values of the variable $u$ at the element nodes and $(x_1^{(e)}, y_1^{(e)})$ are the global coordinates of local node number 1 of element $\Omega_p^{(e)}$. $\psi_j^{(e)}$ are the bilinear Lagrange interpolation functions [93] associated with the element and are given by

$$\begin{aligned} \psi_1^{(e)} &= \left(1 - \frac{\overline{x}}{a_e}\right)\left(1 - \frac{\overline{y}}{b_e}\right) & \psi_2^{(e)} &= \frac{\overline{x}}{a_e}\left(1 - \frac{\overline{y}}{b_e}\right) \\ \psi_3^{(e)} &= \frac{\overline{x}}{a_e}\frac{\overline{y}}{b_e}, & \psi_4^{(e)} &= \left(1 - \frac{\overline{x}}{a_e}\right)\frac{\overline{y}}{b_e} \end{aligned} \tag{7.5.2}$$

Here $a_e$ and $b_e$ represent the horizontal and vertical dimensions of a typical rectangular primal mesh element $\Omega_p^{(e)}$ respectively. If additional dependent variables are present, they can be approximated in a similar manner on each primal mesh element. In the present work we use same set of bilinear Lagrange interpolation functions in approximating all the dependent variables on a given element.

The displacement dual mesh control domain method of first order shear deformation plate theory is developed using Eqs. (7.4.6)-(7.4.10). The primary variables of such formulation are the displacements $(u, v, w)$ and rotations $(\phi_x, \phi_y)$, together called generalized displacements. The first step in developing the dual mesh control domain formulation is to write the integral statements of the governing equations (7.4.6)-(7.4.10) on a typical interior control domain, $\Omega_{CD}^{(I)}$, centered around node $I$ .

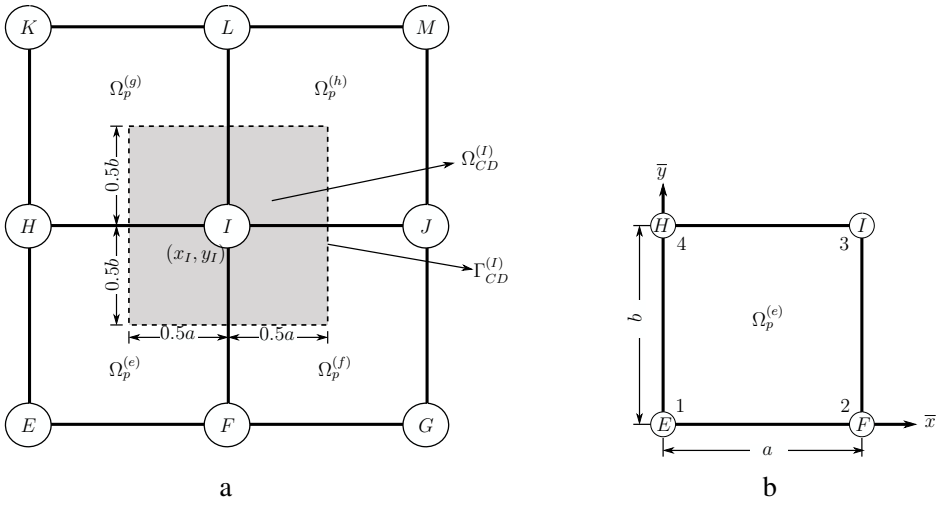


Figure 7.9: (a) Control domain of typical interior node $I$ along with the contributing primal mesh elements. (b) Local coordinate system for a typical primal mesh element $\Omega_p^{(e)}$. The node numbers in circles are global while node numbers outside circles are local to the element [8].

$$
\begin{aligned}
-\int_{\Omega_{CD}^{(I)}} \left\{ \frac{\partial N_{xx}}{\partial x} + \frac{\partial N_{xy}}{\partial y} + f_x \right\} dxdy = 0 \\
-\int_{\Omega_{CD}^{(I)}} \left\{ \frac{\partial N_{xy}}{\partial x} + \frac{\partial N_{yy}}{\partial y} + f_y \right\} dxdy = 0 \\
-\int_{\Omega_{CD}^{(I)}} \left\{ \frac{\partial Q_x}{\partial x} + \frac{\partial Q_y}{\partial y} + q \right\} dxdy = 0 \\
-\int_{\Omega_{CD}^{(I)}} \left\{ \frac{\partial M_{xx}}{\partial x} + \frac{\partial M_{xy}}{\partial y} - Q_x \right\} dxdy = 0 \\
-\int_{\Omega_{CD}^{(I)}} \left\{ \frac{\partial M_{xy}}{\partial x} + \frac{\partial M_{yy}}{\partial y} - Q_y \right\} dxdy = 0
\end{aligned}
\tag{7.5.3}
$$

The next step is to evaluate the integrals in the above equations such that the resulting boundary terms on the boundary of the control domain $\Gamma_{CD}^{(I)}$ (see Fig. 7.9a), represent physically meaningful secondary variables which are dual to the primary variables. Thus we arrive at the following

equations:

$$-\oint_{\Gamma_{CD}^{(I)}}\left[N_{xx}n_x+N_{xy}n_y\right]ds-\int_{\Omega_{CD}^{(I)}}f_x dxdy=0 \tag{7.5.4}$$

$$-\oint_{\Gamma_{CD}^{(I)}}\left[N_{xy}n_x+N_{yy}n_y\right]ds-\int_{\Omega_{CD}^{(I)}}f_y dxdy=0 \tag{7.5.5}$$

$$-\oint_{\Gamma_{CD}^{(I)}}\left[Q_x n_x+Q_y n_y\right]ds-\int_{\Omega_{CD}^{(I)}}q dxdy=0 \tag{7.5.6}$$

$$-\oint_{\Gamma_{CD}^{(I)}}\left[M_{xx}n_x+M_{xy}n_y\right]ds+\int_{\Omega_{CD}^{(I)}}Q_x dxdy=0 \tag{7.5.7}$$

$$-\oint_{\Gamma_{CD}^{(I)}}\left[M_{xy}n_x+M_{yy}n_y\right]ds+\int_{\Omega_{CD}^{(I)}}Q_y dxdy=0 \tag{7.5.8}$$

Further, the stress and moment resultants can be expressed in terms of the displacements and rotations using Eqs. (7.4.4a)-(7.4.4h). Since the control domain spans four different primal mesh elements and since the interpolation functions change from one primal mesh element to the other, each of the above integrals should be broken into four parts with each part corresponding to different primal mesh element that contributes to the control domain. For example, consider Eq. (7.5.4) for a uniform primal mesh (i.e., all primal mesh elements are of same size $a\times b$). Eq. (7.5.4) when evaluated on the part of the control domain $\Omega_{CD}^{(I)}$ which lies inside the primal mesh element $\Omega_p^{(e)}$ (see Fig. (7.9a)) can be written as follows:

$$\begin{aligned}
&\left\{\int_{0.5a}^{a}\left[\frac{A(1-\nu)}{2}\frac{\partial\psi_i^{(e)}}{\partial\overline{y}}\right]_{\overline{y}=0.5b}d\overline{x}+\int_{0.5b}^{b}\left[A\frac{\partial\psi_i^{(e)}}{\partial\overline{x}}\right]_{\overline{x}=0.5a}d\overline{y}\right\}u_i^{(e)}\\
&+\left\{\int_{0.5a}^{a}\left[\frac{A(1-\nu)}{2}\frac{\partial\psi_i^{(e)}}{\partial\overline{x}}\right]_{\overline{y}=0.5b}d\overline{x}+\int_{0.5b}^{b}\left[A\nu\frac{\partial\psi_i^{(e)}}{\partial\overline{y}}\right]_{\overline{x}=0.5a}d\overline{y}\right\}v_i^{(e)}\\
&+\left\{\int_{0.5a}^{a}\left[\frac{B(1-\nu)}{2}\frac{\partial\psi_i^{(e)}}{\partial\overline{y}}\right]_{\overline{y}=0.5b}d\overline{x}+\int_{0.5b}^{b}\left[B\frac{\partial\psi_i^{(e)}}{\partial\overline{x}}\right]_{\overline{x}=0.5a}d\overline{y}\right\}\phi_{x_i}^{(e)}\\
&+\left\{\int_{0.5a}^{a}\left[\frac{B(1-\nu)}{2}\frac{\partial\psi_i^{(e)}}{\partial\overline{x}}\right]_{\overline{y}=0.5b}d\overline{x}+\int_{0.5b}^{b}\left[B\nu\frac{\partial\psi_i^{(e)}}{\partial\overline{y}}\right]_{\overline{x}=0.5a}d\overline{y}\right\}\phi_{y_i}^{(e)}\\
&=\int_{0.5a}^{a}\int_{0.5b}^{b}f_x(\overline{x},\overline{y})d\overline{x}d\overline{y}
\end{aligned} \tag{7.5.9}$$

where $u_i^{(e)}, v_i^{(e)}, \phi_{x_i}^{(e)}, \phi_{y_i}^{(e)}$ represent the nodal values of $u, v, \phi_x$ and $\phi_y$ respectively of primal mesh element $\Omega_p^{(e)}$ and $i = \{1, 2, 3, 4\}$ with summation on repeated index implied.

Similarly, Eq. (7.5.4) when evaluated on the part of the control domain which lies inside the primal mesh element $\Omega_p^{(f)}$ can be written as

$$\begin{aligned}
&\left\{ \int_0^{0.5a} \left[ \frac{A(1-\nu)}{2} \frac{\partial \psi_i^{(f)}}{\partial \overline{y}} \right]_{\overline{y}=0.5b} d\overline{x} - \int_{0.5b}^{b} \left[ A \frac{\partial \psi_i^{(f)}}{\partial \overline{x}} \right]_{\overline{x}=0.5a} d\overline{y} \right\} u_i^{(f)} \\
&+ \left\{ \int_0^{0.5a} \left[ \frac{A(1-\nu)}{2} \frac{\partial \psi_i^{(f)}}{\partial \overline{x}} \right]_{\overline{y}=0.5b} d\overline{x} - \int_{0.5b}^{b} \left[ A\nu \frac{\partial \psi_i^{(f)}}{\partial \overline{y}} \right]_{\overline{x}=0.5a} d\overline{y} \right\} v_i^{(f)} \\
&+ \left\{ \int_0^{0.5a} \left[ \frac{B(1-\nu)}{2} \frac{\partial \psi_i^{(f)}}{\partial \overline{y}} \right]_{\overline{y}=0.5b} d\overline{x} - \int_{0.5b}^{b} \left[ B \frac{\partial \psi_i^{(f)}}{\partial \overline{x}} \right]_{\overline{x}=0.5a} d\overline{y} \right\} \phi_{x_i}^{(f)} \\
&+ \left\{ \int_0^{0.5a} \left[ \frac{B(1-\nu)}{2} \frac{\partial \psi_i^{(f)}}{\partial \overline{x}} \right]_{\overline{y}=0.5b} d\overline{x} - \int_{0.5b}^{b} \left[ B\nu \frac{\partial \psi_i^{(f)}}{\partial \overline{y}} \right]_{\overline{x}=0.5a} d\overline{y} \right\} \phi_{y_i}^{(f)} \\
&= \int_0^{0.5a} \int_{0.5b}^{b} f_x(\overline{x}, \overline{y}) d\overline{x} d\overline{y}
\end{aligned} \tag{7.5.10}$$

For the part of the control domain which lies inside primal mesh element $\Omega_p^{(g)}$ we have

$$\begin{aligned}
&\left\{ - \int_{0.5a}^{a} \left[ \frac{A(1-\nu)}{2} \frac{\partial \psi_i^{(g)}}{\partial \overline{y}} \right]_{\overline{y}=0.5b} d\overline{x} + \int_0^{0.5b} \left[ A \frac{\partial \psi_i^{(g)}}{\partial \overline{x}} \right]_{\overline{x}=0.5a} d\overline{y} \right\} u_i^{(g)} \\
&+ \left\{ - \int_{0.5a}^{a} \left[ \frac{A(1-\nu)}{2} \frac{\partial \psi_i^{(g)}}{\partial \overline{x}} \right]_{\overline{y}=0.5b} d\overline{x} + \int_0^{0.5b} \left[ A\nu \frac{\partial \psi_i^{(g)}}{\partial \overline{y}} \right]_{\overline{x}=0.5a} d\overline{y} \right\} v_i^{(g)} \\
&+ \left\{ - \int_{0.5a}^{a} \left[ \frac{B(1-\nu)}{2} \frac{\partial \psi_i^{(g)}}{\partial \overline{y}} \right]_{\overline{y}=0.5b} d\overline{x} + \int_0^{0.5b} \left[ B \frac{\partial \psi_i^{(g)}}{\partial \overline{x}} \right]_{\overline{x}=0.5a} d\overline{y} \right\} \phi_{x_i}^{(g)} \\
&+ \left\{ - \int_{0.5a}^{a} \left[ \frac{B(1-\nu)}{2} \frac{\partial \psi_i^{(g)}}{\partial \overline{x}} \right]_{\overline{y}=0.5b} d\overline{x} + \int_0^{0.5b} \left[ B\nu \frac{\partial \psi_i^{(g)}}{\partial \overline{y}} \right]_{\overline{x}=0.5a} d\overline{y} \right\} \phi_{y_i}^{(g)} \\
&= \int_{0.5a}^{a} \int_0^{0.5b} f_x(\overline{x}, \overline{y}) d\overline{x} d\overline{y}
\end{aligned} \tag{7.5.11}$$

Finally, Eq. (7.5.4) when evaluated on the part of the control domain $\Omega_{CD}^{(I)}$ which lies inside the

primal mesh element $\Omega_p^{(h)}$ will be

$$
\begin{aligned}
&\left\{ -\int_0^{0.5b} \left[ A\frac{\partial \psi_i^{(h)}}{\partial \overline{x}} \right]_{\overline{x}=0.5a} d\overline{y} - \int_0^{0.5a} \left[ \frac{A(1-\nu)}{2} \frac{\partial \psi_i^{(h)}}{\partial \overline{y}} \right]_{\overline{y}=0.5b} d\overline{x} \right\} u_i^{(h)} \\
&+ \left\{ -\int_0^{0.5b} \left[ A\nu\frac{\partial \psi_i^{(h)}}{\partial \overline{y}} \right]_{\overline{x}=0.5a} d\overline{y} - \int_0^{0.5a} \left[ \frac{A(1-\nu)}{2} \frac{\partial \psi_i^{(h)}}{\partial \overline{x}} \right]_{\overline{y}=0.5b} d\overline{x} \right\} v_i^{(h)} \\
&+ \left\{ -\int_0^{0.5b} \left[ B\frac{\partial \psi_i^{(h)}}{\partial \overline{x}} \right]_{\overline{x}=0.5a} d\overline{y} - \int_0^{0.5a} \left[ \frac{B(1-\nu)}{2} \frac{\partial \psi_i^{(h)}}{\partial \overline{y}} \right]_{\overline{y}=0.5b} d\overline{x} \right\} \phi_{x_i}^{(h)} \\
&+ \left\{ -\int_0^{0.5b} \left[ A\nu\frac{\partial \psi_i^{(h)}}{\partial \overline{y}} \right]_{\overline{x}=0.5a} d\overline{y} - \int_0^{0.5a} \left[ \frac{A(1-\nu)}{2} \frac{\partial \psi_i^{(h)}}{\partial \overline{x}} \right]_{\overline{y}=0.5b} d\overline{x} \right\} \phi_{y_i}^{(h)} \\
&= \int_0^{0.5a} \int_0^{0.5b} f_x(\overline{x},\overline{y}) d\overline{x} d\overline{y}
\end{aligned}
\tag{7.5.12}
$$

Note that

$$
\begin{aligned}
&u_1^{(e)} = U_E, \quad u_2^{(e)} = u_1^{(f)} = U_F, \quad u_2^{(f)} = U_G, \quad u_4^{(e)} = u_1^{((g))} = U_H \\
&u_3^{(e)} = u_4^{(f)} = u_2^{(g)} = u_1^{(h)} = U_I, \quad u_3^{(f)} = u_2^{(h)} = U_J, \quad u_4^{(g)} = U_K \\
&u_3^{(g)} = u_4^{(h)} = U_L, \quad u_3^{(h)} = U_M
\end{aligned}
$$

where $U_E$, $U_F$, $\ldots$ are the nodal values of displacement $u$, numbered with global node numbers. Similar relations hold for other primary variables as well. Using these continuity relations we can obtain the final discretized equation corresponding to Eq. (7.5.4) by adding the Eq. (7.5.9)–Eq. (7.5.12) which can be written in following form

$$K_{11}U_E + K_{12}V_E + K_{14}\Phi_{x_E} + K_{15}\Phi_{y_E} + K_{16}U_F + K_{17}V_F + K_{19}\Phi_{x_F} + K_{1(10)}\Phi_{y_F}$$
$$+K_{1(11)}U_G + K_{1(12)}V_G + K_{1(14)}\Phi_{x_G} + K_{1(15)}\Phi_{y_G} + K_{1(16)}U_H + K_{1(17)}V_H + K_{1(19)}\Phi_{x_H} + K_{1(20)}\Phi_{y_H}$$
$$+K_{1(21)}U_I + K_{1(22)}V_I + K_{1(24)}\Phi_{x_I} + K_{1(25)}\Phi_{y_I} + K_{1(26)}U_J + K_{1(27)}V_J + K_{1(29)}\Phi_{x_J} + K_{1(30)}\Phi_{y_J}$$
$$+K_{1(31)}U_K + K_{1(32)}V_K + K_{1(34)}\Phi_{x_K} + K_{1(35)}\Phi_{y_K} + K_{1(36)}U_L + K_{1(37)}V_L + K_{1(39)}\Phi_{x_L} + K_{1(40)}\Phi_{y_L}$$
$$+ K_{1(41)}U_M + K_{1(42)}V_M + K_{1(44)}\Phi_{x_M} + K_{1(45)}\Phi_{y_M} = F_{x_I}^{(e)} + F_{x_I}^{(f)} + F_{x_I}^{(g)} + F_{x_I}^{(h)} \qquad (7.5.13)$$

The coefficients of $K_{ij}$ are obtained after adding the equations (7.5.9)-(7.5.12) and factoring out the nodal values. Similar discretized equations can be written for Eqs. (7.5.5)-(7.5.8).

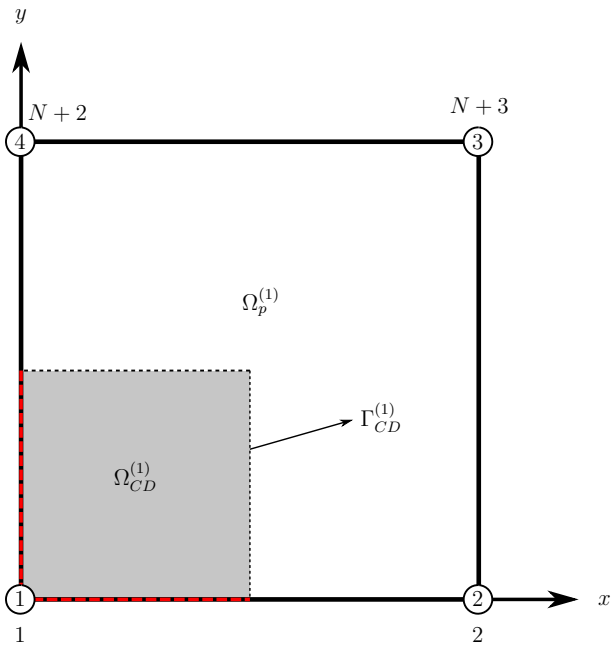


Figure 7.10: Control volume corresponding to global node 1. The numbers in the circle are local node numbers of primal mesh element $\Omega_p^{(1)}$ while the numbers outside are global node numbers [8].

Eq. (7.5.13) was derived for a control domain corresponding to an interior node. Now we will

consider the discretization of Eq. (7.5.4) on a control domain corresponding to a boundary node. Consider the control domain corresponding to node 1 as shown in Fig. 7.10. Eq. (7.5.4) on this control domain can be written as

$$\int_0^{0.5a} [N_{xy}]_{y=0}\, dx - \int_0^{0.5b} [N_{xx}]_{x=0.5a}\, dy - \int_0^{0.5a} [N_{xy}]_{y=0.5b}\, dx + \int_0^{0.5b} [N_{xx}]_{x=0}\, dy = \int_0^{0.5a}\int_0^{0.5b} f_x dx dy \tag{7.5.14}$$

However, we note that the boundary of the control domain represented in red in Fig. 7.10 coincides with the boundary of the computational domain. Since on the boundary of the computational domain we either know the primary variable or the corresponding dual variable because of their duality, we shall not write the integrals on those boundaries of the control domain which coincide with the boundary of the computational domain in terms of the primary variables. Hence, Eq. (7.5.4) will take the form

$$\begin{aligned}
&\left\{ -\int_0^{0.5b} \left[ A\frac{\partial \psi_i^{(1)}}{\partial \overline{x}} \right]_{\overline{x}=0.5a} d\overline{y} - \int_0^{0.5a} \left[ \frac{A(1-\nu)}{2} \frac{\partial \psi_i^{(1)}}{\partial \overline{y}} \right]_{\overline{y}=0.5b} d\overline{x} \right\} u_i^{(1)} \\
&+ \left\{ -\int_0^{0.5b} \left[ A\nu\frac{\partial \psi_i^{(1)}}{\partial \overline{y}} \right]_{\overline{x}=0.5a} d\overline{y} - \int_0^{0.5a} \left[ \frac{A(1-\nu)}{2} \frac{\partial \psi_i^{(1)}}{\partial \overline{x}} \right]_{\overline{y}=0.5b} d\overline{x} \right\} v_i^{(1)} \\
&+ \left\{ -\int_0^{0.5b} \left[ B\frac{\partial \psi_i^{(1)}}{\partial \overline{x}} \right]_{\overline{x}=0.5a} d\overline{y} - \int_0^{0.5a} \left[ \frac{B(1-\nu)}{2} \frac{\partial \psi_i^{(1)}}{\partial \overline{y}} \right]_{\overline{y}=0.5b} d\overline{x} \right\} \phi_{x_i}^{(1)} \\
&+ \left\{ -\int_0^{0.5b} \left[ B\nu\frac{\partial \psi_i^{(1)}}{\partial \overline{y}} \right]_{\overline{x}=0.5a} d\overline{y} - \int_0^{0.5a} \left[ \frac{B(1-\nu)}{2} \frac{\partial \psi_i^{(1)}}{\partial \overline{x}} \right]_{\overline{y}=0.5b} d\overline{x} \right\} \phi_{y_i}^{(1)} \\
&= \int_0^{0.5a}\int_0^{0.5b} f_x(\overline{x},\overline{y}) d\overline{x} d\overline{y} - \int_0^{0.5a} [N_{xy}]_{y=0}\, dx - \int_0^{0.5b} [N_{xx}]_{x=0}\, dy
\end{aligned} \tag{7.5.15}$$

Here $u_i^{(1)}, v_i^{(1)}, \phi_{x_i}^{(1)}, \phi_{y_i}^{(1)}$ represent the nodal values of $u, v, \phi_x$ and $\phi_y$ respectively of primal mesh element $\Omega_p^{(1)}$ and $i = \{1, 2, 3, 4\}$ with summation on repeated index implied.

The line integrals on the right hand side of Eq. (7.3.13) represent the secondary variables dual to the primary variable $u$ on the boundary. For a given boundary value problem, we either know

the value of $u$ on the boundary or its dual. Hence, when $u$ is known on the boundary the stress resultants on the boundary can be computed using Eq. (7.3.13). Conversely, when the stress resultants (secondary variable) is specified on the boundary, Eq. (7.3.13) is used to calculate $u$ on the boundary. Similar procedure holds for the all the control domains which share boundary with the boundary of the computational domain. Fig. 7.8 shows such possible boundary control domains for a rectangular computational domain discretized with rectangular primal mesh elements.

### 7.5.1 Shear locking

It is well known that in the thin plate limit the displacement based finite element models of first order shear deformation theory tend to under predict the deflection when linear interpolations on the all the primary variables is used. Such a phenomenon is called *shear locking* in finite element literature (see [108, 109]). Since we are using bilinear Lagrange interpolation functions for all the primary variables in developing dual mesh control domain formulations of plate, such a locking phenomenon occurs even in displacement dual mesh control domain method. In finite element methods, shear locking is eliminated using reduced integration technique in evaluating the integrals which correspond to the shear stress terms (called selective reduced integration). This is equivalent to considering the shear terms $\left(\phi_x + \frac{\partial w}{\partial x}\right)$ and $\left(\phi_y + \frac{\partial w}{\partial y}\right)$ to be constant when calculating the finite element equations. We shall use the same technique to overcome shear locking in dual mesh control domain method as well (see [7, 10, 112, 113]). Thus in evaluating the following integrals, the shear terms $\left(\phi_x + \frac{\partial w}{\partial x}\right)$ and $\left(\phi_y + \frac{\partial w}{\partial y}\right)$ are considered to be constant within each primal mesh element

$$-\oint_{\Gamma_{CD}^{(I)}} \left[Q_x n_x + Q_y n_y\right] ds, \quad \int_{\Omega_{CD}^{(I)}} Q_x dxdy, \quad \int_{\Omega_{CD}^{(I)}} Q_y dxdy \tag{7.5.16}$$

The value of the constant is taken to be the value of the shear term a the center of the primal

mesh element. For example, consider the integral

$$\begin{aligned}
\int_{\Omega_{CD}^{(I)}} Q_x dxdy &= \int_{x_I-0.5a}^{x_I}\int_{y_I-0.5b}^{y_I} S\left(\phi_x+\frac{\partial w}{\partial x}\right)dxdy + \int_{x_I}^{x_I+0.5a}\int_{y_I-0.5b}^{y_I} S\left(\phi_x+\frac{\partial w}{\partial x}\right)dxdy \\
&+ \int_{x_I-0.5a}^{x_I}\int_{y_I}^{y_I+0.5b} S\left(\phi_x+\frac{\partial w}{\partial x}\right)dxdy + \int_{x_I}^{x_I+0.5a}\int_{y_I}^{y_I+0.5b} S\left(\phi_x+\frac{\partial w}{\partial x}\right)dxdy \\
&= \left[\int_{0.5a}^{a}\int_{0.5b}^{b}\frac{S}{4}d\overline{x}d\overline{y}\right]\sum_{j=1}^{4}\phi_{x_j}^{(e)} + \left[\int_{0.5a}^{a}\int_{0.5b}^{b}\left[S\frac{\partial\psi_i^{(e)}}{\partial\overline{x}}\right]_{(0.5a,0.5b)}d\overline{x}d\overline{y}\right]w_i^{(e)} \\
&+ \left[\int_{0}^{0.5a}\int_{0.5b}^{b}\frac{S}{4}d\overline{x}d\overline{y}\right]\sum_{j=1}^{4}\phi_{x_j}^{(f)} + \left[\int_{0}^{0.5a}\int_{0.5b}^{b}\left[S\frac{\partial\psi_i^{(f)}}{\partial\overline{x}}\right]_{(0.5a,0.5b)}d\overline{x}d\overline{y}\right]w_i^{(f)} \\
&+ \left[\int_{0.5a}^{a}\int_{0}^{0.5b}\frac{S}{4}d\overline{x}d\overline{y}\right]\sum_{j=1}^{4}\phi_{x_j}^{(g)} + \left[\int_{0.5a}^{a}\int_{0}^{0.5b}\left[S\frac{\partial\psi_i^{(g)}}{\partial\overline{x}}\right]_{(0.5a,0.5b)}d\overline{x}d\overline{y}\right]w_i^{(g)} \\
&+ \left[\int_{0}^{0.5a}\int_{0}^{0.5b}\frac{S}{4}d\overline{x}d\overline{y}\right]\sum_{j=1}^{4}\phi_{x_j}^{(h)} + \left[\int_{0}^{0.5a}\int_{0}^{0.5b}\left[S\frac{\partial\psi_i^{(h)}}{\partial\overline{x}}\right]_{(0.5a,0.5b)}d\overline{x}d\overline{y}\right]w_i^{(h)}
\end{aligned} \tag{7.5.17}$$

where $i=\{1,2,3,4\}$ and summation on repeated index is implied. Similarly, we have

$$\begin{aligned}
-\oint_{\Gamma_{CD}^{(I)}} Q_x n_x ds &= \left[\int_{0.5b}^{b}\left[\frac{S}{4}\right]d\overline{y}\right]\sum_{j=1}^{4}\phi_{x_j}^{(e)} + \left[\int_{0.5b}^{b}\left[S\frac{\partial\psi_i^{(e)}}{\partial\overline{x}}\right]_{(0.5a,0.5b)}d\overline{y}\right]w_i^{(e)} \\
&- \left[\int_{0.5b}^{b}\left[\frac{S}{4}\right]d\overline{y}\right]\sum_{j=1}^{4}\phi_{x_j}^{(f)} - \left[\int_{0.5b}^{b}\left[S\frac{\partial\psi_i^{(f)}}{\partial\overline{x}}\right]_{(0.5a,0.5b)}d\overline{y}\right]w_i^{(f)} \\
&+ \left[\int_{0}^{0.5b}\left[\frac{S}{4}\right]d\overline{y}\right]\sum_{j=1}^{4}\phi_{x_j}^{(g)} + \left[\int_{0}^{0.5b}\left[S\frac{\partial\psi_i^{(g)}}{\partial\overline{x}}\right]_{(0.5a,0.5b)}d\overline{y}\right]w_i^{(g)} \\
&- \left[\int_{0}^{0.5b}\left[\frac{S}{4}\right]d\overline{y}\right]\sum_{j=1}^{4}\phi_{x_j}^{(h)} - \left[\int_{0}^{0.5b}\left[S\frac{\partial\psi_i^{(h)}}{\partial\overline{x}}\right]_{(0.5a,0.5b)}d\overline{y}\right]w_i^{(h)}
\end{aligned} \tag{7.5.18}$$

This completes the displacement dual mesh control domain formulation for first order shear deformation theory of rectangular plates.

## 7.6 Numerical examples

### 7.6.1 Axisymmetric circular plates

To illustrate the workings of the dual mesh finite domain models presented in the previous sections, we consider two cases: (a) hinged (or simply supported) and (b) clamped functionally graded circular plates, subjected to uniformly distributed load of intensity $q$. A comparison between the numerical results obtained with FEM and DMFDM models for each case considered is presented. There are three models of FE and two models of DMFD, as summarized below:

- **FE-CP(D)** - Displacement finite element model for CPT
- **FE-CP(M)** - Mixed finite element model for CPT
- **FE-FP(D)** - Displacement finite element model for FST
- **DM-CP(M)** - Mixed dual mesh finite domain model for CPT
- **DM-FP(D)** - Displacement dual mesh finite domain model for FST

We investigate the effect of mesh and power-law index $n$ on the deflections and stresses. We consider a functionally graded circular plate of radius $R = 10$ in, thickness $H = 0.1$ in and subjected to axisymmetric uniformly distributed load intensity $q = 0.5$ lb/in$^2$. The functionally graded material properties are taken to be $E_1 = 3 \times 10^7$ psi, $E_2 = 3 \times 10^6$ psi, and $\nu = 0.3$.

The stresses and stress resultants can be post-computed in the numerical models described. For the displacement models, once the generalized displacements are obtained, their derivatives can be easily determined. Then the stresses can be directly computed from the constitutive relations of Eq. (7.2.3), while the stress resultants and moments can be computed using Eqs. (7.2.4a)-(7.2.4e) or Eqs. (7.2.13a)-(7.2.13d) depending on whether FST is used or CPT is used. For the mixed models, the second derivative of the transverse deflection needs to be calculated from the moment $M_{rr}$, which is determined as a nodal variable in mixed models. The second derivative of transverse

deflection $w$ can be obtained from the following equation:

$$\frac{d^2w}{dr^2} = -\frac{\nu}{r}\frac{dw}{dr} + \overline{B}\left(\frac{du}{dr} + \nu\frac{u}{r}\right) - \frac{1}{D}M_{rr} \tag{7.6.1}$$

The stress resultants can be computed using Eqs. (7.3.1) and (7.3.4) and the stresses can be computed using Eq. (7.2.3).

#### *7.6.1.1 Hinged plates*

The boundary conditions for the *primary variables* of hinged axisymmetric circular plate in various models are as follows:

$$\text{Displacement models:} \qquad u(0) = 0, \quad \frac{dw}{dr}(0) \text{ or } \phi(0) = 0, \quad u(R) = w(R) = 0 \tag{7.6.2}$$

$$\text{Mixed models:} \qquad u(0) = 0, \quad u(R) = w(R) = M(R) = 0 \tag{7.6.3}$$

A comparison between the transverse deflections at the center of a hinged homogeneous circular plate obtained from various models is presented in Table 7.1. When 32 elements are used, all models give the same results as the exact solution (see [107, 114]) up to the fourth decimal point. The mixed finite element model has a slow mesh convergence rate at the origin for transverse deflection, $w$, and hence a non-uniform finite element mesh with a finer mesh at the origin is used in reporting the values of $w(0)$. The non-uniform mesh is chosen such that for two element mesh, the lengths of the elements are in ratio 1:9, with the shortest element being at origin. All the subsequent refinements are made by breaking the finite elements into half. Thus for four element mesh the element lengths would be $\{0.5R, 0.5R, 4.5R, 4.5R\}$ and further refinement is made by breaking these elements into their halves and so on. Since the radius to thickness ratio $R/H = 100$, both classical plate theory and first order shear deformation theory predict the same results.

Figure 7.11(a) contains a comparison of the moment, $M_{rr}$, obtained from displacement and mixed finite element models and mixed dual mesh finite domain model of the CPT when a uniform mesh of 32 elements is used, while Fig. 7.11(b) includes a comparison of the moment, $M_{rr}$,

obtained from displacement finite element model and displacement dual mesh finite domain model of the FST when a uniform mesh of 32 elements is used. While the moments obtained from all the models are very close, the mixed finite element model and mixed dual mesh finite domain model deviate from the displacement finite element model at the origin ($r = 0$). Both mixed models (i.e., mixed FEM and mixed DMFDM models) are prone to give erroneous moments at the origin. It should be noted that this anomalous behavior at the origin is not a characteristic of the dual mesh finite domain method; both the mixed finite element model and mixed dual mesh finite domain model exhibit such behavior. However, the displacements models do not exhibit such a behavior.

Table 7.1: Center transverse deflection, $w(0)$, of hinged homogeneous axisymmetric circular plate as predicted by various models. The results are given in inches [7].

| **Mesh** | **FE-CP(D)** | **FE-CP(M)** | **FE-FP(D)** | **DM-CP(M)** | **DM-FP(D)** |
|---|---|---|---|---|---|
| 2 | 0.1159 | 0.1120 | 0.1076 | 0.1149 | 0.1052 |
| 4 | 0.1159 | 0.1136 | 0.1143 | 0.1156 | 0.1134 |
| 8 | 0.1159 | 0.1155 | 0.1156 | 0.1158 | 0.1153 |
| 16 | 0.1159 | 0.1159 | 0.1159 | 0.1159 | 0.1158 |
| 32 | 0.1159 | 0.1159 | 0.1159 | 0.1159 | 0.1159 |
| 64 | 0.1159 | 0.1159 | 0.1159 | 0.1159 | 0.1159 |
| **Exact** | 0.1159 | 0.1159 | 0.1159 | 0.1159 | 0.1159 |

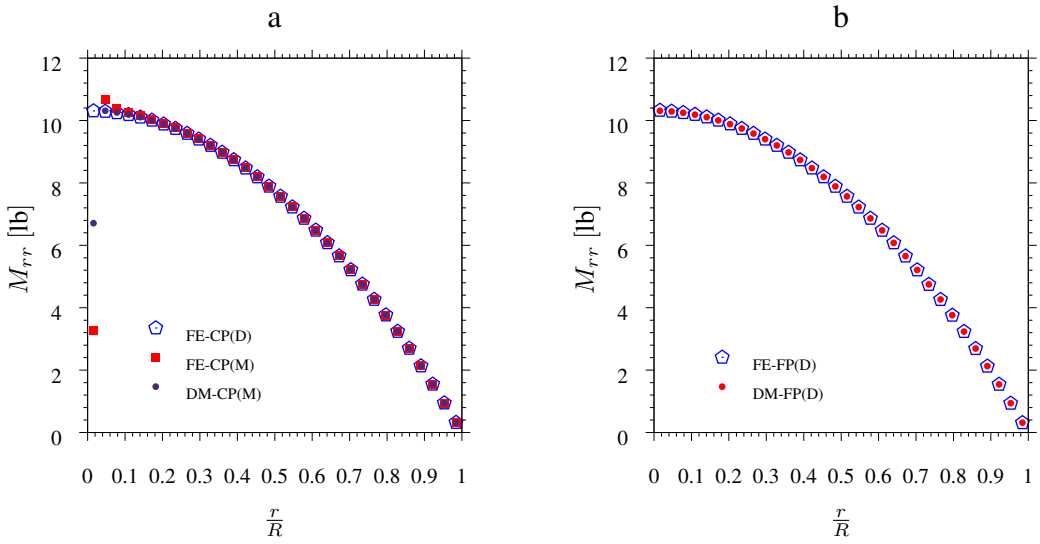


Figure 7.11: Moment of hinged homogeneous circular plate as predicted by various models. (a) Numerical models based on the CPT. (b) Numerical models based on the FST [7].

#### *7.6.1.2 Clamped plates*

The boundary conditions on the *primary variables* of clamped axisymmetric circular plate in various models are as follows:

$$\text{Displacement models:} \quad u(0) = 0, \quad \frac{dw}{dr}(0) \text{ or } \phi(0) = 0,$$
$$u(R) = w(R) = 0, \quad \frac{dw}{dr}(R) \text{ or } \phi(R) = 0 \tag{7.6.4}$$

$$\text{Mixed models:} \quad u(0) = 0, \quad u(R) = w(R) = 0 \tag{7.6.5}$$

A comparison of the stress values, $\sigma_{rr}$, on the top face of the clamped homogeneous circular plate as predicted by various numerical models based on CPT with the analytical solution [107] are presented in Fig. 7.12. Although all the models are in good agreement with the analytical solution for most part of the computational domain, the mixed models (i.e., mixed FEM model and mixed DMCDM model) deviate from the analytical solution at and very close to the origin. This is due to the erroneous prediction of moment $M_{rr}$ near the origin by the mixed models. Further,

Fig. 7.13 contains a comparison of stress $\sigma_{rr}$ on the top face of clamped homogeneous circular plate as predicted by various numerical models based on the FST with that of the analytical solution [107, 114]. Since both the finite element model and dual mesh finite domain model of the FST are displacement based, the stress values are in good agreement with the analytical solution through out the computational domain.

Finally, to illustrate the working of the dual mesh finite domain method in analyzing the functionally graded axisymmetric circular plates, we compare the transverse deflection at the center, $w(0)$, from the analytical solution of the CPT [115] with the transverse deflections obtained from various models described earlier. Various values of the power law index, $n$, are considered to bring out the effect of $n$ on the bending deflections of the plate. Table 7.2 contains a comparison between the various models with that of the analytical solution (of the FST). For this thin plate ($R/H = 100$), both the CPT and the FST predict solutions close to each other [107]; 32 elements are used for the results reported in Table 7.2. Uniform mesh is used in all models except for the mixed FEM model of the CPT. A non-uniform mesh described earlier is used for FE-CP(M) to achieve faster mesh convergence. It can be seen that as the power-law index, $n$, increases the plate stiffness decreases (since plate material tends toward $E_2 < E_1$).

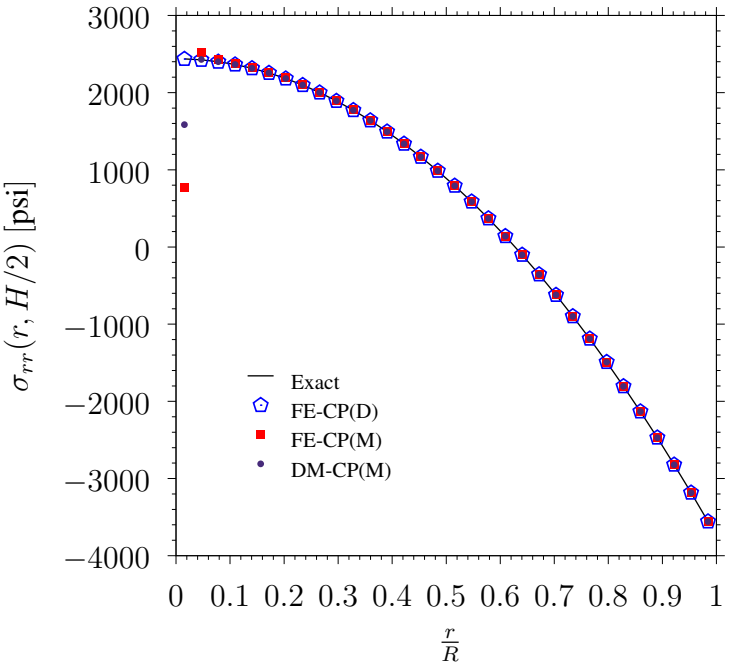


Figure 7.12: Values of $\sigma_{rr}(r, H/2)$ as predicted by various models based on the CPT; comparison with the exact solution [7].

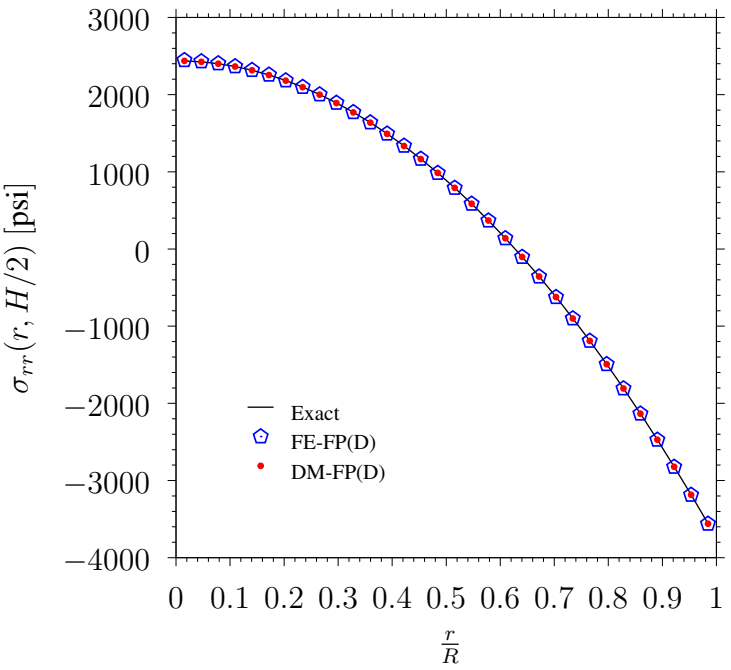


Figure 7.13: Values of $\sigma_{rr}(r, H/2)$ as predicted by various models based on the FSDT; comparison with the exact solution [7].

Table 7.2: Center transverse deflection, $w(0)$, of a clamped FGM axisymmetric circular plate for various values of $n$, as predicted by various models; 32 elements are used in all the models. The results are given in inches [7].

| $n$ | **FE-CP(D)** | **FE-CP(M)** | **DM-CP(M)** | **FE-FP(D)** | **DM-FP(D)** | **FST Exact** |
|---|---|---|---|---|---|---|
| 0.0 | 0.0284 | 0.0285 | 0.0284 | 0.0285 | 0.0284 | 0.0284 |
| 1.0 | 0.0665 | 0.0666 | 0.0665 | 0.0666 | 0.0665 | 0.0666 |
| 2.0 | 0.0976 | 0.0976 | 0.0975 | 0.0977 | 0.0976 | 0.0976 |
| 3.0 | 0.1152 | 0.1152 | 0.1151 | 0.1153 | 0.1152 | 0.1152 |
| 4.0 | 0.1244 | 0.1244 | 0.1242 | 0.1245 | 0.1244 | 0.1244 |
| 5.0 | 0.1296 | 0.1296 | 0.1294 | 0.1297 | 0.1296 | 0.1296 |
| 7.5 | 0.1370 | 0.1370 | 0.1369 | 0.1371 | 0.1370 | 0.1370 |
| 10.0 | 0.1425 | 0.1425 | 0.1424 | 0.1426 | 0.1425 | 0.1425 |
| 12.0 | 0.1467 | 0.1467 | 0.1466 | 0.1468 | 0.1469 | 0.1467 |
| 15.0 | 0.1527 | 0.1528 | 0.1527 | 0.1529 | 0.1527 | 0.1523 |
| 20.0 | 0.1622 | 0.1622 | 0.1621 | 0.1623 | 0.1622 | 0.1622 |

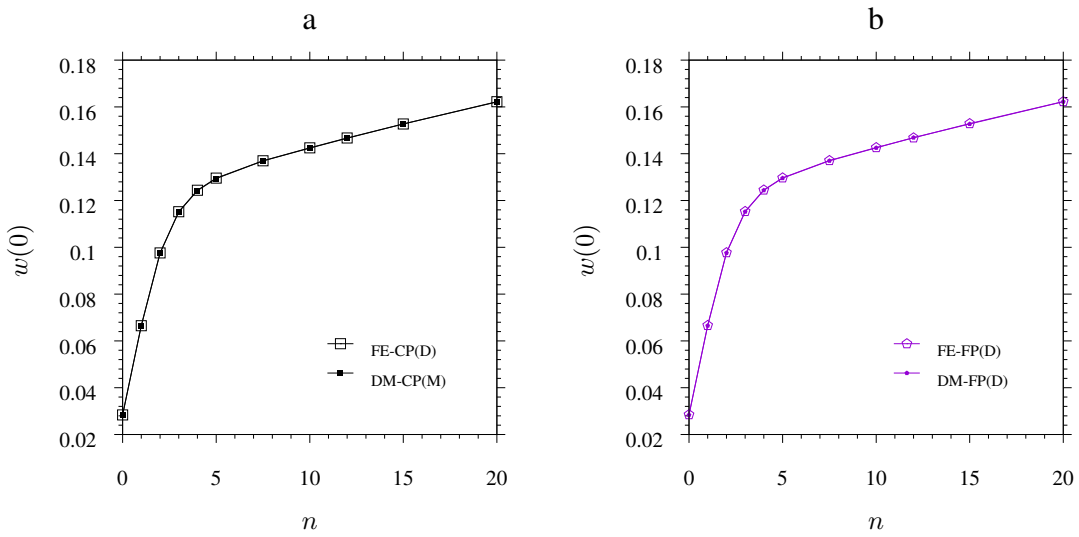


Figure 7.14: Center deflections $w(0)$ of clamped functionally graded circular plates [7].

### 7.6.2 Rectangular plates

Consider a functionally graded plate of length $L = 1$ in (25.4 mm), width $W = 1$ in (25.4 mm) and thickness $H = 0.01$ in (0.254 mm). The material properties of the functionally graded material are taken as

$$E_1 = 3 \times 10^7 \text{ psi} \quad (206.84 \text{ GPa}), \quad E_2 = 3 \times 10^6 \text{ psi} \quad (20.68 \text{ GPa}), \quad \nu = 0.3 \tag{7.6.6}$$

The plate is subjected to a uniformly distributed load of $q = 1$ lb/in$^2$ (0.00689 N/mm$^2$) on the top surface. We consider two different boundary conditions: (a) clamped and (b) simply-supported. Since the loading and boundary conditions result in symmetry about $x$ and $y$ axes, we shall consider only the quarter plate in the first quadrant as the computational domain (see Fig. 7.15). The boundary conditions on the computational domain are then given by

- *Clamped*

$$u = \phi_x = 0 \quad \text{at} \quad x = 0; \qquad v = \phi_y = 0 \quad at \quad \text{at} \quad y = 0$$

$$u = v = w = \phi_x = \phi_y = 0 \quad \text{at} \quad x = L/2 \quad \text{and} \quad y = W/2$$

- *Simply-supported*

$$u = \phi_x = 0 \quad \text{at} \quad x = 0; \qquad v = \phi_y = 0 \quad at \quad \text{at} \quad y = 0$$

$$v = w = \phi_y = 0 \quad \text{at} \quad x = L/2; \qquad u = w = \phi_x = 0 \quad \text{at} \quad y = W/2$$

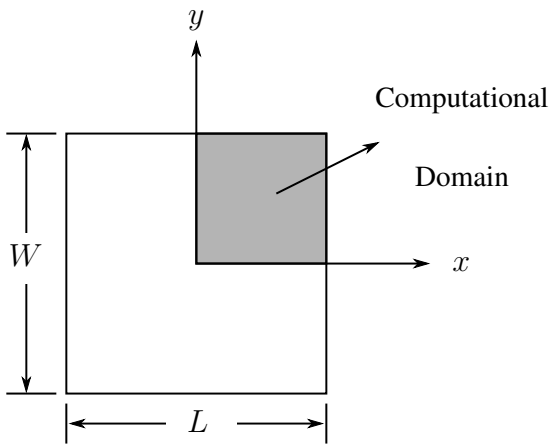


Figure 7.15: Functionally graded square plate along with the chosen coordinate system for numerical analysis. The domain in the first quadrant is taken as computational domain [8].

Further, we define the following dimensionless parameters:

$$\overline{w}(x,y) = w(x,y)\frac{E_1H^3}{qL^4}, \quad \overline{u}(x,y) = u(x,y)\frac{E_1H^2}{qL^3}$$
$$\overline{B} = \frac{B(1-\nu^2)}{E_1H^2}, \quad \overline{D} = \frac{D(1-\nu^2)}{E_1H^3}$$
$$\xi = \frac{2x}{L}, \quad \eta = \frac{z}{H}, \quad \chi = \frac{2\sqrt{x^2+y^2}}{\sqrt{L^2+W^2}}$$
$$\overline{\sigma}_{xx} = \sigma_{xx}\frac{H^2}{qL^2}, \quad \overline{\sigma}_{xy} = \sigma_{xy}\frac{H^2}{qL^2}, \quad \overline{\sigma}_{xz} = \sigma_{xz}\frac{H}{qL}$$

Table 7.3 presents the comparison between the dimensionless transverse center deflections of the functionally graded plate for various values of $n$, subjected to clamped boundary conditions under the action of a uniformly distributed transverse load $q = 1$ lb/in$^2$ as obtained from FEM and DMCDM for various mesh sizes. It can be seen that the for $32 \times 32$ uniform mesh there is no difference between the results from FEM and DMCDM up to $5^{th}$ decimal. For all the further analysis we use a $32 \times 32$ uniform primal mesh for DMCDM and finite element mesh for FEM. Once the displacement field is obtained from the dual mesh control domain method, the strains and stresses can be computed using Eqs.(7.4.2) and (7.4.3), respectively. In the present study, the strains and stresses are evaluated at the center of each element of the primal mesh. This is similar to the evaluation of stresses at single Gauss quadrature point of each finite element of the finite element mesh.

Table 7.3: Dimensionless center deflection, $\overline{w}(0,0)$ of a clamped square plate under uniformly distributed load of $q = 1$ lb/in$^2$ for various values of $n$ [8].

| | n=0 | | n=1 | | n=2 | | n=3 | | n=4 | | n=5 | |
|---|---|---|---|---|---|---|---|---|---|---|---|---|
| Mesh | FEM | DMCDM | FEM | DMCDM | FEM | DMCDM | FEM | DMCDM | FEM | DMCDM | FEM | DMCDM |
| $2 \times 2$ | 0.01326 | 0.01281 | 0.03102 | 0.02997 | 0.04548 | 0.04395 | 0.05370 | 0.05187 | 0.05796 | 0.05601 | 0.06039 | 0.05838 |
| $4 \times 4$ | 0.01368 | 0.01359 | 0.03201 | 0.03174 | 0.04692 | 0.04659 | 0.05544 | 0.05499 | 0.05985 | 0.05937 | 0.06237 | 0.06186 |
| $8 \times 8$ | 0.0138 | 0.01377 | 0.03231 | 0.03222 | 0.04737 | 0.04728 | 0.05592 | 0.05580 | 0.06036 | 0.06024 | 0.06291 | 0.06279 |
| $16 \times 16$ | 0.01383 | 0.01383 | 0.03237 | 0.03234 | 0.04749 | 0.04746 | 0.05604 | 0.05601 | 0.06051 | 0.06048 | 0.06306 | 0.06300 |
| $32 \times 32$ | 0.01384 | 0.01384 | 0.03237 | 0.03237 | 0.04749 | 0.04749 | 0.05607 | 0.05607 | 0.06054 | 0.06054 | 0.06309 | 0.06306 |

Note that the bending stiffness of the plate decreases with increase in $n$. This can be seen from the plot of dimensionless bending stiffness $\overline{D}$ as a function of $n$ in Fig. 7.16a. Thus we expect that the transverse deflection of the plate increases with increase in the value of $n$. Fig. 7.16b presents the dimensionless transverse deflection, $\overline{w}$ along the line $y = 0$ for various values of $n$ of a simply-supported functionally graded plate under the action of uniformly distributed load of $q = 1$ lb/in$^2$. As expected the magnitude of the dimensionless transverse deflection increases with increase in $n$. However, the bending-extension coupling stiffness $B$ first increases and then decreases with increasing $n$. This is shown in Fig. 7.17a, where the dimensionless extensional-bending coupling stiffness is plotted as function of $n$. Thus we expect that the magnitude of the axial deflections of the plate to first increases with increase in $n$ and then decrease. This conjecture is verified in Fig. 7.17b, where the dimensionless axial deflection, $\overline{u}$ of a simply supported functionally graded plate along the line $y = 0$ is plotted for various values of $n$. Further, the results from DMCDM are coincident with the results from FEM in both Fig. 7.16b and Fig. 7.17b.

The dimensionless Young's modulus $\overline{E}$ of the functionally graded plate as a function of dimensionless thickness coordinate $\eta$ for various values of $n$ is presented in Fig. 7.18(a). It can be seen that as $n$ increases the portion of the plate thickness on which the Young's modulus changes decreases. The first order shear deformation theory predicts constant transverse shear strains along the thickness and hence for a homogeneous plate the transverse shear stresses will not be function of the thickness coordinate $z$. However, for a functionally graded plate the Young's modulus changes with the thickness coordinate and hence the shear modulus also changes in a similar fashion (since $\nu$ is assumed to be constant). Thus for a functionally graded plate although the first-order shear deformation theory predicts constant transverse shear strains along the thickness, the transverse shear stresses vary with the thickness coordinate in a similar fashion as Young's modulus as a function of the thickness coordinate. This is shown in Fig. 7.18(b) where the dimensionless transverse shear stress $\overline{\sigma}_{xz}$ is plotted as function of dimensionless thickness coordinate $\eta$ at $(x, y) = (L/128, W/128)$ for clamped boundary conditions. For higher values of $n$, $\overline{\sigma}_{xz}$ is almost constant for the most part of the plate thickness and only changes towards the top surface in a

similar fashion as Young's modulus, as expected. Also the results form DMCDM are compared with the results from FEM in Fig. 7.18(b).

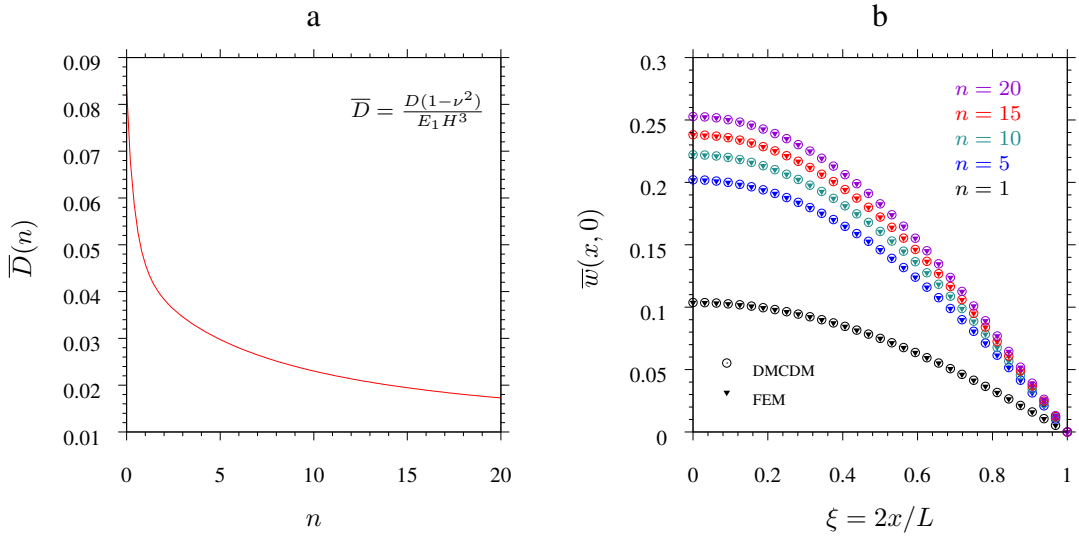


Figure 7.16: (a) Dimensionless bending stiffness as function of $n$. (b) Dimensionless transverse deflection, $\overline{w}$ along $y = 0$ of a simply-supported functionally graded plate under the action of uniformly distributed load $q = 1$ lb/in$^2$ [8].

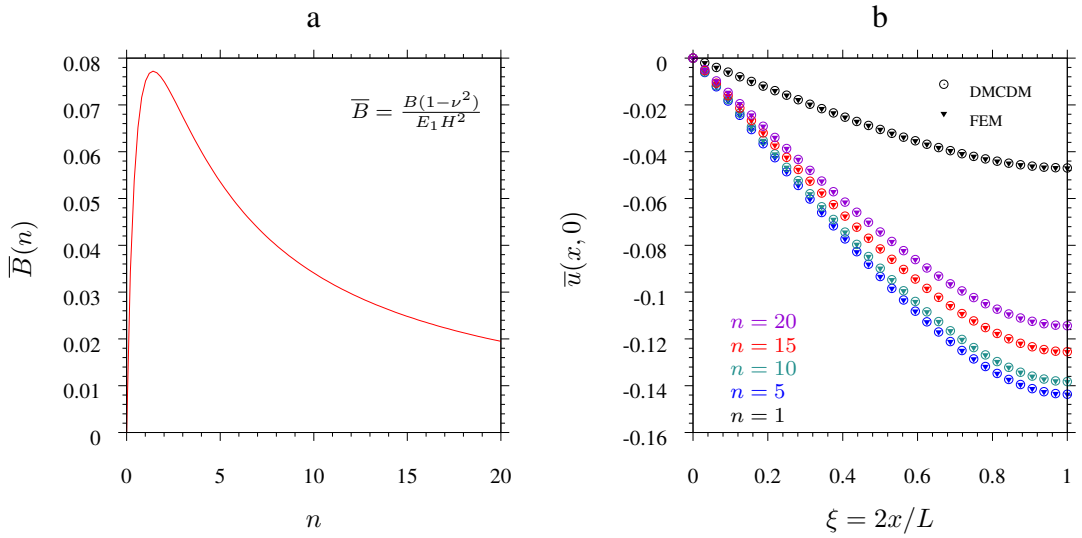


Figure 7.17: (a) Dimensionless extensional-bending coupling stiffness as function of $n$. (b) Dimensionless axial deflection, $\overline{u}$ along $y = 0$ of a simply-supported functionally graded plate under the action of uniformly distributed load $q = 1$ lb/in$^2$ [8].

Finally, Fig. 7.19a and Fig. 7.19b present the dimensionless stresses $\overline{\sigma}_{xx}$ and $\overline{\sigma}_{xy}$ respectively, obtained from DMCDM, on the top surface of the clamped functionally graded plate along the line $x = y$ for various values of $n$. It can be seen that the magnitude of both these dimensionless stresses increases with increasing $n$.

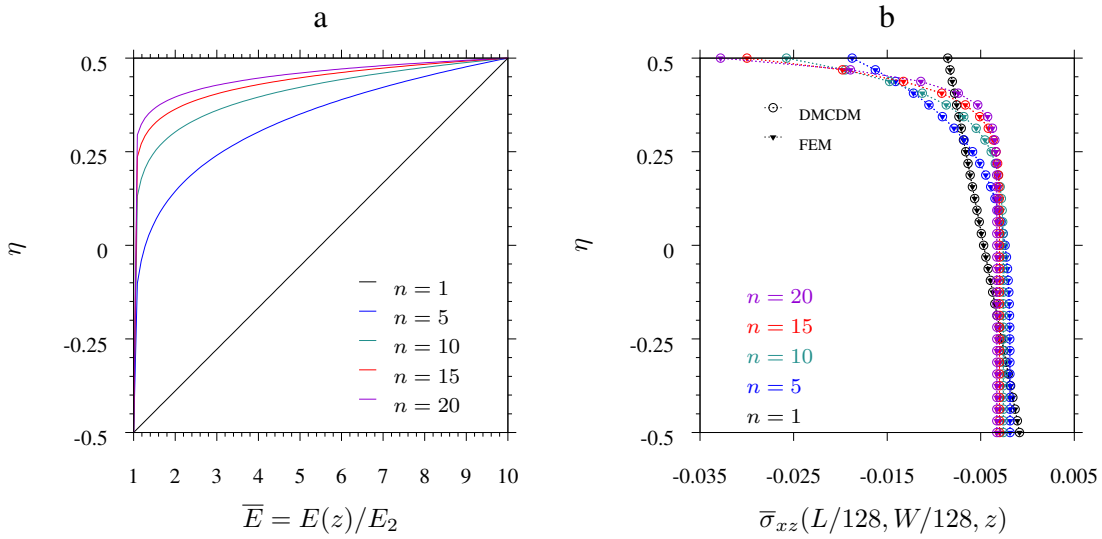


Figure 7.18: (a) Dimensionless Young's modulus $\overline{E}$ as a function of dimensionless thickness coordinate $\eta$ for various values of $n$. (b) Dimensionless stress $\overline{\sigma}_{xz}$ along the thickness of clamped functionally graded plate at $(x, y) = (L/128, W/128)$ [8].

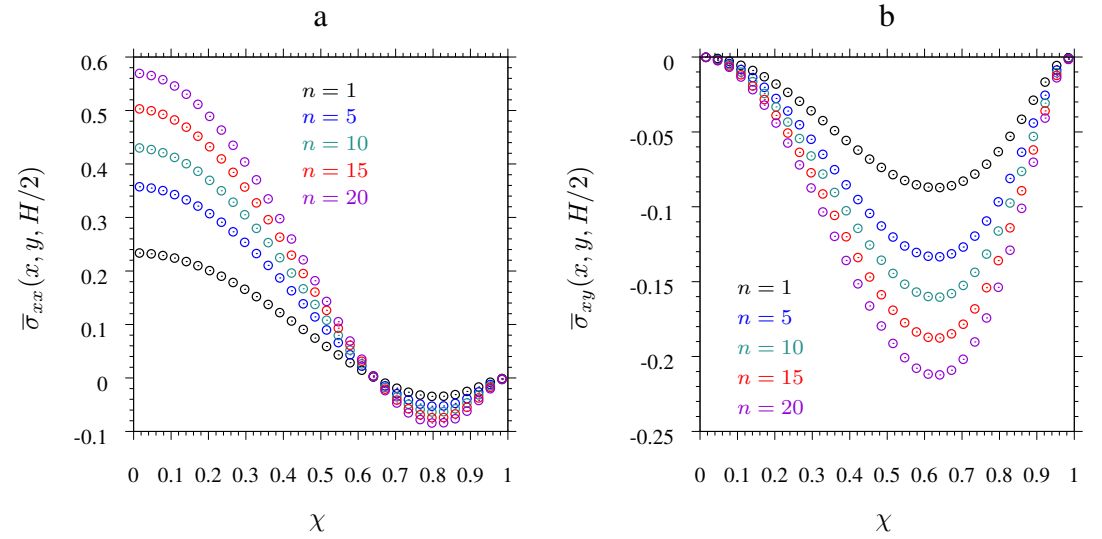


Figure 7.19: (a) Dimensionless stress $\overline{\sigma}_{xx}$ on the top surface along the line $x = y$ for clamped boundary conditions. (b) Dimensionless stress $\overline{\sigma}_{xy}$ on the top surface along the line $x = y$ for clamped boundary conditions [8].

# 8. CONCLUSIONS AND FUTURE WORK

Nonlinear micropolar beam and plate theories and their corresponding finite element models are developed in this dissertation. The developed nonlinear theories are then used in modeling lattice core sandwich beams and plates using a homogenization technique [1, 4, 9]. The methodology considered in this dissertation for modeling lattice core sandwich structures as micropolar beams or plates works well in predicting the global displacement of the lattice structure. However, calculating local deformations and local stress fields within the lattice structure is not a straight forward procedure. Further investigation is needed to develop appropriate methods for recovering local stresses in the lattice structures.

The dual mesh control domain method has a lot of potential applications. The application of dual mesh control domain method to structural elements with linear constitutive relations (linear elastic material) and linear strain-displacement relations (no geometric nonlinearity) was considered in this dissertation [10, 7, 8]. The next natural step is the development of the dual mesh control domain method for beams and plates which include geometric nonlinearity. The simplest case of geometric nonlinearity in beams and plates is due to moderate rotations (see [107]) and can be easily incorporated into the beam and plate theories by including von Kármán nonlinear strains. Further, dual mesh control domain method can also be extended to study 2-D (plane stress and plane strain) and 3-D linear elasticity problems. The problems of large deformation in solid continua, which are described by complete Green-Lagrange strain tensor, require the distinction between current and reference configurations of the body. Thus, the dual mesh control domain method for such problems require updating of the geometry of the computational domain and needs to be explored. Finally, problems involving material nonlinearity (eg. nonlinear hyperelastic material or plasticity) can also be studied using dual mesh control domain method.

# REFERENCES


[1] A. T. Karttunen, J. N. Reddy, and J. Romanoff, "Micropolar modeling approach for periodic sandwich beams," *Composite Structures*, vol. 185, pp. 656–664, 2018.

[2] P. Moongkhamklang, D. M. Elzey, and H. N. Wadley, "Titanium matrix composite lattice structures," *Composites Part A: Applied Science and Manufacturing*, vol. 39, no. 2, pp. 176–187, 2008.

[3] P. Nampally and J. N. Reddy, "Geometrically nonlinear Euler–Bernoulli and Timoshenko micropolar beam theories," *Acta Mechanica*, vol. 231, no. 10, pp. 4217–4242, 2020.

[4] A. T. Karttunen, J. N. Reddy, and J. Romanoff, "Two-scale constitutive modeling of a lattice core sandwich beam," *Composites Part B: Engineering*, vol. 160, pp. 66–75, 2019.

[5] P. Nampally, A. T. Karttunen, and J. N. Reddy, "Nonlinear finite element analysis of lattice core sandwich beams," *European Journal of Mechanics - A/Solids*, vol. 74, pp. 431–439, 2019.

[6] P. Nampally, A. T. Karttunen, and J. N. Reddy, "Nonlinear finite element analysis of lattice core sandwich plates," *International Journal of Non-Linear Mechanics*, vol. 121, p. 103423, 2020.

[7] P. Nampally and J. N. Reddy, "Bending Analysis of Functionally Graded Axisymmetric Circular Plates using the Dual Mesh Finite Domain Method," *Latin American Journal of Solids and Structures*, vol. 17, 2020.

[8] P. Nampally, E. Ruocco, and J. N. Reddy, "Bending analysis of functionally graded rectangular plates using the dual mesh control domain method," *International Journal for Computational Methods in Engineering Science and Mechanics*, vol. 0, no. 0, pp. 1–14, 2021.

[9] A. T. Karttunen, J. N. Reddy, and J. Romanoff, "Two-scale micropolar plate model for web-core sandwich panels," *International Journal of Solids and Structures*, vol. 170, pp. 82–94,

2019.

[10] J. N. Reddy and P. Nampally, "A dual mesh finite domain method for the analysis of functionally graded beams," *Composite Structures*, vol. 251, p. 112648, 2020.

[11] E. Cosserat and F. Cosserat, *Théorie des corps déformables*. A. Hermann et fils, 1909.

[12] A. C. Eringen and E. S. Suhubi, "Nonlinear theory of simple micro-elastic solids, i and ii," *Int. J. Eng. Sci.,*, vol. 2, no. 2, pp. 189–203, 1964.

[13] C. B. Kafadar and A. C. Eringen, "Micropolar media-i the classical theory," *Int. J. Eng. Sci.*, vol. 9, no. 3, pp. 271–305, 1971.

[14] C. B. Kafadar and A. C. Eringen, "Micropolar media-ii the relativisitc theory," *Int. J. Eng. Sci.*, vol. 9, no. 3, pp. 307–329, 1971.

[15] A. Pau and P. Trovalusci, "Block masonry as equivalent micropolar continua: the role of relative rotations.," *Acta. Mech.*, vol. 223, pp. 1455–1471, 2012.

[16] P. Trovalusci, M. Ostoja-Starzewski, M. De Bellis, and A. Murrali, "Scale-dependent homogenization of random composites as micropolar continua," *Eur. J. Mech. A-Solid.*, vol. 49, pp. 396–407, 2015.

[17] P. Trovalusci, L. De Bellis, M, and R. Masiani, "A multiscale description of particle composites: From lattice microstructures to micropolar continua," *Compos. B-Eng.*, vol. 128, pp. 164–173, 2017.

[18] S. Fan and Z. Cheng, "A micropolar model for elastic properties in functionally graded materials," *Advances in Mechanical Engineering*, 2018.

[19] E. A. Ivanova, A. M. Krivtsov, and N. F. Morozov, "Inclusion of the moment interaction in the calculation of the flexural rigidity of nanostructures," *Dokl. Phys.*, vol. 48, pp. 455–458, 2003.

[20] R. S. Lakes, "Experimental microelasticity of two porous solids," *Int. J. Solids Struct.*, vol. 22, pp. 55–63, 1986.

[21] R. S. Lakes, "Experimental micro mechanics methods for conventional and negative poisson's ration cellular solids as cosserat continua," *Trans. ASME J. Eng. Mater. Technol.*, vol. 113, pp. 148–155, 1991.

[22] R. S. Lakes, "Experimental methods for study of cosserat elastic solids and other generalized continua.," *In: Mühlhaus, H.(ed.) Continuum Models for Materials with Micro-Structure*, pp. 1–22, 1995.

[23] J. F. C. Yang and R. S. Lakes, "Experimental study of micropolar and couple stress elasticity in compact bone in bending," *J. Biomech.*, vol. 15, no. 2, pp. 91–98, 1982.

[24] S. K. Park and X. L. Gao, "Bernoulli-Euler beam model based on a modified couple stress theory," *J. Micromech. Microeng.*, vol. 16, no. 11, pp. 2355–2359, 2006.

[25] H. M. Ma, X.-L. Gao, and J. N. Reddy, "A microstructure-dependent Timoshenko beam model based on a modified couple stress theory," *J. Mech. Phys. Solids*, vol. 56, no. 12, pp. 3379–3391, 2008.

[26] H. M. Ma, X. L. Gao, and J. N. Reddy, "A Nonclassical Reddy-Levinson Beam Model Based on a Modified Couple Stress Theory," *Int. J. Multiscale Com.*, vol. 8, no. 2, pp. 167–180, 2010.

[27] J. N. Reddy, "Microstructure-dependent couple stress theories of functionally graded beams," *J. Mech. Phys. Solids*, vol. 59, no. 11, pp. 2382–2399, 2011.

[28] A. Arbind, J. N. Reddy, and A. R. Srinivasa, "Modified couple stress-based third-order theory for nonlinear analysis of functionally graded beams," *Latin American Journal of Solids and Structures*, vol. 11, pp. 459–487, 2014.

[29] B. Wang, J. Zhao, and S. Zhou, "A micro scale Timoshenko beam model based on strain gradient elasticity theory," *Eur. J. Mech. A-Solid.*, vol. 29, no. 4, pp. 591–599, 2010.

[30] R. Ansari, R. Gholami, and S. Sahmani, "Free vibration analysis of size dependent functionally graded microbeams based on the strain gradient Timoshenk beam theory," *Compos. Struct.*, vol. 94, no. 1, pp. 221–228, 2011.

[31] M. H. Kahrobaiyan, M. Asghari, M. Rahaeifard, and M. T. Ahmadian, "A nonlinear strain gradient beam formulation," *Int. J. Eng. Sci.*, vol. 49, no. 11, pp. 1256–1267, 2011.

[32] J. N. Reddy, "Nonlocal thories for bending, buckling and vibration of beams," *Int. J. Eng. Sci.*, vol. 45, no. 2-8, pp. 288–307, 2007.

[33] J. N. Reddy, "Nonlocal nonlonlinear formulations for bending of classical and shear deformation theories of beams and plates," *Int. J. Eng. Sci.*, vol. 48, no. 11, pp. 1507–1518, 2010.

[34] H. T. Thai, "A nonlocal beam theory for bending, buckling and vibration of nanobeams," *Int. J. Eng. Sci.*, vol. 52, pp. 56–64, 2012.

[35] N. Ding, X. Xu, and Z. Zheng, "A size-dependent nonlinear microbeam model based on the micropolar elasticity theory," *Acta Mechanica*, vol. 227, no. 12, pp. 3497–3515, 2016.

[36] A. K. Noor and M. P. Nemeth, "Micropolar beam models for lattice grids with rigid joints," *Comput. Meth. Appl. Mech. Eng.*, vol. 21, no. 2, pp. 249–263, 1980.

[37] A. K. Noor, "Continuum modeling for repetitive lattice structures," *Appl. Mech. Rev.*, vol. 41, no. 7, pp. 285–296, 1988.

[38] F. Dos Reis and J. F. Ganghoffer, "Construction of micropolar continua from the asymptotic homogenization of beam lattices," *Comput. Struct.*, vol. 112-113, pp. 354–363, 2012.

[39] F. Liu, L. Wang, X. Liu, and P. Lu, "Equivalent micropolar beam model for spatial vibration analysis of planar repetitive truss structure with flexible joints," *Int. J. Mech. Sci.*, vol. 165, p. 105202, 2020.

[40] S. Roy Chowdhury and J. N. Reddy, "Geometrically exact micropolar Timoshenko beam and its application in modelling sandwich beams made of architected lattice core," *Composite Structures*, vol. 226, p. 111228, 2019.

[41] S. Ramezani, R. Naghdabadi, and S. Sohrabpour, "Analysis of micropolar elastic beams," *Eur. J. Mech A-Solid.*, vol. 28, no. 2, pp. 202–208, 2009.

[42] F. Y. Huang, B. H. Yan, J. L. Yan, and D. U. Yang, "Bending analysis of micropolar elastic beam using a 3-D finite element method," *Int. J. Eng. Sci.*, vol. 38, no. 3, pp. 275–286, 2000.

[43] S. Abrate and M. Di Sciuva, "Equivalent single layer theories for composite and sandwich structures: A review," *Composite Structures*, vol. 179, pp. 482–494, 2017.

[44] A. C. Eringen, *Microcontinuum Field Theories: I. Foundations and Solids*. Springer Science & Business Media, 2012.

[45] A. Pothier and J. J. Rencis, "Three-dimensional finite element formulation for microelastic solids," *Comput. Struct.*, vol. 51, no. 1, pp. 1–21, 1994.

[46] L. Li and S. Xie, "Finite element method for linear micropolar elasticity and numerical study of some scale effects phenomena in MEMES," *Int. J. Mech. Sci.*, vol. 46, no. 11, pp. 1571–1587, 2004.

[47] K. Roman and L. Steinberg, "Numerical modeling of bending of micropolar plates," *Thin-Walled Structures*, vol. 69, pp. 67–78, 2013.

[48] X. Zhou and G. Cusatis, "Tetrahedral finite element with rotational degrees of freedom for cosserat and cauchy continuum problems," *J. Eng. Mech.*, vol. 141, no. 2, 2015.

[49] R. Ansari, A. H. Shakouri, M. Bazdid-Vahdati, A. Norouzzadeh, and H. Rouhi, "A Nonclassical Finite Element Approach for the Nonlinear Analysis of Micropolar Plates," *Journal of Computational and Nonlinear Dynamics*, vol. 12, nov 2016.

[50] R. Ansari, A. Norouzzadeh, A. H. Shakouri, M. Bazdid-Vahdati, and H. Rouhi, "Finite element analysis of vibrating micro-beams and -plates using a three-dimensional micropolar element," *Thin Wall. Struct.,*, vol. 124, pp. 489–500, 2018.

[51] M. Godio, I. Stefanou, K. Sab, and J. Sulem, "Dynamic finite element formulation for Cosserat elastic plates," *International Journal for Numerical Methods in Engineering*, vol. 101, pp. 992–1018, mar 2015.

[52] L. Li and S. Xie, "Finite element method for linear micropolar elasticity and numerical study of some scale effects phenomena in MEMS," *International Journal of Mechanical Sciences*, vol. 46, no. 11, pp. 1571–1587, 2004.

[53] S. Hassanpour and G. Heppler, "Uncomplicated torsion and bending theories for micropolar elastic beams," in *Proceedings of the 11th World Congess on Computational Mechanics*, jul 2014.

[54] R. A. Regueiro and Z. Duan, "Static and dynamic micropolar linear elastic beam finite element formulation, implementation, and analysis," *J. Eng. Mech.,*, vol. 141, no. 8, 2015.

[55] W. Nowacki, *Theory of Micropolar Elasticity*. New York: Springer, 1970.

[56] W. Nowacki, *Theory of Asymmetric Elasticity*. Pergamon Press, 1986.

[57] V. A. Eremeyev, L. P. Lebedev, and H. Altenbach, *Foundations of Micropolar Mechanics*. SpringerBriefs in Applied Sciences and Technology-Continuum Mechanics, Springer, 2013.

[58] W. Pietraszkiewicz and V. A. Eremeyev, "On natural strain measures of the non-linear micropolar continuum," *Int. J. Solids Struct.*, vol. 46, no. 3-4, pp. 774–787, 2009.

[59] W. Pietraszkiewicz and V. A. Eremeyev, "On vectorially parameterized natural strain measures of the non-linear cosserat continuum," *Int. J. Solids Struct.*, vol. 46, no. 11-12, pp. 2477–2480, 2009.

[60] R. Ansari, A. H. Shakouri, M. Bazdid-Vahdti, A. Norouzzadeh, and R. H, "A Nonclassical Finite Element Approach for the Nonlinear Analysis of Micropolar Plates," *J. Comput. Nonlin. Dyn.,*, vol. 12, no. 1, p. 011019, 2017.

[61] N. A. Fleck, V. S. Deshpande, and M. F. Ashby, "Micro-architectured materials: past, present and future," *Proc. R. Soc. A*, vol. 466, no. 2121, 2010.

[62] J. Bauer, L. R. Meza, T. A. Schaedler, R. Schwaiger, X. Zheng, and L. Valdevit, "Nanolattices: An Emerging Class of Mechanical Metamaterials," *Adv. Mater.*, vol. 29, no. 40, p. 1701850, 2017.

[63] H. G. Allen, *Analysis and Design of Structural Sandwich Panels*. Pergamon Press, 1969.

[64] V. Birman and G. A. Kardomateas, "Review of current trends in research and applications of sandwich structures," *Compos. Part B-Eng.*, vol. 142, pp. 221–240, 2018.

[65] K. F. Karlsson and B. T. Åström, "Manufacturing and applications of structural sandwich components," *Compos. Part A-Appl. S.,*, vol. 28, no. 2, pp. 97–111, 1997.

[66] H. N. G. Wadley, N. A. Fleck, and A. G. Evans, "Fabrication and structural performance of periodic cellular metal sandwich structures," *Composites Science and Technology*, vol. 63, no. 16, pp. 2331–2343, 2003.

[67] J. R. Vinson, *The Behaviour of Sandwich Structures of Isotropic and Composite Materials*. CRC Press, 1999.

[68] J. R. Vinson, "Sandwich Structures," *Applied Mechanics Reviews*, vol. 54, pp. 201–214, may 2001.

[69] A. F. Johnson and G. D. Sims, "Mechanical properties and design of sandwich materials," *Composites*, vol. 17, no. 4, pp. 321–328, 1986.

[70] M. P. Arunkumar, J. Pitchaimani, K. V. Gangadharan, and M. C. L. Babu, "Sound transmission loss characteristics of sandwich aircraft panels: Influence of nature of core," *J. Sandw. Struct. Mater.*, vol. 19, no. 1, pp. 26–48, 2017.

[71] A. Cherniaev and I. Telichev, "Weight-efficiency of conventional shielding systems in protecting unmanned spacecraft from orbital debris," *J. Spacecraft Rockets*, vol. 54, no. 1, pp. 75–89, 2017.

[72] T. N. Bitzer, "Honeycomb marine applications," *J. Reinf. Plast. Compos.,*, vol. 13, pp. 355–360, 1994.

[73] A. P. Mouritz, E. Gellert, P. Burchhill, and K. Challis, "Review of advanced composite structures for naval ships and submarines," *Compos. Struct.,*, vol. 53, pp. 21–41, 2001.

[74] M. S. H. Fatt and D. Sirivolu, "Marine composite sandwich plates under air and water blasts," *Mar. Struct.*, vol. 56, pp. 163–185, 2017.

[75] P. Kujala and A. Klanac, "Steel Sandwich Panels in Marine Applications," *Brodogradnja (brodogradnja@hrbi.hr); Vol.56 No.4*, vol. 56, dec 2005.

[76] F. Roland and B. Metschkow, *Laser welded sandwich panels for shipbuilding and structural steel engineering*. Transactions on the Built Environment, vol 24. WIT Press, 1997.

[77] S. R. Bright and J. W. Smith, "Fatigue performance of laser-welded steel bridge decks," *Structural Engineer*, vol. 82, pp. 31–39, nov 2004.

[78] S. R. Bright and J. W. Smith, "A new design for steel bridge decks using laser fabrication," *The Structural Engineer*, vol. 85, pp. 49–57, nov 2007.

[79] P. Nilsson, M. Al-Emrani, and S. R. Atashipour, "Transverse shear stiffness of corrugated core steel sandwich panels with dual weld lines," *Thin-Walled Structures*, vol. 117, pp. 98–112, 2017.

[80] C. R. Briscoe, S. C. Mantell, J. H. Davidson, and T. Okazaki, "Design procedure for web core sandwich panels for residential roofs," *J. Sandw. Struct. Mater.,*, vol. 13, no. 1, pp. 23–58, 2011.

[81] W. Burton and A. K. Noor, "Assessment of computational models for sandwich panels and shells," *Computer Methods in Applied Mechanics and Engineering*, vol. 124, no. 1, pp. 125–151, 1995.

[82] J. Hohe and L. Librescu, "Advances in the structural modeling of elastic sandwich panels," *Mech. Adv. Mater. Struc.,*, vol. 11, no. 4–5, pp. 395–424, 2004.

[83] E. Carrera and S. Brischetto, "A Survey with Numerical Assessment of Classical and Refined Theories for the Analysis of Sandwich Plates," *Appl. Mech. Rev.,*, vol. 62, no. 1, p. 010803, 2009.

[84] A. S. Sayyad and Y. M. Ghugal, "Bending, buckling and free vibration of laminated composite and sandwich beams: A critical review of literature," *Compos. Struct.*, vol. 171, pp. 486–504, 2017.

[85] J. N. Reddy, *Mechanics of Laminated Composite Plates and Shells: Theory and Analysis*. CRC Press, 2004.

[86] V. Skvortsov and E. Bozhevolnaya, "Two-dimensional analysis of shallow sandwich panels," *Compos. Struct.*, vol. 53, no. 1, pp. 43–53, 2001.

[87] A. Barut, E. Madenci, J. Heinrich, and A. Tessler, "Analysis of thick sandwich construction by a {3,2}-order theory," *International Journal of Solids and Structures*, vol. 38, no. 34, pp. 6063–6077, 2001.

[88] A. Barut, E. Madenci, T. Anderson, and A. Tessler, "Equivalent single-layer theory for a complete stress field in sandwih panels under arbitrarily distributed loading," *Compos. Struct.,*, vol. 58, no. 4, pp. 483–495, 2002.

[89] S. Khakalo, V. Balobanov, and J. Niiranen, "Modelling size-dependent bending, buckling and vibrations of 2D triangular lattices by strain gradient elasticity models: Applications to sandwich beams and auxetics," *Int. J. Eng. Sci.*, vol. 127, pp. 33–52, 2018.

[90] S. Khakalo and J. Niiranen, "Anisotropic strain gradient thermoelasticity for cellular structures: Plate models, homogenization and isogeometric analysis," *J. Mech. Phys. Solids*, vol. 134, p. 103728, 2020.

[91] B. R. Goncalves, A. T. Karttunen, J. Romanoff, and J. N. Reddy, "Buckling and free vibration of shear-flexible sandwich beams using a couple-stress-based finite element," *Compos. Struct.,*, vol. 165, pp. 233–241, 2017.

[92] A. T. Karttunen and J. N. Reddy, "Hierarchy of beam models for lattice core sandwich structures," *International Journal of Solids and Structures*, vol. 204-205, pp. 172–186, 2020.

[93] J. N. Reddy, *An Introduction to the Finite Element Method*. McGraw-Hill, New York, NY, 4th ed., 2019.

[94] S. Mazumder, *Numerical Methods for Partial Differential Equations. Finite Difference and Finite Volume Methods*. New York, NY: Elsevier, 2016.

[95] J. N. Reddy, "A dual mesh finite domain method for the numerical solution of differential equations," *International Journal for Computational Methods in Engineering Science and Mechanics*, vol. 20, no. 3, pp. 212–228, 2019.

[96] J. N. Reddy, M. Matthew, and P. Nampally, "A novel numerical method for the solution of nonlinear equations with applications to heat transfer," jan 2021.

[97] O. A. Bauchau and J. I. Craig, *Structural Analysis: With Applications to Aerospace Structures*, vol. 163. Springer Science & Business Media, 2009.

[98] C. M. Wang, J. N. Reddy, and K. H. Lee, *Shear Deformable Beams and Plates*. Elsevier, 2000.

[99] W. S. Slaughter, *The Linearized Theory of Elasticity*. Birkhäuser Boston, 2002.

[100] J. N. Reddy, *An Introduction to Nonlinear Finite Element Analysis*. Oxford, UK: Oxford University Press, 2nd editio ed., 2015.

[101] R. Schmidt and J. N. Reddy, "A Refined Small Strain and Moderate Rotation Theory of Elastic Anisotropic Shells," *Journal of Applied Mechanics*, vol. 55, no. 3, pp. 611–617, 1988.

[102] J. N. Reddy, *Energy Principles and Variational Methods in Applied Mechanics*. New York, NY: John Wiley& Sons, 3rd ed., 2018.

[103] K. J. Bathe, *Finite Element Procedures*. Englewood Cliffs, NJ: Prentice–Hall, 2006.

[104] G. S. Payette and J. N. Reddy, "A Nonlinear Finite Element Framework for Viscoelastic Beams Based on the High-Order Reddy Beam Theory," *J. Mater. Technol.*, vol. 135, no. 1, pp. 011005–1–011005–11, 2013.

[105] V. A. Eremeyev, A. Skrzat, and F. Stachowicz, "On Finite Element Computations of Contact Problems in Micropolar Elasticity," *Advances in Material Science and Engineering*, vol. 2016, pp. 433–447, 2016.

[106] M. McGregor and M. A. Wheel, "On the Coupling number and characteristic length of micropolar media of differing topology," *Proc. R. Soc. A.*, vol. 470, 2014.

[107] J. N. Reddy, *Theory and Analysis of Elastic Plates and Shells*. CRC Press, Boca Raton, FL, 2nd ed., 2007.

[108] T. J. R. Hughes, M. Cohen, and M. Haroun, "Reduced and selective integration techniques in the finite element analysis of plates," *Nuclear Engineering and Design*, vol. 46, no. 1, pp. 203–222, 1978.

[109] O. C. Zienkiewicz, R. L. Taylor, and J. M. Too, "Reduced integration technique in general analysis of plates and shells," *International Journal for Numerical Methods in Engineering*, vol. 3, no. 2, pp. 275–290, 1971.

[110] G. N. Praveen, C. D. Chin, and J. N. Reddy, "Thermoelastic Analysis of Functionally Graded Ceramic-Metal Cylinder," *Journal of Engineering Mechanics, ASCE*, vol. 125, no. 11, pp. 1259–1266, 1999.

[111] G. N. Praveen and J. N. Reddy, "Nonlinear Transient Thermoelastic Analysis of Functionally Graded Ceramic-Metal Plates," *Journal of Solids and Structures*, vol. 35, no. 33, pp. 4457–4476, 1998.

[112] J. N. Reddy, P. Nampally, and A. R. Srinivasa, "Nonlinear analysis of functionally graded beams using the dual mesh finite domain method and the finite element method," *International Journal of Non-Linear Mechanics*, vol. 127, p. 103575, 2020.

[113] J. N. Reddy, P. Nampally, and N. Phan, "Dual mesh control domain analysis of functionally graded circular plates accounting for moderate rotations," *Composite Structures*, vol. 257, p. 113153, 2021.

[114] J. N. Reddy, "Analysis of functionally graded plates," *International Journal for Numerical Methods in Engineering*, vol. 47, no. 1-3, pp. 663–684, 2000.

[115] M. Naebe, K. Shirvanimoghaddam, J. N. Reddy, C. M. Wang, and S. Kitipornchai, "Functionally graded materials: A review of fabrication and properties," *European Journal of Mechanics - A/Solids*, vol. 5, no. 2, pp. 185–199, 1999.

APPENDIX A

MICROPOLAR BEAM AND PLATE CONSTITUTIVE RELATIONS

## A.1 Micropolar beams

| | **von Kármán Nonlinearity** | |
|---|---|---|
| | VEMBT | VTMBT |
| $N_{xx}^{*(s)}$ | $A_{11}\left(\frac{du_0^E}{dx}+\frac{1}{2}\left(\frac{dw_0^E}{dx}\right)^2\right)$ | $A_{11}\left(\frac{du_0^T}{dx}+\frac{1}{2}\left(\frac{dw_0^T}{dx}\right)^2\right)$ |
| $M_{xx}^{*(s)}$ | $-D_{11}\frac{d^2w_0^E}{dx^2}$ | $D_{11}\frac{d\phi_x^T}{dx}$ |
| $Q_x^{*(s)}$ | $0$ | $\frac{A_{44}}{2}\left(\frac{dw_0^T}{dx}+\phi_x^T\right)$ |
| $Q_x^{*(a)}$ | $-A_{77}\left(\frac{dw_0^E}{dx}+\psi_y^E\right)$ | $\frac{A_{77}}{2}\left(\phi_x^T-\frac{dw_0^T}{dx}-2\psi_y^T\right)$ |
| $P_{yx}^{*}$ | $E_{44}\frac{d\psi_y^E}{dx}$ | $E_{44}\frac{d\psi_y^T}{dx}$ |

Table A.1: Constitutive relations for the von Kármán micropolar beam theories. Superscript * on the resultant terms is used to represent $E$ (for EMBT) or $T$ (for TMBT), depending on beam theory used.

| | **Micropolar Nonlinearity** | |
|---|---|---|
| | NEMBT | NTMBT |
| $\mathfrak{N}_{xx}^{*(s)}$ | $A_{11}\left(\frac{du_0^E}{dx} - \psi_y^E \frac{dw_0^E}{dx}\right)$ | $A_{11}\left(\frac{du_0^T}{dx} - \psi_y^T \frac{dw_0^T}{dx}\right)$ |
| $\mathfrak{M}_{xx}^{*(s)}$ | $-D_{11}\frac{d^2 w_0^E}{dx^2}$ | $D_{11}\frac{d\phi_x^T}{dx}$ |
| $\mathfrak{Q}_x^{*(s)}$ | 0 | $\frac{A_{44}}{2}\left(\frac{dw_0^T}{dx} + \phi_x^T\right)$ |
| $\mathfrak{Q}_x^{*(a)}$ | $-A_{77}\left(\frac{dw_0^E}{dx} + \psi_y^E\right)$ | $\frac{A_{77}}{2}\left(\phi_x^T - \frac{dw_0^T}{dx} - 2\psi_y^T\right)$ |
| $\mathfrak{P}_{yx}^{*}$ | $E_{44}\frac{d\psi_y^E}{dx}$ | $E_{44}\frac{d\psi_y^T}{dx}$ |

Table A.2: Constitutive relations for nonlinear micropolar beam theories. Superscript * on the resultant terms is used to represent $E$ or $T$, depending on beam theory used.

The constants in the constitutive relations of table A.1 and table A.2 are defined as

$$A_{11} = \int_A (\lambda + 2\mu + \kappa) dA \qquad D_{11} = \int_A (\lambda + 2\mu + \kappa) z^2 dA$$
$$A_{44} = \int_A (2\mu + \kappa) dA \qquad A_{77} = \int_A \kappa dA \qquad E_{44} = \int_A \gamma dA$$

where $A$ is the area of cross-section of the beam.

## A.2 Micropolar plates

The constitutive relations for von Kármán micropolar plate theory are:

$$\begin{Bmatrix} N_{xx}^{(s)} \\ N_{yy}^{(s)} \\ N_{xy}^{(s)} \\ N_{xy}^{(a)} \end{Bmatrix} = \begin{bmatrix} A_{11} & A_{12} & 0 & 0 \\ A_{12} & A_{11} & 0 & 0 \\ 0 & 0 & A_{44} & 0 \\ 0 & 0 & 0 & A_{77} \end{bmatrix} \begin{Bmatrix} \frac{\partial u_0}{\partial x} + \frac{1}{2}\left(\frac{\partial w_0}{\partial x}\right)^2 \\ \frac{\partial v_0}{\partial y} + \frac{1}{2}\left(\frac{\partial w_0}{\partial y}\right)^2 \\ \frac{1}{2}\left(\frac{\partial v_0}{\partial x} + \frac{\partial u_0}{\partial y} + \frac{\partial w_0}{\partial x}\frac{\partial w_0}{\partial y}\right) \\ \frac{1}{2}\left(\frac{\partial u_0}{\partial y} - \frac{\partial v_0}{\partial x}\right) \end{Bmatrix} \tag{A.2.1}$$

$$\begin{Bmatrix} M_{xx}^{(s)} \\ M_{yy}^{(s)} \\ M_{xy}^{(s)} \\ M_{xy}^{(a)} \end{Bmatrix} = \begin{bmatrix} D_{11} & D_{12} & 0 & 0 \\ D_{12} & D_{11} & 0 & 0 \\ 0 & 0 & D_{44} & 0 \\ 0 & 0 & 0 & D_{77} \end{bmatrix} \begin{Bmatrix} \frac{\partial \phi_x}{\partial x} \\ \frac{\partial \phi_y}{\partial y} \\ \frac{1}{2}\left(\frac{\partial \phi_y}{\partial x} + \frac{\partial \phi_x}{\partial y}\right) \\ \frac{1}{2}\left(\frac{\partial \phi_x}{\partial y} - \frac{\partial \phi_y}{\partial x}\right) \end{Bmatrix} \tag{A.2.2}$$

$$\begin{Bmatrix} Q_x^{(s)} \\ Q_x^{(a)} \\ Q_y^{(s)} \\ Q_y^{(a)} \end{Bmatrix} = \begin{bmatrix} A_{44} & 0 & 0 & 0 \\ 0 & A_{77} & 0 & 0 \\ 0 & 0 & A_{44} & 0 \\ 0 & 0 & 0 & A_{77} \end{bmatrix} \begin{Bmatrix} \frac{1}{2}\left(\phi_x + \frac{\partial w_0}{\partial x}\right) \\ \frac{1}{2}\left(\phi_x - \frac{\partial w_0}{\partial x} - 2\psi_y\right) \\ \frac{1}{2}\left(\phi_y + \frac{\partial w_0}{\partial y}\right) \\ \frac{1}{2}\left(\phi_y - \frac{\partial w_0}{\partial y} + 2\psi_x\right) \end{Bmatrix} \tag{A.2.3}$$

$$\begin{Bmatrix} P_{xx} \\ P_{yy} \\ P_{xy} \\ P_{yx} \end{Bmatrix} = \begin{bmatrix} E_{11} & E_{12} & 0 & 0 \\ E_{12} & E_{11} & 0 & 0 \\ 0 & 0 & E_{33} & E_{34} \\ 0 & 0 & E_{34} & E_{33} \end{bmatrix} \begin{Bmatrix} \frac{\partial \psi_x}{\partial x} \\ \frac{\partial \psi_y}{\partial y} \\ \frac{\partial \psi_x}{\partial y} \\ \frac{\partial \psi_y}{\partial x} \end{Bmatrix} \tag{A.2.4}$$

The constitutive relations for nonlinear micropolar plate theory are:

$$\begin{Bmatrix} \mathfrak{N}_{xx}^{(s)} \\ \mathfrak{N}_{yy}^{(s)} \\ \mathfrak{N}_{xy}^{(s)} \\ \mathfrak{N}_{xy}^{(a)} \end{Bmatrix} = \begin{bmatrix} A_{11} & A_{12} & 0 & 0 \\ A_{12} & A_{11} & 0 & 0 \\ 0 & 0 & A_{44} & 0 \\ 0 & 0 & 0 & A_{77} \end{bmatrix} \begin{Bmatrix} \frac{\partial u_0}{\partial x} - \psi_y \frac{\partial w_0}{\partial x} \\ \frac{\partial v_0}{\partial y} + \psi_x \frac{\partial w_0}{\partial y} \\ \frac{1}{2}\left(\frac{\partial u_0}{\partial y} + \frac{\partial v_0}{\partial x} + \psi_x \frac{\partial w_0}{\partial x} - \psi_y \frac{\partial w_0}{\partial y}\right) \\ \frac{1}{2}\left(\frac{\partial u_0}{\partial y} - \frac{\partial v_0}{\partial x} - \psi_x \frac{\partial w_0}{\partial x} - \psi_y \frac{\partial w_0}{\partial y}\right) \end{Bmatrix} \tag{A.2.5}$$

$$\begin{Bmatrix} \mathfrak{M}_{xx}^{(s)} \\ \mathfrak{M}_{yy}^{(s)} \\ \mathfrak{M}_{xy}^{(s)} \\ \mathfrak{M}_{xy}^{(a)} \end{Bmatrix} = \begin{bmatrix} D_{11} & D_{12} & 0 & 0 \\ D_{12} & D_{11} & 0 & 0 \\ 0 & 0 & D_{44} & 0 \\ 0 & 0 & 0 & D_{77} \end{bmatrix} \begin{Bmatrix} \frac{\partial \phi_x}{\partial x} \\ \frac{\partial \phi_y}{\partial y} \\ \frac{1}{2}\left(\frac{\partial \phi_x}{\partial y} + \frac{\partial \phi_y}{\partial x}\right) \\ \frac{1}{2}\left(\frac{\partial \phi_x}{\partial y} - \frac{\partial \phi_y}{\partial x}\right) \end{Bmatrix} \tag{A.2.6}$$

$$\begin{Bmatrix} \mathfrak{Q}_{x}^{(s)} \\ \mathfrak{Q}_{x}^{(a)} \\ \mathfrak{Q}_{y}^{(s)} \\ \mathfrak{Q}_{y}^{(a)} \end{Bmatrix} = \begin{bmatrix} A_{44} & 0 & 0 & 0 \\ 0 & A_{77} & 0 & 0 \\ 0 & 0 & A_{44} & 0 \\ 0 & 0 & 0 & A_{77} \end{bmatrix} \begin{Bmatrix} \frac{1}{2}\left(\phi_x + \frac{\partial w_0}{\partial x}\right) \\ \frac{1}{2}\left(\phi_x - \frac{\partial w_0}{\partial x} - 2\psi_y\right) \\ \frac{1}{2}\left(\phi_y + \frac{\partial w_0}{\partial y}\right) \\ \frac{1}{2}\left(\phi_y - \frac{\partial w_0}{\partial y} + 2\psi_x\right) \end{Bmatrix} \tag{A.2.7}$$

$$\begin{Bmatrix} \mathfrak{P}_{xx} \\ \mathfrak{P}_{yy} \\ \mathfrak{P}_{xy} \\ \mathfrak{P}_{yx} \end{Bmatrix} = \begin{bmatrix} E_{11} & E_{12} & 0 & 0 \\ E_{12} & E_{11} & 0 & 0 \\ 0 & 0 & E_{33} & E_{34} \\ 0 & 0 & E_{34} & E_{33} \end{bmatrix} \begin{Bmatrix} \frac{\partial \psi_x}{\partial x} \\ \frac{\partial \psi_y}{\partial y} \\ \frac{\partial \psi_x}{\partial y} \\ \frac{\partial \psi_y}{\partial x} \end{Bmatrix} \tag{A.2.8}$$

The constants in above constitutive relations are defined as

$$A_{11} = \int_{-H/2}^{H/2} (\lambda + 2\mu + \kappa) dz \qquad A_{12} = \int_{-H/2}^{H/2} \lambda dz$$
$$A_{44} = \int_{-H/2}^{H/2} (2\mu + \kappa) dz \qquad A_{77} = \int_{-H/2}^{H/2} \kappa dz$$
$$D_{11} = \int_{-H/2}^{H/2} (\lambda + 2\mu + \kappa) z^2 dz \qquad D_{12} = \int_{-H/2}^{H/2} \lambda z^2 dz$$
$$D_{44} = \int_{-H/2}^{H/2} (2\mu + \kappa) z^2 dz \qquad D_{77} = \int_{-H/2}^{H/2} \kappa z^2 dz$$
$$E_{11} = \int_{-H/2}^{H/2} (\alpha + \beta + \gamma) dz \qquad E_{12} = \int_{-H/2}^{H/2} \alpha dz$$
$$E_{33} = \int_{-H/2}^{H/2} \beta dz \qquad E_{34} = \int_{-H/2}^{H/2} \gamma dz$$

APPENDIX B

FINITE ELEMENT MATRICES OF MICROPOLAR BEAMS AND PLATES

## B.1 Micropolar beams

### B.1.1 Euler-Bernoulli beam theory

We use the following notation in representing the element stiffness and tangent stiffness matrices of Euler-Bernoulli beam theories.

$$^{MN}S_{ij}^{xx} = \frac{dL_i^{(M)}}{dx}\frac{dL_j^{(N)}}{dx}, \quad ^{MN}S_{ij}^{0x} = L_i^{(M)}\frac{dL_j^{(N)}}{dx}, \quad ^{MN}S_{ij}^{x0} = \frac{dL_i^{(M)}}{dx}L_j^{(N)}, \quad ^{MN}S_{ij}^{00} = L_i^{(M)}L_j^{(N)}$$

$$^{MN}S_{IJ}^{x^2x^2} = \frac{d^2H_I^{(M)}}{dx^2}\frac{d^2H_J^{(N)}}{dx^2}, \quad ^{MN}S_{IJ}^{xx} = \frac{dH_I^{(M)}}{dx}\frac{dH_J^{(N)}}{dx}, \quad ^{MN}S_{Ij}^{xx} = \frac{dH_I^{(M)}}{dx}\frac{dL_j^{(N)}}{dx}$$
$$^{MN}S_{iJ}^{xx} = \frac{dL_i^{(M)}}{dx}\frac{dH_J^{(N)}}{dx}, \quad ^{MN}S_{Ij}^{x0} = \frac{dH_I^{(M)}}{dx}L_j^{(N)}, \quad ^{MN}S_{iJ}^{0x} = L_i^{(M)}\frac{dH_J^{(N)}}{dx}$$

where $M, N = \{1, 2, 3\}$, $i, j = \{1, 2, \ldots n\}$ and $I, J = \{1, 2, \ldots 2n\}$. Where $n$ is the number of nodes in a typical finite element.

#### *B.1.1.1 von Kaŕmán micropolar Euler-Bernoulli beam*

$$K_{ij}^{11} = \int_{x_a}^{x_b} A_{11}\,{}^{11}S_{ij}^{xx}dx, \qquad K_{iJ}^{12} = \int_{x_a}^{x_b} \frac{A_{11}}{2}\left(\frac{dw_0^E}{dx}\right){}^{12}S_{iJ}^{xx}dx$$
$$K_{Ij}^{21} = \int_{x_a}^{x_b} A_{11}\left(\frac{dw_0^E}{dx}\right){}^{21}S_{Ij}^{xx}dx,$$
$$K_{IJ}^{22} = \int_{x_a}^{x_b}\left\{D_{11}\,{}^{22}S_{IJ}^{x^2x^2} + \frac{A_{11}}{2}\left(\frac{dw_0^E}{dx}\right)^2{}^{22}S_{IJ}^{xx} + 2A_{77}\,{}^{22}S_{IJ}^{xx}\right\}dx$$
$$K_{Ij}^{23} = \int_{x_a}^{x_b} 2A_{77}\,{}^{23}S_{Ij}^{x0}dx, \qquad K_{iJ}^{32} = \int_{x_a}^{x_b} 2A_{77}\,{}^{32}S_{iJ}^{0x}dx$$
$$K_{ij}^{33} = \int_{x_a}^{x_b}\left\{E_{44}\,{}^{33}S_{ij}^{xx} + 2A_{77}\,{}^{33}S_{ij}^{00}\right\}dx$$

The components of the element tangent stiffness matrix are the same as the components of the element stiffness matrix, except for the following terms:

$$T_{iJ}^{12} = K_{iJ}^{12} + \int_{x_a}^{x_b} \frac{A_{11}}{2} \left( \frac{dw_0^E}{dx} \right) {}^{12}S_{iJ}^{xx} dx, \quad T_{IJ}^{22} = K_{IJ}^{22} + \int_{x_a}^{x_b} A_{11} \left( \frac{du_0^E}{dx} + \left( \frac{dw_0^E}{dx} \right)^2 \right) {}^{22}S_{IJ}^{xx} dx$$

### *B.1.1.2 Micropolar nonlinear Euler-Bernoulli beam*

$$K_{ij}^{11} = \int_{x_a}^{x_b} A_{11} \, {}^{11}S_{ij}^{xx} dx, \quad K_{iJ}^{12} = -\int_{x_a}^{x_b} \frac{A_{11}}{2} \psi_y^E \, {}^{12}S_{iJ}^{xx} dx, \quad K_{ij}^{13} = -\int_{x_a}^{x_b} \frac{A_{11}}{2} \frac{dw_0^E}{dx} \, {}^{13}S_{ij}^{x0} dx$$

$$K_{Ij}^{21} = -\int_{x_a}^{x_b} \frac{A_{11}}{2} \psi_y^E \, {}^{21}S_{Ij}^{xx} dx, \quad K_{IJ}^{22} = \int_{x_a}^{x_b} \left\{ D_{11} \, {}^{22}S_{IJ}^{x^2x^2} + \frac{A_{11}}{2} (\psi_y^E)^2 \, {}^{22}S_{IJ}^{xx} + 2A_{77} \, {}^{22}S_{IJ}^{xx} \right\} dx$$

$$K_{Ij}^{23} = \int_{x_a}^{x_b} \left\{ \frac{A_{11}}{2} \left( \frac{dw_0^E}{dx} \psi_y^E - \frac{du_0^E}{dx} \right) + 2A_{77} \right\} {}^{23}S_{Ij}^{x0} dx, \quad K_{ij}^{31} = -\int_{x_a}^{x_b} \frac{A_{11}}{2} \frac{dw_0^E}{dx} \, {}^{31}S_{ij}^{0x} dx$$

$$K_{iJ}^{32} = \int_{x_a}^{x_b} \left\{ \frac{A_{11}}{2} \left( \frac{dw_0^E}{dx} \psi_y^E - \frac{du_0^E}{dx} \right) + 2A_{77} \right\} {}^{32}S_{iJ}^{0x} dx$$

$$K_{ij}^{33} = \int_{x_a}^{x_b} \left\{ E_{44} \, {}^{33}S_{ij}^{xx} + \frac{A_{11}}{2} \left( \frac{dw_0^E}{dx} \right)^2 {}^{33}S_{ij}^{00} + 2A_{77} \, {}^{33}S_{ij}^{00} \right\} dx$$

$$T_{iJ}^{12} = K_{iJ}^{12} - \int_{x_a}^{x_b} \frac{A_{11}}{2} \psi_y^E \, {}^{12}S_{iJ}^{xx} dx, \qquad T_{ij}^{13} = K_{ij}^{13} - \int_{x_a}^{x_b} \frac{A_{11}}{2} \frac{dw_0^E}{dx} \, {}^{13}S_{ij}^{x0} dx$$

$$T_{Ij}^{21} = K_{Ij}^{21} - \int_{x_a}^{x_b} \frac{A_{11}}{2} \psi_y^E \, {}^{21}S_{Ij}^{xx} dx, \qquad T_{IJ}^{22} = K_{IJ}^{22} + \int_{x_a}^{x_b} \frac{A_{11}}{2} (\psi_y^E)^2 \, {}^{22}S_{IJ}^{xx} dx$$

$$T_{Ij}^{23} = K_{Ij}^{23} + \int_{x_a}^{x_b} \frac{A_{11}}{2} \left( \frac{dw_0^E}{dx} \psi_y^E - \frac{du_0^E}{dx} \right) {}^{23}S_{Ij}^{x0} dx + \int_{x_a}^{x_b} A_{11} \frac{dw_0^E}{dx} \psi_y^E \, {}^{23}S_{Ij}^{x0} dx$$

$$T_{ij}^{31} = K_{ij}^{31} - \int_{x_a}^{x_b} \frac{A_{11}}{2} \frac{dw_0^E}{dx} \, {}^{31}S_{ij}^{0x} dx$$

$$T_{iJ}^{32} = K_{iJ}^{32} + \int_{x_a}^{x_b} \frac{A_{11}}{2} \left( \frac{dw_0^E}{dx} \psi_y^E - \frac{du_0^E}{dx} \right) {}^{32}S_{iJ}^{0x} dx + \int_{x_a}^{x_b} A_{11} \frac{dw_0^E}{dx} \psi_y^E \, {}^{32}S_{iJ}^{0x} dx$$

$$T_{ij}^{33} = K_{ij}^{33} + \int_{x_a}^{x_b} \frac{A_{11}}{2} \left( \frac{dw_0^E}{dx} \right)^2 {}^{33}S_{ij}^{00} dx$$

### B.1.2 The Timoshenko beam theory

We shall use the following notation in representing the element stiffness and tangent stiffness matrices of Timoshenko beam theory.

$$ {}^{MN}S_{ij}^{xx} = \frac{dL_i^{(M)}}{dx}\frac{dL_j^{(N)}}{dx}, \quad {}^{MN}S_{ij}^{0x} = L_i^{(M)}\frac{dL_j^{(N)}}{dx}, \quad {}^{MN}S_{ij}^{x0} = \frac{dL_i^{(M)}}{dx}L_j^{(N)}, \quad {}^{MN}S_{ij}^{00} = L_i^{(M)}L_j^{(N)} $$

where $M, N = \{1, 2, 3, 4\}$, $i, j = \{1, 2, \ldots n\}$. Where $n$ is the number of nodes in a typical finite element.

#### *B.1.2.1 The von Kaŕmán nonlinear Timoshenko beam*

$$
\begin{aligned}
K_{ij}^{11} &= \int_{x_a}^{x_b} A_{11}\, {}^{11}S_{ij}^{xx}dx, \quad K_{ij}^{12} = \int_{x_a}^{x_b} \frac{A_{11}}{2}\left(\frac{dw_0^T}{dx}\right) {}^{12}S_{ij}^{xx}dx \\
K_{ij}^{21} &= \int_{x_a}^{x_b} A_{11}\left(\frac{dw_0^T}{dx}\right) {}^{21}S_{ij}^{xx}dx, \quad K_{ij}^{22} = \int_{x_a}^{x_b}\left\{\frac{A_{11}}{2}\left(\frac{dw_0^T}{dx}\right)^2 + \frac{(A_{44}+A_{77})}{2}\right\} {}^{22}S_{ij}^{xx}dx \\
K_{ij}^{23} &= \int_{x_a}^{x_b}\left(\frac{A_{44}-A_{77}}{2}\right) {}^{23}S_{ij}^{x0}dx, \quad K_{ij}^{24} = \int_{x_a}^{x_b} A_{77}\, {}^{24}S_{ij}^{x0}dx \\
K_{ij}^{32} &= \int_{x_a}^{x_b}\left(\frac{A_{44}-A_{77}}{2}\right) {}^{32}S_{ij}^{0x}dx, \quad K_{ij}^{33} = \int_{x_a}^{x_b}\left\{D_{11}\, {}^{33}S_{ij}^{xx} + \left(\frac{A_{44}+A_{77}}{2}\right) {}^{33}S_{ij}^{00}\right\}dx \\
K_{ij}^{34} &= -\int_{x_a}^{x_b} A_{77}\, {}^{34}S_{ij}^{00}dx, \quad K_{ij}^{42} = \int_{x_a}^{x_b} A_{77}\, {}^{42}S_{ij}^{0x}dx, \quad K_{ij}^{43} = -\int_{x_a}^{x_b} A_{77}\, {}^{43}S_{ij}^{00}dx \\
K_{ij}^{44} &= \int_{x_a}^{x_b}\left\{E_{44}\, {}^{44}S_{ij}^{xx} + 2A_{77}\, {}^{44}S_{ij}^{00}\right\}dx
\end{aligned}
$$

Similarly, the components of the element tangent stiffness matrix are given by

$$ T_{ij}^{MN} = K_{ij}^{MN} $$

except for the following terms

$$T_{ij}^{12} = 2K_{ij}^{12}, \qquad T_{ij}^{22} = K_{ij}^{22} + \int_{x_a}^{x_b} \left( \frac{A_{11}}{2} \left( \frac{du_0^T}{dx} \right) + A_{11} \left( \frac{dw_0^T}{dx} \right)^2 \right) {}^{22}S_{ij}^{xx} dx$$

### *B.1.2.2 The Micropolar nonlinear Timoshenko beam*

$$K_{ij}^{11} = \int_{x_a}^{x_b} A_{11} \, {}^{11}S_{ij}^{xx} dx, \quad K_{ij}^{12} = -\int_{x_a}^{x_b} \frac{A_{11}}{2} \psi_y^T \, {}^{12}S_{ij}^{xx} dx, \quad K_{ij}^{14} = -\int_{x_a}^{x_b} \frac{A_{11}}{2} \frac{dw_0^T}{dx} \, {}^{14}S_{ij}^{x0} dx$$

$$K_{ij}^{21} = -\int_{x_a}^{x_b} \frac{A_{11}}{2} \psi_y^T \, {}^{21}S_{ij}^{xx} dx, \quad K_{ij}^{22} = \int_{x_a}^{x_b} \left\{ \frac{A_{11}}{2} (\psi_y^T)^2 + \frac{(A_{44} + A_{77})}{2} \right\} {}^{22}S_{ij}^{xx} dx$$

$$K_{ij}^{23} = \int_{x_a}^{x_b} \left( \frac{A_{44} - A_{77}}{2} \right) {}^{23}S_{ij}^{x0} dx, \quad K_{ij}^{24} = \int_{x_a}^{x_b} \left\{ \frac{A_{11}}{2} \left( \frac{dw_0^T}{dx} \psi_y^T - \frac{du_0^T}{dx} \right) + A_{77} \right\} {}^{24}S_{ij}^{x0} dx$$

$$K_{ij}^{32} = \int_{x_a}^{x_b} \left( \frac{A_{44} - A_{77}}{2} \right) {}^{32}S_{ij}^{0x} dx, \quad K_{ij}^{33} = \int_{x_a}^{x_b} \left\{ D_{11} \, {}^{33}S_{ij}^{xx} + \left( \frac{A_{44} + A_{77}}{2} \right) {}^{33}S_{ij}^{00} \right\} dx$$

$$K_{ij}^{34} = -\int_{x_a}^{x_b} A_{77} \, {}^{34}S_{ij}^{00} dx, \qquad K_{ij}^{41} = -\int_{x_a}^{x_b} \frac{A_{11}}{2} \frac{dw_0^T}{dx} \, {}^{41}S_{ij}^{0x} dx$$

$$K_{ij}^{42} = \int_{x_a}^{x_b} \left\{ A_{77} + \frac{A_{11}}{2} \left( \frac{dw_0^T}{dx} \psi_y^T - \frac{du_0^T}{dx} \right) \right\} {}^{42}S_{ij}^{0x} dx, \quad K_{ij}^{43} = -\int_{x_a}^{x_b} A_{77} \, {}^{44}S_{ij}^{00} dx$$

$$K_{ij}^{44} = \int_{x_a}^{x_b} \left\{ E_{44} \, {}^{44}S_{ij}^{xx} + 2A_{77} \, {}^{44}S_{ij}^{00} + \frac{A_{11}}{2} \left( \frac{dw_0^T}{dx} \right)^2 {}^{44}S_{ij}^{00} \right\} dx$$

Similarly, the components of the element tangent stiffness matrix are given by

$$T_{ij}^{MN} = K_{ij}^{MN}$$

except for the following terms

$$
\begin{aligned}
T_{ij}^{12} =& K_{ij}^{12} - \int_{x_a}^{x_b} \frac{A_{11}}{2} \psi_y^T \, {}^{12}S_{ij}^{xx} dx, \qquad T_{ij}^{14} = K_{ij}^{14} - \int_{x_a}^{x_b} \frac{A_{11}}{2} \frac{dw_0^T}{dx} \, {}^{14}S_{ij}^{x0} dx \\
T_{ij}^{21} =& K_{ij}^{21} - \int_{x_a}^{x_b} \frac{A_{11}}{2} \psi_y^T \, {}^{21}S_{ij}^{xx} dx, \qquad T_{ij}^{22} = K_{ij}^{22} + \int_{x_a}^{x_b} \frac{A_{11}}{2} (\psi_y^T)^2 \, {}^{22}S_{ij}^{xx} dx \\
T_{ij}^{24} =& K_{ij}^{24} - \int_{x_a}^{x_b} \frac{A_{11}}{2} \frac{du_0^T}{dx} \, {}^{24}S_{ij}^{x0} dx + \int_{x_a}^{x_b} \frac{3A_{11}}{2} \frac{dw_0^T}{dx} \psi_y^T \, {}^{24}S_{ij}^{x0} dx \\
T_{ij}^{41} =& K_{ij}^{41} - \int_{x_a}^{x_b} \frac{A_{11}}{2} \frac{dw_0^T}{dx} \, {}^{41}S_{ij}^{0x} dx \\
T_{ij}^{42} =& K_{ij}^{42} - \int_{x_a}^{x_b} \frac{A_{11}}{2} \frac{du_0^T}{dx} \, {}^{42}S_{ij}^{0x} dx + \int_{x_a}^{x_b} \frac{3A_{11}}{2} \frac{dw_0^T}{dx} \psi_y^T \, {}^{42}S_{ij}^{0x} dx \\
T_{ij}^{44} =& K_{ij}^{44} + \int_{x_a}^{x_b} \frac{A_{11}}{2} \left( \frac{dw_0^T}{dx} \right)^2 \, {}^{44}S_{ij}^{00} dx
\end{aligned}
$$

## B.2 Micropolar plates

We will use the following notation in the defining the coefficients of the element stiffness matrices.

$$
{}^{IJ}S_{ij}^{ab} = \frac{\partial L_i^{(I)}}{\partial a} \frac{\partial L_j^{(J)}}{\partial b}, \quad {}^{IJ}S_{ij}^{0b} = L_i^{(I)} \frac{\partial L_j^{(J)}}{\partial b}, \quad {}^{IJ}S_{ij}^{a0} = \frac{\partial L_i^{(I)}}{\partial a} L_j^{(J)}, \quad {}^{IJ}S_{ij}^{00} = L_i^{(I)} L_j^{(J)}
$$

where $I, J = \{1, 2, 3, 4, 5, 6, 7\}$, $i, j = \{1, 2, \ldots, n\}$ and $a, b = \{x, y\}$.

### B.2.1 von Kaŕmán micropolar plate theory

The non-zero components of the element stiffness matrix of von Kaŕmán micropolar plate theory are:

$$
\begin{aligned}
K_{ij}^{11} &= \int_{\Omega_e} \left\{ A_{11} \, {}^{11}S_{ij}^{xx} + \left( \frac{A_{44} + A_{77}}{2} \right) \, {}^{11}S_{ij}^{yy} \right\} d\Omega_e \\
K_{ij}^{12} &= \int_{\Omega_e} \left\{ A_{12} \, {}^{12}S_{ij}^{xy} + \left( \frac{A_{44} - A_{77}}{2} \right) \, {}^{11}S_{ij}^{yx} \right\} d\Omega_e
\end{aligned}
$$

$$K_{ij}^{13} = \int_{\Omega_e} \left\{ \frac{A_{11}}{2} \left( \frac{\partial w_0}{\partial x} \right) {}^{13}S_{ij}^{xx} + \frac{A_{44}}{4} \left( \frac{\partial w_0}{\partial x} \right) {}^{13}S_{ij}^{yy} + \frac{A_{12}}{2} \left( \frac{\partial w_0}{\partial y} \right) {}^{13}S_{ij}^{xy} + \frac{A_{44}}{4} \left( \frac{\partial w_0}{\partial y} \right) {}^{13}S_{ij}^{yx} \right\} d\Omega_e$$

$$K_{ij}^{21} = \int_{\Omega_e} \left\{ \left( \frac{A_{44} - A_{77}}{2} \right) {}^{21}S_{ij}^{xy} + A_{12} {}^{21}S_{ij}^{yx} \right\} d\Omega_e$$

$$K_{ij}^{22} = \int_{\Omega_e} \left\{ \left( \frac{A_{44} + A_{77}}{2} \right) {}^{22}S_{ij}^{xx} + A_{11} {}^{22}S_{ij}^{yy} \right\} d\Omega_e$$

$$K_{ij}^{23} = \int_{\Omega_e} \left\{ \frac{A_{44}}{4} \left( \frac{\partial w_0}{\partial y} \right) {}^{23}S_{ij}^{xx} + \frac{A_{11}}{2} \left( \frac{\partial w_0}{\partial y} \right) {}^{23}S_{ij}^{yy} + \frac{A_{44}}{4} \left( \frac{\partial w_0}{\partial x} \right) {}^{23}S_{ij}^{xy} + \frac{A_{12}}{2} \left( \frac{\partial w_0}{\partial x} \right) {}^{23}S_{ij}^{yx} \right\} d\Omega_e$$

$$K_{ij}^{31} = \int_{\Omega_e} \left\{ \frac{A_{11}}{2} \left( \frac{\partial w_0}{\partial x} \right) {}^{31}S_{ij}^{xx} + \frac{A_{44}}{4} \left( \frac{\partial w_0}{\partial x} \right) {}^{31}S_{ij}^{yy} + \frac{A_{44}}{4} \left( \frac{\partial w_0}{\partial y} \right) {}^{31}S_{ij}^{xy} + \frac{A_{12}}{2} \left( \frac{\partial w_0}{\partial y} \right) {}^{31}S_{ij}^{yx} \right\} d\Omega_e$$

$$K_{ij}^{32} = \int_{\Omega_e} \left\{ \frac{A_{44}}{4} \left( \frac{\partial w_0}{\partial y} \right) {}^{32}S_{ij}^{xx} + \frac{A_{11}}{2} \left( \frac{\partial w_0}{\partial y} \right) {}^{32}S_{ij}^{yy} + \frac{A_{12}}{2} \left( \frac{\partial w_0}{\partial x} \right) {}^{32}S_{ij}^{xy} + \frac{A_{44}}{4} \left( \frac{\partial w_0}{\partial x} \right) {}^{32}S_{ij}^{yx} \right\} d\Omega_e$$

$$\begin{aligned} K_{ij}^{33} = \int_{\Omega_e} \Bigg\{ & \frac{A_{11}}{2} \left( \frac{\partial u_0}{\partial x} + \left( \frac{\partial w_0}{\partial x} \right)^2 \right) {}^{33}S_{ij}^{xx} + \frac{A_{12}}{2} \left( \frac{\partial v_0}{\partial y} + \frac{1}{2} \left( \frac{\partial w_0}{\partial y} \right)^2 \right) {}^{33}S_{ij}^{xx} \\ & + \frac{A_{44} + A_{77}}{2} \left( {}^{33}S_{ij}^{xx} + {}^{33}S_{ij}^{yy} \right) \\ & + \frac{A_{44}}{4} \left( \frac{\partial u_0}{\partial y} + \frac{\partial v_0}{\partial x} \right) \left( {}^{33}S_{ij}^{xy} + {}^{33}S_{ij}^{yx} \right) + \frac{A_{44}}{4} \left( \frac{\partial w_0}{\partial y} \right)^2 {}^{33}S_{ij}^{xx} \\ & + \frac{A_{44}}{4} \left( \frac{\partial w_0}{\partial x} \right)^2 {}^{33}S_{ij}^{yy} + \frac{A_{44}}{4} \left( \frac{\partial w_0}{\partial y} \frac{\partial w_0}{\partial x} \right) \left( {}^{33}S_{ij}^{xy} + {}^{33}S_{ij}^{yx} \right) \\ & + \frac{A_{12}}{2} \left( \frac{\partial u_0}{\partial x} + \frac{1}{2} \left( \frac{\partial w_0}{\partial x} \right)^2 \right) {}^{33}S_{ij}^{yy} + \frac{A_{11}}{2} \left( \frac{\partial v_0}{\partial y} + \left( \frac{\partial w_0}{\partial y} \right)^2 \right) {}^{33}S_{ij}^{yy} \\ & + \frac{A_{12}}{4} \left( \frac{\partial w_0}{\partial y} \frac{\partial w_0}{\partial x} \right) \left( {}^{33}S_{ij}^{yx} + {}^{33}S_{ij}^{xy} \right) \Bigg\} d\Omega_e \end{aligned}$$

$$K_{ij}^{34} = \int_{\Omega_e} \left( \frac{A_{44} - A_{77}}{2} \right) {}^{34}S_{ij}^{x0} d\Omega_e, \quad K_{ij}^{35} = \int_{\Omega_e} \left( \frac{A_{44} - A_{77}}{2} \right) {}^{35}S_{ij}^{y0} d\Omega_e$$

$$K_{ij}^{36} = -\int_{\Omega_e} A_{77} \, {}^{36}S_{ij}^{y0} d\Omega_e, \quad K_{ij}^{37} = \int_{\Omega_e} A_{77} \, {}^{37}S_{ij}^{x0} d\Omega_e$$

$$K_{ij}^{43} = \int_{\Omega_e} \left( \frac{A_{44} - A_{77}}{2} \right) {}^{43}S_{ij}^{0x} d\Omega_e$$

$$K_{ij}^{44} = \int_{\Omega_e} \left\{ D_{11} \, {}^{44}S_{ij}^{xx} + \left( \frac{D_{44} + D_{77}}{2} \right) {}^{44}S_{ij}^{yy} + \left( \frac{A_{44} + A_{77}}{2} \right) {}^{44}S_{ij}^{00} \right\} d\Omega_e$$

$$K_{ij}^{45} = \int_{\Omega_e} \left\{ D_{12} \, {}^{45}S_{ij}^{xy} + \left( \frac{D_{44} - D_{77}}{2} \right) {}^{45}S_{ij}^{yx} \right\} d\Omega_e, \quad K_{ij}^{47} = -\int_{\Omega_e} A_{77} \, {}^{47}S_{ij}^{00} d\Omega_e$$

$$K_{j}^{53} = \int_{\Omega_e} \left( \frac{A_{44} - A_{77}}{2} \right) {}^{53}S_{ij}^{0y} d\Omega_e, \quad K_{ij}^{54} = \int_{\Omega_e} \left\{ \left( \frac{D_{44} - D_{77}}{2} \right) {}^{54}S_{ij}^{xy} + D_{12} \, {}^{54}S_{ij}^{yx} \right\} d\Omega_e$$

$$K_{ij}^{55} = \int_{\Omega_e} \left\{ \left( \frac{D_{44} + D_{77}}{2} \right) {}^{55}S_{ij}^{xx} + D_{11} \, {}^{55}S_{ij}^{yy} + \left( \frac{A_{44} + A_{77}}{2} \right) {}^{55}S_{ij}^{00} \right\} d\Omega_e$$

$$K_{ij}^{56} = \int_{\Omega_e} A_{77} \, {}^{56}S_{ij}^{00} d\Omega_e, \quad K_{ij}^{63} = -\int_{\Omega_e} A_{77} \, {}^{63}S_{ij}^{0y} d\Omega_e, \quad K_{ij}^{65} = \int_{\Omega_e} A_{77} \, {}^{65}S_{ij}^{00} d\Omega_e$$

$$K_{ij}^{66} = \int_{\Omega_e} \left\{ E_{11} \, {}^{66}S_{ij}^{xx} + E_{33} \, {}^{66}S_{ij}^{yy} + 2A_{77} \, {}^{66}S_{ij}^{00} \right\} d\Omega_e$$

$$K_{ij}^{67} = \int_{\Omega_e} \left\{ E_{12} \, {}^{67}S_{ij}^{xy} + E_{34} \, {}^{67}S_{ij}^{yx} \right\} d\Omega_e$$

$$K_{ij}^{73} = \int_{\Omega_e} A_{77} \, {}^{73}S_{ij}^{0x} d\Omega_e, \quad K_{ij}^{74} = -\int_{\Omega_e} A_{77} \, {}^{74}S_{ij}^{00} d\Omega_e$$

$$K_{ij}^{76} = \int_{\Omega_e} \left\{ E_{34} \, {}^{76}S_{ij}^{xy} + E_{12} \, {}^{76}S_{ij}^{yx} \right\} d\Omega_e$$

$$K_{ij}^{77} = \int_{\Omega_e} \left\{ E_{33} \, {}^{77}S_{ij}^{xx} + E_{11} \, {}^{77}S_{ij}^{yy} + 2A_{77} \, {}^{77}S_{ij}^{00} \right\} d\Omega_e$$

Similarly, the components of the element tangent stiffness matrix are given by

$$T_{ij}^{IJ} = K_{ij}^{IJ}$$

except for the following terms

$$T_{ij}^{13} = 2K_{ij}^{13}, \quad T_{ij}^{23} = 2K_{ij}^{23}, \quad T_{ij}^{31} = 2K_{ij}^{31}, \quad T_{ij}^{32} = 2K_{ij}^{32}$$

$$\begin{aligned}
T_{ij}^{33} = K_{ij}^{33} + \int_{\Omega_e} \Bigg\{ & \frac{A_{11}}{2}\left(\frac{\partial u_0}{\partial x}\right) {}^{33}S_{ij}^{xx} + \frac{A_{44}}{4}\left(\frac{\partial u_0}{\partial y}\right)\left({}^{33}S_{ij}^{xy} + {}^{33}S_{ij}^{yx}\right) + \frac{A_{12}}{2}\left(\frac{\partial u_0}{\partial x}\right) {}^{33}S_{ij}^{yy} \\
& + \frac{A_{44}}{4}\left(\frac{\partial v_0}{\partial x}\right)\left({}^{33}S_{ij}^{xy} + {}^{33}S_{ij}^{yx}\right) + \frac{A_{11}}{2}\left(\frac{\partial v_0}{\partial y}\right) {}^{33}S_{ij}^{yy} + \frac{A_{12}}{2}\left(\frac{\partial v_0}{\partial y}\right) {}^{33}S_{ij}^{xx} \\
& + A_{11}\left(\frac{\partial w_0}{\partial x}\right)^2 {}^{33}S_{ij}^{xx} + \frac{A_{12}}{2}\left(\frac{\partial w_0}{\partial x}\frac{\partial w_0}{\partial y}\right) {}^{33}S_{ij}^{xy} + \frac{A_{44}}{2}\left(\frac{\partial w_0}{\partial x}\frac{\partial w_0}{\partial y}\right)\left({}^{33}S_{ij}^{xy} + {}^{33}S_{ij}^{yx}\right) \\
& + \frac{A_{44}}{4}\left(\frac{\partial w_0}{\partial x}\frac{\partial w_0}{\partial y}\right)\left({}^{33}S_{ij}^{xy} + {}^{33}S_{ij}^{yx}\right) + \frac{A_{44}}{4}\left(\frac{\partial w_0}{\partial x}\right)^2 {}^{33}S_{ij}^{yy} + \frac{A_{44}}{4}\left(\frac{\partial w_0}{\partial y}\right)^2 {}^{33}S_{ij}^{xx} \\
& + \frac{A_{12}}{2}\left(\frac{\partial w_0}{\partial x}\frac{\partial w_0}{\partial y}\right) {}^{33}S_{ij}^{yx} + A_{11}\left(\frac{\partial w_0}{\partial y}\right)^2 {}^{33}S_{ij}^{yy} + \frac{A_{12}}{4}\left(\frac{\partial w_0}{\partial x}\right)^2 {}^{33}S_{ij}^{yy} \\
& + \frac{A_{12}}{4}\left(\frac{\partial w_0}{\partial y}\right)^2 {}^{33}S_{ij}^{xx} + \frac{A_{12}}{4}\left(\frac{\partial w_0}{\partial x}\frac{\partial w_0}{\partial y}\right)\left({}^{33}S_{ij}^{xy} + {}^{33}S_{ij}^{yx}\right) \Bigg\} d\Omega_e
\end{aligned}$$

### B.2.2 Nonlinear micropolar plate theory

The non-zero components of the element stiffness matrix of nonlinear micropolar plate theory are:

$$K_{ij}^{11} = \int_{\Omega_e} \left\{ A_{11}\, {}^{11}S_{ij}^{xx} + \left(\frac{A_{44} + A_{77}}{2}\right) {}^{11}S_{ij}^{yy} \right\} d\Omega_e$$

$$K_{ij}^{12} = \int_{\Omega_e} \left\{ A_{12}\, {}^{12}S_{ij}^{xy} + \left(\frac{A_{44} - A_{77}}{2}\right) {}^{12}S_{ij}^{yx} \right\} d\Omega_e$$

$$\begin{aligned}
K_{ij}^{13} = \int_{\Omega_e} \Bigg\{ & -\frac{A_{11}}{2}\psi_y\, {}^{13}S_{ij}^{xx} - \left(\frac{A_{44} + A_{77}}{4}\right)\psi_y\, {}^{13}S_{ij}^{yy} \\
& + \frac{A_{12}}{2}\psi_x\, {}^{13}S_{ij}^{xy} + \left(\frac{A_{44} - A_{77}}{4}\right)\psi_x\, {}^{13}S_{ij}^{yx} \Bigg\} d\Omega_e
\end{aligned}$$

$$K_{ij}^{16} = \int_{\Omega_e} \left\{ \frac{A_{12}}{2}\left(\frac{\partial w_0}{\partial y}\right) {}^{16}S_{ij}^{x0} + \left(\frac{A_{44} - A_{77}}{4}\right)\left(\frac{\partial w_0}{\partial x}\right) {}^{16}S_{ij}^{y0} \right\} d\Omega_e$$

$$K_{ij}^{17} = \int_{\Omega_e} \left\{ -\frac{A_{11}}{2} \left( \frac{\partial w_0}{\partial x} \right) {}^{17}S_{ij}^{x0} - \left( \frac{A_{44} + A_{77}}{4} \right) \left( \frac{\partial w_0}{\partial y} \right) {}^{17}S_{ij}^{y0} \right\} d\Omega_e$$

$$K_{ij}^{21} = \int_{\Omega_e} \left\{ \left( \frac{A_{44} - A_{77}}{2} \right) {}^{21}S_{ij}^{xy} + A_{12} {}^{21}S_{ij}^{yx} \right\} d\Omega_e$$

$$K_{ij}^{22} = \int_{\Omega_e} \left\{ \left( \frac{A_{44} + A_{77}}{2} \right) {}^{22}S_{ij}^{xx} + A_{11} {}^{22}S_{ij}^{yy} \right\} d\Omega_e$$

$$K_{ij}^{23} = \int_{\Omega_e} \left\{ \left( \frac{A_{44} + A_{77}}{4} \right) \psi_x {}^{23}S_{ij}^{xx} + \frac{A_{11}}{2} \psi_x {}^{23}S_{ij}^{yy} \right.$$
$$\left. - \left( \frac{A_{44} - A_{77}}{4} \right) \psi_y {}^{23}S_{ij}^{xy} - \frac{A_{12}}{2} \psi_y {}^{23}S_{ij}^{yx} \right\} d\Omega_e$$

$$K_{ij}^{26} = \int_{\Omega_e} \left\{ \left( \frac{A_{44} + A_{77}}{4} \right) \left( \frac{\partial w_0}{\partial x} \right) {}^{26}S_{ij}^{x0} + \frac{A_{11}}{2} \left( \frac{\partial w_0}{\partial y} \right) {}^{26}S_{ij}^{y0} \right\} d\Omega_e$$

$$K_{ij}^{27} = \int_{\Omega_e} \left\{ -\left( \frac{A_{44} - A_{77}}{4} \right) \left( \frac{\partial w_0}{\partial y} \right) {}^{27}S_{ij}^{x0} - \frac{A_{12}}{2} \left( \frac{\partial w_0}{\partial x} \right) {}^{27}S_{ij}^{y0} \right\} d\Omega_e$$

$$K_{ij}^{31} = \int_{\Omega_e} \left\{ -\frac{A_{11}}{2} \psi_y {}^{31}S_{ij}^{xx} - \left( \frac{A_{44} + A_{77}}{4} \right) \psi_y {}^{31}S_{ij}^{yy} \right.$$
$$\left. + \left( \frac{A_{44} - A_{77}}{4} \right) \psi_x {}^{31}S_{ij}^{xy} + \frac{A_{12}}{2} \psi_x {}^{31}S_{ij}^{yx} \right\} d\Omega_e$$

$$K_{ij}^{32} = \int_{\Omega_e} \left\{ \left( \frac{A_{44} + A_{77}}{4} \right) \psi_x {}^{32}S_{ij}^{xx} + \frac{A_{11}}{2} \psi_x {}^{32}S_{ij}^{yy} \right.$$
$$\left. - \frac{A_{12}}{2} \psi_y {}^{32}S_{ij}^{xy} - \left( \frac{A_{44} - A_{77}}{4} \right) \psi_y {}^{32}S_{ij}^{yx} \right\} d\Omega_e$$

$$K_{ij}^{33} = \int_{\Omega_e} \left\{ \frac{A_{11}}{2} (\psi_y)^2 {}^{33}S_{ij}^{xx} + \frac{A_{11}}{2} (\psi_x)^2 {}^{33}S_{ij}^{yy} - \frac{A_{12}}{3} (\psi_x \psi_y) {}^{33}S_{ij}^{xy} - \frac{A_{12}}{3} (\psi_x \psi_y) {}^{33}S_{ij}^{yx} \right.$$
$$+ \frac{A_{44} + A_{77}}{2} \left( {}^{33}S_{ij}^{xx} + {}^{33}S_{ij}^{yy} \right) + \left( \frac{A_{44} + A_{77}}{4} \right) (\psi_x)^2 {}^{33}S_{ij}^{xx}$$
$$\left. + \left( \frac{A_{44} + A_{77}}{4} \right) (\psi_y)^2 {}^{33}S_{ij}^{yy} - \left( \frac{A_{44} - A_{77}}{6} \right) (\psi_x \psi_y) \left( {}^{33}S_{ij}^{xy} + {}^{33}S_{ij}^{yx} \right) \right\} d\Omega_e$$

$$K_{ij}^{34} = \int_{\Omega_e} \left( \frac{A_{44} - A_{77}}{2} \right) {}^{34}S_{ij}^{x0} d\Omega_e, \quad K_{ij}^{35} = \int_{\Omega_e} \left( \frac{A_{44} - A_{77}}{2} \right) {}^{35}S_{ij}^{y0} d\Omega_e$$

$$K_{ij}^{36} = \int_{\Omega_e} \Bigg\{ -\frac{A_{12}}{3}\left(\psi_y \frac{\partial w_0}{\partial y}\right) {}^{36}S_{ij}^{x0} - \frac{A_{12}}{3}\left(\psi_y \frac{\partial w_0}{\partial x}\right) {}^{36}S_{ij}^{y0} + \frac{A_{12}}{2}\left(\frac{\partial u_0}{\partial x}\right) {}^{36}S_{ij}^{y0}$$
$$- A_{77}\, {}^{36}S_{ij}^{y0} + \frac{A_{11}}{2}\left(\frac{\partial v_0}{\partial y} + \psi_x \frac{\partial w_0}{\partial y}\right) {}^{36}S_{ij}^{y0} + \frac{A_{44}}{4}\left(\frac{\partial u_0}{\partial y} + \frac{\partial v_0}{\partial x}\right) {}^{36}S_{ij}^{x0}$$
$$- \frac{A_{77}}{4}\left(\frac{\partial u_0}{\partial y} - \frac{\partial v_0}{\partial x}\right) {}^{36}S_{ij}^{x0} + \left(\frac{A_{44}+A_{77}}{4}\right)\left(\psi_x \frac{\partial w_0}{\partial x}\right) {}^{36}S_{ij}^{x0}$$
$$- \left(\frac{A_{44}-A_{77}}{6}\right)\left(\psi_y \frac{\partial w_0}{\partial y}\right) {}^{36}S_{ij}^{x0} - \left(\frac{A_{44}-A_{77}}{6}\right)\left(\psi_y \frac{\partial w_0}{\partial x}\right) {}^{36}S_{ij}^{y0} \Bigg\} d\Omega_e$$

$$K_{ij}^{37} = \int_{\Omega_e} \Bigg\{ -\frac{A_{12}}{3}\left(\psi_x \frac{\partial w_0}{\partial y}\right) {}^{37}S_{ij}^{x0} - \frac{A_{12}}{3}\left(\psi_x \frac{\partial w_0}{\partial x}\right) {}^{37}S_{ij}^{y0} - \frac{A_{12}}{2}\left(\frac{\partial v_0}{\partial y}\right) {}^{37}S_{ij}^{x0}$$
$$+ A_{77}\, {}^{37}S_{ij}^{x0} - \frac{A_{11}}{2}\left(\frac{\partial u_0}{\partial x} - \psi_y \frac{\partial w_0}{\partial x}\right) {}^{37}S_{ij}^{x0} - \frac{A_{44}}{4}\left(\frac{\partial u_0}{\partial y} + \frac{\partial v_0}{\partial x}\right) {}^{37}S_{ij}^{y0}$$
$$- \frac{A_{77}}{4}\left(\frac{\partial u_0}{\partial y} - \frac{\partial v_0}{\partial x}\right) {}^{37}S_{ij}^{y0} - \left(\frac{A_{44}-A_{77}}{6}\right)\left(\psi_x \frac{\partial w_0}{\partial x}\right) {}^{37}S_{ij}^{y0}$$
$$+ \left(\frac{A_{44}+A_{77}}{4}\right)\left(\psi_y \frac{\partial w_0}{\partial y}\right) {}^{37}S_{ij}^{y0} - \left(\frac{A_{44}-A_{77}}{6}\right)\left(\psi_x \frac{\partial w_0}{\partial y}\right) {}^{37}S_{ij}^{x0} \Bigg\} d\Omega_e$$

$$K_{ij}^{43} = \int_{\Omega_e} \left(\frac{A_{44}-A_{77}}{2}\right) {}^{43}S_{ij}^{0x} d\Omega_e, \quad K_{ij}^{45} = \int_{\Omega_e} \left\{ D_{12}\, {}^{45}S_{ij}^{xy} + \left(\frac{D_{44}-D_{77}}{2}\right) {}^{45}S_{ij}^{yx} \right\} d\Omega_e$$

$$K_{ij}^{44} = \int_{\Omega_e} \left\{ D_{11}\, {}^{44}S_{ij}^{xx} + \left(\frac{D_{44}+D_{77}}{2}\right) {}^{44}S_{ij}^{yy} + \left(\frac{A_{44}+A_{77}}{2}\right) {}^{44}S_{ij}^{00} \right\} d\Omega_e$$

$$K_{ij}^{47} = -\int_{\Omega_e} A_{77}\, {}^{47}S_{ij}^{00} d\Omega_e, \quad K_j^{53} = \int_{\Omega_e} \left(\frac{A_{44}-A_{77}}{2}\right) {}^{53}S_{ij}^{0y} d\Omega_e$$

$$K_{ij}^{54} = \int_{\Omega_e} \left\{ \left(\frac{D_{44}-D_{77}}{2}\right) {}^{54}S_{ij}^{xy} + D_{12}\, {}^{54}S_{ij}^{yx} \right\} d\Omega_e, \quad K_{ij}^{56} = \int_{\Omega_e} A_{77}\, {}^{56}S_{ij}^{00} d\Omega_e$$

$$K_{ij}^{55} = \int_{\Omega_e} \left\{ \left(\frac{D_{44}+D_{77}}{2}\right) {}^{55}S_{ij}^{xx} + D_{11}\, {}^{55}S_{ij}^{yy} + \left(\frac{A_{44}+A_{77}}{2}\right) {}^{55}S_{ij}^{00} \right\} d\Omega_e$$

$$K_{ij}^{61} = \int_{\Omega_e} \left\{ \frac{A_{12}}{2}\left(\frac{\partial w_0}{\partial y}\right) {}^{61}S_{ij}^{0x} + \left(\frac{A_{44}-A_{77}}{4}\right)\left(\frac{\partial w_0}{\partial x}\right) {}^{61}S_{ij}^{0y} \right\} d\Omega_e$$

$$K_{ij}^{62} = \int_{\Omega_e} \left\{ \frac{A_{11}}{2}\left(\frac{\partial w_0}{\partial y}\right) {}^{63}S_{ij}^{0y} + \left(\frac{A_{44}+A_{77}}{4}\right)\left(\frac{\partial w_0}{\partial x}\right) {}^{62}S_{ij}^{0x} \right\} d\Omega_e$$

$$K_{ij}^{63} = \int_{\Omega_e} \Bigg\{ -\frac{A_{12}}{3}\left(\psi_y \frac{\partial w_0}{\partial y}\right) L_i^{(6)}\, {}^{63}S_{ij}^{0x} - \frac{A_{12}}{3}\left(\psi_y \frac{\partial w_0}{\partial x}\right) {}^{63}S_{ij}^{0y} + \frac{A_{12}}{2}\left(\frac{\partial u_0}{\partial x}\right) {}^{63}S_{ij}^{0y}$$
$$- A_{77} L_i^{(6)}\, {}^{63}S_{ij}^{0y} + \frac{A_{11}}{2}\left(\frac{\partial v_0}{\partial y} + \psi_x \frac{\partial w_0}{\partial y}\right) {}^{63}S_{ij}^{0y} + \frac{A_{44}}{4}\left(\frac{\partial u_0}{\partial y} + \frac{\partial v_0}{\partial x}\right) {}^{63}S_{ij}^{0x}$$
$$- \frac{A_{77}}{4}\left(\frac{\partial u_0}{\partial y} - \frac{\partial v_0}{\partial x}\right) {}^{63}S_{ij}^{0x} + \left(\frac{A_{44}+A_{77}}{4}\right)\left(\psi_x \frac{\partial w_0}{\partial x}\right) {}^{63}S_{ij}^{0x}$$
$$- \left(\frac{A_{44}-A_{77}}{6}\right)\left(\psi_y \frac{\partial w_0}{\partial y}\right) {}^{63}S_{ij}^{0x} - \left(\frac{A_{44}-A_{77}}{6}\right)\left(\psi_y \frac{\partial w_0}{\partial x}\right) {}^{63}S_{ij}^{0y} \Bigg\} d\Omega_e$$

$$K_{ij}^{65} = \int_{\Omega_e} A_{77}\, {}^{65}S_{ij}^{00} d\Omega_e$$

$$K_{ij}^{66} = \int_{\Omega_e} \Bigg\{ E_{11}\, {}^{66}S_{ij}^{xx} + E_{44}\, {}^{66}S_{ij}^{yy} + 2A_{77}\, {}^{66}S_{ij}^{00}$$
$$+ \frac{A_{11}}{2}\left(\frac{\partial w_0}{\partial y}\right)^2 {}^{66}S_{ij}^{00} + \frac{A_{44}+A_{77}}{4}\left(\frac{\partial w_0}{\partial x}\right)^2 {}^{66}S_{ij}^{00} \Bigg\} d\Omega_e$$

$$K_{ij}^{67} = \int_{\Omega_e} \Bigg\{ E_{12}\, {}^{67}S_{ij}^{xy} + E_{45}\, {}^{67}S_{ij}^{yx} - \frac{A_{12}}{3}\left(\frac{\partial w_0}{\partial x}\frac{\partial w_0}{\partial y}\right) {}^{67}S_{ij}^{00}$$
$$- \left(\frac{A_{44}-A_{77}}{6}\right)\left(\frac{\partial w_0}{\partial x}\frac{\partial w_0}{\partial y}\right) {}^{67}S_{ij}^{00} \Bigg\} d\Omega_e$$

$$K_{ij}^{71} = \int_{\Omega_e} \Bigg\{ -\frac{A_{11}}{2}\left(\frac{\partial w_0}{\partial x}\right) {}^{71}S_{ij}^{0x} - \left(\frac{A_{44}+A_{77}}{4}\right)\left(\frac{\partial w_0}{\partial y}\right) {}^{71}S_{ij}^{0y} \Bigg\} d\Omega_e$$

$$K_{ij}^{72} = \int_{\Omega_e} \Bigg\{ -\frac{A_{12}}{2}\left(\frac{\partial w_0}{\partial x}\right) {}^{72}S_{ij}^{0y} - \left(\frac{A_{44}-A_{77}}{4}\right)\left(\frac{\partial w_0}{\partial y}\right) {}^{72}S_{ij}^{0x} \Bigg\} d\Omega_e$$

$$K_{ij}^{73} = \int_{\Omega_e} \Bigg\{ -\frac{A_{12}}{3}\left(\psi_x \frac{\partial w_0}{\partial y}\right) {}^{73}S_{ij}^{0x} - \frac{A_{12}}{3}\left(\psi_x \frac{\partial w_0}{\partial x}\right) {}^{73}S_{ij}^{0y} - \frac{A_{12}}{2}\left(\frac{\partial v_0}{\partial y}\right) {}^{73}S_{ij}^{0x}$$
$$+ A_{77}\, {}^{73}S_{ij}^{0x} - \frac{A_{11}}{2}\left(\frac{\partial u_0}{\partial x} - \psi_y \frac{\partial w_0}{\partial x}\right) {}^{73}S_{ij}^{0x} - \frac{A_{44}}{4}\left(\frac{\partial u_0}{\partial y} + \frac{\partial v_0}{\partial x}\right) {}^{73}S_{ij}^{0y}$$
$$- \frac{A_{77}}{4}\left(\frac{\partial u_0}{\partial y} - \frac{\partial v_0}{\partial x}\right) {}^{73}S_{ij}^{0y} - \left(\frac{A_{44}-A_{77}}{6}\right)\left(\psi_x \frac{\partial w_0}{\partial x}\right) {}^{73}S_{ij}^{0y}$$
$$+ \left(\frac{A_{44}+A_{77}}{4}\right)\left(\psi_y \frac{\partial w_0}{\partial y}\right) {}^{73}S_{ij}^{0y} - \left(\frac{A_{44}-A_{77}}{6}\right)\left(\psi_x \frac{\partial w_0}{\partial y}\right) {}^{73}S_{ij}^{0x} \Bigg\} d\Omega_e$$

$$K_{ij}^{74} = -\int_{\Omega_e} A_{77}\, {}^{74}S_{ij}^{00} d\Omega_e$$

$$K_{ij}^{76} = \int_{\Omega_e} \Bigg\{ E_{45}\, {}^{76}S_{ij}^{xy} + E_{12}\, {}^{76}S_{ij}^{yx} - \frac{A_{12}}{3} \left( \frac{\partial w_0}{\partial x} \frac{\partial w_0}{\partial y} \right) {}^{76}S_{ij}^{00} - \left( \frac{A_{44} - A_{77}}{6} \right) \left( \frac{\partial w_0}{\partial x} \frac{\partial w_0}{\partial y} \right) {}^{76}S_{ij}^{00} \Bigg\} d\Omega_e$$

$$K_{ij}^{77} = \int_{\Omega_e} \Bigg\{ E_{44}\, {}^{77}S_{ij}^{xx} + E_{11}\, {}^{77}S_{ij}^{yy} + 2A_{77}\, {}^{77}S_{ij}^{00} + \frac{A_{11}}{2} \left( \frac{\partial w_0}{\partial x} \right)^2 {}^{77}S_{ij}^{00} + \frac{A_{44} + A_{77}}{4} \left( \frac{\partial w_0}{\partial y} \right)^2 {}^{77}S_{ij}^{00} \Bigg\} d\Omega_e$$

Similarly, the components of the element tangent stiffness matrix are given by

$$T_{ij}^{IJ} = K_{ij}^{IJ}$$

except for the following terms

$$T_{ij}^{13} = 2K_{ij}^{13}, \quad T_{ij}^{16} = 2K_{ij}^{16}, \quad T_{ij}^{17} = 2K_{ij}^{17}, \quad T_{ij}^{23} = 2K_{ij}^{23}$$

$$T_{ij}^{26} = 2K_{ij}^{26}, \quad T_{ij}^{27} = 2K_{ij}^{27}, \quad T_{ij}^{31} = 2K_{ij}^{31}, \quad T_{ij}^{32} = 2K_{ij}^{32}$$

$$T_{ij}^{61} = 2K_{ij}^{61}, \quad T_{ij}^{62} = 2K_{ij}^{62}, \quad T_{ij}^{71} = 2K_{ij}^{71}, \quad T_{ij}^{72} = 2K_{ij}^{72}$$

$$T_{ij}^{33} = K_{ij}^{33} + \int_{\Omega_e} \Bigg\{ -\frac{2A_{12}}{3} (\psi_x \psi_y) \left( {}^{33}S_{ij}^{xy} + {}^{33}S_{ij}^{yx} \right) + \frac{A_{11}}{2} (\psi_x)^2 {}^{33}S_{ij}^{yy} + \left( \frac{A_{44} + A_{77}}{4} \right) (\psi_x)^2 {}^{33}S_{ij}^{xx} - \left( \frac{A_{44} - A_{77}}{3} \right) (\psi_x \psi_y) \left( {}^{33}S_{ij}^{xy} + {}^{33}S_{ij}^{yx} \right) + \frac{A_{11}}{2} (\psi_y)^2 {}^{33}S_{ij}^{xx} + \left( \frac{A_{44} + A_{77}}{4} \right) (\psi_y)^2 {}^{33}S_{ij}^{yy} \Bigg\} d\Omega_e$$

$$
\begin{aligned}
T_{ij}^{36} =& K_{ij}^{36} + \int_{\Omega_e} \Bigg\{ \left(\frac{A_{44}-A_{77}}{4}\right)\left(\frac{\partial u_0}{\partial y}\right) {}^{36}S_{ij}^{x0} + \frac{A_{12}}{2}\left(\frac{\partial u_0}{\partial x}\right) {}^{36}S_{ij}^{y0} \\
&+ \left(\frac{A_{44}+A_{77}}{4}\right)\left(\frac{\partial v_0}{\partial x}\right) {}^{36}S_{ij}^{x0} + \frac{A_{11}}{2}\left(\frac{\partial v_0}{\partial y}\right) {}^{36}S_{ij}^{y0} + \frac{3A_{11}}{2}\left(\psi_x \frac{\partial w_0}{\partial y}\right) {}^{36}S_{ij}^{y0} \\
&- \frac{2A_{12}}{3}\left(\psi_y \frac{\partial w_0}{\partial y}\right) {}^{36}S_{ij}^{x0} - \frac{2A_{12}}{3}\left(\psi_y \frac{\partial w_0}{\partial x}\right) {}^{36}S_{ij}^{y0} \\
&+ 3\left(\frac{A_{44}+A_{77}}{4}\right)\left(\psi_x \frac{\partial w_0}{\partial x}\right) {}^{36}S_{ij}^{x0} - \left(\frac{A_{44}-A_{77}}{3}\right)\left(\psi_y \frac{\partial w_0}{\partial x}\right) {}^{36}S_{ij}^{y0} \\
&- \left(\frac{A_{44}-A_{77}}{3}\right)\left(\psi_y \frac{\partial w_0}{\partial y}\right) {}^{36}S_{ij}^{x0} \Bigg\} d\Omega_e \\
T_{ij}^{37} =& K_{ij}^{37} + \int_{\Omega_e} \Bigg\{ -\frac{A_{11}}{2}\left(\frac{\partial u_0}{\partial x}\right) {}^{37}S_{ij}^{x0} - \left(\frac{A_{44}+A_{77}}{4}\right)\left(\frac{\partial u_0}{\partial y}\right) {}^{37}S_{ij}^{y0} \\
&- \frac{A_{12}}{2}\left(\frac{\partial v_0}{\partial y}\right) {}^{37}S_{ij}^{x0} - \left(\frac{A_{44}-A_{77}}{4}\right)\left(\frac{\partial v_0}{\partial x}\right) {}^{37}S_{ij}^{y0} + \frac{3A_{11}}{2}\left(\psi_y \frac{\partial w_0}{\partial x}\right) {}^{37}S_{ij}^{x0} \\
&- \frac{2A_{12}}{3}\left(\psi_x \frac{\partial w_0}{\partial y}\right) {}^{37}S_{ij}^{x0} - \frac{2A_{12}}{3}\left(\psi_x \frac{\partial w_0}{\partial x}\right) {}^{37}S_{ij}^{y0} \\
&+ 3\left(\frac{A_{44}+A_{77}}{4}\right)\left(\psi_y \frac{\partial w_0}{\partial y}\right) {}^{37}S_{ij}^{y0} - \left(\frac{A_{44}-A_{77}}{3}\right)\left(\psi_x \frac{\partial w_0}{\partial x}\right) {}^{37}S_{ij}^{y0} \\
&- \left(\frac{A_{44}-A_{77}}{3}\right)\left(\psi_x \frac{\partial w_0}{\partial y}\right) {}^{37}S_{ij}^{x0} \Bigg\} d\Omega_e \\
T_{ij}^{63} =& K_{ij}^{63} + \int_{\Omega_e} \Bigg\{ \left(\frac{A_{44}-A_{77}}{4}\right)\left(\frac{\partial u_0}{\partial y}\right) {}^{63}S_{ij}^{0x} + \frac{A_{12}}{2}\left(\frac{\partial u_0}{\partial x}\right) {}^{63}S_{ij}^{0y} \\
&+ \left(\frac{A_{44}+A_{77}}{4}\right)\left(\frac{\partial v_0}{\partial x}\right) {}^{63}S_{ij}^{0x} + \frac{A_{11}}{2}\left(\frac{\partial v_0}{\partial y}\right) {}^{63}S_{ij}^{0y} + \frac{3A_{11}}{2}\left(\psi_x \frac{\partial w_0}{\partial y}\right) {}^{63}S_{ij}^{0y} \\
&- \frac{2A_{12}}{3}\left(\psi_y \frac{\partial w_0}{\partial y}\right) {}^{63}S_{ij}^{0x} - \frac{2A_{12}}{3}\left(\psi_y \frac{\partial w_0}{\partial x}\right) {}^{63}S_{ij}^{0y} \\
&+ 3\left(\frac{A_{44}+A_{77}}{4}\right)\left(\psi_x \frac{\partial w_0}{\partial x}\right) {}^{63}S_{ij}^{0x} - \left(\frac{A_{44}-A_{77}}{3}\right)\left(\psi_y \frac{\partial w_0}{\partial x}\right) {}^{63}S_{ij}^{0y} \\
&- \left(\frac{A_{44}-A_{77}}{3}\right)\left(\psi_y \frac{\partial w_0}{\partial y}\right) {}^{63}S_{ij}^{0x} \Bigg\} d\Omega_e \\
T_{ij}^{66} =& K_{ij}^{66} + \int_{\Omega_e} \left\{ \frac{A_{11}}{2}\left(\frac{\partial w_0}{\partial y}\right)^2 {}^{66}S_{ij}^{00} + \frac{A_{44}+A_{77}}{4}\left(\frac{\partial w_0}{\partial x}\right)^2 {}^{66}S_{ij}^{00} \right\} d\Omega_e \\
T_{ij}^{67} =& K_{ij}^{67} + \int_{\Omega_e} \left\{ -\frac{2A_{12}}{3}\left(\frac{\partial w_0}{\partial x}\frac{\partial w_0}{\partial y}\right) {}^{67}S_{ij}^{00} - \left(\frac{A_{44}-A_{77}}{3}\right)\left(\frac{\partial w_0}{\partial x}\frac{\partial w_0}{\partial y}\right) {}^{67}S_{ij}^{00} \right\} d\Omega_e
\end{aligned}
$$

$$
\begin{aligned}
T_{ij}^{73} =& K_{ij}^{73} + \int_{\Omega_e} \Bigg\{ -\frac{A_{11}}{2} \left( \frac{\partial u_0}{\partial x} \right) {}^{73}S_{ij}^{0x} - \left( \frac{A_{44} + A_{77}}{4} \right) \left( \frac{\partial u_0}{\partial y} \right) {}^{73}S_{ij}^{0y} \\
& - \frac{A_{12}}{2} \left( \frac{\partial v_0}{\partial y} \right) {}^{73}S_{ij}^{0x} - \left( \frac{A_{44} - A_{77}}{4} \right) \left( \frac{\partial v_0}{\partial x} \right) {}^{73}S_{ij}^{0y} + \frac{3A_{11}}{2} \left( \psi_y \frac{\partial w_0}{\partial x} \right) {}^{73}S_{ij}^{0x} \\
& - \frac{2A_{12}}{3} \left( \psi_x \frac{\partial w_0}{\partial y} \right) {}^{73}S_{ij}^{0x} - \frac{2A_{12}}{3} \left( \psi_x \frac{\partial w_0}{\partial x} \right) {}^{73}S_{ij}^{0y} \\
& + 3 \left( \frac{A_{44} + A_{77}}{4} \right) \left( \psi_y \frac{\partial w_0}{\partial y} \right) {}^{73}S_{ij}^{0y} - \left( \frac{A_{44} - A_{77}}{3} \right) \left( \psi_x \frac{\partial w_0}{\partial x} \right) {}^{73}S_{ij}^{0y} \\
& - \left( \frac{A_{44} - A_{77}}{3} \right) \left( \psi_x \frac{\partial w_0}{\partial y} \right) {}^{73}S_{ij}^{0x} \Bigg\} d\Omega_e \\
T_{ij}^{76} =& K_{ij}^{76} + \int_{\Omega_e} \left\{ -\frac{2A_{12}}{3} \left( \frac{\partial w_0}{\partial x} \frac{\partial w_0}{\partial y} \right) {}^{76}S_{ij}^{00} - \left( \frac{A_{44} - A_{77}}{3} \right) \left( \frac{\partial w_0}{\partial x} \frac{\partial w_0}{\partial y} \right) {}^{76}S_{ij}^{00} \right\} d\Omega_e \\
T_{ij}^{77} =& K_{ij}^{77} + \int_{\Omega_e} \left\{ \frac{A_{11}}{2} \left( \frac{\partial w_0}{\partial x} \right)^2 {}^{77}S_{ij}^{00} + \frac{A_{44} + A_{77}}{4} \left( \frac{\partial w_0}{\partial y} \right)^2 {}^{77}S_{ij}^{00} \right\} d\Omega_e
\end{aligned}
$$

APPENDIX C

DMCDM-DISCRETE FORMS OF VARIOUS FUNCTIONS

## C.1 Straight beams

For a function $a(x)$ and $c(x)$, which are assumed to be primal mesh element wise constant, and an independent variable $u(x)$, the following relations are useful in deriving the discretized equations straight beams using DMCDM [10]:

$$\int_{x_a^{(I)}}^{x_b^{(I)}} c\,u\,dx = \tfrac{1}{8}\left[C_{I-1}h_{I-1}U_{I-1} + 3\left(C_{I-1}h_{I-1} + C_I h_I\right)U_I + C_I h_I U_{I+1}\right] \tag{C.1.1}$$

$$\int_{0}^{0.5h_1} a\,u(x)\,dx = \tfrac{1}{8}A_1 h_1\left(U_2 + 3U_1\right)$$

$$\int_{x_b^{(N)}-0.5h_N}^{x_b^{(N)}} a\,u(x)\,dx = \tfrac{1}{8}A_N h_N\left(3U_{N+1} + U_N\right) \tag{C.1.2}$$

$$\int_{x_a^{(I)}}^{x_b^{(I)}} a\,\frac{du}{dx}\,dx = 0.5\left[-A_{I-1}U_{I-1} + \left(A_{I-1} - A_I\right)U_I + A_I U_{I+1}\right] \tag{C.1.3}$$

$$\int_{0}^{0.5h_1} a\,\frac{du}{dx}\,dx = 0.5\,A_1\left(U_2 - U_1\right) \tag{C.1.4}$$

$$\int_{x_b^{(N)}-0.5h_N}^{x_b^{(N)}} a\,\frac{du}{dx}\,dx = 0.5\,A_N\left(U_{N+1} - U_N\right) \tag{C.1.5}$$

$$\left[a\,\frac{du}{dx}\right]_{x_a^{(I)}}^{x_b^{(I)}} = \frac{A_{I-1}}{h_{I-1}}U_{I-1} - \left(\frac{A_{I-1}}{h_{I-1}} + \frac{A_I}{h_I}\right)U_I + \frac{A_I}{h_I}U_{I+1} \tag{C.1.6}$$

$$\left[a\,\frac{du}{dx}\right]_0 = \frac{A_1}{h_1}U_2 - \frac{A_1}{h_1}U_1, \quad \left[a\,\frac{du}{dx}\right]_{x_b^{(I)}+0.5h_N} = \frac{A_N}{h_N}U_{N+1} - \frac{A_N}{h_N}U_N \tag{C.1.7}$$

$$\left[a\,u(x)\right]_{x_a^{(I)}}^{x_b^{(I)}} = 0.5\left[-A_{I-1}U_{I-1} + \left(A_{I-1} - A_I\right)U_I + A_I U_{I+1}\right] \tag{C.1.8}$$

$$\left[a\,u(x)\right]_0^{0.5h_1} = 0.5\,A_1\left(U_2 - U_1\right), \quad \left[a\,u(x)\right]_{0.5h_1} = 0.5\,A_1\left(U_1 + U_2\right) \tag{C.1.9}$$

$$\left[a\,u(x)\right]_{x_b^{(I)}-0.5h_N}^{x_b^{(N)}} = 0.5\,A_N\left(U_{N+1} - U_N\right), \quad \left[a\,u(x)\right]_{0.5h_N} = 0.5\,A_N\left(U_N + U_{N+1}\right) \tag{C.1.10}$$

## C.2 Circular plate

For a functions $a(r)$, which is assumed to be primal mesh element wise constant, and an independent variable $u(r)$, the following relations are useful in deriving the discretized equations of axisymmetric circular plate using DMCDM [7]:

$$\left[ar\frac{du}{dr}\right]_{r_a^{(I)}}^{r_b^{(I)}} = \left(\frac{r_a^{(I)}a_{I-1}}{h_{I-1}}\right)U_{I-1} - \left(\frac{r_a^{(I)}a_{I-1}}{h_{I-1}} + \frac{r_b^{(I)}a_I}{h_I}\right)U_I + \left(\frac{r_b^{(I)}a_I}{h_I}\right)U_{I+1} \tag{C.2.1}$$

$$\left[ar\frac{du}{dr}\right]_{r=0.5h_1} = \frac{a_1}{2}(U_2 - U_1), \qquad \left[ar\frac{du}{dr}\right]_{r=R-0.5h_N} = \frac{a_N(R-0.5h_N)}{h_N}(U_{N+1} - U_N) \tag{C.2.2}$$

$$[rau]_{r_a^{(I)}}^{r_b^{(I)}} = -\left(\frac{r_a^{(I)}a_{I-1}}{2}\right)U_{I-1} + \left(\frac{r_b^{(I)}a_I - r_a^{(I)}a_{I-1}}{2}\right)U_I + \left(\frac{r_b^{(I)}a_I}{2}\right)U_{I+1} \tag{C.2.3}$$

$$[rau]_{r=0.5h_1} = \frac{a_1h_1}{4}(U_1 + U_2), \qquad [rau]_{r=R-0.5h_N} = \frac{a_N(R-0.5h_N)}{2}(U_{N+1} + U_N) \tag{C.2.4}$$

$$[au]_{r_a^{(I)}}^{r_b^{(I)}} = -\left(\frac{a_{I-1}}{2}\right)U_{I-1} + \left(\frac{a_I - a_{I-1}}{2}\right)U_I + \left(\frac{a_I}{2}\right)U_{I+1} \tag{C.2.5}$$

$$[au]_{r=0.5h_1} = \frac{a_1}{2}(U_1 + U_2), \qquad [au]_{r=R-0.5h_N} = \frac{a_N}{2}(U_N + U_{N+1}) \tag{C.2.6}$$

$$[r^2au]_{r_a^{(I)}}^{r_b^{(I)}} = -\frac{r_a^{(I)^2}a_{I-1}}{2}U_{I-1} + \left(\frac{r_b^{(I)^2}a_I - r_a^{(I)^2}a_{I-1}}{2}\right)U_I + \frac{r_b^{(I)^2}a_I}{2}U_{I+1} \tag{C.2.7}$$

$$[r^2au]_{r=0.5h_1} = \frac{a_1h_1^2}{8}(U_1 + U_2), \qquad [r^2au]_{r=R-0.5h_N} = \frac{a_N(R-0.5h_N)^2}{2}(U_N + U_{N+1}) \tag{C.2.8}$$

$$\left[r^2a\frac{du}{dr}\right]_{r_a^{(I)}}^{r_b^{(I)}} = \frac{r_a^{(I)^2}a_{I-1}}{h_{I-1}}U_{I-1} - \left(\frac{r_b^{(I)^2}a_I}{h_I} + \frac{r_a^{(I)^2}a_{I-1}}{h_{I-1}}\right)U_I + \frac{r_b^{(I)^2}a_I}{h_I}U_{I+1} \tag{C.2.9}$$

$$\left[r^2a\frac{du}{dr}\right]_{r=0.5h_1} = \frac{a_1h_1}{4}(U_2 - U_1), \qquad \left[r^2a\frac{du}{dr}\right]_{r=R-0.5h_N} = \frac{a_N(R-0.5h_N)^2}{h_N}(U_{N+1} - U_N) \tag{C.2.10}$$